RADIO INTERFEROMETRIC SEARCHES FOR GALACTIC CENTER PULSARS AND FAST RADIO BURSTS

A Dissertation

Presented to the Faculty of the Graduate School

of Cornell University

in Partial Fulfillment of the Requirements for the Degree of

Doctor of Philosophy

by

Robert Stockton Wharton

August 2017

© 2017 Robert Stockton Wharton

ALL RIGHTS RESERVED

RADIO INTERFEROMETRIC SEARCHES FOR GALACTIC CENTER PULSARS AND FAST RADIO BURSTS

Robert Stockton Wharton, Ph.D.

Cornell University 2017

We investigate the pulsar population in the Galactic center and discuss novel observational strategies to discover pulsars in orbit around the black hole Sgr A*. In order to motivate these searches, we first use published multi-wavelength observations to set constraints on the allowed population of radio pulsars in the Galactic center. Since the parameters of any search depend strongly on the scattering of pulsar signals in the interstellar medium, we study the distribution of free electrons along the line of sight to the Galactic center. Next, we conduct a single pulse analysis on pulses from the radio-emitting magnetar J1745−2900. This analysis provides additional information on the amount of scattering along the line of sight and presents an opportunity to study a rare type of neutron star whose presence in the vicinity of Sgr A* may have important implications for the pulsar population in the Galactic center. Using the Karl G. Jansky Very Large Array (VLA) we conduct two Galactic center pulsar searches using newly developed pulsar observing modes. Finally, we use the new fast-visibility VLA observing mode to provide the first arcsecond localization of a Fast Radio Burst.

BIOGRAPHICAL SKETCH

Robert Stockton Wharton was born in New Castle[1], Delaware in 1987. In 1994, he moved with his family just across the border into Pennsylvania, where he stayed through high school. Wharton attendend the Pennsylvania State University where he studied Physics and Mathematics. In graduate school at Cornell University, he studied pulsar astronomy. He will continue his pulsar work at the Max Planck Institute for Radio Astronomy in the fall.

[1]Though quite far from the center of the Galaxy, New Castle is located at the exact center of the Twelve-Mile Circle that defines the border between Delaware and Pennsylvania (as well as a small portion of the border with New Jersey). The circle has a strange history that goes back to the early seventeenth century when Dutch settlers first attempted to colonize the area. In true colonial fashion, the settlers claimed the region as their own, forcibly removed the native population, and then almost immediately all died. Swedish colonists came in next and took the land from the Dutch. After a few years the Dutch set up a fort in New Castle and took back the land from the Swedes. Less than a decade later the English kicked out the Dutch and Delaware was included in the charter given to William Penn by Charles II. This soon led to a border dispute with Maryland, which claimed the land under the charter given to them by Charles I. It turns out, the cartographically challenged Charleses had decreed contradictory and impossible borders for the territories.

The surveyor-astronomer duo of Charles Mason and Jeremiah Dixon were sent in to resolve the border dispute. They surveyed the Delmarva penninsula and then (more memorably) westward along the current Pennsylvania-Maryland border. They made measurements on the journey out west and, to mitigate random errors, made the same measurements on the return trip back east. Mason and Dixon noticed a systematic error present in both trips, which Nevil Maskelyne interpreted as the gravitational deflection of the astronmers' plumb line by the Allegheny Mountains. Maskelyne later used this technique to determine the average density of the Earth.

On the other side of the Delaware River, the border defined by the Twelve-Mile Circle between Delaware and New Jersey has also been disputed. Delaware claims all of the Delaware River enclosed within the circle, which means that as soon as you step into the Delaware River from New Jersey side, you are in Delaware. This is different from nearly all other river borders that adopt the middle of the river as the border line. Extemely low-stakes litigation between the two states over a tiny sliver of land has been ongoing since the 1800s and has reached the Supreme Court several times. In the 1934 case of *New Jersey v. Delaware*, the states were prohibited from litigating the matter again. Despite this prohibition, the most recent border dispute case was decided by the court in 2008.

To my family.

ACKNOWLEDGEMENTS

As someone of very modest talent and ambition, it is only through the constant support of others that I have been able to pursue my interests to the extent that I have. There are countless people who have helped me over the years (either directly or indirectly). Space constraints prevent me from thanking you all individually, but if you're out there, thanks!

I do want to single out some people though.

Most importantly, I would like to thank my parents for all the love and support they have given me over the years. They have enthusiastically cheered me on every step of the way and for this I am both fortunate and grateful.

Jim Cordes and Shami Chatterjee have made all of the work presented in this thesis possible. I have enjoyed my time working in the pulsar group and learned a great deal from both of you.

Walid Majid supported me for a couple summers at JPL. I always enjoyed my trips to Pasadena to work with Walid and appreciate his help and guidance.

I also want to thank the many collaborators who helped with much of this work. Joe Lazio and Paul Demorest in particular were tremendously helpful as I struggled to learn as much as possible about the VLA.

Finally, I want to thank my friends at Cornell who shared this experience with me. Specifically, thanks to Matt and Alemi who got lunch with me almost every day for more years than any of us probably care to admit.

TABLE OF CONTENTS

LIST OF TABLES

LIST OF FIGURES

CHAPTER 1

INTRODUCTION

Centers hold secrets. Enclosed and isolated, the innermost regions of natural and constructed spaces have long been associated with a sense of mystery. Sometimes this is religious or reverential. In the Hebrew Bible, the inner sanctum of Solomon's Temple was called the Holy of Holies and housed the Ten Commandments. Far more often, though, the mysterious center is terrifying. At the center of the Labyrinth, Theseus found the monstrous Minotaur. At the heart of a brutally colonized continent, Marlowe found Kurtz driven mad with power. The most startling example of a central horror comes from the *Divine Comedy*. In Dante's pre-Copernican cosmology, the Earth is the center of the universe and at the center of the Earth are the concentric circles of Hell. In the innermost ring of this nesting-doll netherworld (at the *exact* center of the universe), the three-faced devil is trapped for eternity in waist-deep ice, feasting on history's greatest traitors and whipping up a massive windstorm with three sets of giant bat wings. But then again, there's a delicious Tootsie Roll at the center of every Tootsie Roll Pop, so maybe we are over-thinking this.

At the center of our Galaxy is a supermassive black hole called Sagittarius A* (Sgr A*). It is four million times more massive than the Sun and has an event horizon (the point within which not even light can escape) that extends out to about 0.1 AU (roughly a third of the size of the orbit of Mercury). While no light escapes from the black hole, its immediate surroundings produce very bright emission in radio and X-rays (Genzel et al. 2010). The shadow of the event horizon against the bright emission of the accretion disk may be soon resolved by the Event

Horizon Telescope[1], which is a global array of telescopes observing at millimeter wavelengths.

Since the black hole cannot be imaged directly, its properties have to be inferred from its effects on the environment. Currently, the best way of doing this is to monitor the orbits of bright stars around Sgr A*. Several groups have conducted the painstaking observations over the last 25 years to observe dozens of stars orbit around the black hole (Gillessen et al. 2017). While these observations prove that Sgr A* must be a black hole and give measurements of its mass to about 10%, they are ultimately limited by the resolution available to ground-based telescopes. In order to measure any other properties of the black hole, another method is needed. Finding and observing a radio pulsar in orbit around Sgr A* is one way to do this.

Radio pulsars are neutron stars with extremely strong magnetic fields that produce very bright beamed radio emission. As the neutron star rotates, these beams sweep across the sky like a lighthouse. When the radio beam crosses along the line of sight of an observer, that observer sees a pulse. Since both the rotation period and the average shape of the pulse are remarkably stable in time, the pulsar acts as an astrophysical clock of exquisite precision. By observing the arrival times of pulses, an observer can determine the orbit of a pulsar and even in extreme cases map out the spacetime along the line of sight (Lorimer & Kramer 2004).

Finding even a single radio pulsar in a 10 year or less orbit around Sgr A* (comparable to the current stars being observed) may allow for the measurement of the mass, spin, and even quadrupole moment of the black hole to a high degree of precision (Liu et al. 2012). From these measurements it is possible to test key predictions about black holes, like their simplicity (No Hair Theorem) and the

[1]http://eventhorizontelescope.org

existence of an event horizon (Cosmic Censorship Conjecture). Additionally, such a pulsar could be used to improve the measurement of the distance to the Galactic center, a key Galactic parameter.

No pulsar has yet been found in a suitable orbit around Sgr A*, despite many targeted searches (Johnston et al. 2006; Deneva et al. 2009; Macquart et al. 2010) and the expectation of a large population of neutron stars in the inner Galaxy (Pfahl & Loeb 2004). While it is possible that there are simply too few pulsars to expect a detection, there are also a number of observational difficulties that may have prevented new discoveries. At a distance of 8.3 kpc from the Sun (Gillessen et al. 2009), the Galactic center is farther away than most known pulsars, which means the pulsars will appear much fainter. The inner degree or so of the Galactic center also contains a large number of supernova remnants, star forming regions, and other bright radio structures which increase the noise of any pulsar survey (LaRosa et al. 2000). Finally, the line of sight from the Earth to Sgr A* contains a turbulent electron plasma that distorts the pulsar signal in a manner that can be mitigated but not removed (Lazio & Cordes 1998a; Bower et al. 2014).

The enormous scientific reward for finding a puslar in orbit around Sgr A* strongly motivates the development of new search strategies and techniques. In order to conduct useful surveys, we need to first understand why pulsars have been missed before. In this thesis, we will seek to determine the nature of the Galactic center pulsar population and understand why these pulsars have eluded detection. Building on this work, we will develop and implement new observing strategies for finding Galactic center pulsars with the Karl G. Jansky Very Large Array (VLA).

An outline of this thesis is as follows. In Chapter 2, we set constraints on the total pulsar population based on a variety of previously published observations

over a wide range of wavelengths. In Chapter 3, we investigate the distribution of free electrons along the line of sight to the Galactic center, which is essential for designing effective searches. In Chapter 4, we present a single pulse analysis of pulses from the Galactic center magnetar J1745–2900. In Chapter 5, we presents the results of a VLA search for pulsars in the immediate vicinity of Sgr A* using a new phased-array pulsar observing mode. In Chapter 6 we present the premliminary results of a search for pulsars in the inner parsec around Sgr A* using the VLA in a new fast-sample visibility observing mode at 2–4 GHz. Finally, in Chapter 7, we use the fast-sample observing method developed for Galactic center pulsar searches to achieve the first arcsecond localization of a Fast Radio Burst.

CHAPTER 2

MULTIWAVELENGTH CONSTRAINTS ON PULSAR POPULATIONS IN THE GALACTIC CENTER[1]

2.1 Introduction

The discovery of one or more pulsars in the inner parsecs around Sgr A*, the massive black hole (MBH) at the center of our Galaxy, would provide an invaluable tool for studying the innermost regions of the Galactic Center (GC). Most of the current understanding of the inner parsec comes from infrared observations of the nuclear star cluster (for a recent review, see Genzel et al. 2010). The nuclear star cluster is centered on Sgr A* and consists of young massive stars at a projected radius of $r \approx 0.5$ pc and a dense collection of B-stars (the "S-stars") within $r \leq 0.04$ pc with the closest orbit passing just 6×10^{-4} pc (≈100 AU) from Sgr A* (Schödel et al. 2002; Ghez et al. 2003). Two decades of monitoring the orbits of these S-stars has yielded the mass of the central object to be $M = 4 \times 10^6 M_\odot$, unambiguously classifying it as a MBH (Ghez et al. 2008; Gillessen et al. 2009).

Despite the success of tracking stellar orbits in the infrared, the sensitivity of this method is ultimately limited by source confusion. The detection of a radio pulsar at a similar distance with an orbital period of $P_{orb} \lesssim 100$ yr would provide unparalleled tests of gravity in the strong-field regime. The timing of such a pulsar could allow the measurement of the spin or quadrupole moment of the MBH (Pfahl & Loeb 2004; Laguna & Wolszczan 1997; Wex & Kopeikin 1999; Liu et al. 2011). Additionally, a pulsar found anywhere in the inner few parsecs of the Galaxy

[1]Previously Published: Wharton, R. S., Chatterjee, S., Cordes, J. M., Deneva, J. S., & Lazio, T. J. W. 2012, *ApJ*, 753, 108

would provide a useful probe of the GC environment. The mere detection of a pulsar would place constraints on the star formation history and measurements of the dispersion measure and pulse broadening times would provide information on the electron density distribution of the region.

However, even with the detection of almost 2000 radio pulsars in the Galaxy (Manchester et al. 2005) and several directed searches of the GC, only five pulsars have been found within $15'$ of Sgr A* and the closest of these is $11'$ away (Deneva et al. 2009; Johnston et al. 2006; Bates et al. 2011). While these few objects indicate the existence of a GC pulsar population, the perceived dearth of pulsars near Sgr A* is the result of interstellar scattering from turbulent plasma, which temporally broadens pulses to approximately $2000\nu_{\rm GHz}^{-4}$ s (where $\nu_{\rm GHz}$ is the observing frequency in GHz) at the center of the Galaxy (Cordes & Lazio 2002). Pulse broadening makes it almost impossible to detect even long-period pulsars in periodicity searches at commonly used frequencies ($\nu \sim 1$ GHz). To mitigate the deleterious effects of interstellar scattering, periodicity searches of the GC have migrated to higher frequencies ($\nu \sim 10$ GHz). However, since pulsars have power-law spectra of the form $S(\nu) \propto \nu^{\alpha}$ (with $\alpha < 0$), increasing the observing frequency also decreases the observable flux density. To date, high-frequency searches have produced no new detections using existing 100-m class telescopes (Deneva 2010; Macquart et al. 2010)

Even though the absence of pulsar detections in the central parsecs of the GC is well explained by scattering effects, the existence of a GC pulsar population was established by Deneva et al. (2009) based on the five pulsars on the outskirts of the region that cannot be explained as foreground disk objects. Since future surveys can benefit from better knowledge of the pulsar populations in the GC, we

use a suite of multiwavelength observations to set constraints on the number and distribution of pulsars in the inner regions of the Galaxy on ∼100 pc and ∼1 pc scales. An illustration of the structure of the GC on these scales is shown in Figure 2.1.

In this paper, we present observational constraints on the pulsar populations in the GC. A brief overview of the conventions and notations used in this paper are presented in Section 2.2. In Section 2.3, population limits are set from the detections of pulsars in the inner 15′ and from non-detections in the vicinity of Sgr A* on parsec scales. In Section 2.4, a catalog of steep-spectrum radio sources in the inner 150 pc is considered. Interferometric measurements of the spectrum of Sgr A* are used in Section 2.5 to set upper limits on the pulsar population in the GC on arcsecond scales. In Section 2.6, *Fermi* observations of the diffuse gamma-ray flux of the inner degree of the GC are used to estimate the millisecond pulsar population in the GC. In Section 2.7, infrared observations of young massive stars are used to estimate the number of neutron stars produced in the inner parsec of the Galaxy. *Chandra* X-ray observations of pulsar wind nebulae are used to constrain the pulsar population in the inner 20 pc in Section 2.8. In Section 2.9, limits are set on the intrinsic neutron star population in the GC based on the estimated supernova rate. Finally, in Section 2.10, the estimates are summarized and discussed.

2.2 Conventions and Notations

We note briefly a few conventions and notations that we adopt in this paper. The name "Sgr A*" is used to describe both the MBH and the compact radio source at

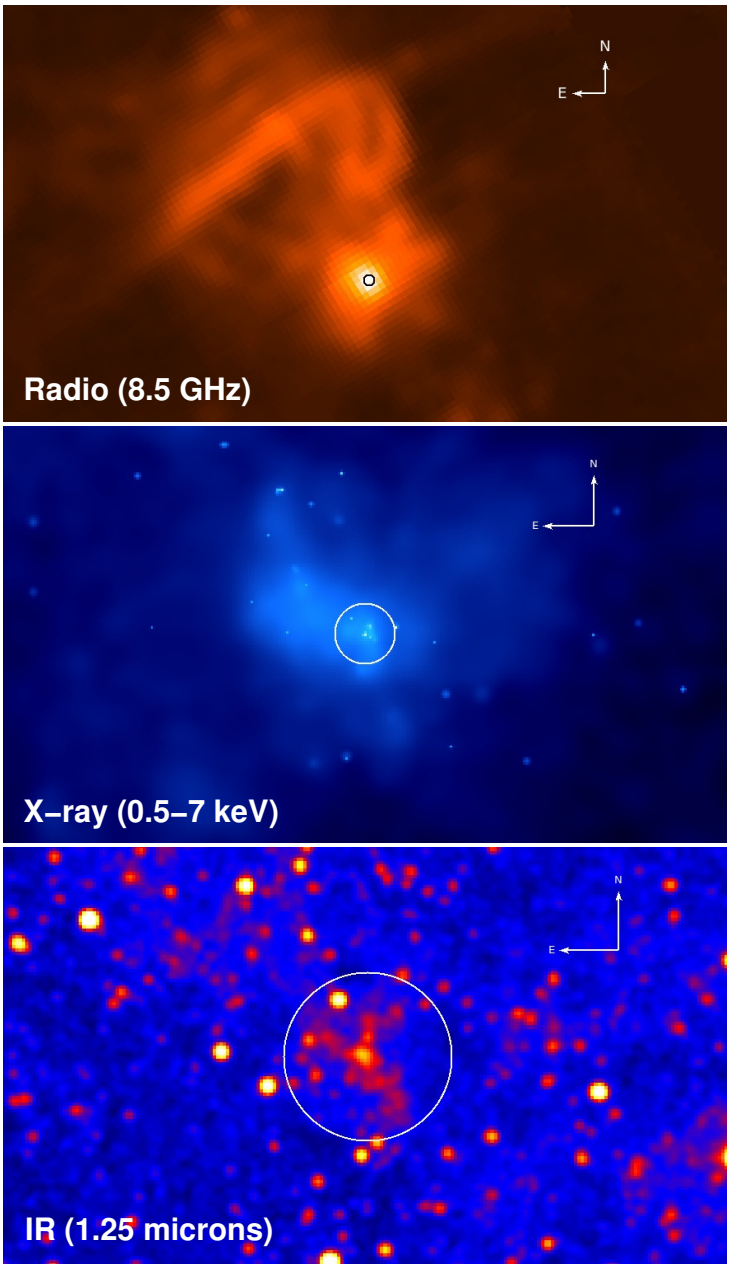

Figure 2.1: **Views of the inner GC region at radio, X-ray and infrared wavelengths**. From top to bottom, the GC is shown in radio at 8.5 GHz as observed with the Green Bank Telescope (data courtesy Casey Law), in 0.5–7 keV X-rays as observed with the *Chandra* ACIS-I instrument, and at J band (1.25 μm) as observed in 2MASS (Skrutskie et al. 2006). In each panel, a circle with radius 25″ (corresponding to 1 pc at 8.5 kpc) is centered on Sgr A* with J2000 coordinates of ($17^{\rm h}45^{\rm m}40\overset{\rm s}{.}0409$, $-29°00'28\overset{''}{.}118$) given by Reid & Brunthaler (2004).

the dynamical center of the Galaxy. In the event where a distinction must be made (for example, Section 2.5), "Sgr A*" is taken to mean the observed radio source. All distances from Sgr A* are given as a projected distance unless explicitly stated otherwise. The distance from Earth to Sgr A* is taken to be $d = 8.5$ kpc (Ghez et al. 2008; Gillessen et al. 2009).

Pulse broadening times are taken from the NE2001 electron density model of Cordes & Lazio (2002). The NE2001 model accounts for the geometry of the scattering region in the GC, and as such, it is preferable over empirical fits to pulsars in the Galactic disk (e.g. Bhat et al. 2004), which do not consider the particular scattering geometry of the GC. As discussed in Deneva et al. (2009), NE2001 tends to overestimate the scattering times for the five pulsars closest to Sgr A* by factors of $\sim 10^2 - 10^3$. However, these pulsars likely lie along the edges of the GC scattering region where slight ($\sim$0.1 kpc) changes to the line of sight distance can cause dramatic (factors of $\sim 10^4$) changes in scattering times with only modest (factor of $\sim$2) changes in DM. Additionally, we note that the scattering times of pulsars deeper in the GC will be highly constrainted by the measured angular scattering of Sgr A* itself.

Pulse broadening times are found at arbitrary observing frequencies by scaling the 1 GHz values given by NE2001 as $\propto \nu^{-4}$ (Lambert & Rickett 1999). However, see Löhmer et al. (2001) for potentially significant deviations from this scaling in highly scattered pulsars.

All pulsar population estimates are given as the number of active radio pulsars beamed towards the Earth, where a beaming fraction of $f_b = 0.2$ is assumed for all pulsars. The fixed beaming fraction of $f_b = 0.2$ comes from a simple model in which the magnetic dipole moment is oriented randomly with respect to the rotation axis

(Emmering & Chevalier 1989). A better empirical fit to the data is provided by the period-dependent model of Tauris & Manchester (1998), which typically finds $f_b \sim 0.1$ for isolated pulsars. However, since the Tauris & Manchester (1998) model does not include millisecond pulsars that may have beaming fractions as high as $f_b \approx 0.5 - 0.9$ (Kramer et al. 1998), we adopt the $f_b = 0.2$ value as a population-wide representative value. As this factor only shows up in our analysis as a multiplicative constant, it is trivial to scale our results to different beaming fractions.

In many of the limits presented below, it will be necessary to utilize a distribution for pulsar pseudo-luminosities ($L = Sd^2$). We adopt the power-law distribution of Lorimer et al. (2006) with a minimum cutoff in preference to distributions that do not require cutoffs like the log-normal model of Faucher-Giguère & Kaspi (2006). Both are two parameter models and the power-law distribution provides a much better empirical fit to the observations (see, e.g., Figure 6 of Lorimer et al. 2006). However, if the log-normal distribution were used instead of the power-law in the calculations below, the total pulsar populations predicted would be larger by factors of 10-100 owing to the much larger fraction of low luminosity objects. As a result, our adoption of the power-law pseudo-luminosity distribution is a conservative one in the sense that using another distribution would predict a *larger* pulsar population.

Lastly, we note that in some cases our constraints will involve all types of pulsars, while others involve one of two subsets of pulsars: the "canonical" pulsars (CPs) and recycled or "millisecond" pulsars (MSPs). CPs have periods of $P \sim 1$ s, surface magnetic fields $B \sim 10^{12}$ G and active radio lifetimes of $\tau \sim 10^7$ years, while MSPs have periods $P \lesssim 10$ ms, low surface magnetic fields $B \lesssim 10^9$ G and

active radio lifetimes of $\tau \sim 10^9 - 10^{10}$ years.

2.3 Constraints from Pulsar Surveys of the GC

Several pulsar searches have been conducted in the inner degree of the Galaxy. To date, only five pulsars have been detected within $15'$ of Sgr A*, with none closer than $11'$ (Manchester et al. 2005). To have any chance of making detections in the inner few arcminutes of the Galaxy, higher observing frequencies must be used to overcome the roughly $2000\nu_{\rm GHz}^{-4}$ s broadening times caused by scattering. Deep searches have been attempted at frequencies from 4–15 GHz, but have made no detections in the inner few parsecs around Sgr A* (Johnston et al. 2006; Deneva 2010; Macquart et al. 2010). Both the pulsar detections in "low-frequency" (2–3 GHz) surveys and the absence of detections in high-frequency (4–15 GHz) directed searches can be used to constrain the GC pulsar population.

2.3.1 GC Pulsar Detections in Low-Frequency Surveys

The five known pulsars within $15'$ of Sgr A* currently provide the best direct evidence for an intrinsic GC pulsar population. Of these five pulsars, two were detected at 3.1 GHz with the Parkes radio telescope (Johnston et al. 2006) and three[2] were detected at 2 GHz with the Green Bank Telescope (Deneva et al. 2009). In each of these surveys, the expected number of detectable disk pulsars in the field of view is $\ll 1$. Thus, the detections strongly suggest a pulsar population in the GC that is distinct from that of the disk.

[2]One of these pulsars, J1746−2850, was independently discovered by Bates et al. (2011) in a Parkes 6.5 GHz multibeam survey.

In an attempt to constrain the number and spatial distribution of the GC pulsars, Deneva et al. (2009) simulated the pulsar population to determine what would be consistent with the survey detections. A simple two-component density model of the form

$$n_{GC} \propto \exp\left(-\frac{h^2}{H_{GC}^2}\right) \exp\left(-\frac{r^2}{R_{GC}^2}\right) \tag{2.1}$$

was adopted with $H_{GC} = 26$ pc fixed to coincide with the scale height of the scattering screen in the NE2001 electron density model of Cordes & Lazio (2002). The density distribution was normalized so that, for a given R_{GC}, there were a total of N_{GC} pulsars (not necessarily beamed towards Earth) associated with the population.

Using Monte Carlo methods, Deneva et al. (2009) then generated 1000 pulsar populations consistent with Eq. 2.1 for each (R_{GC}, N_{GC}) pair and determined how many of these pulsars would have been detected in their 2.1 GHz survey. Searching over a grid of values and performing a maximum likelihood analysis, Deneva et al. (2009) found lower bounds of $N_{GC} \gtrsim 2000$ and $R_{GC} \gtrsim 0.3$ kpc for the parameters. Thus, this analysis provides additional evidence for an intrinsic pulsar population in the GC.

Although Deneva et al. (2009) have set a lower bound on N_{GC}, this parameter applies to the entire GC population and does not necessarily translate into a lower bound on the number of pulsars within a particular distance from Sgr A*. For example, a distribution with $N_{GC} = 2000$ and $R_{GC} = 0.3$ kpc will produce a very different number of pulsars within 100 pc of Sgr A* than will a distribution with $N_{GC} = 2000$ and $R_{GC} = 0.6$ kpc. Regardless, the existence of a pulsar population in the GC is firmly established.

We note briefly that the primary reason the Deneva et al. (2009) analysis does

not find upper bounds on the parameters N_{GC} and R_{GC} even after extending the grid to $N_{GC} = 10^4$ and $R_{GC} = 5$ kpc is that the only constraints come from the detections in the survey region ($r \lesssim 50$ pc). Incorporating survey results from the inner few degrees of the Galaxy would certainly introduce upper bounds to the parameters.

With this in mind, it is instructive to consider the results at a fixed R_{GC}. From Figure 4 of Deneva et al. (2009), we see that a wide range of N_{GC} values with $N_{GC} \gtrsim 500$ are equally likely for $R_{GC} = 0.1$ kpc. Thus, a very conservative lower bound on the number of pulsars in the inner 100 pc of the Galaxy that are beamed towards Earth is $N_{psr} \gtrsim 100$ (where we have assumed a beaming fraction of 0.2).

2.3.2 High-Frequency Pulsar Searches of the Central Parsec

Recently, searches of the central few parsecs around Sgr A* have been conducted with the Green Bank Telescope (GBT) at 5 GHz and 9 GHz (Deneva 2010) and at 15 GHz (Macquart et al. 2010). No pulsars were detected in any of these searches. We follow a similar analysis to that of Macquart et al. (2010) to estimate an upper limit to the pulsar population based on the absence of detections.

Observations

The 5 and 9 GHz observations were carried out by Deneva (2010) in 2006. Since no pulsar candidates were detected, limits on the flux density of periodic signals

may be set using the radiometer equation

$$S_{min,\nu} = \frac{mT_{sys}}{\eta G\sqrt{N_h N_{pol}\Delta\nu T_{obs}}}, \tag{2.2}$$

where T_{sys} is the system temperature, G is the telescope gain, $\eta \approx 0.8$ is a correction factor that accounts for system imperfections and the digitization of the signal, $N_h = 16$ is the maximum number of harmonics summed in a periodicity search, $N_{pol} = 2$ is the number of polarization channels summed, $\Delta\nu = 800$ MHz is the receiver bandwidth and $T_{obs} = 6.5$ hr is the observation time. The telescope gain is given by $G = 1.85$ K/Jy and $G = 1.8$ K/Jy for observing frequencies of 5 and 9 GHz, respectively. The value of m is determined by the detection significance threshold set at $m\sigma$. In this FFT search the threshold was set to 6σ, so $m = 6$.

The system temperature of the telescope is given by[3] $T_{sys} = T_{rec} + T_{bg}$. The receiver temperature of the GBT[4] is 18 K at 5 GHz and 27 K at 9 GHz. The dominant contribution to the background temperature is the bright extended Sgr A Complex (comprised of Sgr A East and Sgr A West), which surrounds Sgr A*. We may set lower bounds on this background using data from a multiwavelength survey by Law et al. (2008), which imaged the GC at 1.4, 5 and 9 GHz. Only lower bounds may be set since a non-trivial iterative scheme was used to subtract out the noise contributions from the atmosphere. Law et al. (2008) found the flux density of the Sgr A Complex to be 85 Jy beam^{-1} at 5 GHz and 39 Jy beam^{-1} at 9 GHz, which translate to background temperatures of $T_{bg} = 157$ K and $T_{bg} = 70$ K, respectively. Thus, the system temperature is $T_{sys} = 175$ K at 5 GHz and $T_{sys} = 97$ K at 9 GHz. From Eq. 2.2, we find that $S_{min,\nu} = 29$ μJy at 5 GHz and $S_{min,\nu} = 17$ μJy at 9 GHz.

[3]We take T_{rec} to include all non-astronomical contributions to the system temperature from the receiver, spillover effects, and the atmosphere.

[4]GBT Proposer's Guide: `http://www.gb.nrao.edu/gbtprops/man/GBTpg.pdf`

Likewise, Macquart et al. (2010) conducted a search for pulsars at 14.8 and 14.4 GHz using the GBT in 2006 and 2008. The Macquart et al. (2010) search used a 10σ detection threshold and combined observations to get an effective observation time of $T_{obs} \approx 9.75$ hr. The system temperature was determined to be $T_{sys} \approx 35$ K by firing a noise diode on a calibrator source. No pulsars were detected and a 10σ detection threshold flux density of $S_{min,\nu} \approx 10$ μJy is set from the 14.4 GHz measurements.

Upper Limits on Observable Pulsar Population

Assuming that a given pulsar in the GC will be detected with some probability p_d, binomial statistics can be used to find the maximum number of pulsars consistent with zero detections. The simplest way to determine p_d is to set it equal to the fraction of pulsars bright enough to be seen in each survey when placed at Sgr A*. This fraction can be estimated from the 1.4 GHz pseudo-luminosity function, which is given by $dN/d\log L \propto L^{-\beta}$ taken over a range of pseudo-luminosities from $L_{min} = 0.1$ mJy kpc^2 to $L_{max} = 10^4$ mJy kpc^2. We adopt a value of $\beta = -0.7$ as an average of the two fits found by Lorimer et al. (2006) of over 1000 pulsars observed in the Parkes Multibeam Survey. The detection probability is then given by $p_d = f_L(L > L_{det})$, where

$$L_{det} = S_{min,\nu} \left(\frac{1.4 \text{ GHz}}{\nu} \right)^{-1.7} d_{gc}^2 \tag{2.3}$$

and $S_{min,\nu}$ is the minimum detectable flux density of the search. Using the $S_{min,\nu}$ values found by each search (see Table 2.1) we find that $p_d = (0.027, 0.020, 0.015)$ at $\nu = (5, 9, 15)$ GHz.

Given the above detection probabilities and the lack of any detections in the surveys, the upper limits to the number of pulsars (at 99% confidence level) are

found to be $N = (170, 230, 299)$ for the 5, 9 and 15 GHz observations, respectively. However, since a pulsar with a spin period less than the pulse broadening time would have a greatly reduced chance of being detected, the calculated upper limits are for pulsars with $P \gtrsim \tau_{sc}$. Using the 1 GHz scattering time from the NE2001 model of Cordes & Lazio (2002) and scaling ($\propto \nu^{-4}$) to the appropriate frequency, the scatter broadening times are found to be $\tau_{sc} = (4.2, 0.44, 0.05)$ s at observing frequencies of $\nu = (5, 9, 15)$ GHz.

Implications for Total GC Pulsar Population

The upper limits of Section 2.3.2 are only valid for pulsars within certain period ranges. To make an estimate of the total number of pulsars, knowledge of the underlying pulsar period distribution is needed. Though the period distribution of pulsars in the inner parsecs of the GC is entirely unknown, a reasonable approximation would be to assume the same distribution as the local pulsar population (to reduce observational biases). From the ATNF pulsar catalog[5] (Manchester et al. 2005), we see that there are 88 pulsars within 1 kpc of Earth. Of these, 5 have $P > 4.2$ s, 38 have $P > 0.44$ s and 55 have $P > 50$ ms. This gives $f_P(P > 4.2 \text{ s}) = 0.06$, $f_P(P > 0.44 \text{ s}) = 0.43$ and $f_P(P > 50 \text{ ms}) = 0.63$ for the fractions of pulsars with periods greater than the scatter broadening times.

Assuming these values are representative of the GC population, we can estimate upper bounds on the total number of pulsars (regardless of period) to be $N_{max} = N/f_P$. Applying these corrections to the estimates of Section 2.3.2 gives $N_{max} =$

[5] http://www.atnf.csiro.au/research/pulsar/psrcat/

ν (GHz) (1)	S_{min} (μJy) (2)	τ_{sc} (s) (3)	$f_L(L > L_{det})$ (4)	$N(P \gtrsim \tau_{sc})$ (5)	$f_P(P > \tau_{sc})$ (6)	N/f_P (7)	r (pc) (8)	Ref (9)
4.85	29	4.2	0.027	< 170	0.06	< 2830	3.0	(1)
6.6	550†	1.28	0.002	< 2220	0.17	< 13000	4.0	(2)
8.4	200	0.46	0.003	< 1380	0.43	< 3200	3.0	(3)
8.50	17	0.44	0.020	< 230	0.43	< 535	1.5	(1)
14.4	10	0.05	0.015	< 299	0.63	< 475	1.0	(4)

Table 2.1: **Pulsar Upper Limits of High-Frequency Surveys of the Central Parsecs**. Columns 1 and 2 give the center frequency and minimum detection threshold, respectively, of a given survey. Column 3 gives the scattering time at the survey center frequency of a pulse originating from the GC as calculated with the NE2001 model (Cordes & Lazio 2002). Column 4 gives the fraction of pulsars bright enough to be detected at the GC with the survey sensitivity (see Eq. 2.3). Column 5 gives 99% upper limit values to the number of pulsars that could potentially have been seen by the survey (that is, have $P \gtrsim \tau_{sc}$). Column 6 gives the fraction of pulsars in the ATNF catalog (Manchester et al. 2005) that have periods longer than the scattering time and Column 7 gives an estimated upper bound for the total number of pulsars in the GC. Column 8 gives the projected radial distance of the beamsize at the distance of Sgr A* and Column 9 gives the reference from which the survey was taken: (1) Deneva 2010; (2) Bates et al. 2011; (3) Johnston et al. 2006; (4) Macquart et al. 2010.
†The value provided for S_{min} here is 9 times that given in Section 2.2 of Bates et al. (2011), which we believe to be a calulation error.

$(2830, 535, 475)$ for observing frequencies of $\nu = (5, 9, 15)$ GHz.

The half-power beam width of the GBT is $\theta(\nu) \approx 150''(\nu/5\ \mathrm{GHz})^{-1}$. At Sgr A*, the projected radii of these beams are $r \approx (3.0, 1.5, 1.0)$ pc at 5, 9 and 15 GHz, respectively. Thus, we estimate that there are as many as $N_{max} < 2830$ pulsars beamed towards Earth within $r \approx 3.0$ pc of Sgr A*, $N_{max} < 535$ within $r \approx 1.5$ and $N_{max} < 475$ within $r \approx 1$ pc.

The results of this section are summarized in Table 2.1. In addition to the surveys of Deneva (2010) and Macquart et al. (2010), we also include for reference the less sensitive GC pointings from surveys by Johnston et al. (2006) and Bates et al. (2011).

Caveats

A number of assumptions are made in the upper limit estimates of the previous sections, so it is important to consider what happens if the assumptions fail. The first assumption is that the probability of detecting a pulsar (with period large enough not to be smeared out by interstellar scattering) is equal to the fraction of pulsars with 1.4 GHz pseudo-luminosities large enough to be detected at the GC. Since the detection probability only considers the best-case sensitivity of the telescope and ignores any effects of radio-frequency interference at the telescope end or intermittency at the pulsar end, it is likely to be an overestimate. An overestimate of the detection probability would result in an underestimate of the upper bound on the number of pulsars.

Another assumption is that the 1.4 GHz pseudo-luminosity distribution of pulsars in the GC is the same as those in the Galactic field. However, if the GC region

contains a larger number of low-luminosity MSPs, then the detection probability will again be overestimated and the upper limit underestimated. One could also imagine the case where enough bright young pulsars exist in the GC as a result of recent star formation to skew the pseudo-luminosity distribution to higher luminosities. In that case, the detection probability would be an underestimate and the upper limits an overestimate.

We have also assumed that the upper limits are for pulsars with $P > \tau_{sc}$. However, as the scattering time gets to be a significant fraction of the pulsar period, it will start to smear out the signal and reduce the number of detectable harmonics. Since this is a gradual process, it will likely make some pulsars undetectable even with $P > \tau_{sc}$. As a result, we would be overestimating the minimal detectable period, which would cause the upper bound to be an underestimate.

Finally, we have assumed that the period distribution of the pulsars within one kiloparsec of Earth is representative of the GC population. This certainly does not have to be the case, as the star formation histories of the Galactic field and GC are likely to be different. For example, the GC could potentially have a much higher concentration of young pulsars and old MSPs as compared to the Galactic disk. The increased stellar encounter rate in the GC could favor MSP production and any recent starburst would favor young pulsars. In both cases, the periods would be biased low. Thus, the period distribution would be skewed lower than assumed and the fraction of pulsars with periods greater than a certain value will be overestimated. This will result in the upper bound being underestimated.

Since most of the assumptions made tend to decrease the upper limits, our estimates are best interpreted as the most restrictive upper bounds to the pulsar population in the inner few parsecs of the GC.

2.4 Radio Point Sources

Motivated by the study of GC pulsar search methods by Cordes & Lazio (1997), Lazio & Cordes (2008) performed a VLA survey of compact radio sources in the inner degree of the Galaxy. Though pulsars cannot be identified by their pulsed emission in an imaging survey, promising pulsar candidates may be found by looking for steep-spectrum sources with angular diameters consistent with the angular broadening of point sources caused by scattering at locations near Sgr A* ($\approx 1''$ at 1 GHz). Of the 170 compact radio sources cataloged, Lazio & Cordes (2008) estimate that the number of pulsars included is of order $\sim$10. Based on this survey, upper limits to the pulsar population within 1° ($\approx$150 pc) of Sgr A* may be estimated.

2.4.1 Observations

The survey was conducted at observing frequencies of 1.4 and 5 GHz with the VLA in the A configuration. A total of 13 fields arranged in a hexagonal grid covered the region of the GC out to roughly 1° (150 pc) from Sgr A* (the half-power radius of the VLA primary beam is $15'$ at 1.4 GHz). The typical resolution for the survey was a synthesized beam size of $2\farcs4 \times 1\farcs3$.

Sources were indentified using a method similar to that of Lazio & Cordes (1998b). Essentially, a histogram of intensities was constructed from the image of the primary beam for each field. If the field just contained noise, the intensity histogram would be a Gaussian with a mean of zero and a standard deviation equal to the thermal noise of 0.05 mJy per synthesized beam. Sources could then be determined by looking for deviations from this noise-only histogram. In practice,

the histogram was found to have larger tails than a Gaussian, with zero mean and a standard deviation of ≈0.5 mJy beam^{-1}. Since the resolution is comparable to the scattering size of a point source at the distance of Sgr A*, a 10σ detection threshold of $S_{det} \approx 5$ mJy was adopted for the survey.

2.4.2 Pulsar Population Estimate

Given that $N_{obs} \sim 10$ pulsars were likely observed, the total pulsar population in the survey region can be estimated as $N_{psr} \sim N_{obs}/f_L$, where f_L is the fraction of pulsars luminous enough to be detected at the distance of Sgr A*. Taking the survey detection threshold to be $S_{det} = 5$ mJy at 1.4 GHz, a pulsar must have a 1.4 GHz pseudo-luminosity of at least $L_{det} = 360$ mJy kpc^2 to be detected at the distance of Sgr A*. The fraction of pulsars with $L > L_{det}$ can be determined from the 1.4 GHz pulsar luminosity function, which has the form $dN/d\log L \propto L^{-\beta}$. The range of pulsar pseudo-luminosities is taken from $L_{min} = 0.1$ mJy kpc^2 to $L_{max} = 10^4$ mJy kpc^2 and the exponent in the distribution function is taken to be $\beta = 0.7$ (Lorimer et al. 2006). From this distribution, the fraction of pulsars luminous enough to be detected is $f_L = 3 \times 10^{-3}$. For $N_{obs} \sim 10$ pulsars detected in the survey, we expect a total population of $N_{psr} \sim 3000$ pulsars within 1° (150 pc) of Sgr A*.

Though $N_{psr} \sim 3000$ is the nominal population estimate from the survey, a broader range results if the assumptions do not exactly hold. For instance, Lazio & Cordes (2008) estimate that $N_{obs} \sim 10$ of the unidentified steep-spectrum point sources will ultimately turn out to be radio pulsars. However, this number could range from zero to about 30. If one takes $N_{obs} = 30$, repeating the above analysis gives a pulsar population of $N_{psr} \sim 10^4$. Additionally, one may consider the case in

which no pulsars were detected. Despite a follow-up observation of 15 of the pulsar candidates in this survey by Deneva (2010) with the GBT, none of the candidates have to date been confirmed. Assuming zero detections, an analysis similar to that in Section 2.3.2 gives an upper limit to the pulsar population of $N_{psr} \leq 1500$ at a 99% confidence level. These two extremes illustrate that although the survey allows for an estimate of the pulsar population in the inner degree of about 3000, the actual number could be below 1500 or as high as 10^4. As a result, we take $N_{psr} \lesssim 10^4$ as a conservative upper bound.

Finally, we note that although the survey covers the region within 1° (150 pc) of Sgr A*, there will be reduced sensitivity in the field centered on Sgr A*. The reduced sensitivity is the result of increased background temperatures and greater sidelobes from the extended structure of the inner GC. In addition, since the scatter-broadening of point sources in the vicinity of Sgr A* ($\approx 1''$) is comparable to the resolution of the survey, source confusion may become important in the innermost regions of the GC. Therefore, this survey would be largely insensitive to a fairly compact population of pulsars in the inner tens of arcseconds around Sgr A*.

2.5 Radio Spectrum of Sgr A*

In this section, limits are placed on the maximum allowable number of pulsars in the inner parsecs of the GC based on radio interferometer observations of Sgr A* on arcsecond scales ($1'' \approx 0.04$ pc at 8.5 kpc). Due to the finite resolution of interferometers and the broadening of angular diameters as a result of the interstellar scattering of radio waves, the Sgr A* radio source is actually extended ($\approx 1''$ at

1 GHz). Flux measurements of Sgr A* will therefore include a contribution from a collection of pulsars, if such a population exists. Although these pulsars will be unresolved, upper limits on the total population may be set based on the total flux density of Sgr A* in a manner analogous to similar constraints placed on pulsars in globular clusters (Fruchter & Goss 1990).

We consider a model in which the observed flux density of Sgr A* is actually the combination of two components. The first component is that due to radio emission from the immediate environment of the MBH itself, which we assume is described accurately by high frequency observations where the pulsar component is negligible. The second component is that due to the population of pulsars near the MBH. This pulsar component becomes important at lower frequencies both because radio pulsars typically have steep spectra and the angular resolution of radio telescopes scales with frequency such that a larger region around the MBH is sampled at lower frequencies. By requiring that this model flux be consistent with existing observations, constraints may be set on the maximum number of pulsars allowed in the inner parsec of the Galaxy.

2.5.1 Observations

Two different measurements of the spectrum of Sgr A* over a wide range of frequencies are considered (An et al. 2005; Falcke et al. 1998). An et al. (2005) conducted simultaneous measurements of Sgr A* from 300 MHz to 43 GHz using the VLA (A-configuration) and the GMRT. Falcke et al. (1998) made simultaneous measurements of Sgr A* using the VLA (A-configuration), the Berkeley-Illinois-Maryland Array, the Nobeyama 45 m telescope, and the Institut de Radioastronomie Millimetrique (IRAM) 30 m telescope from 1.4 GHz to 235 GHz. Both groups observed

a broken power-law spectrum with a break around 10 GHz. Since the power-law spectrum of pulsars decreases with increasing frequency, a population of pulsars contributes significantly only at lower frequencies. As a result, we consider the spectrum of Sgr A* only below the break frequency at 10 GHz.

2.5.2 Spectral Model

We model the measured flux density of the compact radio source Sgr A* as the sum of contributions from a collection of pulsars and a point source associated with the MBH attenuated by free-free absorption according to

$$S_{\rm Sgr}(\nu) = \left[S_{{\rm BH},\nu_0} \left(\frac{\nu}{\nu_0} \right)^{\alpha_{\rm bh}} + N(\nu) S_{{\rm psr},\nu_0} \left(\frac{\nu}{\nu_0} \right)^{\alpha_{\rm psr}} \right] \exp(-\nu_f^2/\nu^2). \tag{2.4}$$

The emission from the immediate vicinity of the MBH, $S_{{\rm BH},\nu_0}$, is taken to be a point source with a power-law spectrum with spectral index $\alpha_{\rm bh}$. $N(\nu)$ is the number of pulsars contained in the solid angle of the effective point-spread function or beam size, which depends strongly on frequency (see Section 2.5.3). We use a simplified scaling for the free-free absorption that ignores the frequency dependence of the Gaunt factor. The free-free absorption factor has a turnover frequency ν_f (An et al. 2005). The flux density per pulsar, $S_{{\rm psr},\nu_0}$, is taken to be the mean of the 1.4 GHz pulsar pseudo-luminosity distribution given by $dN/d\log L \propto L^{-0.7}$ (Lorimer et al. 2006) with a lower cutoff of $L_{min} = 0.1$ mJy kpc^2 and an upper cutoff of $L_{max} = 10^4$ mJy kpc^2. The mean observed flux density at 1.4 GHz is $S_{\rm psr,1.4} = 99$ μJy. Since pulsar radio flux scales with frequency as a simple power-law, we can scale our flux density as $S_\nu \propto \nu^{\alpha_{\rm psr}}$. We fix $\alpha_{\rm psr} = -1.7$ as a nominal value for the pulsar spectral index (Maron et al. 2000; Lorimer et al. 1995), but also consider values of -1.0 and -2.5 to test any major spectral index dependence.

2.5.3 Effective Angular Resolution

The number of pulsars included in a flux measurement of Sgr A* can be written as an integral of the number of pulsars per unit solid angle,

$$N(\nu) = \int d\Omega \frac{dn_p}{d\Omega}. \tag{2.5}$$

The integral is over the effective solid angle $\Omega_{\rm eff}(\nu) = (\pi/4)\theta^2_{\rm eff}(\nu)$, where

$$\theta_{\rm eff}(\nu) = \left[\theta^2_{\rm b}(\nu) + \theta^2_{\rm sc}(\nu)\right]^{1/2} = \left(\theta^2_{\rm b_0}\nu^{-2} + \theta^2_{\rm sc_0}\nu^{-4}\right)^{1/2} \tag{2.6}$$

is the effective resolution with the subscript "0" representing values at 1 GHz and the frequencies are in GHz units. The effective resolution is the quadrature sum of the resolution of the interferometer and the angular extent of Sgr A* caused by scattering. The scaling for the synthesized array beam $\theta_{\rm b}$ ($\propto \nu^{-1}$) assumes a fixed array configuration and the scattering diameter $\theta_{\rm sc}$ ($\propto \nu^{-2}$) scales in conformance to measurements of Sgr A* and OH/IR masers (e.g. Frail et al. 1994). Our treatment assumes that scattered images are circular whereas in fact some are elliptical, but given that we are making order of magnitude estimates of pulsar numbers, the differences are not important.

The angular diameter of Sgr A* is dominated by interstellar scattering at low frequencies, with an observed major axis of $\theta_{\rm sc_0} = 1\farcs2$ (Bower et al. 2006). For the VLA in the A configuration and ignoring any effects of foreshortening, the half-power beam width is $\theta_{\rm b_0} = 1\farcs95$ (Bridle 1989).

The effective resolution of the VLA observations is then

$$\theta_{\rm eff}(\nu) = 1\farcs2\,\nu^{-2}\left(1 + 2.6\ \nu^2\right)^{1/2}. \tag{2.7}$$

The two contributions are equal at $\nu = 0.6$ GHz, so at frequencies lower than this

the resolution is completely scattering dominated and the resolution solid angle scales steeply with frequency as ν^{-4}.

Additionally, a single data point measured with the GMRT will be considered in our analysis, so a similar effective resolution must be constructed for this telescope. Roy & Rao (2004) measure the resolution to be $11\farcs4 \times 7\farcs6$ at 620 MHz. Converting this ellipse to a circle of equal area and scaling to 1 GHz gives $\theta_{\mathrm{b}_0} = 5\farcs77$ for the GMRT. Combining this with scattering as above, gives

$$\theta_{\mathrm{eff}}(\nu) = 1\farcs2\,\nu^{-2}\left(1 + 23.1\;\nu^{2}\right)^{1/2}. \tag{2.8}$$

For the GMRT, the two components of the effective resolution are equal at $\nu = 0.2$ GHz.

2.5.4 Candidate Pulsar Distributions

We choose three physically-motivated distributions as model pulsar populations. The distributions are illustrated below in Figure 2.2.

The first (Model A) assumes a constant number of pulsars per unit solid angle, $dn_p/d\Omega = \text{constant}$, so the number of pulsars scales as

$$N_A(\nu) = N_1\left[\frac{\Omega_{\mathrm{eff}}(\nu)}{\Omega_1}\right], \tag{2.9}$$

where Ω_1 is the solid angle enclosing N_1 pulsars. In the fitting below, Ω_1 is set so that N_1 gives the number of pulsars in the inner parsec. Referring to Eq. 2.4, it may be seen that when scattering dominates the effective resolution, the contribution to the unabsorbed spectrum from pulsars increases very rapidly as $N_A(\nu)\nu^{\alpha_{\mathrm{psr}}} \propto \nu^{-5.7}$. Free-free absorption attenuates much of the flux, thus allowing a significant pulsar population to remain hidden in spectral measurements.

In Model B, we assume that $dn_p/d\Omega \propto \Omega^{-0.7}$, corresponding to the surface density scaling observed for Wolf-Rayet and O-star populations in the inner parsec (Genzel et al. 2010). This yields

$$N_B(\nu) = N_1 \left[\frac{\Omega_{\rm eff}^{0.3}(\nu)}{\Omega_1^{0.3}} \right]. \tag{2.10}$$

However, the observed populations of Wolf-Rayet and O-stars have an inner cutoff at $\theta \approx 1''$ (Bartko et al. 2010). This core may affect the pulsar population in many ways, but we shall just consider two here. In both distributions, the pulsar surface density goes as $dn_p/d\Omega \propto \Omega^{-0.7}$ outside the inner cutoff, as before. Inside the cutoff, one of the distributions (call it Model B-1) has $dn_p/d\Omega = {\rm const}$ and the other (call it Model B-2) has $dn_p/d\Omega = 0$. These models give

$$N_{B1}(\nu) = \begin{cases} N_1 \left[\dfrac{\Omega_{\rm eff}^{0.3}(\nu) - 0.7\Omega_0^{0.3}}{\Omega_1^{0.3} - 0.7\Omega_0^{0.3}} \right], & \Omega_{\rm eff} \geq \Omega_0 \\ \\ N_1 \left[\dfrac{0.3\Omega_0^{0.7}\Omega}{\Omega_1^{0.3} - 0.7\Omega_0^{0.3}} \right] & \Omega_{\rm eff} < \Omega_0 \end{cases} \tag{2.11}$$

and

$$N_{B2}(\nu) = \begin{cases} N_1 \left[\dfrac{\Omega_{\rm eff}^{0.3}(\nu) - \Omega_0^{0.3}}{\Omega_1^{0.3} - \Omega_0^{0.3}} \right], & \Omega_{\rm eff} \geq \Omega_0 \\ \\ 0 & \Omega_{\rm eff} < \Omega_0 \end{cases} \tag{2.12}$$

pulsars enclosed within $\Omega_{\rm eff}$.

In Model C, we consider a compact population of pulsars contained in a solid angle much smaller than any resolution solid angle so that $dn_p/d\Omega$ is effectively a delta function. A compact distribution close to Sgr A* could conceivably arise as a product of dynamical friction (Morris 1993; Miralda-Escudé & Gould 2000). Here we simply have

$$N_C(\nu) = N_1. \tag{2.13}$$

In addition to the above three, one may consider other models for the pulsar distribution. For example, the pulsars could be arranged in a central core with a

diffuse halo. However, most of these other distributions can be made as combinations of those we consider. As a result, we do not expect the final answers to change by more than an order of magnitude.

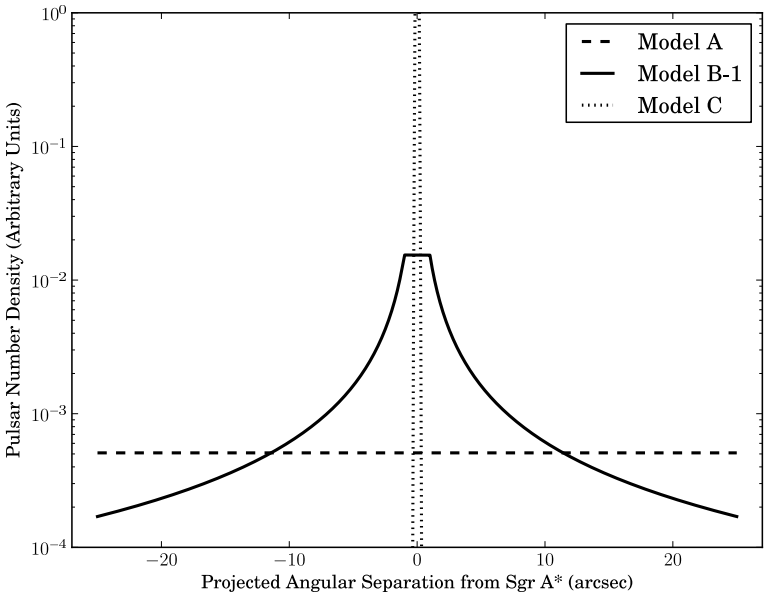

Figure 2.2: **Pulsar number density as a function of angular separation from Sgr A* for each of the three distribution models**. The distributions have been normalized in this figure so that each model produces the same number of pulsars enclosed within the inner parsec ($\theta_r \approx 25''$). See Section 2.5.4 for a description of each model.

2.5.5 Model Fitting

To test our distributions, we calculated the χ^2 values of the model given by Eq. 2.4 with each of the three distributions against the VLA and GMRT data from An et al. (2005) and Falcke et al. (1998). We fix the pulsar spectral index at $\alpha_{\rm psr} = -1.7$ and the flux density per pulsar at $S_{{\rm psr},\nu_0} = 99$ μJy at 1.4 GHz, as described in Section 2.5.2. The flux from the point source associated with the MBH is

normalized such that the total measured flux of Sgr A* exactly matches the data at 8.45 GHz. The spectral index of the MBH point source ($\alpha_{\rm bh}$), the number of pulsars (N_1) and the free-free cutoff frequency (ν_f) are allowed to vary. The number of pulsars, N_1, is taken within an angular distance of $\theta = 25''$, which corresponds to a projected radial distance of $r \approx 1$ pc from Sgr A*. The allowed ranges for each parameter were chosen to be consistent with current measurements and are presented below in Table 2.2. For reference, the best fit values for the model with no pulsars present are $\alpha_{\rm bh} = 0.15$ and $\nu_f = 0.26$ GHz.

For each grid point in the three-dimensional parameter space, we calculate χ^2 between the measured flux and our model and evaluate the likelihood function assuming independent Gaussian statistics for measurement errors,

$$\mathcal{L}(N_1, \alpha_{\rm bh}, \nu_f) = \prod_{i=1}^{N_p} \left(2\pi\sigma_i^2\right)^{-\frac{1}{2}} \exp\left\{-\frac{[S_{\rm Sgr}(\nu_i) - S_{obs}(\nu_i)]^2}{2\sigma_i^2}\right\} \tag{2.14}$$

$$\propto \exp\left(-\frac{1}{2}\chi^2\right). \tag{2.15}$$

The likelihood function is then marginalized over $\alpha_{\rm bh}$ and ν_f to get a distribution for N_1. The marginalized likelihood functions for the number of pulsars within 1 pc of Sgr A* are plotted in Figure 2.3.

	Parameter Ranges		
Model	N_1	$\alpha_{\rm bh}$	ν_f (GHz)
A	[0, 50000, 100]	[0.05, 0.40, 0.01]	[0.05, 1.00, 0.01]
B	[0, 50000, 100]	[0.05, 0.40, 0.01]	[0.05, 1.00, 0.01]
C	[0, 5000, 10]	[0.05, 0.40, 0.01]	[0.05, 1.00, 0.01]

Table 2.2: **Searched Parameters for Each Pulsar Distribution Model**. Data given as [min, max, step size]

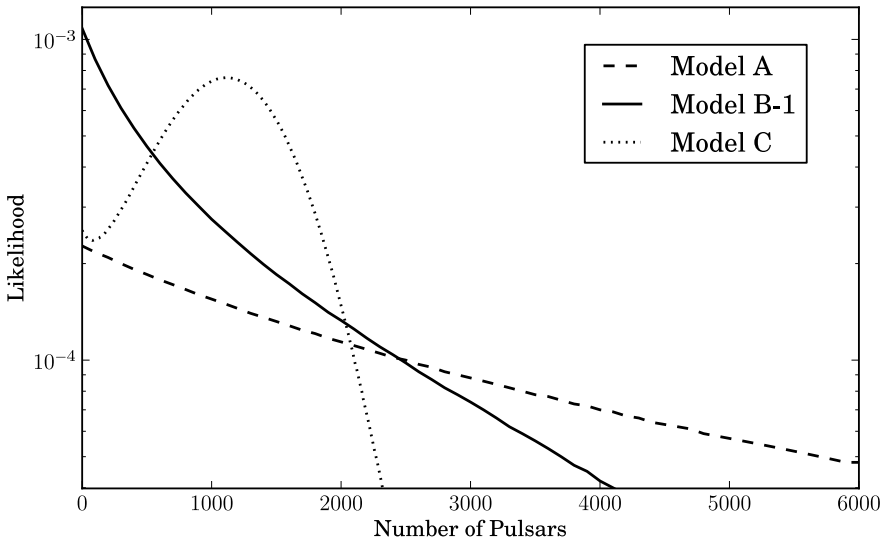

Figure 2.3: **Likelihood functions for three pulsar distributions models** (see Section 2.5.4 for a description of each model). The likelihoods have been marginalized over the parameters $\alpha_{\rm bh}$ and ν_f and normalized so that $\int \mathcal{L}(N) = 1$. In each case, the pulsar spectral index was taken to be $\alpha_{\rm psr} = -1.7$.

2.5.6 Results

The best-fit parameters for the maximum likelihood (ML) number of pulsars within the inner parsec of the GC for each model is provided in Table 2.3 and the the resulting spectra are plotted in Figure 2.4. The number quoted in Table 2.3 is the ML number of pulsars as determined from the likelihood distribution and the uncertainties denote the most compact 68% confidence interval around the ML value. If the ML value for a distribution is zero, then the upper limits are given at the 68% confidence level. In addition to the fiducial pulsar spectral index of $\alpha_{\rm psr} = -1.7$, we include spectral indices of -1.0 and -2.5. For comparison, the best fit parameters for the model with the number of pulsars fixed at zero is also included in Table 2.3 and odds ratios are calculated against this "null" model.

It is interesting to note that although Models A and B give only upper limits to the pulsar population (of $\lesssim 10^3 - 10^4$), Model C provides a non-zero maximum likelihood value of $\sim 10^3$. Additionally, Model C provides a better fit than the model with no pulsars at all (the "null" model in Table 2.3).

In all of the models considered, an increase in the maximum number of pulsars is accompanied by an increase in the free-free turnover frequency. The increased free-free absorption is required to mask the bright low-frequency tail of a large pulsar population. Current estimates of free-free absorption in the region near Sgr A* give turnover frequencies around 330 MHz (Pedlar et al. 1989). Estimates of the free-free absorption of the flux from Sgr A*, however, assume a power-law flux density for Sgr A* and would likely underestimate the absorption if a pulsar population were present. As a result, any independent measurement of the free-free absorption along the line of sight of Sgr A* that does not assume a spectrum of the Sgr A* source could place an important constraint on the pulsar population in the inner parsecs of the Galaxy.

From current radio measurements of the inner parsec of the GC, total pulsar populations (that is, both CPs and MSPs) of up to $\sim 10^3$ are consistent with observations, regardless of the underlying spatial distribution.

2.6 Diffuse Gamma-Ray Emission and MSPs

MSPs are known gamma-ray sources (Abdo et al. 2009a). As a result, we may set constraints on the MSP population in the GC by measuring the diffuse gamma-ray emission from the GC. In a recent analysis of the first two years of data from the Fermi Gamma-Ray Space Telescope, Hooper & Goodenough (2011, herafter, HG)

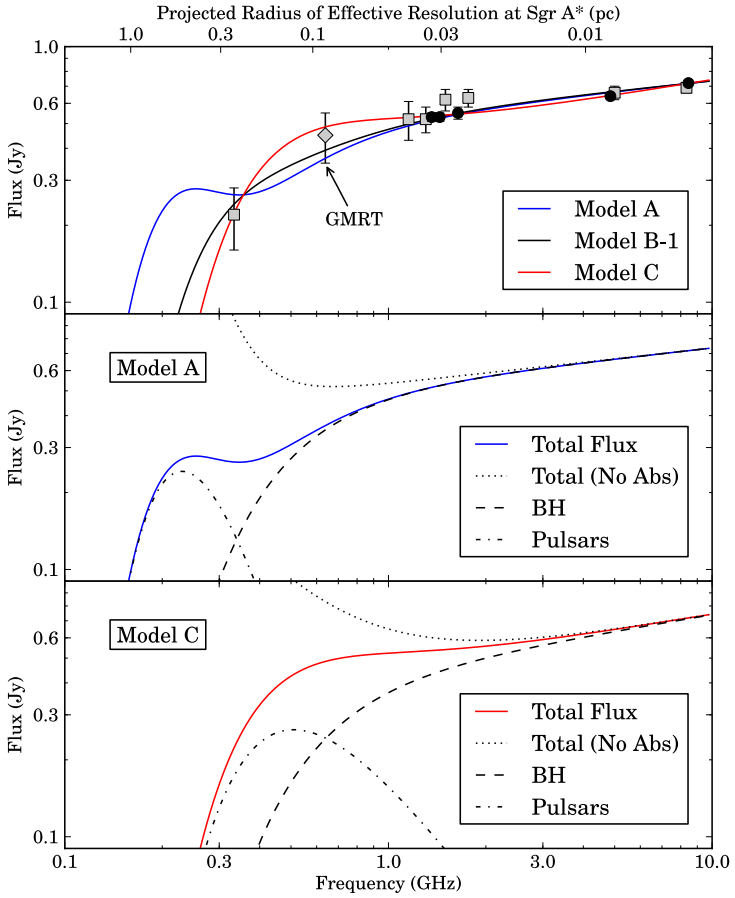

Figure 2.4: **Model Spectra**. *Top:* Fit curves for model pulsar distributions to the VLA (squares) and GMRT (diamond) data from An et al. (2005) and VLA (filled circles) data from Falcke et al. (1998). Since the best fit for Models A and B-1 indicate that the most probable number of pulsars is zero, we have instead plotted the best fit assuming the 68% confidence upper limit number of pulsars are present. The upper axis gives the projected radial distance of the effective resolution beam at the distance of Sgr A* using the VLA (for details, see Section 2.5.3). Note that although the fits were made using both the VLA and GMRT data, the curves above only apply to the VLA data points (squares and filled circles). *Middle and Bottom:* Components to the observed flux of Sgr A* from the MBH point source and surrounding pulsars for Models A and C. Note how the pulsar component in Model A rises quickly with decreasing frequency as a result of both the pulsar spectrum and the increasing number of pulsars in the beam. The total unabsorbed flux is also shown for comparison.

		Model Parameters					
Model	$\alpha_{\rm psr}$	$N_1(\times 10^3)$	$\alpha_{\rm bh}$	ν_f (GHz)	N_{dof}	χ^2_r	Odds
A	-1.0	< 16.2	0.14	0.37	10	1.08	$10^{-0.64}$
	-1.7	< 7.4	0.14	0.38	10	1.16	$10^{-1.05}$
	-2.5	< 2.2	0.14	0.38	10	1.17	$10^{-1.35}$
B-0	-1.0	$5.3^{+2.5}_{-5.3}$	0.17	0.45	10	0.79	$10^{-0.55}$
	-1.7	< 4.9	0.15	0.53	10	1.07	$10^{-1.21}$
	-2.5	< 0.9	0.13	0.47	10	1.27	$10^{-1.42}$
B-1	-1.0	< 3.8	0.14	0.40	10	1.06	$10^{-0.85}$
	-1.7	< 1.5	0.13	0.41	10	1.14	$10^{-1.03}$
	-2.5	< 0.4	0.14	0.38	10	1.17	$10^{-1.22}$
B-2	-1.0	< 2.4	0.14	0.36	10	1.07	$10^{-1.02}$
	-1.7	< 1.2	0.14	0.38	10	1.13	$10^{-1.00}$
	-2.5	< 0.4	0.14	0.38	10	1.17	$10^{-1.23}$
C	-1.0	$1.4^{+0.5}_{-0.7}$	0.25	0.40	10	0.55	$10^{+0.28}$
	-1.7	1.1 ± 0.4	0.21	0.47	10	0.59	$10^{+0.12}$
	-2.5	$1.1^{+0.4}_{-0.6}$	0.17	0.58	10	0.75	$10^{-0.46}$
Null	–	0	0.15	0.26	11	0.81	1.0

Table 2.3: **Number of Pulsars within 1 pc for Given Model and Spectral Index**. Best fit model parameters for maximum likelihood (ML) number of pulsars. If the ML number of pulsars is zero, then the 68% confidence upper limit is used and reported with a "<". The "Null" model fixes the number of pulsars at zero.

observed an excess of gamma-ray flux towards the inner 1° (150 pc) of the GC, with a significant excess within 0.25° (≈ 40 pc). HG argued that the signal is consistent with the annihilation of 7–10 GeV dark matter particles with a cusped halo distribution around Sgr A* and difficult to explain using known astrophysical sources. Abazajian (2011), however, claimed that while the spectrum may be inconsistent with the *average* pulsar spectrum, it is consistent with *some* pulsar spectra and therefore could be explained by astrophysical sources. HG provide a

spectrum for the gamma-ray excess in the GC of the form

$$\frac{dN_\gamma}{dE} \propto E^{-\Gamma} \exp\left(-E/E_{cut}\right) \tag{2.16}$$

where $\Gamma = 0.99^{+0.10}_{-0.09}$ and $E_{cut} = 1.92^{+0.21}_{-0.17}$ GeV. These parameter values are consistent (to current uncertainties) with the spectra of 16 out of 46 pulsars in the first Fermi LAT catalog of gamma-ray pulsars (Abdo et al. 2010a). We proceed assuming that the observed excess seen by HG is real (however, see Boyarsky et al. 2011), follows the spectrum fit by HG and is entirely caused by a collection of MSPs in the GC.

The spectrum is normalized so that $E^2 dN_\gamma/dE \approx 10^{-7}$ GeV cm^{-2} s^{-1} at $E = 1.0$ GeV based on the HG plots, giving

$$\frac{dN_\gamma}{dE} = 1.7 \times 10^{-7}\ \mathrm{GeV}^{-1}\mathrm{cm}^{-2}\mathrm{s}^{-1} \left(\frac{E}{1\ \mathrm{GeV}}\right)^{-0.99} \exp\left(-\frac{E}{1.92\ \mathrm{GeV}}\right). \tag{2.17}$$

Calculating the integrated energy flux from the above spectrum over 0.1 to 100 GeV as

$$S_\gamma = \int_{0.1\ \mathrm{GeV}}^{100\ \mathrm{GeV}} E \frac{dN_\gamma}{dE} dE \tag{2.18}$$

and letting $L_\gamma = 4\pi d^2 f_\Omega S_\gamma$, we find that the gamma-ray luminosity of a source at the GC is $L_\gamma \approx 4 \times 10^{36}$ erg s$^{-1} f_\Omega$. The correction factor, f_Ω, is similar to the beaming fraction in radio pulsars and is generally taken to be unity in most modern models (Watters et al. 2009).

Following calculations made to estimate the number of MSPs in globular clusters (Abdo et al. 2010b), we can estimate the MSP population of the GC as

$$N_{\mathrm{MSP}} = \frac{L_\gamma}{\langle \dot{E} \rangle \langle \eta_\gamma \rangle} \tag{2.19}$$

where $\dot{E}$ is the total spindown luminosity of a MSP, $\eta_\gamma = L_\gamma/\dot{E}$ is the "efficiency" of converting spin-down power into gamma-rays, and angled brackets denote an

average over the population. The values of $\langle \dot{E} \rangle$ and $\langle \eta_\gamma \rangle$ are taken from the local ($d < 1$ kpc) MSP population to avoid selection effects. The mean spin-down luminosity is taken to be $\langle \dot{E} \rangle = 1.1 \times 10^{34}$ erg s^{-1} from the 27 MSPs within 1 kpc of Earth listed in the ATNF catalog (Manchester et al. 2005). Since $\langle \eta_\gamma \rangle \propto L_\gamma \propto d^2$, the uncertainties in $\langle \eta_\gamma \rangle$ are dominated by distance uncertainties and values range from $\langle \eta_\gamma \rangle = 10^{-3} - 1$ in the first *Fermi* gamma-ray pulsar catalog (Abdo et al. 2010a). To mitigate this distance problem, we take only those seven nearby pulsars in the catalog for which distances could be measured accurately with parallax. For these pulsars, we find $\langle \eta_\gamma \rangle = 0.08 \pm 0.04$. Using Eq. 2.19, we get an estimate of $N_{\rm MSP} \approx 5000$. In order to contribute the observed excess, these pulsars would be located within 1° (150 pc) of Sgr A*, with the highest concentration within 0.25° (40 pc).

Our estimate for the number of MSPs in the GC is esentially an upper bound for the population. However, modeling the background component of the diffuse gamma-ray emission in the GC is still somewhat uncertain (Abdo et al. 2009b) and, as a result of this uncertainty, our estimate can only be taken as an approximate upper limit. Additionally, as this is a measure of the excess gamma-ray flux in the region (with the Galactic plane and a central point source coincident with Sgr A* subtracted), there exists the possiblity that a signicant number of MSPs are unaccounted for in this estimate. Assuming the HG gamma-ray excess in the GC is real and does not suffer from systematic errors in background subtraction, we see that it is not inconsistent with a centrally concentrated population of $\sim 10^3$ MSPs in the inner tens of parsecs from Sgr A*.

Finally, we note that similar estimates for the MSP population in the GC have been made in the past. Wang et al. (2005) used a model proposed by Zhang &

Cheng (1997) to predict the emission of gamma-rays from MSPs as a function of global pulsar parameters like spin period and polar magnetic field. They used Monte Carlo methods to simulate a population of pulsars and measured the total gamma-ray luminosity. Comparing this luminosity to measured values from EGRET, Wang et al. (2005) estimated a GC MSP population of $N_{\rm MSP} \approx 6000$ in the EGRET field ($r \approx 1.5°$, 220 pc).

2.7 Massive Stars in the Galactic Center

The central parsec of the GC is one of the most active massive star formation regions in the Milky Way and is currently known to contain about 200 young massive stars (Genzel et al. 2010). As massive stars are the progenitors of neutron stars (NSs), we may use current stellar populations to estimate the number of pulsars in this region.

The inner parsec stellar population is divided into three fairly distinct regions. The innermost region ($R \leq 1''$) is the so-called "S-star Cluster" of main sequence B-stars. These stars can be fitted with a standard Salpeter IMF for a single star formation event or for a continuous star-forming population with ages of a few Myr to 60 Myr (Bartko et al. 2010). Outside this region ($1'' \leq R \leq 12''$), the stars are largely arranged in at least one disk (possibly two) of mass $M \sim 10^4 M_\odot$ with a top-heavy IMF of $dN/dm \propto m^{-0.45}$ (Bartko et al. 2010). The early-type stars in this region appear to have been formed in a starburst ∼6 Myr ago. Outside the disk region ($R \geq 12''$) the stellar population is again consistent with a Salpeter IMF.

Following similar calculations by Lazio & Cordes (2008) and Faucher-Giguère

& Loeb (2011), the current stellar populations can be used to estimate the number of radio pulsars harbored in the central parsec. The number of active CPs and MSPs beamed towards Earth are estimated to be

$$N_{\rm CP} = f_{psr} f_b f_\tau f_v N_{ns} \tag{2.20}$$

and

$$N_{\rm MSP} = f_{psr} f_b f_\tau f_v f_r N_{ns}, \tag{2.21}$$

respectively, where N_{ns} is the number of NSs in the inner parsec, f_{psr} is the fraction of NSs that form pulsars, $f_b = 0.2$ is the beaming fraction, f_τ is the fraction of pulsars with ages less than the typical pulsar radio lifetime, f_v is the fraction of pulsars with birth velocities small enough to be retained in the inner parsec and f_r is the fraction of NSs that are recycled into MSPs. The fraction of NSs that form pulsars is taken to be $f_{psr} \sim 1$, although this factor is still fairly uncertain (Lazio & Cordes 2008). The terms N_{ns}, f_τ, f_v and f_r are discussed below.

2.7.1 Neutron Star Population in the Inner Parsec (N_{ns})

The total number of NSs residing in the inner parsec may be estimated from current observations of the massive star population. Velocity measurements of stars allow for the total dynamical mass enclosed within a few parsecs of Sgr A* to be determined. Subtracting the mass of the MBH gives an extended mass of $\sim 10^6\ M_\odot$ in stars within a parsec of Sgr A* (Genzel et al. 1996; Schödel et al. 2009). With the total mass of stars established, the number of NSs can be calculated for a given initial mass function (IMF) and mass range of stars that end their lives as NSs.

A typical NS progenitor mass range is $9M_\odot < M < 25M_\odot$ (Heger et al. 2003).

However, such ranges are theoretically determined for only isolated non-rotating stars and rely on mass-loss and stellar wind models that are poorly constrained by observations (Heger et al. 2003). If very massive stars have higher mass-loss rates than modeled, then NSs could form from stars with initial masses above $\gtrsim 25 M_\odot$. That this may be the case is supported by the limited observational constraints. For example, Muno et al. (2006) detected an X-ray pulsar in the young Galactic cluster Westerlund 1 that requires a progenitor mass of $M > 40 M_\odot$ to have formed in the age of the cluster.

To calculate the number of NSs produced by the GC massive star population, we consider IMFs of the form $dN/dm \propto m^{-\alpha}$ over a range of masses from $0.1 M_\odot$ to $100 M_\odot$. For the case of the standard Salpeter IMF ($\alpha = 2.35$) observed in most of the inner parsec and a progenitor mass range of $9 M_\odot < M < 25 M_\odot$, a total of $N_{ns} \approx 4900$ NSs are produced. If the top-heavy IMF ($\alpha = 0.45$) observed in the young disks is taken to hold for the whole central parsec, a total of $N_{ns} \approx 5700$ are produced. If a wider range of progenitor masses is taken, say $9 M_\odot < M < 40 M_\odot$ to allow the Muno et al. (2006) observation, the total NS populations increase to $N_{ns} \approx 5700$ and $N_{ns} \approx 9500$ for the Salpeter and top-heavy IMFs, respectively. Even given a wide range in IMF and progenitor mass, the above results are consistent to an order of magnitude with a NS population of $N_{ns} \sim 10^4$. In terms of NSs formed per stellar mass, we find a value of $\beta_{ns} \sim 10^{-2} M_\odot^{-1}$ for the $\sim 10^6 M_\odot$ worth of stars within a parsec of Sgr A*.

2.7.2 Fraction of Still-Active Pulsars (f_τ)

The typical lifetimes over which pulsars maintain active radio emission are $\tau \sim 10^7$ yr for CPs and $\tau \sim 10^9 - 10^{10}$ yr for MSPs. As a result, the fraction of

pulsars formed recently enough to still be active must be considered in estimates of the observable population. This factor will depend on the star formation history (SFH) of the region. In the case of continuous star formation, the active fraction of pulsars can be estimated to be $f_\tau \sim \tau/t_{sf}$, where t_{sf} is amount of time elapsed since the star formation began.

2.7.3 Fraction of Pulsars Retained (f_v)

From the high observed velocities ($\sim 10^2 - 10^3$ km s^{-1}) of some pulsars, it has been inferred that NSs are given a large "kick" velocity at birth as a result of binary disassociation or an asymmetric supernova explosion (or both). A pulsar created in the inner parsec will be retained in the inner parsec only if its birth velocity does not exceed the local escape velocity of its orbit around Sgr A*. Assuming only the influence of a MBH of mass $M \approx 4 \times 10^6$ M$_\odot$, the escape velocity at a distance r from Sgr A* is given by

$$v_e(r) = 185 \text{ km s}^{-1} \left(\frac{M}{4 \times 10^6 \text{ M}_\odot}\right)^{1/2} \left(\frac{r}{1 \text{ pc}}\right)^{-1/2}. \tag{2.22}$$

Assuming a Maxwellian distribution of birth velocities with a mean of $\langle v_{birth} \rangle = 380$ km s^{-1} (Faucher-Giguère & Kaspi 2006), we find retention fractions of $f_v \approx 0.1$ and $f_v \approx 0.25$ for radial distances of $r = 1$ pc and $r = 0.5$ pc, respectively. However, the actual shape of the pulsar birth velocity distribution is not well constrained and one may worry that the Maxwellian distribution is arbitrary. In an analysis of pulsar velocities, Faucher-Giguère & Kaspi (2006) consider six different pulsar velocity distributions. Repeating our calculation for each distribution, we find retention fractions in the ranges of $f_v \approx 0.05 - 0.4$ and $f_v \approx 0.1 - 0.5$ for distances of $r = 1$ pc and $r = 0.5$ pc, respectively.

If no other effects are important, we would expect a retention fraction of $f_v \gtrsim 0.1$. However, a similar analysis to the one performed above would underestimate the retained NS populations in globular clusters by orders of magnitude. Observations of pulsars and low-mass X-ray binaries (LMXBs) suggest that up to $\sim$10% of all NSs formed in some globular clusters may be retained (Pfahl et al. 2002). However, current models for isolated pulsars predict that $\lesssim 1\%$ of NSs will have birth velocities below the $\lesssim 50$ km s^{-1} globular cluster escape velocities. This "retention problem" is currently an unsolved problem, but likely has to do with the high stellar densities and binary fractions found in the cores of globular clusters (see Pfahl et al. 2002, and references within). Since the GC has even higher stellar densities than cores of globular clusters, we expect a similar heightening of the retention fraction and thus adopt as a nominal value $f_v \sim 1$.

2.7.4 Fraction of Pulsars Recycled to MSPs (f_r)

MSPs are thought to be formed when a NS in a binary gains angular momentum through accretion of matter in a process known as "recycling" (Alpar et al. 1982; Bhattacharya & van den Heuvel 1991). Thus, the fraction of NSs recycled into MSPs must be determined to estimate the MSP population. Within 3 kpc of the Sun, the birthrate of pulsars with 400 MHz pseudo-luminosities above 1 mJy kpc^2 is observed to be $\sim 10^{-3}$ yr^{-1} and $\gtrsim 10^{-6}$ yr^{-1} for CPs and MSPs, respectively (Lyne et al. 1998). Using these birthrates, we may infer that the recycling fraction is at least $f_r \gtrsim 10^{-3}$ in the Galactic disk. The increased stellar density and stellar encounter rate in the GC will very likely increase this fraction. LMXBs, the assumed progenitors of MSPs, have been found to be $\sim$100 times more abundant in globular clusters than the general Galactic field (Clark 1975; Katz 1975). As

the central parsec of the GC has a higher stellar density than globular clusters, we would expect at least a similar overabundance of LMXBs and their resultant MSPs as is seen in globular clusters. As a result, we adopt a recycling fraction of $f_r \sim 0.1$.

2.7.5 Pulsar Estimates for Various Star Formation Histories

As the star formation history (SFH) of the central parsec of the GC is still somewhat uncertain, we will consider two general SFHs suggested by current observations. In the first case, we take the massive-star disk(s) to have formed in a well-defined starburst ∼6 Myr ago (Paumard et al. 2006; Bartko et al. 2010) and assume the rest of the central parsec has experienced continous star formation over the age of the Galaxy. In the second case, we consider SFHs based on spectrophotometry of cool giant stars which indicate that most of the stars in the inner parsec were formed $\gtrsim 5$ Gyr ago but also show an increased star formation rate in the last ∼100 Myr (Blum et al. 2003; Pfuhl et al. 2011).

Continuous Star Formation + Disk Starburst

In the first SFH, pulsars can come from both the general population of stars in the central parsec and the young disk population. For the general population, we take the total mass of stars to be $M \sim 10^6 M_\odot$ and assume continuous star formation over the last $\sim 10^{10}$ yr. From the parameters discussed above, the total number of NSs is found to be $N_{ns} \sim 10^4 \left(\beta_{ns}/10^{-2}\mathrm{M}_\odot^{-1}\right)$. Taking a CP active radio lifetime of $\tau \sim 10^7$ yr, continuous star formation over $\sim 10^{10}$ yr will give the fraction of

CPs still active to be $f_\tau \sim 10^{-3}$. From Eq. 2.20, the CP contribution from the continuous star forming region of the inner parsec is

$$N_{\rm CP}^{\rm gen} \sim 2 \left(\frac{f_v}{1.0}\right) \left(\frac{\beta_{ns}}{0.01\ {\rm M}_\odot^{-1}}\right) \left(\frac{M}{10^6\ {\rm M}_\odot}\right). \tag{2.23}$$

For MSPs with a radio lifetime of $\sim 10^{10}$ yr, the fraction still active is $f_\tau \sim 1$. Adopting the recycling fraction of $f_r \sim 0.1$ discussed above, the contribution of MSPs from the general population of the inner parsec is given by Eq. 2.21 as

$$N_{\rm MSP}^{\rm gen} \sim 200 \left(\frac{f_v}{1.0}\right) \left(\frac{f_r}{0.1}\right) \left(\frac{\beta_{ns}}{0.01\ {\rm M}_\odot^{-1}}\right) \left(\frac{M}{10^6\ {\rm M}_\odot}\right). \tag{2.24}$$

Additionally, the contribution of pulsars from the massive-star disk(s) must be considered. The disk is assumed to have a population of stars formed in a starburst event $\sim 6 \times 10^6$ yr ago with a total stellar mass of $\sim 10^4 M_\odot$ (Paumard et al. 2006; Bartko et al. 2010). Since the age of the disk is comparable to the active radio lifetime of a CP, the fraction of CPs still active is taken to be $f_\tau \sim 1$. From Eq. 2.20, the CP contribution from the disk is found to be

$$N_{\rm CP}^{\rm disk} \sim 20 \left(\frac{f_v}{1.0}\right) \left(\frac{\beta_{ns}}{0.01\ {\rm M}_\odot^{-1}}\right) \left(\frac{M_{disk}}{10^4\ {\rm M}_\odot}\right). \tag{2.25}$$

The disk population is not expected to produce any currently observable MSPs as the short timescale of $\sim 6 \times 10^6$ yr provides insufficient time to create and evolve a NS population into MSPs. As a result, this first SFH produces roughly $N_{\rm CP} \sim 20$ CPs and $N_{\rm MSP} \sim 200$ MSPs.

SFH from Observations of Cool Giant Stars

The SFH has also been estimated by comparing simulated populations with the observed cool giant stars in the central parsec. Such simulations allow the average star formation rate to be calculated as a function of look-back time for a few

coarse time bins. In two separate analyses, both Blum et al. (2003) and Pfuhl et al. (2011) found that $\gtrsim$80% of the stellar mass in the central parsec was formed $\gtrsim$5 Gyr ago and that there has been increased star formation in the last $\sim$100 Myr. In their best fit models, Blum et al. (2003) found an average star formation rate of $\sim 3 \times 10^{-3} M_{\odot} \mathrm{yr}^{-1}$ within 2 pc of Sgr A* from 10-100 Myr ago and Pfuhl et al. (2011) found an average star formation rate of $\sim 10^{-3} M_{\odot} \mathrm{yr}^{-1}$ within 1 pc of Sgr A* from 50-200 Myr ago. Both cases are consistent with $\sim 10^5 M_{\odot}$ worth of stars being formed in the inner parsec of the GC in the last $\sim$100 Myr.

If there has been continuous star formation in the last $\sim$100 Myr, then the fraction of still active CPs would be $f_\tau \sim 0.1$. Taking all other parameters as before, the continuous formation of $\sim 10^5 M_{\odot}$ worth of stars over the last $\sim 10^8$ yr would produce

$$N_{\mathrm{CP}}^{\mathrm{con}} \sim 20 \left(\frac{f_v}{1.0} \right) \left(\frac{\beta_{ns}}{0.01 \ \mathrm{M}_{\odot}^{-1}} \right) \left(\frac{M \left(t < 10^8 \ \mathrm{yr} \right)}{10^5 \ \mathrm{M}_{\odot}} \right). \tag{2.26}$$

If the recent star formation all took place in the last $\sim 10^7$ yr, then the fraction of CPs still active would be $f_\tau \sim 1$. In this case, the number of active CPs would be

$$N_{\mathrm{CP}}^{\mathrm{burst}} \sim 200 \left(\frac{f_v}{1.0} \right) \left(\frac{\beta_{ns}}{0.01 \ \mathrm{M}_{\odot}^{-1}} \right) \left(\frac{M \left(t < 10^8 \ \mathrm{yr} \right)}{10^5 \ \mathrm{M}_{\odot}} \right). \tag{2.27}$$

In either of the above cases, the majority ($\gtrsim$90%) of the star formation took place at look-back times $\gtrsim 10^8$ yr ago. As a result, the number of MSPs produced will be approximately the same as the first SFH considered, namely $N_{\mathrm{MSP}} \sim 200$.

Upper Limits to the Pulsar Population

Using the above estimates of CP and MSP populations for a range of observationally supported SFHs, upper limits may be set on the total allowable number of pulsars in the inner parsec. For CPs, the most favorable formation sce-

narios produce $N_{\rm CP} \sim 200$. For MSPs, a variety of SFHs consistently produce $N_{\rm MSP} \sim 200\,(f_r/0.1)$. Since the recycling fraction is unknown for the extreme conditions of the inner GC, an upper limit of $N_{\rm MSP} \sim 2000$ may be set by adopting $f_r \sim 1$. Thus, observations of current stellar populations place an upper limit of a few $\times\, 10^3$ on the number of active radio pulsars beamed towards Earth in the inner parsec of the GC.

2.8 Pulsar Wind Nebulae in Inner 20 pc

Using a total of 1 Ms of *Chandra* ACIS–I observations of the inner parsecs of the GC, Muno et al. (2008) compiled a catalog of 34 diffuse X-ray emitting features. Based on the X-ray luminosities and sizes of the sources in their catalog, Muno et al. (2008) expect ∼20 pulsar wind nebulae (PWNe) to be present within 20 pc of Sgr A*. Since PWNe are powered by pulsars, we may use this inferred population of PWNe to estimate the pulsar population in the inner 20 pc of the GC.

Pulsars can lose their rotational kinetic energy by the release of relativistic winds of charged particles. The winds exert a pressure upon and deposit energy into the surrounding interstellar medium, producing luminous PWNe that radiate across the electromagnetic spectrum (see, e.g., Gaensler & Slane 2006). As a result, the luminosity of the PWN will be directly related to the spin-down luminosity of the pulsar given by

$$\dot{E} = -dE_{rot}/dt = 4\pi^2 I \dot{P}/P^3, \tag{2.28}$$

where I and P are the moment of inertia and period, respectively, of the pulsar.

Since the spin-down luminosity of a pulsar decreases with increasing age, one would expect the most luminous PWNe to contain young pulsars (however, older

pulsars may be "recycled" sufficiently to power PWNe as described by Cheng et al. 2006). Of the 30 confirmed pulsars associated with PWNe, 25 have characteristic ages ($\tau_c = P/2\dot{P}$) of $\tau_c \lesssim 10^6$ yr and 23 have characteristic ages $\tau_c \lesssim 10^5$ yr (Roberts 2004). Thus, we adopt a lifetime for a typical PWN of $t_{pwn} \sim 10^5$ yr.

Given the observed number of PWNe in the GC ($N_{obs} \sim 20$) and a typical lifetime of $t_{pwn} \sim 10^5$ yr, we find a mean rate of formation of PWNe over the last $\sim 10^5$ yr to be

$$\beta_{pwn} \sim 2 \times 10^{-4} \text{ yr}^{-1} \left(\frac{N_{pwn}}{20}\right) \left(\frac{t_{pwn}}{10^5 \text{ yr}}\right)^{-1}. \tag{2.29}$$

Assuming that the PWN formation rate has remained constant over the last $\sim 10^7$ yr, we may estimate the number of CPs in the inner 20 pc to be

$$N_{\rm CP} \sim \beta_{pwn} \tau_{psr} f_b f_v f_{pwn}^{-1}, \tag{2.30}$$

where $\tau_{psr} \sim 10^7$ yr is the typical radio lifetime of a CP, $f_b = 0.2$ is the beaming fraction, f_v is the fraction of pulsars with birth velocities low enough to be retained in the inner 20 pc, and $f_{pwn} \sim 1$ is the fraction of pulsars that form PWNe.

Taking the mass of the central 20 pc to be $M = 3 \times 10^7\ M_\odot$ (Lindqvist et al. 1992), we find that pulsars must have velocities $v_{birth} < 115$ km s^{-1} to remain gravitationally bound to the inner 20 pc. From the birth velocity distributions considered by Faucher-Giguère & Kaspi (2006), we find $f_v \approx 0.05 - 0.30$. However, the distance traveled by a pulsar is given by

$$d \approx 10 \text{ pc} \left(\frac{v}{100 \text{ km s}^{-1}}\right) \left(\frac{t}{10^5 \text{ yr}}\right). \tag{2.31}$$

Thus, pulsars with velocities high enough to become gravitationally unbound will also have velocities high enough to escape the inner 20 pc on timescales comparable to the PWN lifetime. As a result, the PWNe observed within the inner 20 pc are very likely to remain there and we can take $f_v \sim 1$.

From Eq. 2.30, we see that if the PWN birth rate has been constant over the last $\sim 10^7$ yr, we would expect

$$N_{\rm CP} \sim 400 \left(\frac{N_{pwn}}{20}\right) \left(\frac{t_{pwn}}{10^5 \text{ yr}}\right)^{-1} \left(\frac{f_{pwn}}{1.0}\right)^{-1} \tag{2.32}$$

CPs within 20 pc of Sgr A*.

Finally, we note that of the $\sim$20 PWN candidates identified by Muno et al. (2008), 4 fall within a projected radial distance of 1 pc from Sgr A*. Assuming the number of pulsars scales accordingly, then Eq. 2.32 predicts $N_{CP} \sim 80$ CPs within the inner parsec of the GC.

2.9 Supernova Rate in the Galactic Center

Neutron stars are formed as the end products of core-collapse supernovae (CCSN). An estimate of the rate of CCSN in the GC would therefore offer a constraint on the pulsar population. The CCSN rate is estimated below for both $r < 150$ pc and $r < 20$ pc.

2.9.1 CCSN Rate Within $r < 150$ pc of Sgr A*

By measuring the total mass of ^{26}Al in the Galaxy, Diehl et al. (2006) estimate the Galactic CCSN rate to be $\beta_{CCSN} = 1.9 \pm 1.1$ century^{-1}. One may, in principle, scale this estimate to smaller regions of the Galaxy using massive star populations. Taking the inner 500 pc to contain 10% of the Galaxy's massive star formation (Figer 2008) we can estimate that the inner $\sim$150 pc contains $\sim$2% of the massive star formation and therefore should have a CCSN rate of $\beta_{CCSN} \approx 0.04$ century^{-1}.

Crocker et al. (2011) estimate a similar rate and show that it is consistent with SN rate estimates from infrared observations, stellar composition, X-ray emission, gas turbulence, and high-velocity compact clouds (see Crocker et al. 2011, and references within). We may now estimate the CP population in the GC to be

$$N_{\rm CP} = f_{psr} f_b f_v \tau_{psr} \beta_{CCSN} \tag{2.33}$$

where $\beta_{CCSN} \approx 4 \times 10^{-4} \mathrm{yr}^{-1}$ is the CCSN rate, $\tau_{psr} \sim 10^7$ yr is the mean canonical pulsar lifetime, $f_b = 0.2$ is the fraction of pulsars beamed toward Earth, f_v is the fraction of pulsars with birth velocities small enough to be retained by the GC and $f_{psr} \sim 1$ is the fraction of CCSN that result in active pulsars. Using the distributions from Faucher-Giguère & Kaspi (2006), the fraction of pulsars with birth velocities smaller than the escape velocity $v_e \approx 200$ km s^{-1} at 150 pc ranges from $f_v \approx 0.1 - 0.4$. These values give an estimate of $N_{\rm CP} \sim 100$. Likewise, accounting for the longer ages for MSPs ($\tau_{psr} \sim 10^{10}$ yr), we can estimate the MSP population to be $N_{\rm MSP} \sim 10^5 f_r$, where f_r is the fraction of NSs that get recycled to MSPs (see Section 2.7.4).

2.9.2 CCSN Rate in Inner 20 pc from X-ray Observations

Studies of diffuse X-ray emission can also provide insight into the SN rate in the GC. Using over 600 ks of *Chandra* ACIS–I observations, Muno et al. (2004) found that the diffuse X-ray emissions in the GC could be explained by a two-temperature plasma composed of a "soft" component ($kT \approx 0.8$ keV) and a "hard" component ($kT \approx 8$ keV). Assuming the soft component of the plasma is primarily heated by SNe, an estimate for the SN rate can be made by observing the loss of energy from the inner 20 pc.

Let us first consider the case in which the soft component of the plasma just cools radiatively. The X-ray luminosity of the soft component of the plasma in the inner 20 pc is $L_X \approx 3 \times 10^{36}$ erg s^{-1} (Muno et al. 2004). If each SN transfers $\sim$1% of its total kinetic energy of $\sim 10^{51}$ erg to the plasma, then a SN rate of $\beta_{SN} \approx 10^{-5}$ yr^{-1} is required to maintain the currently observed temperature. Taking this rate to be constant and $f_v \sim 0.1$ (see Section 2.8) gives an estimate for the CP population of $N_{\rm CP} \sim 2\,(f_v/0.1)$.

If the plasma is unconfined, it can also cool through adiabatic expansion. Rough estimates put this cooling rate at $L_{ad} \approx 9 \times 10^{38}$ erg s^{-1} (Muno et al. 2004), which would require a SN rate of $\beta_{SN} \approx 3 \times 10^{-3}$ yr^{-1}. Again assuming this rate is constant and $f_v \sim 0.1$ as above, the estimated CP population is $N_{\rm CP} \sim 600\,(f_v/0.1)$.

The above estimates assume that the SN rate is constant over the radio lifetime of a CP ($\sim 10^7$ yr). However, the SN rate estimates are only required to hold over a characteristic cooling time of $t_c \sim E/L$, where $E \sim 5 \times 10^{50}$ erg s^{-1} is the total thermal energy stored in the plasma and L is the appropriate cooling luminosity (Muno et al. 2004). The cooling timescales for radiative cooling and adiabatic expansion are 5×10^6 yr and 2×10^4 yr, respectively.

Keeping this caveat in mind, the assumption of a constant SN rate does allow useful bounds to be put on the pulsar populations in the GC. Taking a constant SN rate from radiative cooling to be a lower bound and a constant SN rate from adiabatic expansion to be an upper bound, we find the CP population in the inner 20 pc to be $1 \lesssim N_{\rm CP} \lesssim 10^3$. Likewise, for MSPs with $\tau \sim 10^{10}$ yr, we estimate a population of $10^3 f_r \lesssim N_{\rm MSP} \lesssim 10^6 f_r$, where f_r is the fraction of NSs recycled into MSPs (see Section 2.7.4).

2.10 Discussion

2.10.1 Summary of Estimates

We have used observations over a wide range of wavelengths to make order of magnitude estimates of the number of pulsars allowed within $r \leq 1$ pc and $r \leq 150$ pc of Sgr A*. The estimates are summarized in Table 2.4.

Pulsar Population Within $r \leq 150$ pc

Limits on the pulsar population within 150 pc of Sgr A* may be set using the five known pulsars in the inner $15'$, the catalog of compact radio sources by Lazio & Cordes (2008), measurements of an excess gamma-ray flux by Hooper & Goodenough (2011) and estimates of the Galactic core-collapse supernova rate.

The five known pulsars in the inner $15'$ provide the strongest current evidence for an intrinsic pulsar population in the GC region. A Monte Carlo population analysis by Deneva et al. (2009) showed that the pulsar detections in the survey by Deneva et al. (2009) indicate a population of at least $N \gtrsim 100$ pulsars within 100 pc of Sgr A*.

The catalog of compact radio sources compiled by Lazio & Cordes (2008) allows for upper limits to be placed on the pulsar population in the inner 150 pc. The VLA survey produced a total of 170 compact steep-spectrum sources. Although pulsars cannot be unequivocally classified in an imaging survey, Lazio & Cordes (2008) estimate that $N \sim 10$ of the sources were likely pulsars. Using this estimate and the survey sensitivities, a conservative upper bound of $N \lesssim 10^4$ may be set

on the pulsar population in this region. Even if it turns out that there are no pulsars in the catalog, an upper limit of $N \lesssim 10^3$ may be set to 99% confidence level. We note that although these upper limits should hold for the entire survey region, the increasing background temperature and sidelobes caused by extended emission towards the inner GC mean that the inner field of the survey (half-power radius of 15′) likely experienced decreased sensitivity and could potentially hide a significant pulsar population in the immediate vicinity of Sgr A*.

Using the first two years of *Fermi* data, Hooper & Goodenough (2011) claim to have detected an excess diffuse gamma-ray flux in the inner 150 pc of the Galaxy, which they attribute to annihilating dark matter particles. If we assume the gamma-rays come instead from a collection of MSPs, an upper limit to the number of MSPs in the GC may be set. Following similar calculations for globular clusters by Abdo et al. (2010b), we find that the excess is consistent with a population of $\sim 5 \times 10^3$ MSPs. This estimate is nominally an upper limit, but considering the systematic uncertainties in current GC gamma-ray background models and difficulties subtracting the point source associated with Sgr A*, we adopt this value as only a lower limit on the upper bound of MSPs in the inner 150 pc.

As radio pulsars are formed in core-collapse SNe, the SN rate also provides a constraint on the pulsar population in the GC. By scaling down the Galactic SN rate based on massive star populations in a manner similar to that of Crocker et al. (2011), we estimate a SN of $\beta_{CCSN} \approx 0.04$ century^{-1}. Such a SN rate indicates a CP population of $N_{\rm CP} \sim 100$ and an MSP population of $N_{\rm MSP} \sim 10^5 f_r$, where f_r is the recycling fraction discussed in Section 2.7.2. Since the recycling fraction of field pulsars is $f_r \gtrsim 10^{-3}$ and potentially as high as $f_r \sim 0.1$ in globular clusters, we adopt a nominal value of $f_r \sim 10^{-2}$, so $N_{\rm MSP} \sim 10^3 (f_r / 10^{-2})$.

Finally, we note that all of the upper limits considered for pulsar populations on the large scale of 150 pc may not include contributions from the few inner parsecs as a result of decreased sensitivity or failure to incorporate recent starburst activity. As a result, we consider these limits mainly applicable in the region 1 pc $\lesssim r \lesssim$ 150 pc. The above estimates are consistent with a total pulsar population (that is, both CPs and MSPs) of $10^2 \lesssim N_{psr} \lesssim 10^4$, a CP population of $N_{\rm CP} \lesssim 10^2$ and an MSP population of $N_{\rm MSP} \lesssim 10^4$.

Pulsar Population Within $r \leq 1$ pc

Limits on the pulsar population in the inner parsec of the GC have been set using the non-detections of high frequency directed pulsar searches, the spectrum of Sgr A* on arcsecond scales, the population and star-formation history of the massive star progenitors of NSs, the observations of ∼20 PWN candidates in the inner 20 pc, and the limits on the SN rate based on X-ray observations in the inner 20 pc.

Directed pulsar searches of the inner parsec of the Galaxy have been conducted with the GBT at frequencies of 5, 9 and 15 GHz (Deneva et al. 2009; Macquart et al. 2010). Since none of these searches made any detections, an upper limit may be set on the total pulsar population that is still consistent with a null result. Using the survey parameters provided in the Deneva et al. (2009) and Macquart et al. (2010) surveys, we find that up to $N_{psr} \lesssim 10^3$ pulsars (both CPs and MSPs) may be present in the inner parsec.

Since the compact radio source Sgr A* is broadened by interstellar scattering (≈1″ at 1 GHz), the observed flux density may actually be a combination of the emission near the MBH and a diffuse component from a population of unresolved

pulsars. By requiring that this two-component system reproduce the observed spectrum of Sgr A*, constraints may be placed on the pulsar population on arc-second scales. We consider a variety of spatial distributions and find that a total population of $\sim 10^3$ pulsars is consistent with flux density measurements, regardless of spatial distribution. The existence of such a large pulsar population would distort the low-frequency measurements of the intrinsic spectrum of Sgr A* and the free-free absorption along the line of sight of Sgr A*.

Upper limits to the total pulsar population can also be set by studying the populations of massive stars that end their lives as NSs. Infrared observations of the present day population of massive stars allows for estimates of the star formation history. We consider the case of two general SFHs and find that the CP population can get as high as $N_{\rm CP} \lesssim 200$ only under the most favorable conditions. More typical estimates for the CP population are $N_{\rm CP} \sim 20$, with most of these being formed in the young disk of massive stars located $\approx$0.5 pc from Sgr A*. The MSPs are less sensitive to the exact SFH and produce populations of $N_{\rm MSP} \sim 200$ with an upper limit of $N_{\rm MSP} \lesssim 2000$ for a range of reasonable SFHs.

Upper limits on the number of CPs in the inner parsecs of the GC may be set using the detection of $\sim$20 PWNe within 20 pc of Sgr A*. Using the $\sim$20 PWN candidates compiled by Muno et al. (2008) in a catalog of diffuse X-ray sources and assuming PWNe are produced at a constant rate, we find that as many as 400 CPs may reside in the inner 20 pc. If the CP distribution follows that of the PWN candidates, then as many as 80 CPs could reside in the inner parsec.

Finally, we consider measurements of the soft ($kT \approx 0.8$ keV) component of the diffuse X-ray plasma in the inner 20 pc. Assuming that the plasma was heated by the transfer of kinetic energy from SNe, we may set an upper limit on the number

of pulsars in this region (Muno et al. 2004). By considering two different cooling regimes, we find that the most extreme cooling scenario will produce a population of up to $\sim 10^3$ CPs and $\sim 10^6 f_r$ MSPs. Thus, we can set upper bounds of $N_{\rm CP} \lesssim 10^3$ and $N_{\rm MSP} \lesssim 10^4 (f_r/10^{-2})$ for CPs and MSPs in the inner 20 pc.

Overall, we find that the above estimates are consistent with a CP population of $N_{\rm CP} \lesssim 100$ and an MSP population of $N_{\rm MSP} \lesssim 10^3$ in the inner parsec of the GC.

2.10.2 Conclusions

Current observations of the GC are consistent with a population of up to $\sim 10^3$ active pulsars beamed towards Earth within the central parsec around Sgr A*. This total population may consist of up to $N_{\rm CP} \lesssim 100$ CPs and as many as $N_{\rm MSP} \lesssim 10^3$ MSPs. Such a population could distort the low-frequency measurements of both the spectrum of Sgr A* and free-free absorption along the line of sight of Sgr A*. However, even with a potentially sizeable collection of pulsars, the difficult observing conditions of the inner regions of the GC will make individual detections a challenge. The strong interstellar scattering and large pulse broadening times mean that typical pulsar periodicity searches at radio wavelengths will be sensitive to pulsars only at high observing frequencies and large bandwidths (Cordes & Lazio 1997). Even if most of the pulsars lie below the detection threshold, "giant" pulses intrinsic to the pulsar or as the result of an enhancement through multipath scattering may make a pulsar visible a search for single pulses. Since there may be many more MSPs than CPs, one may search for pulsars using interferometer

	$r \leq 1$ pc			$r \leq 150$ pc		
Method	CP	MSP	Total	CP	MSP	Total
Pulsar Surveys	$\lesssim 10^3$	–	–	–	–	$\gtrsim 10^2$
Radio Point Sources	–	–	–	–	–	$\lesssim 10^4$
Radio Spectrum A	–	–	$< 7.4 \times 10^3$	–	–	–
Radio Spectrum B-1	–	–	$< 1.5 \times 10^3$	–	–	–
Radio Spectrum C	–	–	$(1.1 \pm 0.4) \times 10^3$	–	–	–
Diffuse Gamma-ray	–	–	–	–	$\sim 5 \times 10^3$	–
Massive Stars[a]	$\lesssim 10^2$	$\lesssim 10^3$	$\lesssim 10^3$	–	–	–
PWNe	10^2	–	–	–	–	–
Supernovae[a,b]	$\lesssim 10^3$	$\lesssim 10^4 (f_r/10^{-2})$	$\lesssim 10^4$	10^2	$10^3\,(f_r/10^{-2})$	–

Table 2.4: **Summary of Pulsar Population Estimates by Method**. (a) Typical values for the "recycling fraction" are $f_r \gtrsim 10^{-3}$ in the Galactic field and potentially as high as $f_r \gtrsim 0.1$ in the central parsec (see Section 2.7.4). (b) Supernovae estimate given at $r \leq 20$ pc and $r \leq 150$ pc

imaging surveys of compact radio objects similar to that of Lazio & Cordes (2008). Finally, search methods should be considered at wavelengths less affected by the scattering effects of the ISM. Since many MSPs produce gamma-ray emission, a directed search of the GC region with the *Fermi* LAT could potentially detect a pulsar in a blind periodicity search.

Despite the difficulties in finding pulsars in the GC, the detection of a pulsar orbiting Sgr A* with an orbital period of $P_{orb} \lesssim 100$ yr would provide an unparalleled test of gravity in the strong-field regime and could potentially allow the measurement of the spin and quadrupole moment of the MBH (Pfahl & Loeb 2004; Laguna & Wolszczan 1997; Wex & Kopeikin 1999; Liu et al. 2011). Additionally, the detection of even one pulsar in the inner few parsecs would provide an excellent probe of the magneto-ionic material, the gravitational potential, and the star formation history in the vicinity of Sgr A*. In light of the significant scientific rewards and a potentially sizeable target population, we strongly recommend continued pulsar searches in the GC across a wide range of wavelengths.

CHAPTER 3

THE DISTRIBUTION OF FREE ELECTRONS TOWARDS THE GALACTIC CENTER[1]

3.1 Introduction

The propagation of radio waves from the Galactic center is severely affected by scattering caused by turbulence-driven electron density fluctuations in the interstellar medium (ISM). The first evidence for this came shortly after the discovery of Sgr A*, the radio source associated with the massive black hole at the center of the Galaxy. Davies et al. (1976) found that the apparent angular diameter of Sgr A* scaled with frequency as $\theta_{\rm sc} \propto \nu^{-2}$, a clear indication of strong scattering. Subsequent measurements have confirmed that the scattering disk of Sgr A* is an ellipse with major axis $\theta_{\rm maj} \approx 1''\nu_{\rm GHz}^{-2}$ and axial ratio $\rho = \theta_{\rm maj}/\theta_{\rm min} \approx 2$ (Lo et al. 1985, 1993; Bower et al. 2006). The discovery of a population of OH/IR stars (late-type stars with atmospheric OH maser emission) with comparable or larger scattering diameters firmly established the existence of an extended ($\approx 1^\circ \times 0.^\circ 5$) region of enhanced scattering around Sgr A* (van Langevelde & Diamond 1991; van Langevelde et al. 1992; Frail et al. 1994).

While the large angular diameter of a radio source in the Galactic center demonstrates the existence of scattering material along the line of sight (LOS), it does not determine the detailed distribution of that material along the LOS. As a result, it was unclear whether the scattering material was itself located within the Galactic center or if it was located in the Galactic disk and by chance intersected the LOS. To differentiate between these possibilities requires the measurement of

[1] R. S. Wharton

at least two observables with different dependencies on the LOS distribution of the scattering material. The angular broadening of the observed source size and the temporal broadening of the observed pulse width of a radio pulsar is an example of such measurements.

Since there were no known radio pulsars in the inner degree of the Galactic center at the time, Lazio & Cordes (1998a) sought to determine the distribution of free electrons by other means. They noted that although the angular broadening of a single source does not determine the distribution of the scattering material, the combined measurement of many sources can constrain the properties of model distributions. Using this approach, Lazio & Cordes (1998a) combined the scattering sizes of Sgr A* and OH/IR stars with measurements of the free-free emission and extragalactic source counts to perform a global likelihood analysis of scattering models toward the Galactic center. They found that the data were best described by a hyperstrong scattering screen located $D_{\rm s} = 133^{+200}_{-80}$ pc from Sgr A*. The hyperstrong scattering model predicts that pulsars found in the vicinity of Sgr A* would have large dispersion measures (DM $\approx$ 2000 pc cm^{-3}) and very large pulse broadening times ($\tau_{\rm sc} \approx$ 2000 s at 1 GHz). Since pulse broadening scales as $\tau_{\rm sc} \propto \nu^{-4}$, this model motivated pulsar searches at higher frequencies (Cordes & Lazio 1997).

Five pulsars have been discovered within about 20′ of Sgr A* with large DMs (DM $\approx 900-1500$ pc cm^{-3}), but smaller scattering times ($\tau_{\rm sc} \lesssim 1$ s at 1 GHz) than predicted by the hyperstrong scattering model (Deneva et al. 2009; Johnston et al. 2006). Despite this discrepancy, these pulsar properties can be made consistent with the model if the pulsars are located in front of the scattering material (i.e., closer to the observer). The five Galactic center pulsars were discovered at ob-

serving frequencies of $2-3$ GHz. Even though Johnston et al. (2006) and Deneva et al. (2009) observed at higher frequencies (8.1 and 8.9 GHz, respectively), no pulsars were discovered within $10'$ of Sgr A*. Still higher frequency searches were conducted (e.g., Macquart et al. 2010, at 15 GHz), but no pulsars were discovered in the inner few arcminutes of the Galaxy at radio wavelengths.

In April 2013, the magnetar J1745−2900 was discovered in outburst by *Swift*/BAT during a scheduled observation of Sgr A* (Kennea et al. 2013). A *NuSTAR* follow-up by Mori et al. (2013) found a 3.76 s period in X-rays and a *Chandra* observation by Rea et al. (2013) localized the source to $2\farcs4$ from Sgr A*. Radio detections were soon made and the measured DM and RM were found to be the highest of any pulsar, consistent with location very near to Sgr A* (Shannon & Johnston 2013; Eatough et al. 2013). A multifrequency study of temporal scattering by Spitler et al. (2014a) found that the pulse broadening time of J1745−2900 is consistent with $\tau_{\rm sc}(\nu) = 1.3$ s $\nu_{\rm GHz}^{-4}$ from $1.2-18.95$ GHz. VLBA observations by Bower et al. (2014) found that the angular broadening of J1745−2900 is comparable to Sgr A* at 8.4 GHz. Combining their angular broadening measurements with the temporal broadening measurements of Spitler et al. (2014a), Bower et al. (2014) find that the scattering measurements are consistent with a thin-screen model with a screen located at $D_{\rm s} = 5.8 \pm 0.3$ kpc from Sgr A* if the magnetar is located near Sgr A* and both are seen through the same scattering screen.

The observed properties of J1745−2900 are dramatically different from those predicted by the hyperstrong scattering model. The pulse broadening time is three orders of magnitude smaller and the scattering material, if modeled as a thin screen, is pushed out of the Galactic center and into the disk almost 6 kpc away from Sgr A* (2.5 kpc from the Sun). In light of the surprising results from

J1745−2900 and the new observational data accumulated since Lazio & Cordes (1998a) developed their model, it is necessary to reconsider the distribution of free electrons along the line of sight to the Galactic center using all of the currently available observational constraints.

In this paper, we consider three models of the distribution of free electrons toward the inner degree of the Galactic center: (1) a single uniform thin screen, (2) a uniform thin screen with additional contributions from the Galactic disk and the Galactic center, and (3) a heterogeneous Galactic center scattering screen. The basic properties of the three models are given in Section 3.2. The relations between the line of sight integrals and the observables of each model are determined in Section 3.3. In Section 3.4, the models are compared against a range of observational data including the scattering properties of Sgr A* and J1745−2900 the five Galactic center pulsars, angular broadening of OH masers, extragalactic radio sources, free-free absorption and emission, radio recombination line measurements, Hα observations, known HII regions, and other highly scattering LOSs in the Galaxy. In Section 3.5, the models are reviewed in light of the observational data. The two models that best explain the known data are discussed in Section 3.6 and several observing campaigns to better understand the region are suggested. Finally, in Section 3.7, we present some concluding remarks.

3.2 Three Electron Density Distribution Models

The Galactic center region (taken here to be anything within $\theta \leq 30'$ of Sgr A*) is a dynamic and complex collection of HII regions, supernova remnants, and large sites of active and vigorous star formation. Coherent structures of ionized gas exist

on a range of scales from the $\sim 1^\circ$ belt of clouds encircling Sgr A* to filaments with widths less than an arcsecond (see Figures 3.4 and 3.5 for an infrared view). Since this complicated field is sampled by line of sight integrals toward only a few directions, any simple model will almost certainly have some deficiencies. With this in mind, we present three general models for the three-dimensional distribution of free electrons along the line of sight to the inner degree of the Galaxy (see Figure 3.1). The formalism for evaluating these models is presented in Section 3.3 and the allowed parameter ranges are set by the observational constraints in Section 3.4.

Model 1 approximates the distribution of free electrons as a single thin screen located along the LOS at a distance $D_{\rm s}$ from the source. The screen is oriented transverse to the LOS with a thickness, Δs, that is small compared to the distance from the source to the observer ($\Delta s \ll D$). The screen is taken to be of unlimited transverse extent. This model is motivated by the scattering measurements of J1745−2900 and is entirely determined by simultaneous measurements of the angular size and pulse broadening time of a pulsar. Though Model 1 will match the scattering measurements of J1745−2900 by construction, it must also match the many other observable tracers of ionized gas if it is to be deemed viable.

Model 2 is an extension of thin disk of Model 1 to include contributions from the Galactic disk and the Galactic center. The disk component of the electron density distribution is taken to uniformly fill the space between the observer and the source. The Galactic center component is centered on Sgr A* and is assumed to uniformly fill a region out to $D_{\rm gc}$. The extent of the Galactic center component, $D_{\rm gc}$, is assumed to be no larger than about 1 kpc (corresponding to the size of the Galactic bar) and likely falls within the 150 pc region that defines the

1 degree field of view considered in this paper. Both the disk and Galactic center components to the electron density distributions are motivated by the observed dispersion measures of pulsars in the inner regions of the Galaxy.

Model 3 is essentially the hyperstrong scattering screen developed by Lazio & Cordes (1998a) but with modifications to allow for the observed scattering properties of J1745−2900. Like Lazio & Cordes (1998a), the primary dispersing and scattering material of Sgr A* and the OH/IR stars is very near the Galactic center ($D_{\rm s} \approx 150$ pc) and has a scattering strength many orders of magnitude larger than other such regions in the Galaxy. Unlike Lazio & Cordes (1998a) and Models 1 and 2, this model does not assume a homogeneous scattering screen. Instead, the scattering region is taken to be spatially heterogeneous. This can be thought of as a screen with holes or gaps, or as a collection of small scattering regions with some filling factor. If the scattering regions are small enough, this model could result in scattering measurements with different frequency scalings than typically expected for a screen of infinite transverse extent (Cordes & Lazio 2001).

3.3 Line of Sight Integrals and Observables

Relating the three-dimensional electron density distribution models presented in Section 3.2 to observable quantites discussed in Section 3.4 requires the use of integrals along the line of sight. The most commonly used line of sight integrals are the dispersion measure (DM), the emission measure (EM), and the scattering measure (SM):

$$\mathrm{DM} = \int_0^D n_{\rm e}(s) ds \quad \left[\mathrm{pc\ cm^{-3}}\right] \tag{3.1}$$

$$\mathrm{EM} = \int_0^D n_{\rm e}^2(s) ds \quad \left[\mathrm{pc\ cm^{-6}}\right] \tag{3.2}$$

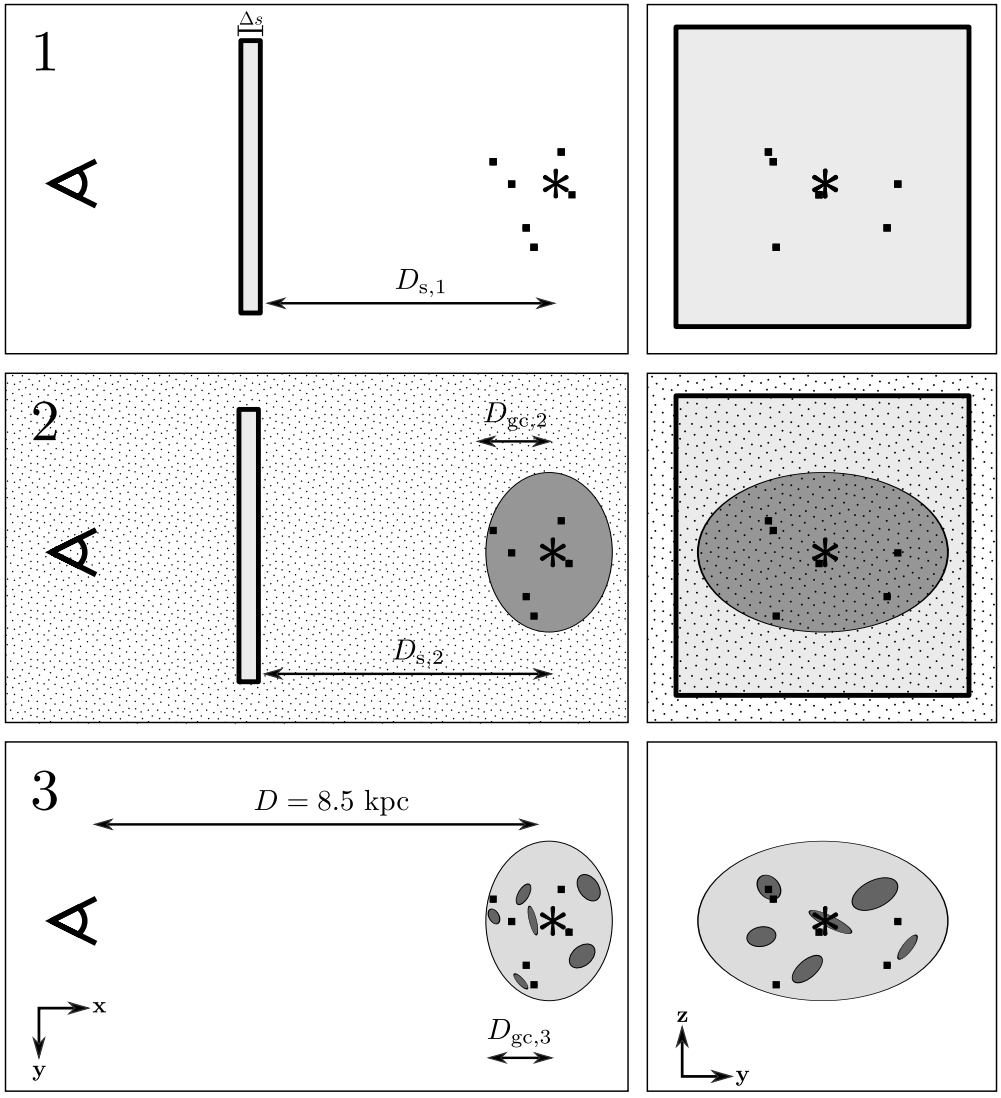

Figure 3.1: **Schematic illustration of the three models of the free electron distribution**. The models are described in Section 3.2. The top row shows Model 1 with a single thin screen (light grey). The middle row shows Model 2 with a thin screen (light grey), Galactic disk component (dots), and a Galactic center component (dark grey). The bottom row shows Model 3 as a heterogeneous region in the Galactic center. The left column of each row gives a top-down view of the line of sight from the observer to the Galactic center. The right column gives a projected view of the Galactic center as seen by the observer. In both columns, Sgr A* is represented by an asterisk and an example collection of five sources is represented by squares.

$$\mathrm{SM} = \int_0^D C_n^2(s) ds \ \left[\mathrm{kpc\ m^{-20/3}}\right]. \tag{3.3}$$

The DM and EM are simply moments of the electron density, $n_e(s)$, along the line of sight distance, D, from the source to the observer. Similarly, the scattering measure is the integral over $C_n^2(s)$, which is the coefficient of the power-law wavenumber spectrum of electron density fluctuations given by

$$P_{\delta_{n_e}}(q) = C_n^2 q^{-\beta}, \qquad \frac{2\pi}{\ell_0} \leq q \leq \frac{2\pi}{\ell_1} \tag{3.4}$$

defined over a range of length scales between the inner (ℓ_1) and outer (ℓ_0) cutoffs. Since it is the electron density fluctuations that gives rise to scattering, the $C_n^2(s)$ term quantifies the strength of scattering at any given point along the line of sight.

The DM and EM are easily determined from observable quantities. The DM is directly measured from the frequency-dependent time delay between the arrival of pulses from a pulsar. The EM can be inferred from measurements of the optical depth,

$$\tau_\nu = 3.28 \times 10^{-7} \left(\frac{T_\mathrm{e}}{10^4\ \mathrm{K}}\right)^{-1.35} \left(\frac{\nu}{1\ \mathrm{GHz}}\right)^{-2.1} \left(\frac{\mathrm{EM}}{1\ \mathrm{pc\ cm^{-6}}}\right), \tag{3.5}$$

the Hα intensity[2] (Haffner et al. 1998)

$$I_{\mathrm{H}\alpha} = 1\ \mathrm{R} \left(\frac{\mathrm{EM}}{2.75\ \mathrm{pc\ cm^{-6}}}\right) \left(\frac{T_\mathrm{e}}{10^4\ \mathrm{K}}\right)^{-0.9} e^{-2.2E(B-V)}, \tag{3.6}$$

and from observations of radio recombination lines (RRLs). The SM, on the other hand, cannot be directly inferred from the pulse broadening time (τ_sc) and the angular broadening (θ_sc) because these observables depend on the distribution of the scattering material along the LOS. Instead, one must use the estimators SM_τ and SM_θ given by

$$\mathrm{SM}_\tau = 6 \int_0^D C_n^2(s)\, (s/D)\, (1 - s/D)\, ds \tag{3.7}$$

[2]The Hα intensity, $I_{\mathrm{H}\alpha}$, is measured in Rayleighs, where 1 Rayleigh = $10^6/4\pi$ photons cm^{-2} s^{-1} sr^{-1}

and

$$\mathrm{SM}_\theta = \begin{cases} \mathrm{SM}, & \text{extragalactic} \\ 3\int_0^D C_n^2(s)\,(s/D)^2\,ds, & \text{Galactic} \end{cases} \tag{3.8}$$

where the integral is taken from the source ot the observer.

The estimators can then be expressed in terms of τ_{sc} and θ_{sc} as

$$\mathrm{SM}_\tau = \left(\frac{\tau_d}{1.1\ \mathrm{ms}}\right)^{5/6} \left(\frac{D}{1\ \mathrm{kpc}}\right)^{-5/6} \nu_{\mathrm{GHz}}^{11/3} \tag{3.9}$$

and

$$\mathrm{SM}_\theta = \left(\frac{\theta_d}{71\ \mathrm{mas}}\right)^{5/3} \nu_{\mathrm{GHz}}^{11/3}. \tag{3.10}$$

Combining measurements of τ_{sc} and θ_{sc} with a model for $C_n^2(s)$ then allows the determination of SM. Finally, one may relate the LOS integrals to each other by adopting a model for small-scale structure in the ISM. Expressions for one such model are provided in Appendix 3.8.

Given the above relations between LOS integrals and observables, we can express the models in terms of the LOS integrals so that they may be compared with the observational constraints in Section 3.4.

Model 1: For the single thin screen of Model 1, the scattering measure estimators are

$$\mathrm{SM}_{\theta,1} = 3\left(\frac{D_{\mathrm{s}}}{D}\right)^2 C_n^2(D_{\mathrm{s}})\,\Delta s = 3\left(\frac{D_{\mathrm{s}}}{D}\right)^2 \mathrm{SM}_{\mathrm{s}} \tag{3.11}$$

and

$$\mathrm{SM}_{\tau,1} = 6\left(\frac{D_{\mathrm{s}}}{D}\right)\left(1-\frac{D_{\mathrm{s}}}{D}\right) C_n^2(D_{\mathrm{s}})\,\Delta s = 6\left(\frac{D_{\mathrm{s}}}{D}\right)\left(1-\frac{D_{\mathrm{s}}}{D}\right) \mathrm{SM}_{\mathrm{s}} \tag{3.12}$$

where D_{s} is the distance of the screen from the source and $\mathrm{SM}_{\mathrm{s}} \equiv C_n^2(D_{\mathrm{s}})\,\Delta s$ is the scattering measure of the screen. The emission measure of the screen is related

to the scattering measure as

$$\mathrm{EM_{s,1}} = 544.6 \text{ pc cm}^{-6} \left(\frac{\ell_0}{1 \text{ pc}}\right)^{2/3} \epsilon^{-2} \left(1 + \epsilon^2\right) \mathrm{SM_s} \tag{3.13}$$

and the scattering measure is related to the dispersion measure as

$$\mathrm{SM_{s,1}} = 10^{-3} C_{\mathrm{SM}} F_{\mathrm{s}} \, \mathrm{DM_s^2} / \Delta s \tag{3.14}$$

where Δs is the thickness of the screen in parsecs and F_{s} is a fluctuation parameter that roughly quantifies the turbulence (see Section 3.8).

Model 2: For Model 2, the scattering measure estimators are comprised of components from the screen, Galactic center, and disk, so we have

$$\mathrm{SM}_{\theta,2} = 3 \left(\frac{D_{\mathrm{s}}}{D}\right)^2 \mathrm{SM_s} + \left(\frac{D_{\mathrm{gc}}}{D}\right)^2 \mathrm{SM_{gc}} + \mathrm{SM_d} \tag{3.15}$$

and

$$\mathrm{SM}_{\tau,2} = 6 \left(\frac{D_{\mathrm{s}}}{D}\right) \left(1 - \frac{D_{\mathrm{s}}}{D}\right) \mathrm{SM_s} + \left(\frac{D_{\mathrm{gc}}}{D}\right) \left(3 - 2\frac{D_{\mathrm{gc}}}{D}\right) \mathrm{SM_{gc}} + \mathrm{SM_d} \tag{3.16}$$

where the subscripts "s", "gc", and "d" correspond to the screen, Galactic center, and disk components. Distances are measured from the source. Because of the geometric weighting, the scattering measure contribution from the Galactic center will be negligible as long as $\mathrm{SM_{gc}}/\mathrm{SM_s} \ll (D_{\mathrm{s}}/D_{\mathrm{gc}})^2$.

The total emission measure from this model is simply the sum of the component emission measures

$$\mathrm{EM_2} = \mathrm{EM_s} + \mathrm{EM_{gc}} + \mathrm{EM_d} \tag{3.17}$$

where each of the component EM values can be related back to the corresponding SM values using Equation 3.13. Similarly, the total dispersion measure is

$$\mathrm{DM_2} = \mathrm{DM_s} + \mathrm{DM_{gc}} + \mathrm{DM_d} \tag{3.18}$$

which can be related back to the SM values using Equation 3.14.

Model 3: For Model 3, the formulation of the line of sight integrals for the heterogeneous Galactic center screen is mostly the same as for the homogeneous single screen in Model 1, the main difference being that the Model 3 screen parameters will depend on sky position. However, the observable quantities do not, in general, have the simple relation to the scattering measure estimators presented in Equations 3.9 and 3.10. Instead, the observed frequency dependence of these quantities changes as the size of the scattering disk approaches the size of the scattering region (Cordes & Lazio 2001).

3.4 Observational Constraints

Using the tools of Section 3.3, the three electron density distribution models of Section 3.2 can be tested against a wide range of multiwavelength observational constraints. In each case, the observational data are presented and allowed parameters for the model are determined.

3.4.1 Scattering of Sgr A* and J1745−2900

Observational Data

Observations at centimeter wavelengths over the last 30 years have consistently measured the scattering disk of Sgr A* to be an ellipse with major axis (scaled to 1 GHz) $\theta_{\rm maj,1} \approx 1''$, axial ratio $\rho = \theta_{\rm maj}/\theta_{\rm min} \approx 2$, and position angle PA $\approx 90^\circ$ (Lo et al. 1985, 1993; Bower et al. 2006). The current scattering law for the scattering

disk of Sgr A* is a major axis of $\theta_{\rm maj} = (1.309 \pm 0.015)$ mas $(\lambda/{\rm cm})^2$, a minor axis of $\theta_{\rm min} = 0.64^{+0.04}_{-0.05}$ mas $(\lambda/{\rm cm})^2$, and a position angle PA $= 78^{+0.8}_{-1.0}$ deg over the range of wavelengths from $2 - 20$ cm (Bower et al. 2004, 2006).

After the discovery of the radio-emitting magnetar J1745−2900, observations were conducted to measure both the angular and temporal broadening caused by scattering. Bower et al. (2014) conducted contemporaneous interferometric imaging of Sgr A* and J1745−2900 with the VLBA at 8.7 GHz. Over three observations, they found an average angular size of $16.11^{+0.37}_{-0.77} \times 8.77^{+1.09}_{-1.07}$ mas at $83.2^{\circ}{}^{+1}_{-1.5}$ for Sgr A* and $14.2^{+0.7}_{-0.7} \times 10.3^{+0.8}_{-0.9}$ mas at $81^{\circ}{}^{+7}_{-7}$ for J1745−2900. These two scattering disks are roughly consistent with each other and with the predicted size of Sgr A* at this wavelength (15.2×7.4 mas).

Spitler et al. (2014a) measured the pulse broadening of J1745−2900 from $\nu = 1.2 - 18.95$ GHz and found that it scaled as $\tau_{\rm sc} = \tau_1 \, \nu_{\rm GHz}^{\alpha}$ with $\tau_1 = 1.3 \pm 0.2$ s and $\alpha = -3.8 \pm 0.2$. This result is consistent with the expected scaling of $\tau_{\rm sc} \propto \nu^{-4}$, but is three orders of magnitude smaller than predicted by the hyperstrong scattering model of Lazio & Cordes (1998a).

Model Constraints

Given the angular and temporal broadening measurements of J1745−2900, the values of the scattering measure estimators can be calculated using Equations 3.9 and 3.10. The extrapolated 1 GHz scattering time from Spitler et al. (2014a) is $\tau_1 = 1.3$ s and the geometric mean of the major and minor axes of the scattering disk measured by Bower et al. (2014) scaled to 1 GHz as $\theta \propto \nu^{-2}$ is $\theta_1 = 908$ mas. Using these values gives ${\rm SM}_\tau = 61$ kpc m$^{-20/3}$ and ${\rm SM}_\theta = 70$ kpc m$^{-20/3}$.

Model 1 – The measurement of SM_θ and SM_τ entirely defines Model 1. Solving Equations 3.11 and 3.12 for D_s (assuming J1745−2900 is at the Galactic center distance of $D = 8.5$ kpc) gives a source-screen distance of $D_\mathrm{s} = 5.9$ kpc, which is consistent with the value obtained by Bower et al. (2014). The required scattering measure of the Model 1 screen at $D_\mathrm{s} = 5.9$ kpc is $\mathrm{SM}_{s,1} = 48$ kpc m$^{-20/3}$.

Model 2 – The exact location of the screen along the line of sight in Model 2 will depend on the contribution of the disk and Galactic center components to the estimators given in Equations 3.15 and 3.16. If the screen dominates scattering, then the distance and properties will be similar to Model 1. However, if the disk or Galactic center components contribute significantly, they will act to *increase* the distance D_s from the source to the screen.

Model 3 – The estimators must be calculated at similar frequencies for Model 3 because the spatial variability of the screen means that τ_sc and θ_sc may not scale consistently over all frequencies. Spitler et al. (2014a) report scattering times from a single pulses of $\tau_{8.4} = 0.3 \pm 0.4$ ms at 8.36 GHz. This gives an upper limit of $\mathrm{SM}_\tau \leq 137$ kpc m$^{-20/3}$ for J1745−2900. Combined with $\mathrm{SM}_\theta = 70$ kpc m$^{-20/3}$, this gives a minimum distance of $D_\mathrm{s} \geq 4.3$ kpc for a single screen. This is much larger than the $D_\mathrm{gc} \approx 150$ pc expected for the Galactic center scattering region, so J1745−2900 must be seen through a gap in the screen. If Sgr A* is viewed through the Galactic center scattering region, then the required scattering measure is $\mathrm{SM}_\mathrm{gc} = 7.5 \times 10^4 (D_{\mathrm{s},3}/150 \text{ pc})^{-2}$ kpc m$^{-20/3}$.

3.4.2 Pulsars within $10 - 15'$ from Sgr A*

Observational Data

In addition to J1745−2900, there are five canonical radio pulsars in the Galactic center region with angular separations of about $10' - 15'$ from Sgr A* (Deneva et al. 2009; Johnston et al. 2006). These pulsars have dispersion measures between DM $= 963 - 1456$ pc cm^{-3}, which are lower than that of J1745−2900 (DM $= 1778$ pc cm^{-3}), but still within the highest 1% of dispersion measures in the Galaxy (Manchester et al. 2005). Three of the five pulsars have estimated pulse broadening times at 2 GHz of $\tau_2 \approx 50 - 140$ ms, which are comparable to J1745−2900 ($\tau_2 \approx 80$ ms). The other two pulsars (J1745−2910 and J1746−2850) have pulse broadening times that were too small to measure in the discovery observations (Deneva et al. 2009), but upper limits of about $\tau_2 \lesssim 50$ ms can be reasonably set based on the pulse widths. The upper limits are at least $1 - 3$ times smaller than the measured pulse broadening times (see Table 3.1 for properties of each pulsar). No angular broadening measurements exist for any of these pulsars.

Although the five pulsars and J1745−2900 have roughly similar properties ($\tau_1 \sim 1$ s, DM ~ 1000 pc cm^{-3}), there are moderate differences among them. The most interesting case is that of pulsars J1746−2850 and J1746−2849, which are separated by only about $1'.2$ on the sky. J1746−2850 has a dispersion measure that is ΔDM ≈ 500 pc cm^{-3} greater than J1746−2849 and a pulse broadening time that is at least three times larger. Since the transverse separation between the two pulsars is small, it is most likely that the differences arise as a result of different path lengths along the line of sight *in the Galactic center*. This is entirely possible as these two pulsars are located in the Arches region of the Galactic center near

the Quintuplet cluster and Pistol HII region, where bright thermal emission is seen in radio (e.g., Lang et al. 2005, 2001) and Paschen-α (Wang et al. 2010).

Model Constraints

Model 1 – The homogeneous single screen of Model 1 predicts that all the pulsars in the Galactic center region will have the same scattering properties as J1745−2900. While similar in magnitude, the scattering times of these pulsars differ from that of J1745−2900 by as much as a factor of three.

Model 2 – The discrepancies among the pulsars can be explained in Model 2 as a contribution from the Galactic center component to the free electron distribution. The difference in dispersion measure between J1746−2850 and J1746−2849 is explained naturally as arising from the Galactic center. Although separated by only $\Delta\theta = 1\farcm2$ on the sky, both pulsars are $\approx 12'$ (30 pc at 8.5 kpc) from Sgr A*, so it is reasonable to assume that they may be separated by a similar amount along the line of sight. If so, the difference in dispersion measure can be accounted for by an average Galactic center electron density of

$$\langle n_{\rm e,gc} \rangle = \Delta{\rm DM}/\Delta s \approx 500 \text{ pc cm}^{-3}/30 \text{ pc} = 17 \text{ cm}^{-3}, \tag{3.19}$$

which is consistent with the $n_{\rm e,gc} \approx 10$ cm^{-3} estimated in Lazio & Cordes (1998a) and used in the NE2001 model (Cordes & Lazio 2002).

The pulsar dispersion measures can also be used to set limits on the DM contribution of the screen in Model 2. The smallest dispersion measure of any of the Galactic center pulsars is DM = 963 pc cm^{-3}, which acts as an upper limit on the DM contribution from the screen and the Galactic disk. The disk component can be estimated from electron density models of the Galaxy, which predict

DM $\approx 600 - 700$ pc cm^{-3} along the line of sight toward, but not including, the Galactic center (Taylor & Cordes 1993; Cordes & Lazio 2002). Using the NE2001 value of DM = 670 pc cm^{-3} gives an upper limit of $\mathrm{DM_{s,2}} \approx 300$ pc cm^{-3} for the dispersion measure of the screen.

If the screen covers 1° and is located 2.6 kpc from Earth (5.9 kpc from Sgr A*), then it has a transverse size of about 45 pc. To avoid a peculiar geometry, the depth of this screen should be similiar, so $\Delta s \approx 45$ pc. The mean electron density for the screen is then $\langle n_{\mathrm{e,s2}} \rangle = \mathrm{DM_{s,2}}/\Delta s \approx 7$ cm^{-3}.

Using the scattering measure, dispersion measure, and depth of the screen, the fluctuation parameter can be estimated using Equation 3.14 to be

$$F_2 \approx 13 \left(\frac{\mathrm{SM}_{s,2}}{48 \text{ kpc m}^{-20/3}} \right) \left(\frac{\mathrm{DM}_{s,2}}{300 \text{ pc cm}^{-3}} \right)^{-2} \left(\frac{\Delta s}{45 \text{ pc}} \right). \tag{3.20}$$

The outer scale of turbulence, ℓ_0, can be written in terms of the fluctuation parameter as

$$\ell_0 = 0.02 \text{ pc } \left(\frac{F_2}{13} \right)^{-3/2} \epsilon^3 \left(\zeta \eta^{-1} \right)^{-3/2}, \tag{3.21}$$

which, for a single cloud ($\zeta = 1$, $\eta = 1$), is a strict upper limit since $\epsilon \leq 1$.

Model 3 – The variations in scattering times and dispersion measures among the pulsars (J1745−2900 included) can be explained in Model 3 as arising from the variations in the Galactic center scattering screen.

Name	ℓ (deg)	b (deg)	$\Delta\theta_{\mathrm{Sgr\ A*}}$ (arcmin)	DM (pc cm^{-3})	$\tau_{\mathrm{sc,1}}$ (s)	τ_{sc} (ms)	Freq of τ_{sc} (GHz)	Ref
(1)	(2)	(3)	(4)	(5)	(6)	(7)	(8)	(9)
J1745−2900	359.944	−0.047	0.04	1778	1.3			a,e
J1746−2849	0.148	−0.023	12.0	1456	1.3	266	1.5	b
					2.0	140	1.95	b
J1746−2856	0.132	−0.228	15.6	1168	0.65	170	1.4	c
					1.4	15	3.1	c
J1745−2912	359.799	−0.177	12.0	1130	2.3	25	3.1	c
J1745−2910	359.763	−0.054	10.8	1088	< 0.78	< 54	1.95	b
J1746−2850	0.134	−0.044	11.4	963	< 0.50	< 100	1.5	b
					< 0.65	< 45	1.95	b
J1747−2809	0.869	0.076	52.1	1133	0.19	13	1.95	d

Table 3.1: **Scattering Parameters of Pulsars within 1° of Sgr A***. The columns give (1) the name of the pulsar, (2) Galactic longitude, (3) Galactic latitude, (4) angular separation from Sgr A* in arcmin, (5) dispersion measure, (6) extrapolated 1 GHz scattering time $\tau_{\mathrm{sc,1}}$ according to $\tau_{\mathrm{sc,1}} = \tau_{\mathrm{sc}}\nu^4_{\mathrm{sc,GHz}}$ where (7) τ_{sc} is the measured pulse broadening time at (8) the given frequency. Columns (1)-(4) use data from the ATNF Pulsar Catalog (Manchester et al. 2005). The references given in (9) are (a) Spitler et al. 2014a, (b) Deneva et al. 2009, (c) Johnston et al. 2006, (d) Camilo et al. 2009, (e) Eatough et al. 2013.

3.4.3 OH Masers

Observational Data

The two main types of OH masers in the Galactic center region are the 1612 MHz line emission that is radiatively pumped in the atmospheres of OH/IR stars and the 1720 MHz line associated with supernova remnants (SNRs). The OH/IR stars have intrinsically small ($\lesssim 20$ mas) radio emission regions and are located in the Galactic center, making them excellent probes of the scattering environment (van Langevelde et al. 1992). Lindqvist et al. (1992) studied 134 OH/IR stars within 100 pc of Sgr A* and found that they are distributed with standard deviations of $\sigma_\ell \approx 50$ pc and $\sigma_b \approx 35$ pc along the Galactic longitude and latitude, respectively. Of these, only eight OH/IR stars within $30'$ of Sgr A* have measured angular diameters. Seven of these have scattering diameters exceeding $1''$ at 1612 MHz (the eighth is only 103 mas) and at least six show anisotropic scattering (van Langevelde & Diamond 1991; van Langevelde et al. 1992; Frail et al. 1994). Taking the scattering size to be the geometric mean of the major and minor axes and scaling to 1 GHz according to $\theta_{\rm sc} \propto \nu^{-2}$, gives angular sizes of $\theta_{\rm sc,1} \approx 1\farcs6 - 3\farcs1$, which are $1.9 - 3.8$ times as large as the geometric mean of the scattering ellipse of Sgr A* at 1 GHz, $\theta_{\rm Sgr\ A*} = 0\farcs8$. The locations and scattering disks of the OH/IR stars with measured angular diameters are shown in Figure 3.4.

In addition to the OH/IR stars, there are 1720 MHz OH masers in the Sgr A complex within $2'$ of Sgr A*. Seven of these masers have measured scattering sizes between $0\farcs6 - 1\farcs4$ at 1720 MHz and one is unresolved by the VLA synthesized beam of $2\farcs48 \times 1\farcs28$ (Yusef-Zadeh et al. 1999). Since these masers are associated with shock fronts near SNRs, it is not clear that they are necessarily

intrinsically compact regions. As a result, the observed sizes should be considered upper bounds to the scattering sizes, even though it is unlikely that the sources make up a considerable fraction of the observed size. Table 3.2 lists the angular broadening measurements for the OH/IR stars, 1720 MHz OH masers, Sgr A*, and J1745−2900.

Model Constraints

The excess scattering of the OH/IR stars relative to Sgr A* is difficult to explain with only a single scattering screen. From Equations 3.8 and 3.10, the ratio of the angular broadening size of an OH/IR star and Sgr A* is

$$\left(\frac{\theta_{\rm sc,OH}}{\theta_{\rm sc,Sgr}}\right)^{5/3} = \left(\frac{D_{\rm s,OH}}{D_{\rm s,Sgr}}\right)^{2} \left(\frac{D_{\rm OH}}{D_{\rm Sgr}}\right)^{-2} \left(\frac{\rm SM_{OH}}{\rm SM_{Sgr}}\right). \tag{3.22}$$

Model 1 – In the case of a single homogeneous screen, like Model 1, Equation 3.22 reduces to

$$\left(\frac{\theta_{\rm sc,OH}}{\theta_{\rm sc,Sgr}}\right) = \left(\frac{1 - D_{\rm o,s}/D_{\rm OH}}{1 - D_{\rm o,s}/D_{\rm Sgr}}\right)^{6/5}. \tag{3.23}$$

where $D_{\rm o,s}$ is the distance from the observer to the screen. The only way to increase the size of the OH/IR scattering disk relative to that of Sgr A* is to increase the distance to the OH/IR star, $D_{\rm OH}$. However, the ratio reaches a maximum of $\theta_{\rm sc,OH}/\theta_{\rm sc,Sgr} = (1 - D_{\rm o,s}/D_{\rm Sgr})^{-6/5} \approx 1.5$ for $D_{\rm s} \approx 5.9$ kpc. Thus, even if the OH/IR stars were not localized to the Galactic center and $D_{\rm OH}$ was a completely free parameter, a homogeneous single screen still could not account for the observed scattering sizes.

The differences in observed scattering size are inconsistent with the homogeneous single screen of Model 1, but they could be explained if the uniformity

requirement is relaxed and the scattering measure is allowed to vary across the screen. In this case, the the excess scattering would be attributed to scattering measures along the line of sight to the OH/IR stars that are about $3 - 6$ times as large as toward Sgr A*. This would result in correspondingly larger emission measures towards the larger OH masers (c.f., Equation 3.13).

Model 2 – The excess angular broadening of the OH/IR stars relative to Sgr A* could be the result of scattering in the Galactic center component. However, since the OH/IR scattering sizes are $1.9 - 3.8$ times as large as that of J1745−2900 and Sgr A*, this would mean that the Galactic center component alone could scatter images to the same extent as the thin screen.

Model 3 – The different observed sizes of the OH/IR scattering disks arise naturally in Model 3 from the differing distances of these stars along the line of sight from the scattering screen. Placing the OH/IR stars at distances $1.7 - 3.0$ times as far from the Galactic center screen as Sgr A* produces angular sizes $1.9 - 3.8$ times as large as Sgr A*. For a screen located $D_{\rm s,3} = 150$ pc, this results in the OH/IR stars being $100 - 300$ pc behind Sgr A*. Since the orbital scale of these stars is only about 50 pc, the screen will either need to be moved closer to Sgr A* or the scattering strength needs to be increased toward the OH/IR stars.

Name	ℓ (deg)	b (deg)	$\Delta\theta_{\rm Sgr\ A*}$ (arcmin)	$\theta_{\rm sc,1}$ (arcsec)	$\theta_{\rm sc}$ (mas)	Freq of $\theta_{\rm sc}$ (GHz)	ρ	Ref
(1)	(2)	(3)	(4)	(5)	(6)	(7)	(8)	(9)
Sgr A*	359.944	−0.046	–	900	11.9	8.7	2.0	a
J1745−2900	359.944	−0.047	0.04	915	12.1	8.7	1.4	a
A	359.940	−0.067	1.3	1887	637	1.720	1.3	b
B1	359.956	−0.042	0.7	1599	540	1.720	2.5	b
B2	359.956	−0.042	0.7	1557	526	1.720	1.4	b
B4	359.956	−0.041	0.8	1720	581	1.720	2.6	b
D	359.935	−0.066	1.3	2540	858	1.720	1.3	b
E	359.936	−0.066	1.3	2395	809	1.720	1.4	b
G1	359.928	−0.062	1.4	3883	1312	1.720	1.2	b
OH 359.986-0.061 (8)	359.986	−0.061	2.7	2459	946	1.612	2.9	c
OH 359.880-0.087 (7)	359.880	−0.087	4.6	2759	1062	1.612	1.3	c
OH 359.762+0.120 (4)	359.762	0.120	14.8	1707	657	1.612	3.3	c
OH 0.190+0.036 (3)	0.190	0.036	15.5	267	103	1.612	1.0	d
OH 0.319-0.040 (2)	0.319	−0.040	22.5	3118	1200	1.612	1.0	c
OH 359.581-0.240 (6)	359.581	−0.240	24.7	1676	644	1.612	4.1	c
OH 0.334-0.181 (1)	0.334	−0.181	24.7	3160	1216	1.612	2.0	c
OH 359.517+0.001 (5)	359.517	0.001	25.8	2130	819	1.612	2.1	c
OH 0.892+1.342	0.892	1.342	100.8	146	56	1.612	1.0	e

Table 3.2: **Angular Broadening Measurements of Sources Seen Through the Galactic Center**. The columns give (1) the name of the source, (2) Galactic longitude, (3) Galactic latitude, (4) angular separation from Sgr A* in arcmin, (5) extrapolated 1 GHz scattering disk diameter $\theta_{\rm sc,1}$ according to $\theta_{\rm sc,1} = \theta_{\rm sc}\nu^2_{\rm sc,GHz}$ where (6) $\theta_{\rm sc}$ is the geometric mean of the observed scattering ellipse $\theta_{\rm sc} = (\theta_{\rm maj}\theta_{\rm min})^{1/2}$ at (7) the given frequency with (8) axial ratio $\rho = \theta_{\rm maj}/\theta_{\rm min}$. The references are given in (9) are (a) Bower et al. 2014, (b) Yusef-Zadeh et al. 1999, (c) Frail et al. 1994, (d) van Langevelde & Diamond 1991, (e) van Langevelde et al. 1992.

3.4.4 Extragalactic Radio Sources

Observational Data

Observing an extragalactic source through the Galactic center provides a very useful constraint on the scattering medium because the scattering size of an extragalactic source is a factor $D_{\rm GC}/D_{\rm s}$ larger than a source near Sgr A* (for a thin-screen, at least). To date, the only clearly identified extragalactic source in the inner $30'$ of the Galaxy is the FRII galaxy, G359+0.18. This source is $15'$ from Sgr A* and is only scattered to $\approx 20''$ at 330 MHz, which is much less than the $\gtrsim 400''$ expected from the hyperstrong scattering region (Lazio et al. 1999). Additionally, Roy (2013) reports on the detection of four candidate extragalactic sources (including G359+0.18) within $\Delta\theta = 0.^{\circ}7$ of Sgr A* at 255 MHz. These sources have reported 300 MHz scattering sizes between $\theta_{300} = 10 - 26''$. With the exception of G359+0.18, these candidate extragalactic sources all lie at latitudes ($|b| \gtrsim 0.^{\circ}3$) outside the enhanced scattering region occupied by the OH/IR stars.

Though there are no other known extragalactic sources seen through the Galactic center, there are radio sources that have unknown Galactic residency. Considering these sources, Lazio & Cordes (1998a) report a reduced number of source counts in pointings close to the Galactic center at 1.28 and 1.66 GHz. This would be expected if the scattering is large enough that the sources would be resolved out. However, Roy (2013) finds that the source counts at 154 MHz and 255 MHz are consistent with predictions within $\Delta\theta = 0.^{\circ}7$ of Sgr A*.

Model Constraints

Model 1 – For a thin-screen located a distance $D_{\rm s}$ from the Galactic center, the observed size of an extragalactic source seen through this screen is $\theta_{\rm xgal} = (D_{\rm GC}/D_{\rm s})\,\theta_{\rm GC}$, where $\theta_{\rm GC}$ is the size of a source at the Galactic center. From Section 3.4.1, the screen is located at a distance $D_{\rm s,1} = 5.9$ kpc from Sgr A*. Using the 1 GHz scattering size of $\theta_1 = 0\farcs8$ for Sgr A*, this model predicts a size of $\theta_{1,\rm x} = 1\farcs2$ for an extragalactic source at 1 GHz. Scaling to 330 MHz as $\theta_{\rm sc} \propto \nu^{-2}$, this results in a 330 MHz scattering size of $\theta_{0.33,x} = 11''$, which is comparable to the $\theta_{0.33,x} \approx 20''$ observed for G359+0.18. Likewise, the $\theta_{0.3,x} \approx 13''$ predicted at 300 MHz is comparable to the three other candidate extragalactic sources.

Model 2 – The predicted extragalactic source sizes in Model 2 will be similar to Model 1 if the screen dominates the scattering. If the Galactic center component contributes significantly, then the scattering size will increase toward the $\theta_{0.33,\rm x} \gtrsim 400''$ predicted by a screen within 150 pc of Sgr A*.

Model 3 – The scattering size of G359+0.18 can be accounted for in Model 3 if the scattering strength is weaker along that particular line of sight. Since this model is of a heterogeneous screen, the scattering size of Sgr A* cannot be used to predict the size of an extragalactic source seen along another line of sight, as is possible in the other models.

3.4.5 Free-free Absorption and Emission

Observational Data

The free-free optical depth of a plasma with electron temperature $T_{\rm e}$ is related to the emission measure by Equation 3.5, so the free-free emission and absorption can be used to constrain the emission measure. For an optically thin plasma, the emission measure can be expressed in terms of the thermal component of the brightness temperature ($T_{\rm b,th} \approx T_{\rm e}\tau_\nu$) as

$$\mathrm{EM_{ff,e}} = 3.9 \times 10^4 \text{ pc cm}^{-6} \left(\frac{T_{\rm b,th}}{1 \text{ K}}\right) \left(\frac{T_e}{10^4 \text{ K}}\right)^{0.35} \left(\frac{\nu}{10 \text{ GHz}}\right)^{2.1}. \tag{3.24}$$

By measuring the thermal component of the brightness temperature, an upper limit can be set on the emission measure of the scattering material along the line of sight from the observer to the source. Only an upper limit may be set because some of the observed flux may arise from behind the source where it could not contribute to the scattering.

Following Lazio & Cordes (1998a), we estimate the thermal brightness temperature to be 60% of the reported values in the Handa et al. (1987) 10 GHz brightness temperature maps (see Figure 3.3). A more recent analysis of the Galactic center region by Law et al. (2008) suggests that the thermal contribution to the observed emission is closer to ≈30% at 10 GHz, but we will use 60% as a conservative upper limit. With this correction, typical values are are $T_{\rm b,th} \sim 0.1 - 1$ K toward OH/IR stars $\sim 20'$ from Sgr A*. The temperatures toward OH/IR stars and pulsars closer than $\sim 20'$ from Sgr A* are complicated by nonthermal emission from the radio arc and Sgr A* itself, so no reliable estimates can be made.

In addition to the free-free emission, the free-free absorption can also be used

to constrain the allowed values for the emission measure along the line of sight. Low-frequency GMRT measurements of the extended sources Sgr A East and the $7'$ halo indicate 154 MHz optical depths of $\tau_{154} = 2.3 \pm 0.3$ and $\tau_{154} = 1.8 \pm 0.5$, respectively (Roy & Rao 2009; Roy 2013). The emission measure required to produce the observed optical depths is

$$\mathrm{EM_{ff,a}} = 1.2 \times 10^5 \text{ pc cm}^{-6} \left(\frac{\tau_{154}}{2.0}\right) \left(\frac{T_e}{10^4 \text{ K}}\right)^{1.35}. \tag{3.25}$$

This value is likely to be only an upper limit because some of the absorption of emission from Sgr A East and the $7'$ halo could occur in Sgr A West. Although this limit is an order of magnitude larger that imposed by Equation 3.24 for $T_{\mathrm{b,th}} \sim 1$ K, it provides a stronger constraint for the OH/IR stars and pulsars closer to Sgr A* for which the inferred thermal component of the brightness temperature is $T_{\mathrm{b,th}} \gtrsim 10$ K.

Model Constraints

Model 1 – The scattering measure needed to reproduce the scattering measurements of J1745−2900 in Model 1 gives an emission measure (from Equation 3.13) of

$$\mathrm{EM_{s,1}} = 5.2 \times 10^4 \text{ pc cm}^{-6} \left(\frac{\ell_0}{1 \text{ pc}}\right)^{2/3} \left(\frac{1+\epsilon^{-2}}{2}\right) \left(\frac{\mathrm{SM_{s,1}}}{48 \text{ kpc m}^{-20/3}}\right), \tag{3.26}$$

which is slightly larger than the limit imposed by thermal temperature maps. However, these can easily be brought into agreement by reducing the outer scale of turbulence, ℓ_0.

Model 2 – Model 2 falls somewhere between the limits imposed by Models 1 and 3 based on the relative contributions of the screen and Galactic center

components. For the case where the screen dominates the scattering, the limit of $\ell_0 \lesssim 0.02$ pc set from the pulsar measurements gives

$$\mathrm{EM}_{\mathrm{s},2} = 3800 \text{ pc cm}^{-6} \left(\frac{\ell_0}{0.02 \text{ pc}}\right)^{2/3} \left(\frac{1+\epsilon^{-2}}{2}\right) \left(\frac{\mathrm{SM}_{\mathrm{s},1}}{48 \text{ kpc m}^{-20/3}}\right), \quad (3.27)$$

which agrees nicely with the brightness temperature limits.

Model 3 – The emission measure for a screen at $D_{\mathrm{s},3} = 150$ pc is

$$\mathrm{EM}_{\mathrm{s},3} = 8.1 \times 10^7 \text{ pc cm}^{-6} \left(\frac{\ell_0}{1 \text{ pc}}\right)^{2/3} \left(\frac{1+\epsilon^{-2}}{2}\right) \left(\frac{\mathrm{SM}_{\mathrm{s},3}}{7.5 \times 10^7 \text{ kpc m}^{-20/3}}\right), \quad (3.28)$$

which requires $\ell_0 \lesssim 10^{-5}$ pc to meet the emission measure contraints.

3.4.6 Low-Frequency Radio Recombination Lines

Observational Data

Radio recombination lines (RRLs) are tracers of ionized gas, where different frequencies are sensitive to different pressure, temperature, or density regimes. Low-frequency RRLs ($\nu \lesssim 500$ MHz) in particular are effective probes of low-density ($0.5 < n_{\mathrm{e}} < 50$ cm^{-3}) ionized gas with large ($\gtrsim 10'$) angular extent (Roshi & Anantharamaiah 2001). Anantharamaiah & Bhattacharya (1986) used the Ooty radio telescope (ORT) to observe the Galactic center region at 325 MHz with beam sizes of $2^\circ \times 1^\circ$ and $2^\circ \times 6'$. By comparing the RRLs measured at 325 MHz with similar data at 1400 MHz, they estimate that the ionized gas along the line of sight has $n_{\mathrm{e}} \sim 7$ cm^{-3}, pathlength $\Delta s \approx 10 - 60$ pc, EM $\approx 500 - 2900$ pc cm^{-6}, and $T_{\mathrm{e}} \approx 2000 - 6000$ K.

Roshi & Anantharamaiah (2001) perform similar observations with the ORT for the inner Galaxy ($330^\circ < \ell < 80^\circ$) at 327 MHz with a beam size of $2^\circ \times 6'$. At

$\ell = 0°$, they find that the best fit parameters for a cloud along the line of sight are density of $n_e = 11.3$ cm^{-3} and path length of $\Delta s = 25$ pc, which gives an emission measure of EM $\approx n_e^2 \Delta s \approx 3200$ pc cm^{-6}. The authors conclude that low-frequency RRLs in the inner Galaxy most likely come from low-density envelopes (typical size $\sim 20 - 200$ pc) around HII regions (typical size $\sim 1 - 10$ pc).

Model Constraints

The emission measure and density inferred from the RRL measurements are in very good agreement with the $\mathrm{EM}_{s,2} \approx 3800$ pc cm^{-6} and $\langle n_{e,s2} \rangle \approx 7$ cm^{-3} estimated for the screen component of Model 2 in Sections 3.4.2 and 3.4.5. It is important to note, though, that the large beam sizes of these RRL surveys mean that signal from smaller angular structures could remain undetected due to beam dilution. Additionally, it could be that the RRL signal observed may originate outside of the enhanced scattering region considered in this paper.

3.4.7 Hα Measurements

Observational Data

The Hα recombination line is a tracer of ionized gas that can be used to estimate the emission measure. From Equation 3.6, the emission measure can be expressed in terms of the observed Hα intensity as

$$\mathrm{EM} = 2.75 \text{ pc cm}^{-6} \left(\frac{T_e}{10^4 \text{ K}} \right)^{0.9} \left(\frac{I_{H\alpha}}{1 \text{ R}} \right) e^{2.2E(B-V)}. \tag{3.29}$$

Since the Hα emission is heavily obscured by dust along the line of sight to the Galactic center, an extinction law is needed to appropriately deal with the redden-

ing term, $E(B-V)$.

Marshall et al. (2006) provide a 3-D extinction map of the inner Galaxy ($|\ell| < 100°$, $|b| < 10°$) generated by comparing 2MASS color excess to a population synthesis model of the Galaxy. The map provides K_s band extinction magnitudes, A_{K_s}, as a function of distance for 64,000 lines of sight spaced in steps of $15'$ in ℓ and b. The A_{K_s} can be converted to A_K as $A_K = 0.95 A_{K_s}$ (as in Marshall et al. 2006), which can then be converted to visual extinction, A_V, using the conversion factors from Mathis (1990). Finally, the reddening is related to the visual extinction by $E(B-V) = A_V/R_V$, where $R_V = 3.1$. Thus, the conversion from K_s band extinction to reddening is $E(B-V) = 2.848 A_{K_s}$.

Combining the three-dimensional extinction map with measurements of the Hα intensity provides a crude estimate for the emission measure as a function of distance from the observer. Using data from the Southern H-Alpha Sky Survey Atlas (SHASSA, Gaustad et al. 2001), which has a resolution of $0'.8$ and a sensitivity of 0.5 R, the Hα intensity toward Sgr A* is $I_{\mathrm{H}\alpha} \approx 40$ R. The $10'$ region around Sgr A* has smoothly varying values in the range $I_{\mathrm{H}\alpha} \approx 30 - 50$ R.

In Figure 3.2, the emission measure is shown as a function of distance from the observer using Equation 3.6 with $I_{\mathrm{H}\alpha}$ from SHASSA and $E(B-V)$ calculated from the three-dimensional extinction map of Marshall et al. (2006). Values are shown for five lines of sight toward the Galactic center. In each case, a clump or screen with EM $\sim 10^4$ pc cm^{-6} would need to be about $1.5 - 2$ kpc from the observer to fully account for the observed Hα intensity.

Model Constraints

The results presented in Figure 3.2 set the minimum distance from the Sun along the line of sight for a screen with a given emission measure to be consistent with the observed Hα intensity. For Models 1 and 2, these measurements set a minimum distance of about $1.5 - 2$ kpc from the observer (that is, $D_{\rm s} \leq 6.5 - 7$ kpc). For Model 3 and the Galactic center component of Model 2, the Hα measurements set no practical limit on the allowed emission measures because the extinction beyond about 3 kpc from the observer becomes so great as to allow EM $\gtrsim 10^6$ pc cm^{-6}.

3.4.8 Infrared Counterparts to HII Regions

Observational Data

Many HII regions can be identified by a common infrared morphology in which $\sim$10μm emission surrounds $\sim$20μm emission. Sources with this morphology and coincident radio continuum emission are very likely to be HII regions (Anderson et al. 2011, 2013). Using the 8μm data from GLIMPSE (Benjamin et al. 2003a) and the 24μm data from MIPSGAL (Carey et al. 2009), the line of sight can be searched for potential HII regions. Any coincident Hα emission toward candidate HII regions would signify that it is relatively close (≤ 2 kpc) from the observer.

Figure 3.4 shows a $2^\circ \times 1\overset{\circ}{.}5$ (300 $\times$ 220 pc) region of the Galactic center in GLIMPSE 8μm (green) and MIPSGAL 24μm (red). SHASSA Hα intensity is illustrated with blue contours. Figure 3.5 gives a labeled schematic version of Figure 3.4. There are many examples here of the HII infrared morphology of 24μm emission (red) surrounded by 8μm (green). The regions with clear Hα emission

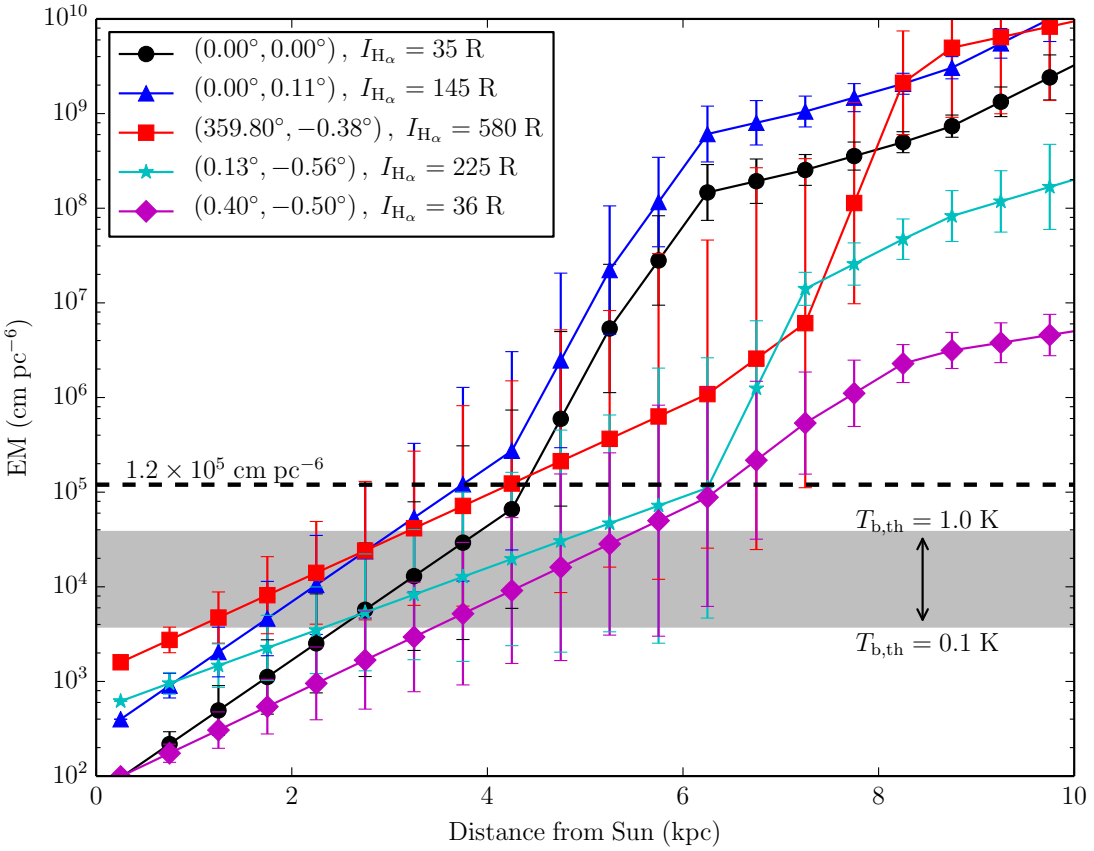

Figure 3.2: Hα **constraints on emission measure of ionized gas along LOS to GC**. Curves give the distance at which a cloud with emission measure EM produces the observed Hα intensity along a given LOS toward Sgr A* and four inner Galaxy HII regions. The emission measure is calculated from Equation 3.6 using *SHASSA* Hα intensities and the three-dimensional extinction model of Schultheis et al. (2014). Points to the left of each curve (for fixed EM) would result in higher Hα intensities than observed, so they can be ruled out. Points to the right of each curve result it lower Hα intensities than observed, but cannot be ruled out as there may be foreground contributions to the Hα intensity along the LOS to a cloud. The horizontal dashed line gives the approximate upper limit for the emission measure toward Sgr A* set by optical depth measurements (see Section 3.4.5). The grey band gives the EM values that correspond to 10 GHz thermal brightness temperatures between $0.1 - 1.0$ K, which are typical of the region (see Figure 3.3).

that surround the Galactic center are known HII regions cataloged by Sharpless (1959) with designations Sh2-16 through Sh2-20. They are almost certainly nearby (ie, $d \leq 2$ kpc from Earth) because they are seen in Hα, but there appear to be no solid distance measurements in the literature.

The bright (in parts, saturated) region centered around $(\ell, b) = (0.^\circ1, -0.^\circ05)$ is comprised of the thermal "Arches", the "Sickle", and the "Galactic center bubble." The Arches and the Sickle are thermal HII regions ionized by the Quintuplet and Arches clusters, and are located in the Galactic center (Lang et al. 2001, 2010). The Galactic center bubble is dust emission likely associated with this ionized gas (Rodríguez-Fernández et al. 2001; Simpson et al. 2007). Since this region is so bright, it is possible that an HII region along the line of sight could could be missed in the infrared. If it were far enough away from the observer, it could also be missed in Hα intensity. While there are no obvious counterparts to the proposed HII region along the line of sight to Sgr A*, it may be that one remains undetected.

Model Constraints

For Models 1 and 2, there appears to be no obvious infrared counterpart to a scattering screen in these images. It is possible, though, that the signature from a region of ionized gas along the line of sight toward Sgr A* is simply missed due to the very bright background.

Since Models 1 and 2 both have a homogeneous single screen component, they would be unable to account for the properties of a source viewed through a small unmodelled HII clump along the line of sight. Examining Figure 3.4, there appear to be only a few such cases. The OH/IR star, OH0.334-0.181, is very near to Sh2-

20, which shows up clearly in both Hα and infrared. The pulsar J1745−2912 and the OH/IR star OH359.581+0.240 both appear along the edge of Sh2-16 where Hα levels are above background levels. Aside from these three, there are no other lines of sight to OH/IR stars or pulsars that pass through an obvious foreground HII region.

The complex structure and great number of small HII regions seen at low $|b|$ around Sgr A* in Figure 3.4 support the idea of a heterogeneous scattering environment in the immediate vicinity of the Galactic center.

3.4.9 Highly Scattered Lines of Sight Outside the Galactic Center

The line of sight to the Galactic center is one of the most heavily scattered of any in the Galaxy, but there are three other sources that experience a similar amount of scattering. The radio sources Cygnus X-3 (a microquasar), NGC 6334B (an AGN seen through a star-forming region), and B1849+005 (an AGN) all have angular broadening sizes that are comparable or greater than Sgr A*. The known properties of the scattering material toward these sources is briefly described here for comparison to the Galactic center.

Observational Data

Cygnus X-3 is a variable radio source with a scatter-broadenened angular size of $\theta_1 \approx 0\farcs5$ at 1 GHz with an axial ratio of about 1.4 (Wilkinson et al. 1994; Molnar et al. 1995). The radio source is at least 10 kpc away from the Sun along a line of

sight that passes through the Orion and Perseus arms. It is seen through a large ($\approx 2^\circ$ degree radius) collection of HII regions within the Cygnus X radio emission region and passes next to the Cyg OB2 association ($D \approx 1.8$ kpc from the Sun). Molnar et al. (1995) studied this region and identified the HII region DR11 as the the likely cause of the scattering. They also estimate the emission measure toward Cygnus X-3 to be EM ≈ 6000 cm^{-3}. Additionally, Wilkinson et al. (1994) estimate that the outer scale of turbulence is $\ell_0 \sim 0.01$ pc based on the changes in image anisotropy with frequency.

NGC 6334B is an extragalactic radio source with a 1 GHz scattering size of $\theta_1 \approx 7''$, the largest known (Moran et al. 1990). NGC 6334B is seen through NGC 6334A, one of the six regions of star formation that make up the NGC 6334 complex that spans about 10 pc at 1.7 kpc. Trotter et al. (1998) estimate that the outer scale of turbulence to be $\ell_0 \lesssim 3 \times 10^{-3}$ pc based on changing anisotropy of the scattering disk. They also quote an upper limit to the emission measure as EM $\lesssim 1.5 \times 10^5$ pc cm^{-6} from Schraml & Mezger (1969).

B1849+005 is an extragalactic source with a 1 GHz scattering size of $\theta_1 \approx 0\farcs6$. It is located about $13'$ from the radio pulsar B1849+00, which has a 1 GHz scattering time of $\tau_1 \sim 0.5$ s (Bhat et al. 2004). Lazio (2004) studied the enhanced scattering toward B1849+005 and ultimately found that there was no one source along the line of sight that could account for the observed scattering.

Model Constraints

While none of these highly scattered lines of sight can constrain the properties of our three models, they do provide a useful comparison to see what parameter values actually occur in the Galaxy. In particular, the scattering of Cygnus X-

3 may be the most useful analog for the Galactic center since the radio source is at a distance similar to Sgr A*, is viewed through a few Galactic arms, and is thought to be scattered by an HII region about 2 kpc from the Sun. In fact, the derived properties of the free electrons along this line of sight (ℓ_0, EM) are very similar to those estimated for the screen in Model 2. The main discrepancy between Cygnus X-3 and the Galactic center is that the scattering material is clearly identified and associated with a well known complex (the Cygnus X region) that is seen in radio and infrared.

NGC 6334B and B1849+005 are less applicable for comparison with the Galactic center because they are extragalactic sources. However, B1849+005 provides the useful example of a highly scattered source with no obvious multiwavelength counterparts. Although, at $(\ell, b) = (33.^{\circ}4, 0.^{\circ}2)$, B1849+005 is also viewed through almost the entire Galactic disk.

3.5 Review of Models

The observational constraints presented in Section 3.4 do not determine all of the free parameters in the three electron density models considered, but they do restrict the range of possible values. Here we consider each model in light of all the available observational data.

3.5.1 Model 1

The homogeneous single screen of Model 1 can reproduce the scattering measurements of Sgr A* and J1745−2900 if the screen has $\mathrm{SM}_{\mathrm{s},1} \approx 48$ kpc $\mathrm{m}^{-20/3}$ and

is located $D_{\rm s,1} = 5.9$ kpc from Sgr A*. Such a screen is also consistent with the observed scattering size of the extragalactic source G359+0.18, the constraints imposed by the Hα measurements, and can be made consistent with the free-free emission measurements with only minor adjustments.

However, this model fails to explain the scattering measurements of the nearby pulsars and OH/IR stars. The pulsars J1746−2850 and J1746−2849, which have significantly different dispersion measures and pulse broadening times despite being separated by only 1.′2 on the sky, are particularly difficult to explain with Model 1. As a result, Model 1 is insufficient to fully explain the observational data toward the Galactic center and will no longer be considered.

3.5.2 Model 2

Model 2 extends the simple thin screen of Model 1 to also include contributions to the free electron distribution from Galactic disk and the Galactic center. From Galactic free electron density models, the disk contribution to the dispersion measure along the line of sight to Sgr A* is taken to be $\mathrm{DM_d} \approx 670$ pc cm^{-3}. Using the pulsar with the lowest dispersion measure in the Galactic center region (J1745−2850, DM = 963 pc cm^{-3}) as an upper limit to the combined contributions from the disk and screen, an upper limit of $\mathrm{DM_{s,2}} \lesssim 300$ pc cm^{-3} can be set. If the screen depth is to be comparable to its width, then $\Delta s \approx 45$ pc and $\langle n_{\rm e,s} \rangle \approx 7$ cm^{-3}.

If the screen dominates scattering, then it needs to have $\mathrm{SM_{s,2}} = 48$ kpc m$^{-20/3}$ and be $D_{\rm s,2} = 5.9$ kpc from Sgr A* to account for the scattering properties of J1745−2900 and Sgr A*. To achieve this scattering measure from a screen with

$\mathrm{DM_{s,2}} \approx 300$ pc cm^{-3} requires a fluctuation parameter of $F_2 \approx 13$ and an upper limit to the outer scale of turbulence of $\ell_0 \lesssim 0.02$ pc (see Equations 3.20 and 3.21). Reducing $\mathrm{DM_{s,2}}$ increases the fluctuation parameter and reduces the outer scale of turbulence. From Equation 3.27, the scattering measure and outer scale set the emission measure of the screen to be $\mathrm{EM_{s,2}} \approx 3800$ pc cm^{-6}.

Model 2 is consistent with the scattering measurements of Sgr A* and J1745−2900, the observed properties of the five pulsars in the Galactic center, the free-free emission from thermal maps, the Hα observations, and has properties that are remarkably similar to the gas probed by low-frequency RRLs.

However, it is difficult to account for the range of scattering sizes of OH/IR stars with Model 2. In principle, these could be explained through additional scattering from the Galactic center component of the model. In this case, the different sizes of OH/IR stars are caused by varying displacements through the Galactic center component.

From Equations 3.15 and 3.16, the distance of the screen from the source is

$$x_{\mathrm{s},2} = \left(1 + \frac{1}{2}\frac{\mathrm{SM}_{\tau,\mathrm{s}}}{\mathrm{SM}_{\theta,\mathrm{s}}}\right)^{-1} \tag{3.30}$$

where

$$\mathrm{SM}_{\tau,\mathrm{s}} = \mathrm{SM}_{\tau} - x_{\mathrm{gc}}\left(3 - 2x_{\mathrm{gc}}\right)\mathrm{SM}_{\mathrm{gc}} - \mathrm{SM}_{\mathrm{d}} \tag{3.31}$$

and

$$\mathrm{SM}_{\theta,\mathrm{s}} = \mathrm{SM}_{\theta} - x_{\mathrm{gc}}^2\mathrm{SM}_{\mathrm{gc}} - \mathrm{SM}_{\mathrm{d}} \tag{3.32}$$

denote the contribution of the screen component to the observed SM_{τ} and SM_{θ}, respectively, with $x_i = D_i/D$ being the fractional distance from the source to component i. Since $\mathrm{SM}_{\tau} < \mathrm{SM}_{\theta}$ from the scattering measurements toward J1745−2900, the distance of the screen from Sgr A* increases with increasing $\mathrm{SM_{gc}}$. For $x_{\mathrm{gc}} \ll 1$,

the scattering measure for the Galactic center component has an upper limit of approximately

$$\mathrm{SM_{gc}} \lesssim \frac{1}{3}\left(\mathrm{SM}_\tau - \mathrm{SM_d}\right)/x_{\mathrm{gc}} \tag{3.33}$$

which means that the Galactic center contribution to SM_θ is

$$\mathrm{SM}_{\theta,\mathrm{gc}} = x_{\mathrm{gc}}^2 \mathrm{SM_{gc}} \lesssim \frac{1}{3}\left(\mathrm{SM}_\tau - \mathrm{SM_d}\right) x_{\mathrm{gc}} \lesssim \frac{1}{3}\mathrm{SM}_\theta x_{\mathrm{gc}}, \tag{3.34}$$

so the Galactic center cannot contribute enough angular broadening to account for the OH/IR stars.

Although Model 2 can explain almost all the observational data, it cannot fully account for the scattering of the OH/IR stars.

3.5.3 Model 3

The heterogeneous screen of Model 3 is consistent with almost all of the observational constraints. However, this is in large part due to the great flexibility of the model (ie, no directional dependence on the scattering screen) and it being entirely within the crowded and obscured Galactic center. The dispersion measures and scattering times of the five Galactic center pulsars can be explained as being viewed through different scattering regions or as different depths into the same scattering region. The OH/IR stars can be explained similarly.

To account for the scattering size of Sgr A* requires that the scattering region in the Galactic center have a scattering measure of $\mathrm{SM_{gc}} = 7.5 \times 10^4 (D_{\mathrm{s},3}/150\ \mathrm{pc})^{-2}\ \mathrm{kpc\ m^{-20/3}}$. For such a large scattering measure to still be consistent with the free-free emission observations, the outer scale of turbulence must be $\ell_0 \lesssim 10^{-5}$ pc. However, the scattering properties of J1745−2900 cannot

be accounted for by any scattering material in the Galactic center. This means that even though they are separated by only $2\farcs4$, Sgr A* and J1745−2900 must be viewed through different scattering screens. Furthermore, the screen that scatters J1745−2900 needs to be at least $D_{\rm s} = 5.9$ kpc from the Galactic center.

3.5.4 Summary

Of the three proposed models in Section 3.2, Models 2 and 3 can account for most of the observations, but neither is perfect. For example, Model 2 cannot explain the large scattering sizes of the OH/IR stars. To do so requires another scattering component be added to the model that scatters the OH/IR stars but does not affect any of the other measurements. This could be done by adding a patchy Galactic center screen of comparable strength to that of Model 3 that avoids Sgr A* and J1745−2900. Alternatively, the extra scattering could be due to different clouds that fall along the line of sight to the OH/IR stars and happen to produce comparable amounts of angular broadening.

Similarly, the heterogeneous Galactic center screen of Model 3 can explain most of the observations, but cannot account for the properties of J1745−2900. The combined temporal and angular broadening measurements of J1745−2900 require a scattering component outside of the Galactic center. If Sgr A* is only scattered by the Galactic center scattering component, then this scenario requires dramatic changes in line of sight scattering strength on the scale of arcseconds.

It is interesting to note that the major deficiency of Model 2 is best addressed by Model 3 and *vice versa*. This may be an indication that the true distribution of free electrons is described not by Model 2 or Model 3, but something in between.

3.6 Discussion

Of the three models considered, Models 2 and 3 best reproduce known measurements. Here we discuss the observational consequences of both models and recommend further observations to better determine the electron density distribution toward the Galactic center.

3.6.1 Model Predictions

The dominant scattering component of Model 2 is the thin screen located $D_{\rm s,2} \approx 6$ kpc from Sgr A*, so the scattering properties of the five Galactic center pulsars will be similar to J1745−2900. Since the extrapolated pulse broadening times of these pulsars at 1 GHz are $\tau_{\rm sc,1} \sim 1$ s, the angular broadening at the same frequency should be $\theta_{\rm sc,1} \sim 1''$. The scattering disks of the pulsars could be elliptical like J1745−2900 with axial ratios of $\rho \approx 1.5$, but larger values of $\rho \gtrsim 2$ seen in OH/IR stars are unlikely. The pulse broadening times and angular diameters of the pulsars should scale as $\tau_{\rm sc} \propto \nu^{-4}$ and $\theta_{\rm sc} \propto \nu^{-2}$ over a wide range of observing frequencies.

The outer scale of turbulence for the scattering screen is $\ell_0 \lesssim 0.02$ pc, which could introduce some frequency dependent size changes. If the scattering disk of one of the sources is elliptical with some axial ratio and position angle (ρ_0, PA_0), then on scales smaller than ℓ_0 these parameters should remain relatively constant. However, once the projected size of the scattering disk on the screen exceeds the outer scale [$x \sim \theta_{\rm sc}\,(D - D_{\rm s,2}) \gtrsim \ell_0$], then the axial ratio will shrink and the position angle may change as the scattering disk becomes rounder as a result of averaging over multiple outer scale lengths. For $D_{\rm s,2} \approx 6$ kpc and $\ell_0 \lesssim 0.02$ pc, the scattering size of J1745−2900 is equal to the outer scale of

turbulence at $\nu_{\rm outer} \approx 0.74$ GHz $\left(\frac{\ell_0}{0.02 \text{ pc}}\right)^{-1/2}$.

In contrast to Model 2, the heterogeneous scattering region of Model 3 does not require a consistent scaling law for the angular and temporal broadening. In fact, for a scattering disk with projected size comparable to the size of the scattering matterial, the frequency scalings can depart dramatically from $\tau_{\rm sc} \propto \nu^{-4}$ and $\theta_{\rm sc} \propto \nu^{-2}$ as shown by Cordes & Lazio (2001).

3.6.2 Future Observations

The current observational data cannot distinguish the two models of the free electron distribution toward the Galactic center because there are too few well-studied lines of sight. This problem can be easily rectified by making more complete scattering measurements toward known sources and discovering new sources. Specifically, making angular broadening measurements of the Galactic center pulsars, conducting a long-term monitoring campaign of J1745−2900 while it is still in a radio-emitting state, and measuring the scattering size of more of the many known OH/IR stars within $20'$ of Sgr A* would each help greatly in determining the distribution of free electrons toward the Galactic center.

Interferometric imaging of the five pulsars within $10'-15'$ of Sgr A* will provide a useful constraint on the thin screen of Model 2. Ideally, these observations would be conducted over a range of frequencies to determine how the size and shape of the scattering disks change. Combining these data with measurements of the pulse broadening time over the same frequencies would further constrain the location and extent of the scattering material along the line of sight.

The magnetar J1745−2900 should be studied for as long as it remains in the radio-emitting state. Interferometric imaging of J1745−2900 at a range of frequencies below 8 GHz will set limits on the extent of any very small scattering region and will nicely complement the pulse broadening measurements over the same range by Spitler et al. (2014a). Any deviation from the $\theta_{\rm sc} \propto \nu^{-2}$ frequency scaling or change of shape in the scattering ellipse could indicate edge effects from the scattering material. A long-term monitoring campaign will set limits on the timescale over which the scattering properties change. Such a campaign could also set a lower limit on the outer scale of turbulence by measuring dispersion measure fluctuations.

Scattering measurements toward new sources in the Galactic center would be very useful in determining the variation in strength (if any) of the scattering material transverse to the line of sight. The most promising class of new targets is the OH/IR stars. Although only eight OH/IR stars have measured angular diamters within $2\farcs7 - 25\farcs8$ of Sgr A*, Sjouwerman et al. (1998) catalog over 155 OH/IR stars within $18'$ of Sgr A*. The eight OH/IR stars were originally selected as part of the van Langevelde et al. (1992) sample because they were bright. Since the luminosity of OH/IR stars is variable on timescales from $P \sim 400 - 2000$ days (van Langevelde et al. 1993), it is likely that the brightest OH/IR stars today are not the same as those measured in the early 1990s. Thus, a new campaign to measure the angular diameters of OH/IR stars in the Galactic center will provide scattering measurements along different lines of sight, which will set constraints on the variability of the scattering material transverse to the line of sight.

3.7 Conclusions

In this paper, we presented three models for the distribution of free electrons toward the inner degree of the Galactic center: (1) A uniform single thin screen, (2) a thin scattering screen with additional components in the Galactic disk and the Galactic center, and (3) a heterogeneous Galactic center scattering screen. Each of these models was tested against a wide range of multiwavelength observational data.

Although none of the models considered explained all of the observational data, Models 2 and 3 were able to satisfy most of the constraints. To distinguish between these two models requries further study of the region. We suggest three observations that would greatly enhance our understanding of the electron density distribution along the line of sight. Interferometric imaging of the five pulsars in the Galactic center, combined with pulse broadening measurements, would constrain the line of sight distance to the large scale scattering region. Angular diameter measurements of new OH/IR stars would provide more lines of sight to determine how the observed scattering varies across the Galactic center region. Finally, long-term monitoring of J1745−2900 will set limits on the apparent sizes of the scattering regions.

The dramatic reconsideration of Galactic center electron density models as a result of the discovery of J1745−2900 shows how important pulsars are to the study of the ISM and strongly motivates searches to find more.

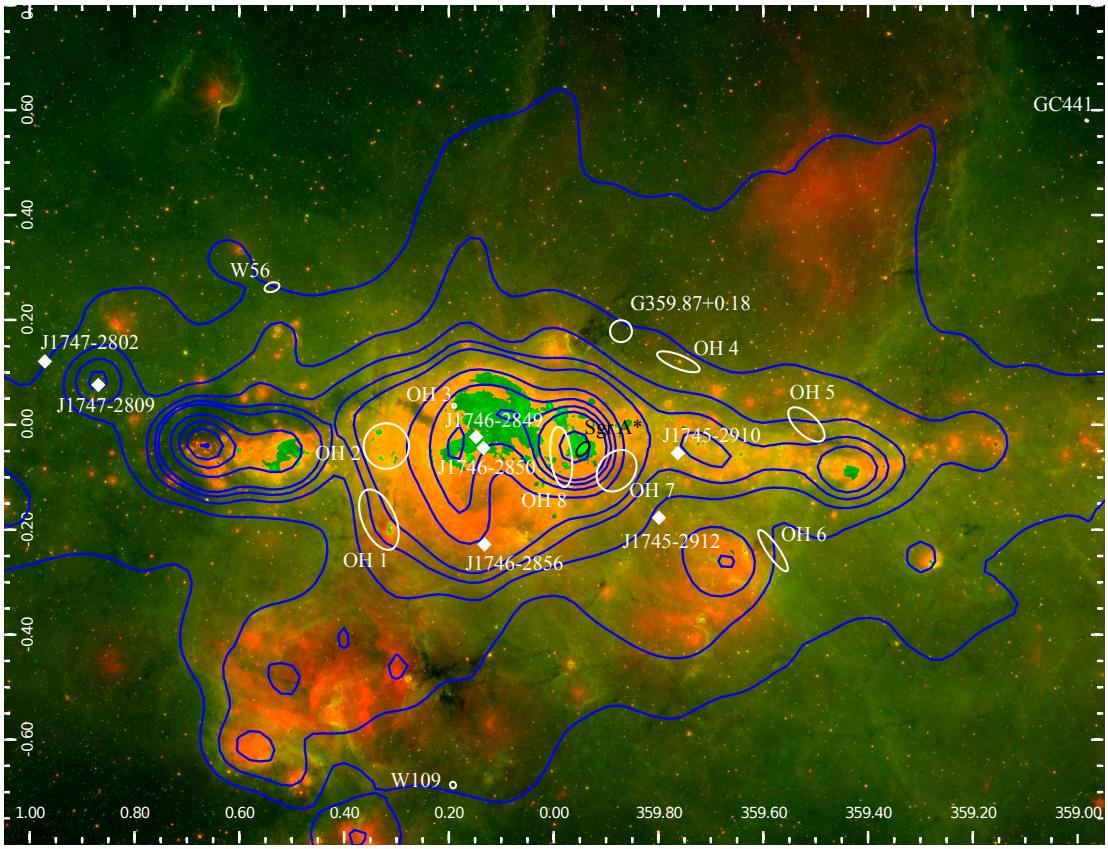

Figure 3.3: **Composite image of the Galactic center region in infrared and radio**. Shown are 8.5μm data (green) taken with *Spitzer* IRAC for *GLIMPSE* (Benjamin et al. 2003a; Churchwell et al. 2009a), 24μm data (red) taken with *Spitzer* MIPS for *MIPSGAL* (Carey et al. 2009), and 10 GHz sky temperature (blue contours) from the map of Handa et al. (1987). The MIPS instrument saturates in the region around Sgr A* and the top of the Galactic center bubble, which is why the 8.5μm data can be seen through here. The 10 GHz sky temperature contours are $0.2 - 1.0$ K in steps of 0.2 K, $1 - 5$ K in steps of 1 K, and $5 - 20$ K in steps of 5 K. The scattering disks of OH/IR stars, extragalactic radio sources, and Sgr A* are plotted as ellipses that are 100 times larger than the true values. The locations of radio pulsars are denote by white diamonds (J1745−2900 is not included here, but is coincident with Sgr A*). The OH/IR stars are simply numbered here, the full names can be found in Table 3.2. A schematic representation of this plot is given in Figure 3.5.

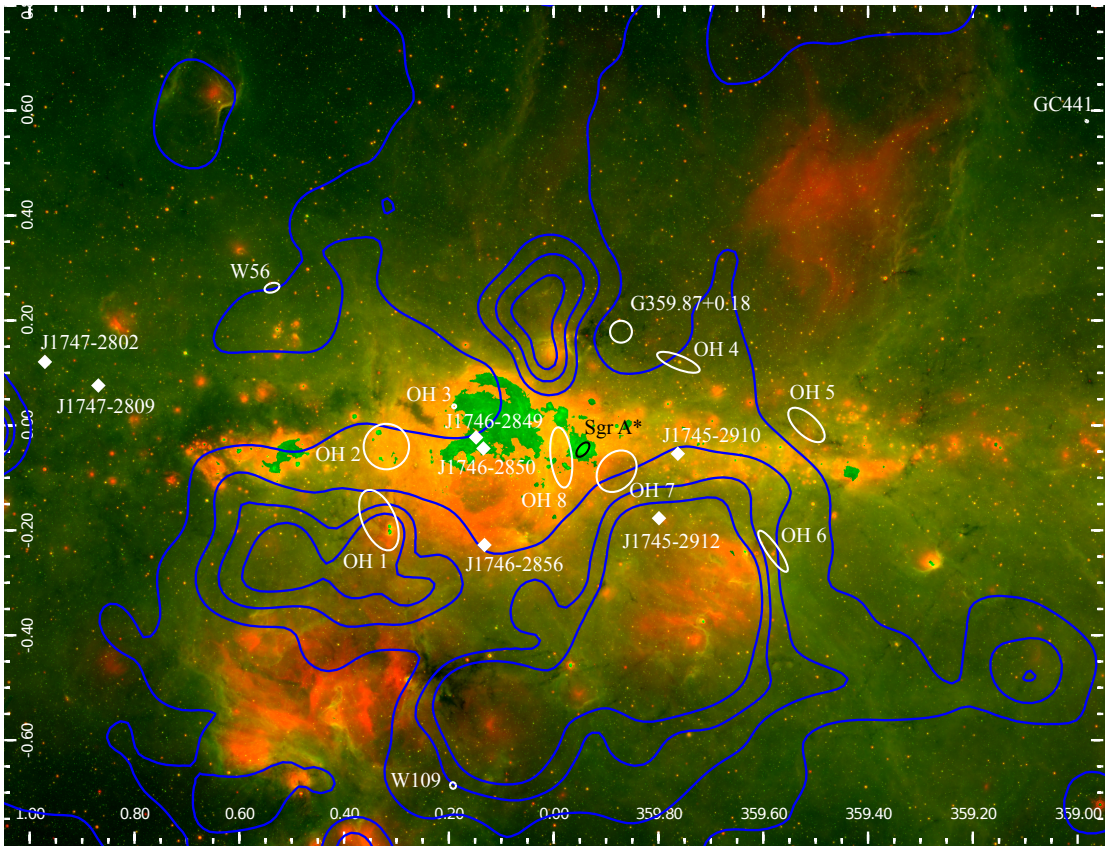

Figure 3.4: **Composite image of the Galactic center region in infrared and** Hα. Shown are 8.5μm data (green) taken with *Spitzer* IRAC for *GLIMPSE* (Benjamin et al. 2003a; Churchwell et al. 2009a), 24μm data (red) taken with *Spitzer* MIPS for *MIPSGAL* (Carey et al. 2009), and Hα (blue contours) from *SHASSA* (Gaustad et al. 2001). The MIPS instrument saturates in the region around Sgr A* and the top of the Galactic center bubble, which is why the 8.5μm data can be seen through here. The Hα contours are at 25, 50, 75, and 100 Rayleighs. The scattering disks of OH/IR stars, extragalactic radio sources, and Sgr A* are plotted as ellipses that are 100 times larger than the true values. The locations of radio pulsars are denote by white diamonds (J1745−2900 is not included here, but is coincident with Sgr A*). The OH/IR stars are simply numbered here, the full names can be found in Table 3.2. A schematic representation of this plot is given in Figure 3.5.

3.8 Appendix: Relations between LOS Integrals

It will be useful to have relations between DM, EM, and SM so that single measurements can be used to constrain each of these line of sight integrated quantities. Using the cloudlet model (see, e.g., Cordes & Lazio 2002), the differential relations for DM, EM, and SM, are

$$\begin{aligned} d\mathrm{DM} &= n_e ds \\ d\mathrm{EM} &= n_e^2 ds \\ d\mathrm{SM} &= C_{\mathrm{SM}} F n_e^2 ds \end{aligned} \tag{3.35}$$

where $C_{\mathrm{SM}} = (10.2/3(2\pi)^{1/3})$ m$^{-20/3}$ cm^6 is a constant to get SM into conventional units and F is the fluctuation parameter given by

$$F = \zeta \epsilon^2 \eta^{-1} \ell_0^{-2/3} \tag{3.36}$$

where $\epsilon^2 = \langle \delta n_e \rangle^2 / \bar{n}_e^2 \leq 1$ is the fractional variance of electron density fluctuations within the clouds, η is the cloud filling factor, $\zeta = \langle \bar{n}_e^2 \rangle / \langle \bar{n}_e \rangle^2$ is the cloud-to-cloud variation in mean electron density, and ℓ_0 is the outer scale of turbulence.

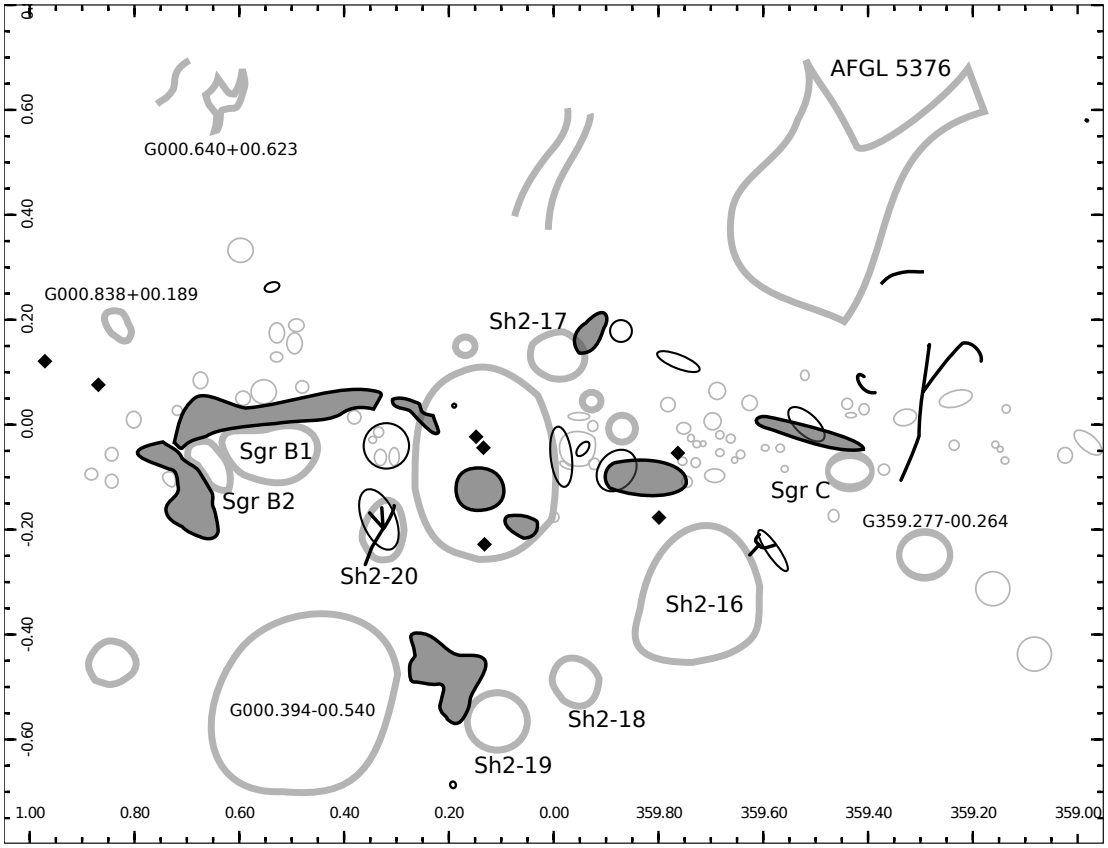

Figure 3.5: **Schematic representation of the structures in the Galactic center region**. Bright regions with the expected morphology of HII regions (see Section 3.4.8 for details) are outlined with thick grey lines. Sources that correpsond to known HII regions are labeled. The thin grey lines denote smaller and less bright candidate HII regions. The thick black lines denote infrared dark clouds (filled) or filaments (lines). The locations of the radio pulsars are indicated by black diamonds and the scattering disks of known radio sources are shown as thin black ellipses at 100 times the actual size.

CHAPTER 4

SINGLE PULSES FROM THE GALACTIC CENTER MAGNETAR[1]

4.1 Introduction

The discovery of a radio-emitting magnetar in the Galactic center presents an enormous opportunity to study both a rare class of magnetars and the distribution of free electrons along the line of sight (LOS) to Sgr A*. J1745−2900 is one of only four magnetars known to produce pulsed radio emission. Like the other three radio-emitting magnetars, XTE J1810−197, 1E 1547.0−5408, and J1622−4950 (Camilo et al. 2006, 2007; Levin et al. 2010), J1745−2900 shows bright spiky emission with a flat spectral index and an inconstant integrated pulse profile (Lynch et al. 2015; Torne et al. 2015, 2017). Careful study of these objects in their active radio state will reveal what relation they have to canonical radio pulsars.

Since J1745−2900 is only $\Delta\theta \approx 2\farcs4$ (projected distance of ∼0.1 pc at 8.5 kpc) from Sgr A*, it is also an excellent source to study the magneto-ionic environment in the immediate vicinity of the black hole as well as the distribution of free-electrons along the LOS to the Galactic center. Observations at radio frequencies have already found that J1745−2900 has the highest dispersion measure (DM) and rotation measure (RM) of any known pulsar (Shannon & Johnston 2013; Eatough et al. 2013). Multi-frequency measurements of the pulse broadening time (caused by multipath scattering) have shown that the 1 GHz pulse broadening time is $\tau_{1\,\mathrm{GHz}} = 1.3 \pm 0.2\,\mathrm{s}$ (Spitler et al. 2014a), which is almost three orders of magnitude less than previously expected (Lazio & Cordes 1998a). By combining the time-

[1]R. S. Wharton, S. Chatterjee, J. M. Cordes, G. C. Bower, B. J. Butler, A.T. Deller, P. Demorest, T. J. W. Lazio, W. A. Majid, S. M. Ransom (Submitting to *ApJ*)

domain scattering measurements of Spitler et al. (2014a) with VLBA imaging measurements of the angular broadening of J1745−2900, Bower et al. (2014) have placed important constraints on the distribution of scattering material along the LOS to Sgr A*.

To study the radio emission of J1745−2900 and measure the dispersion and scattering parameters along the LOS to the Galactic center, we have conducted a single pulse analysis using data taken with the Karl G. Jansky Very Large Array (VLA) in a new phased-array pulsar mode. This new observing mode allows large observing bandwidths (e.g., $\nu_{\rm obs} = 8 - 12$ GHz), making the VLA one of the most sensitive telescopes capable of observing the Galactic center. The rest of the paper is outlined as follows. In Section 4.2, we discuss the observations. In Section 4.3, we explore the time and frequency evolution of the observed average profile and describe how it fits in the context of multi-epoch observations of J1745−2900. In Section 4.4, we consider the phase and amplitude fluctuations of single pulses in each of the profile components of J1745−2900. In Section 4.5, we measure the dispersion and scattering parameters of J1745−2900 and in Section 4.6 we summarize our results.

4.2 Observations

As part of a search for radio pulsars in the immediate vicinity of Sgr A*, we observed the Galactic center with the phased VLA in a new pulsar observing mode that utilizes the full available bandwidth in each receiver band and produces search-mode channelized time series data in real-time. Observations were conducted during the transition from D→DnC configuration on two consecutive

days (2014 Sep 15−16, MJD 56915−6) for 6.5 hours per day. Each observation consisted of alternating scans of 600 s on Sgr A* followed by 100 s scans on the calibrator J1744−3116. We used 4096 MHz of simultaneous bandwidth in two 2048 MHz windows centered on 8.2 GHz and 11.1 GHz to avoid very strong radio frequency interference (RFI) at 9.6 GHz. The time and frequency resolution were set to $\delta t = 0.2$ ms and $\Delta\nu = 4$ MHz based on the considerations of a Galactic center pulsar search. Since J1745−2900 falls within the synthesized beam of the phased array at 10 GHz in DnC configuration, our Galactic center search data contained the very large collection of single pulses analyzed here. More details on the Galactic center search and the new pulsar processing mode will be provided in an upcoming paper (Wharton et al., in prep).

In addition to the Galactic center search data, we also utilize data taken as part of a phased-array campaign to monitor J1745−2900 with the VLA. The observations were conducted at 8.6 GHz with 256 MHz and typically lasted about an hour per epoch. More information on this observing campaign can be found in Bower et al. (2015).

4.3 Profile Evolution

For most radio pulsars, the mean pulse profile is remarkably stable in time as a result of the stability of the magnetic field that guides the radio emission (Helfand et al. 1975). Secular profile changes seen in a few pulsars are caused by changes in the structure or orientation of the magnetic field. For example, the steady separation of two components in the profile of the Crab pulsar (B0531+21) is explained by the gradual drift of the magnetic field axis towards the equator (Lyne

et al. 2013). Profile changes are also seen in a few double neutron star binary pulsars like B1913+16 where geodetic precession gradually changes the direction of the magnetic field axis (Kramer 1998). We examine the evolution of the mean pulse profile of J1745−2900 in both time and frequency and determine the likely origin of any changes.

4.3.1 Time Evolution

To generate a mean profile for each of our two observations, we de-disperse and fold the data at the appropriate dispersion measure (DM) and period for each epoch. We searched over a range of trial DMs centered on the DM = 1778 pc cm^{-3} found by Eatough et al. (2013). Next, each of the de-dispersed time series were folded over a range of trial periods using the Fast Folding Algorithm (FFA, Staelin 1969). Taking the best-fit parameters to be those that maximize the squared difference between the folded profile and a straight line, we found a dispersion measure of DM = 1758 pc cm^{-3} and spin periods of P_1 = 3.76452590(2) s and P_2 = 3.76452893(2) s.

The mean profiles for both days are shown in Figure 4.1. They have been normalized so that the area under each pulse is the same, which allows an easier comparison. Overall, the two mean profiles are almost identical. Each is comprised of four main profile components (C0, C1, C2, and C3) with very similar substructure in each of the components (Figure 4.1). The main differences are a slight amplitude change of C1 relative to C2 and C3 and a shift in the peak of the relatively faint C0.

While the mean profiles appear consistent over 1 day, this is not the case on

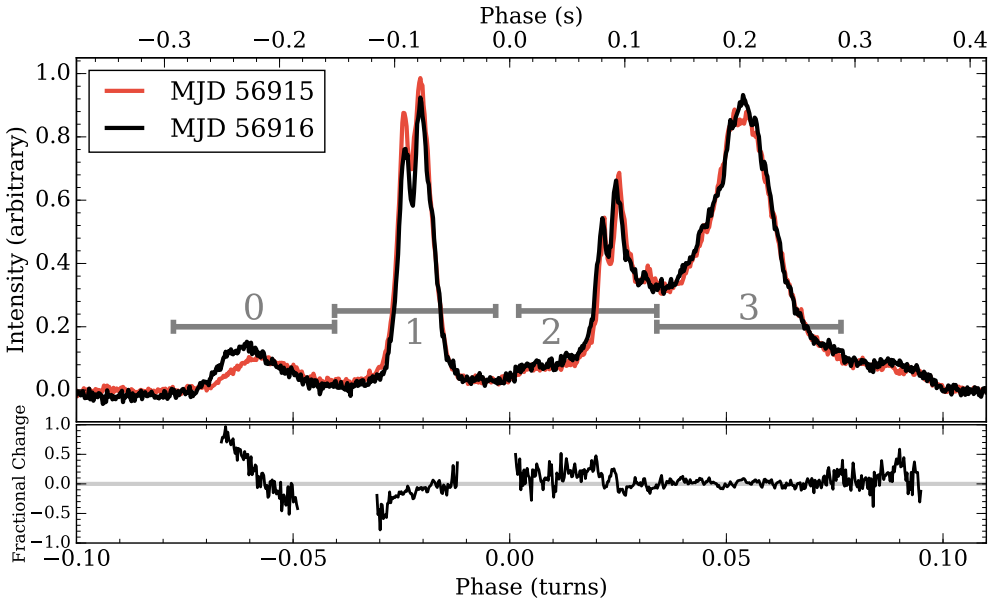

Figure 4.1: **Short-term Profile Changes of J1745−2900** *Upper Panel:* Mean profiles of J1745−2900 observed on two consecutive days. The profiles have been normalized so that the area under each is the same. The numbered bars give the name and range of the four profile components. *Lower Panel:* The fractional difference between the two profiles.

much longer time-scales. Figure 4.2 shows a collection of J1745−2900 profiles generated from phased-array VLA data spanning ∼600 days. In addition to one of our profiles (MJD 56915), there are six profiles from a phased-array monitoring campaign using the phased VLA at 8.5 GHz with 256 MHz of bandwidth (Bower et al. 2015). Since no phase-connected timing solution exists over this interval (Kaspi et al. 2014; Lynch et al. 2015), we have simply aligned the profiles by the rightmost peak (our C3).

From Figure 4.2, it is clear that J1745−2900 has significant profile changes on time-scales of $\lesssim$100 days. From MJD 56486–56710, there appears to be a gradual separation of two components. By MJD 56772, the gradual evolution has given way to more dramatic changes in which components emerge and disappear. This behavior is also seen over a shorter period of time (but with much higher observing

cadence) in the 8.5 GHz GBT monitoring campaign of J1745−2900 by Lynch et al. (2015).

Profile evolution on time-scales of $\lesssim 100$ days could plausibly be caused by large-scale changes to the magnetosphere or by changes in the LOS scattering caused by the motion of a heterogeneous scattering screen through the LOS to J1745−2900. In the latter case, the expected time scale for change would just be the refractive time-scale, $\tau_{\rm r} \sim d\,\theta_{\rm sc}/v$, where d is the distance from the observer to a single scattering screen, $\theta_{\rm sc}$ is the observed angular size of the pulsar, and v is the relative velocity between the pulsar and the scattering screen. Bower et al. (2015) estimate that $\tau_{\rm r} \sim 800$ days ($d = 3$ kpc, $\theta_{\rm d} = 15$ mas, $v = 100$ km s^{-1}), which is far too long to account for the profile changes seen on time-scales of $\lesssim 100$ days. Thus, the changes to the mean profile of J1745−2900 are likely intrinsic.

4.3.2 Frequency Evolution

In many pulsars, there is a gradual change in profile shape with frequency because higher frequency radio emission is thought to originate at lower heights in the magnetosphere. We can test whether there is a similar effect in our J1745−2900 data by splitting the 4 GHz bandwidth into four 1 GHz sub-bands (B0, B1, B2, B3) and generating mean profiles for each band. The resulting profiles are shown in Figure 4.3 along with the fractional difference between the profile generated from the highest frequency sub-band and the other three sub-bands.

From Figure 4.3, we see that the mean profile of J1745−2900 is essentially consistent from 7.7 to 11.6 GHz, with a few slight changes. For one, each of the peaks in the components C1, C2, and C3 narrow with increasing frequency.

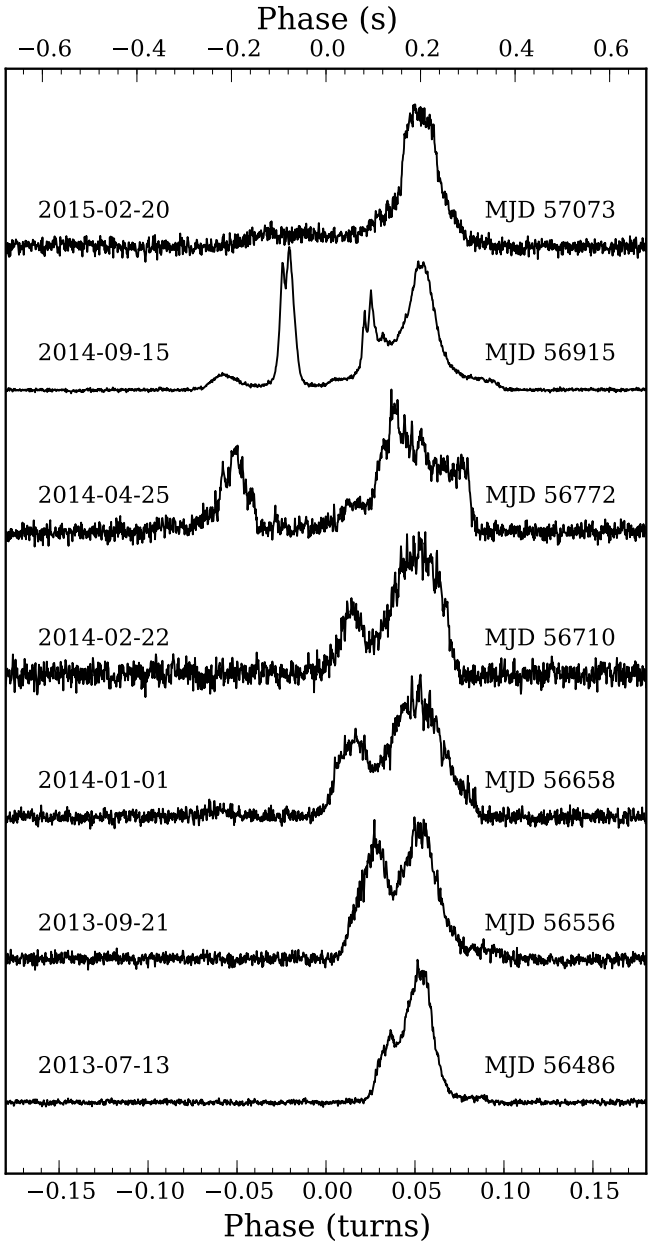

Figure 4.2: **Long-term profile evolution of J1745−2900**. Folded pulse profiles of J1745−2900 from phased-array VLA observations. The profile for MJD 56915 comes from a 6.5 hour observation using 4 GHz of bandwidth. The remaining profiles are from data taken during a monitoring campaign of the magnetar at 8.5 GHz using 256 MHz of bandwidth and observing times of about an hour (Bower et al. 2015). The pulse profiles have been aligned by eye so that the rightmost peak (our C3) of each pulse is roughly aligned.

Another slight change is that the height of the bridge from C2 to C3 appears to increase with frequency, although this may be an artifact of the normalization of the pulses to equal area. Finally, it seems as though the amplitude of C1 decreases with increasing frequency. All of these changes are consistent with the behavior seen in typical pulsars.

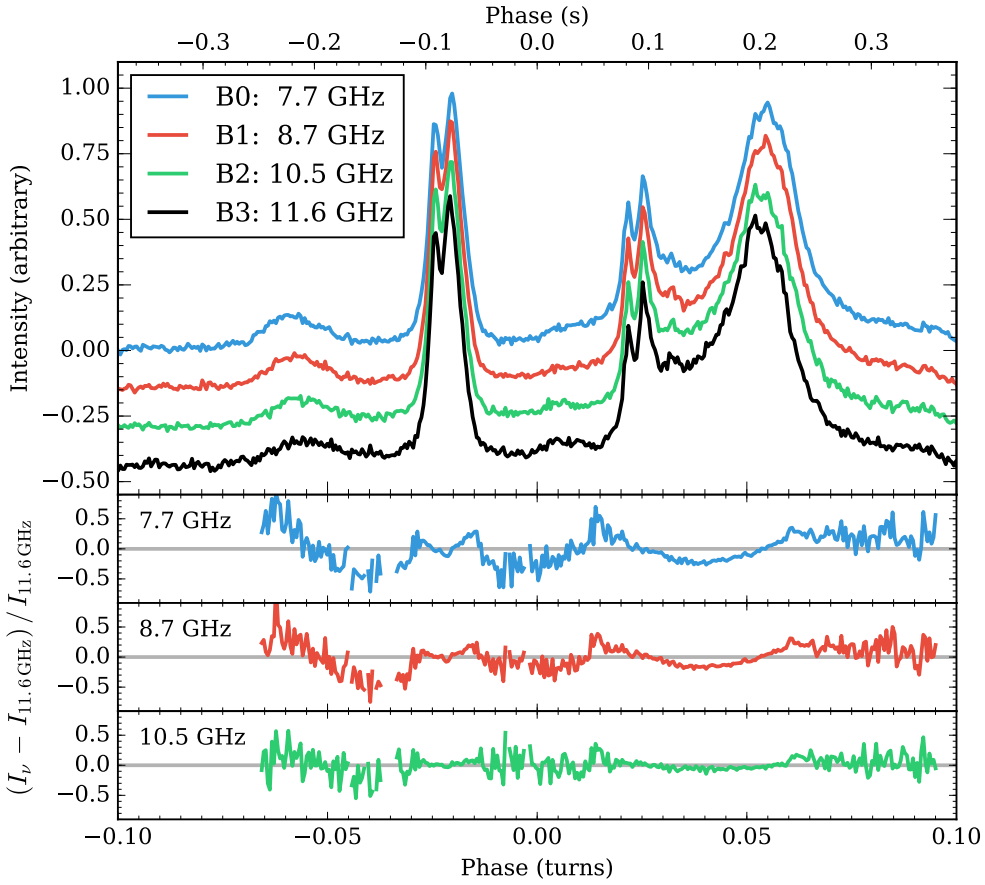

Figure 4.3: **Frequency evolution of J1745−2900 pulse profile**. *Upper Panel:* Mean profiles generated using 1 GHz sub-bands. The center frequency of each sub-band is shown in the legend. The profiles have been normalized so that the area under each pulse is the same. *Lower Panels:* Fractional difference between each of the three lower sub-bands and the sub-band centered on 11.6 GHz.

4.4 Single Pulse Phase and Amplitude Fluctuations

In each of our observations, we have collected single pulse data from nearly 5000 rotations of J1745−2900. Owing to the brightness of the magnetar and the excellent sensitivity of the VLA, individual sub-pulses are clearly seen in almost every rotation. Figure 4.4 shows a selection of 900 rotations ($\approx$ 3400 s) of the magnetar. The 100 s ($\approx$ 27 rotations) calibrator scans are seen as gaps in between the 600 s ($\approx$ 160 rotations) on source scans. The profile components are comprised of very narrow sub-pulses that show obvious signs of rotational phase jitter. As such, this is an excellent data set to quantify the jitter and to search for any correlations in the properties of sub-pulses ocurring in each of the profile components.

4.4.1 Single Pulse Characterization

In order to quantify the jitter and single pulse behavior of J1745−2900, the amplitude, arrival time, and width of the pulse in each profile component need to be determined for every rotation of the magnetar. This is done using a matched filtering technique in which the intensity, $I(t)$, of a pulse is represented as a scaled and shifted template, $G(t)$, in the presence of noise so that

$$I(t) = b\,G(t-\tau) + c + n(t) \tag{4.1}$$

where b and c are constants and $n(t)$ is noise. The scale (b) and shift (τ) parameters are found through fitting in the Fourier domain (Taylor 1992).

In pulsar timing, the template is typically taken to be the mean profile. Pulse jitter makes the mean profile too broad, so we instead draw from a template bank of Gaussian functions with full-width at half-maximum (FWHM) values of $w = 2^m \delta t$

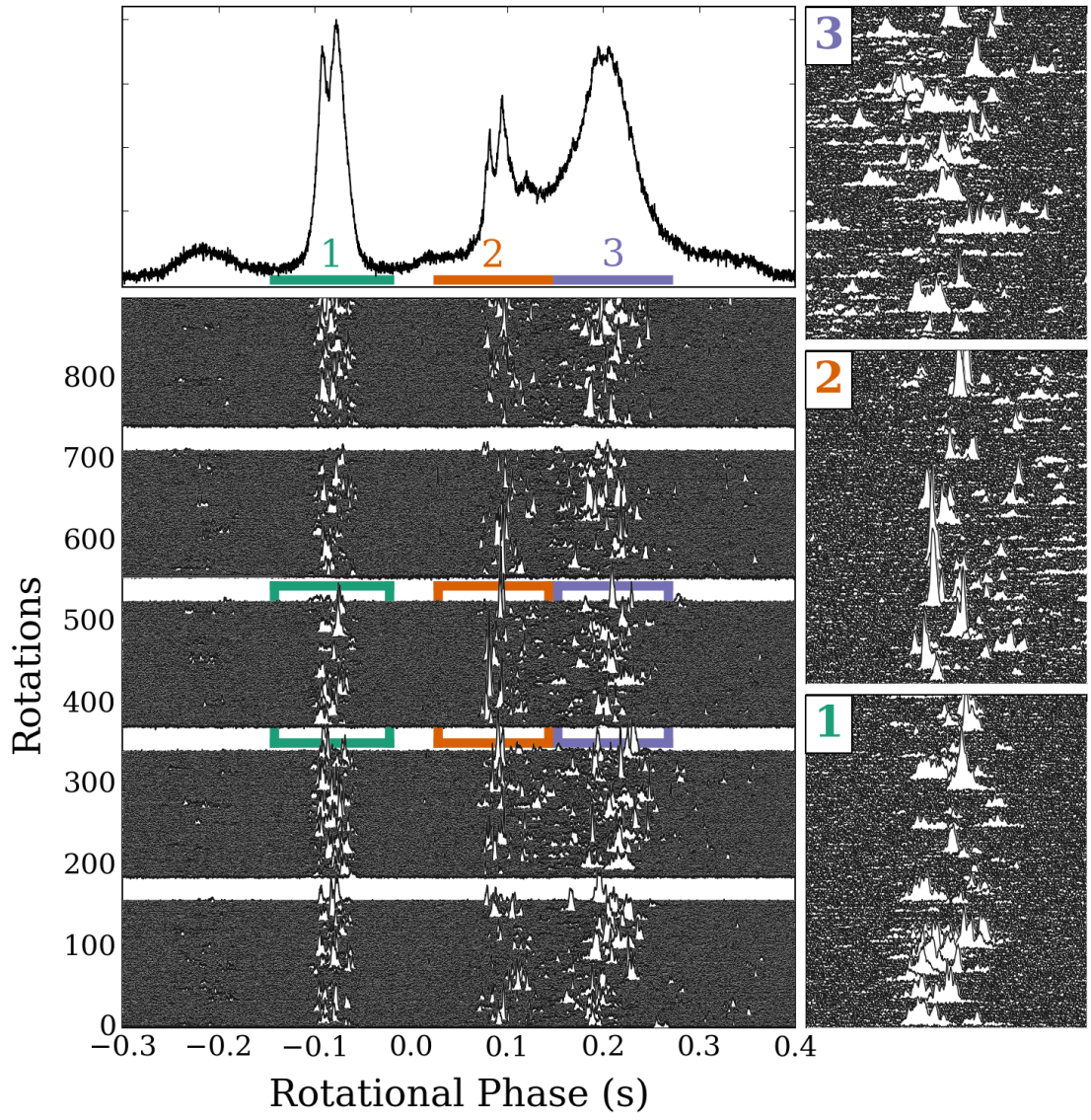

Figure 4.4: **Stacked single pulses from 900 rotations (≈ 3400 s) of J1745−2900**. The 100 s (≈ 27 rotations) calibrator scans are seen as gaps in between the 600 s (≈ 160 rotations) on source scans. The upper panel shows the mean profile from the full observation. Panels on the right give a zoomed in view of the pulses showing 120 ms of rotational phase over one 600 s on source scan.

for $m \in [1, 8]$, which is $0.2 - 51.2$ ms for $\delta t = 0.2$ ms. Thus, our fitting procedure returns an estimate for the amplitude ($\hat{b}$), time-of-arrival offset ($\hat{\tau}$), and width ($\hat{w}$) of a pulse within each profile component for each rotation of the magnetar.

4.4.2 Pulse Jitter

Given the time-of-arrival (TOA) offsets for pulses in each profile component, the contribution of pulse jitter to the overall TOA uncertainty can now be estimated. The TOA uncertainty, $\sigma_{\rm TOA}$, can be expressed as

$$\sigma^2_{\rm TOA} = \sigma^2_{\rm S/N} + \sigma^2_{\rm DISS} + \sigma^2_{\rm J} \tag{4.2}$$

where $\sigma_{\rm S/N}$ is the template fitting error, $\sigma_{\rm DISS}$ is the contribution to the uncertainty caused by diffractive interstellar scintillation (DISS), and $\sigma_{\rm J}$ is the pulse jitter. The template fitting error will depend on the pulse signal to noise ratio (S/N), but for our data set we see $\sigma_{\rm S/N} \lesssim 0.1$ ms.

The DISS term is the result of averaging each pulse over a finite number of scintles in the time-frequency plane and can be estimated as $\sigma_{\rm DISS} \approx \tau_{\rm d}/\sqrt{N_{\rm s}}$, where $\tau_{\rm d}$ is the scattering time and $N_{\rm s}$ is the number of scintles. The number of scintles is given by

$$N_{\rm s} \approx \left(1 + \eta\frac{B}{\Delta\nu_{\rm d}}\right)\left(1 + \eta\frac{T}{\Delta t_{\rm d}}\right) \tag{4.3}$$

where η is the scintle filling factor, B is the bandwidth, T is the integration time, $\Delta\nu$ is the channel width and $\Delta t_{\rm d}$ and $\Delta\nu_{\rm d}$ are the diffractive time-scale and bandwidth, respectively. The diffraction bandwidth is related to the scattering time as $\Delta\nu_{\rm d} = 1.16/(2\pi\tau_{\rm d})$ (Cordes & Rickett 1998), so we expect $\Delta\nu_{\rm d} \approx 920$ Hz $(\tau_{\rm d}/0.2\ {\rm ms})^{-1}$ if the scattering time at 10 GHz is 0.2 ms. The diffractive time-scale is estimated to be $\Delta t_{\rm d} = \ell_{\rm d}/v = \lambda/(2\pi\theta_{\rm d}v) \sim 1$ s, where $\lambda = 3.5$ cm, $\theta_{\rm d} = 15$ mas, and $v \sim 100$ km s^{-1} (Bower et al. 2015). Taking $\eta \approx 0.3$, $T = 3.76$ s, and $B = 4$ GHz, we find that the DISS contribution to the TOA uncertainty is only $\sigma_{\rm DISS} \approx 0.1$ μs.

The TOA uncertainty is simply the standard deviation of the TOA offsets

($\hat{\tau}$) measured for the pulses in each profile component with typical values being $\sigma_{\rm TOA} \gtrsim 20$ ms. Since $\sigma_{\rm TOA} \gg \sigma_{\rm S/N} \gg \sigma_{\rm DISS}$, the TOA uncertainty is entirely dominated by the jitter so $\sigma_{\rm J} \approx \sigma_{\rm TOA}$.

The pulse phase jitter is expected to be correlated within an observing band, but can decorrelate over larger bandwidths. In a study of millisecond pulsars, Shannon et al. (2014) found that the jitter in PSR J0437−4715 decorrelates over frequency separations of ~ 2 GHz. To test the jitter correlation bandwidth of J1745−2900, we split the full 4 GHz band into four 1 GHz sub-bands (centered on frequencies of 7.7, 8.7, 10.5, and 11.6 GHz), characterize the pulses in each component for each sub-band, and then compare the results. Figure 4.5 shows the TOA offsets measured in component C1 for all the sub-bands plotted against each other. Plots from other profile components are similar. The pulse phase jitter in J1745−2900 is highly correlated over 4 GHz of bandwidth.

4.4.3 Correlations between Profile Components

In Section 4.4.2, we found that the TOA uncertainty of sub-pulses falling within each profile component is dominated by jitter. Here we explore whether there are any correlations between the TOA offsets or amplitudes of these pulses. Any correlation in the properties of pulses either within one profile component or between different components would indicate some large-scale structure in the magnetosphere or even a common region for pulsed emission.

To look for correlations, we first generate time series data for the pulse properties of interest from each profile component using the methods described in Section 4.4.1 and a threshold of $({\rm S/N})_{\rm min} = 5$. We determine the TOA offset ($\hat{\tau}[n]$),

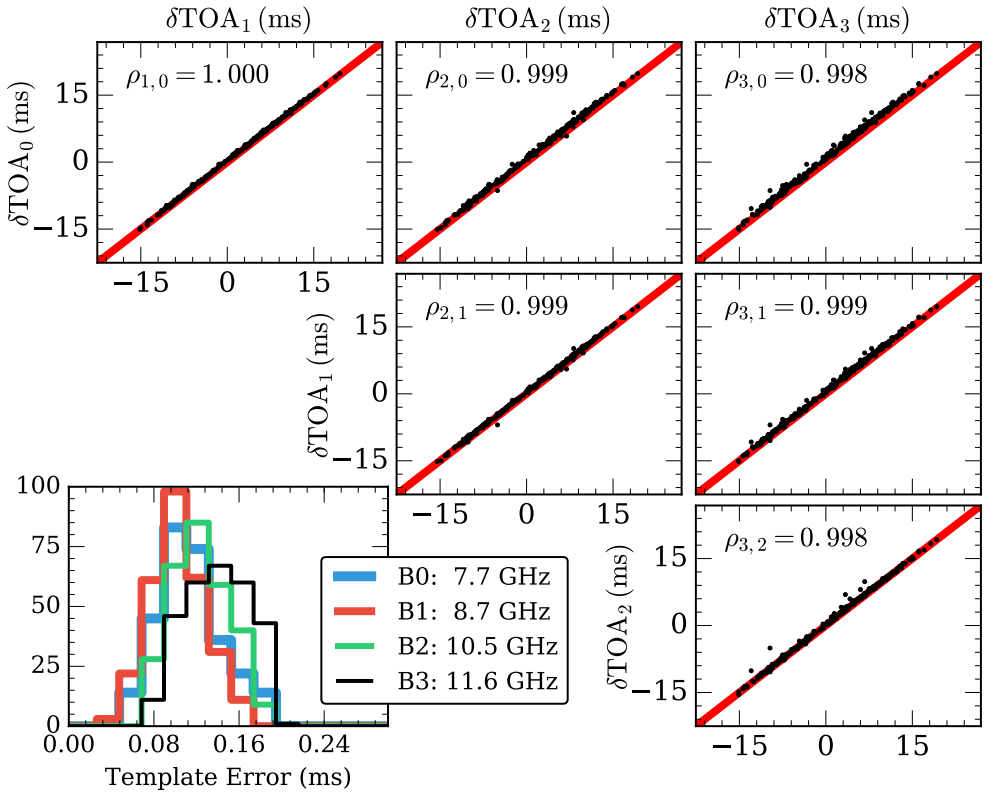

Figure 4.5: **Correlations between subband TOA offsets**. Comparison of time-of-arrival offsets for single pulses from profile component C1 measured in four 1 GHz sub-bands. We selected the 288 pulses detected with S/N > 5 in all four bands and calculated the TOA offsets using a gaussian template with a full-width at half-max of 10 ms (black dots). The correlation coefficient for each pairwise comparison of sub-bands is shown in each panel and the red lines in each plot show a correlation coefficient of $\rho = 1$. The lower left panel shows the distribution of time uncertainties in the fitting of each single pulse.

the pulse amplitude ($\hat{b}[n]$), and a binary value ($\Theta[n]$) indicating the presence of an above threshold pulse all as a function of the pulse number (n). Next, the cross-correlation function (CCF) is calculated between the time series of two profile components for each pulse parameter of interest. We denote the CCF as

$$\mathrm{CCF}_{ij}(x)[n] = (x_i \star x_j)\,[n] \tag{4.4}$$

where x is the time series parameter $(\hat{b}, \hat{\tau}, \Theta)$ from the profile components $i, j \in \{\mathrm{C0}, \mathrm{C1}, \mathrm{C2}, \mathrm{C3}\}$. To avoid the periodicity introduced by the calibrator scans,

the CCFs are calculated using data from each on-source scan and then averaged together over all scans.

To determine the significance of any CCF peaks, we shuffle all the values in the time series of each parameter and re-calculate the CCF, repeating this process 1000 times. Since the shuffled time series should have no correlations, we can use these results to set the 99% confidence level for any lag value in the CCFs.

The results of this analysis are shown in Figure 4.6. We calculate $\mathrm{CCF}_{ij}(x)[n]$ for each parameter $(\hat{b}, \hat{\tau}, \Theta)$ for component pairs $(i, j) = (\mathrm{C1}, \mathrm{C2})$, $(\mathrm{C1}, \mathrm{C3})$, and $(\mathrm{C2}, \mathrm{C3})$. Component C0 was excluded because it had far fewer above threshold pulses ($N = 62$) than C1 ($N = 1023$), C2 ($N = 1030$), and C3 ($N = 1169$). While most of the CCFs appear to be consistent with noise, there is a small but significant correlation in the occurrence of pulses in C1 and C2 at zero lag. This means that pulses in C1 and C2 occur during the same rotation of J1745−2900 more often than would be expected if they were completely independent.

4.4.4 Pulse Flux Distributions

The pulse flux distribution can also be used to characterize the emission from pulsars. For many pulsars, the flux distribution is well described by a log-normal distribution (Burke-Spolaor et al. 2012), whereas for pulsars that emit giant pulses, the distribution follows a power-law (Lundgren et al. 1995). Studies of the radio-emitting magnetar, J1622−4950, found good agreement with a log-normal distribution of pulse fluence (Levin et al. 2012). However, neither model seems to fit the magnetar XTE J1810−197 particularly well (Serylak et al. 2009).

Using the de-dispersed and folded data from MJD 56915, we can calculate

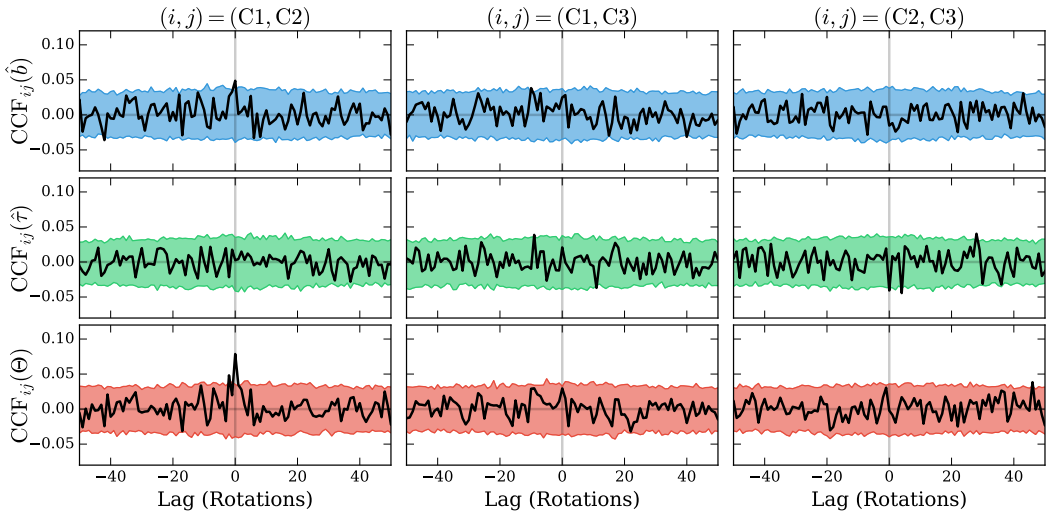

Figure 4.6: **Cross-correlation function (CCF) between the time series of pulse properties measured in the three brightest pulse profile components**. The black lines denote the observed CCF and the light shaded regions denote the 99% confidence limit estimated by reshuffling the pulse order (see text for details). *Upper Row:* CCF of observed pulse amplitudes ($\hat{b}$). *Middle Row:* CCF of observed pulse TOA offsets ($\hat{\tau}$). *Lower Row:* CCF of above threshold pulse occurrence (Θ).

the normalized flux for each profile component at every rotation of J1745−2900. This is done by calculating the mean intensity over all the phase bins in each profile component for each rotation and then normalizing by the mean intensity in those same bins over all rotations. Since there will be some contribution to this distribution from (not necessarily Gaussian) noise, we also calculate a noise distribution for each profile component from an equally sized window at phase bins outside the region of pulsed emission. The results are shown in Figure 4.7. Overall, the results are more similar to the log-normal distributions of most pulsars than the power-law distributions spanning several orders of magnitude that are seen in pulsars with giant pulse emission like the Crab (Lundgren et al. 1995).

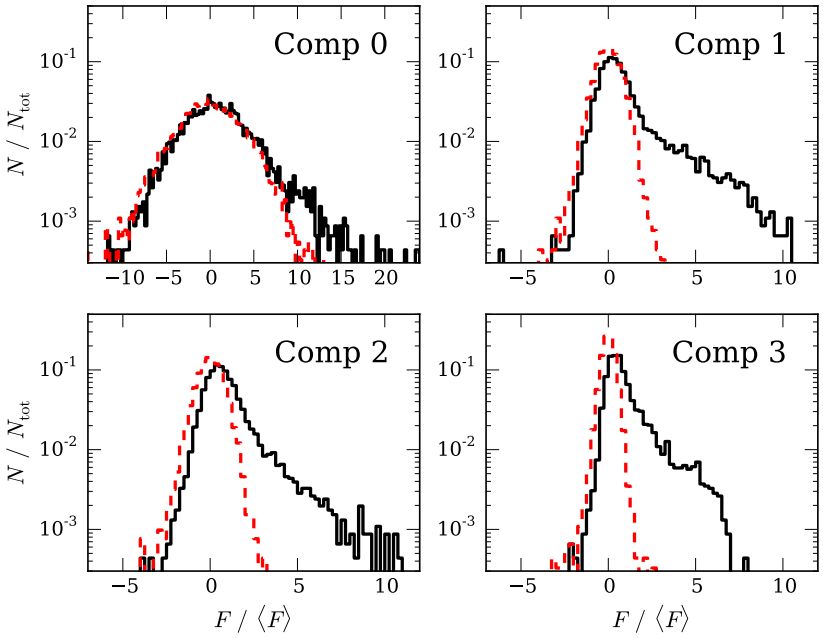

Figure 4.7: **Pulse amplitude histograms for the four pulse profile components**. In each case, the amplitude of a pulse is calculated as the average intensity over all phase bins in the component and is expressed in terms of the average amplitude in that component over the the whole observation. These normalized intensities are binned (black line). A noise histogram (red line) is calculated for each component from an off-pulse region with width equal to that of the component.

4.5 Dispersion and Pulse Broadening in Single Pulses

As a bright radio-emitting magnetar in the immediate vicinity of Sgr A*, J1745−2900 is an excellent tool for studying the magneto-ionic environment towards the Galactic center. In particular, measurements of the pulse broadening time and the dispersion measure provide useful contraints on the distribution of free electrons along the line of sight. Measurements of the dispersion measure and scattering time are easiest for bright and narrow pulse profiles. The broad jitter-dominated average profile of J1745−2900 is not well suited for these measurements, but some of the bright single pulses are. Here we use a set of the brightest narrow pulses to estimate the dispersion and scattering parameters for J1745−2900.

4.5.1 Method

Using the brightest narrow pulses from the J1745−2900 data set (Figure 4.8), we can measure the dispersion and scattering by modeling the frequency dependent delay across the observing band. For the case where the scattering time is small compared to the pulse width, the time of arrival (TOA) of a pulse is

$$\tau(\nu) = k_{\rm DM}{\rm DM}\left(\frac{\nu}{1\ {\rm GHz}}\right)^{\alpha_{\rm DM}} + \tau_{\rm sc}\left(\frac{\nu}{1\ {\rm GHz}}\right)^{\alpha_{\rm sc}} + t_0 \tag{4.5}$$

where DM is the dispersion measure, $\alpha_{\rm DM}$ is the scaling index of the dispersion law, $\tau_{\rm sc}$ is the scattering time at 1 GHz, $\alpha_{\rm sc}$ is the scaling index of the scattering law, and t_0 is an offset. The dispersion index for a cold electron plasma is $\alpha_{\rm DM} = -2$, but leaving it a free parameter allows for a test of the known dispersion law. To avoid a degeneracy in fitting the indices, the scattering index is fixed at $\alpha_{\rm sc} = -4.0$, which is consistent with the results of Spitler et al. (2014a).

Using the full channelized time series data, sub-band TOAs for each pulse were determined using the same matched filter method used in 4.4.1. To ensure a sufficient pulse S/N in each sub-band, 8 channels are averaged together to split the band into 128 sub-bands. From the measured TOAs and TOA uncertainties, we fit our model. Since the model is non-linear, we do a full Bayesian parameter estimation.

Assuming normally distributed errors in the measured sub-band TOA values, the likelihood function is

$$\mathcal{L}(\tau|{\rm DM}, \alpha, t_0, \tau_{\rm sc}) = \prod_{i=0}^{N-1} \frac{1}{\sqrt{2\pi\sigma_{\tau,i}^2}} \exp\left[-\frac{1}{2}\left(\frac{\tau_i - \tau(\nu_i)}{\sigma_{\tau,i}}\right)^2\right] \tag{4.6}$$

where τ_i and $\sigma_{\tau,i}$ are the TOA and TOA uncertainty in the sub-band with center frequency ν_i. Wide priors are adopted for each of the four parameters. Normal

distributions are used for DM ($\mu_{\rm DM} = 2000$ pc cm^{-3}, $\sigma_{\rm DM} = 1000$ pc cm^{-3}), α ($\mu_\alpha = -2$, $\sigma_\alpha = 2$), and t_0 ($\mu_t = 0$ ms, $\sigma_t = 500$ ms). For the 1 GHz scattering time $\tau_{\rm sc}$, an exponential distribution with mean $\lambda_\tau = 1000$ ms is used as a prior. Combining these priors with the likelihood, we construct and sample the posterior distribution using Markov chain Monte Carlo (MCMC). We use the `emcee` MCMC sampler (Foreman-Mackey et al. 2013), which is a Python implementation of the affine invariant sampler of Goodman & Weare (2010). We consider both the case where α is a free paramter (α-free) and where $\alpha = -2$ is fixed (α-fixed).

4.5.2 Results

Parameter estimates from the TOA model fitting (for both α-free and α-fixed) are shown in Table 4.1. When the dispersion index is allowed to vary, it is in every case found to be consistent with the expected cold plasma value of $\alpha = -2$. Only upper limits can be placed on the 1 GHz scattering time ($\tau_{\rm sc}$) in the α-free model. This is not too surprising because the scattering time at 10 GHz is expected to be $\tau_{\rm sc,10} \sim 0.1$ ms, which is only half a time-bin. This small offset can also be more easily absorbed into other parameters in the α-free case.

In the α-fixed model where the dispersion index has been fixed at $\alpha = -2$, the estimates of the DM and $\tau_{\rm sc}$ are much more precise. The best-fit scattering time is non-zero for two pulses (albeit with rather large uncertainties). The average value of the dispersion measure is DM $= 1761.5^{+1.8}_{-2.1}$ pc cm^{-3}. The uncertainties in the individual DM measurements are asymmetrical, which comes from the correlation between the DM and $\tau_{\rm sc}$ estimates. Figure 4.9 shows marginalized posterior distributions for the fit of the Pulse 4717 data. From the lower-left panel of that plot, it is clear that as the scattering time decreases, the dispersion measure increases.

Since there is a minimum allowed scattering time ($\tau_{sc} = 0$ ms), the upper limits to the DM estimates are smaller than the lower limits. The difference between the measured TOAs and the best-fit model TOAs are shown for each pulse in Figure 4.8.

Pulse	Component	Fit α		Fixed $\alpha = -2$	
		α	τ_{sc} (ms)	DM (pc cm^{-3})	τ_{sc} (ms)
202	3	$-1.997^{+0.013}_{-0.009}$	< 6040	$1764.9^{+2.3}_{-3.5}$	< 4400
747	3	$-1.999^{+0.026}_{-0.014}$	< 5030	$1761.2^{+3.9}_{-4.8}$	< 6060
1119	1	$-2.001^{+0.025}_{-0.022}$	< 3570	$1763.7^{+5.0}_{-5.0}$	< 6990
1348	3	$-2.004^{+0.025}_{-0.014}$	< 2990	$1762.5^{+3.2}_{-5.6}$	< 6400
2577	3	$-2.006^{+0.015}_{-0.012}$	< 5990	$1765.3^{+2.0}_{-6.3}$	100^{+1169}_{-100}
4717	2	$-2.004^{+0.009}_{-0.008}$	< 2610	$1763.3^{+2.6}_{-4.3}$	417^{+810}_{-368}

Table 4.1: **Parameter estimates from single pulse fitting**. Reported uncertainties define the innermost compact 68% confidence interval. Upper limits are given at the 95% confidence limit. The set of parameters on the left are from a fit in which the dispersion index α is fit (α-free) and the parameters on the right are from a fit where the dispersion index is fixed at $\alpha = -2$ (α-fixed).

4.5.3 Comparison with Previous Results

There have been only a few measurements of the dispersion and scattering of pulses from J1745−2900 and all of these measurements were made shortly after the magnetar radio emission turned on. Eatough et al. (2013) measured the dispersion measure of J1745−2900 to be DM $= 1778 \pm 3$ pc cm^{-3} using observations at 2.5 GHz and 8.35 GHz. Spitler et al. (2014a) conducted a multi-frequency study of J1745−2900 using multiple telescopes to measure the parameters of the scattering law. They found a 1 GHz scattering time of $\tau_{sc,1} = 1300 \pm 200$ ms and a scattering index of $\alpha_{sc} = -3.8 \pm 0.2$. Pennucci et al. (2015) observed J1745−2900 with the

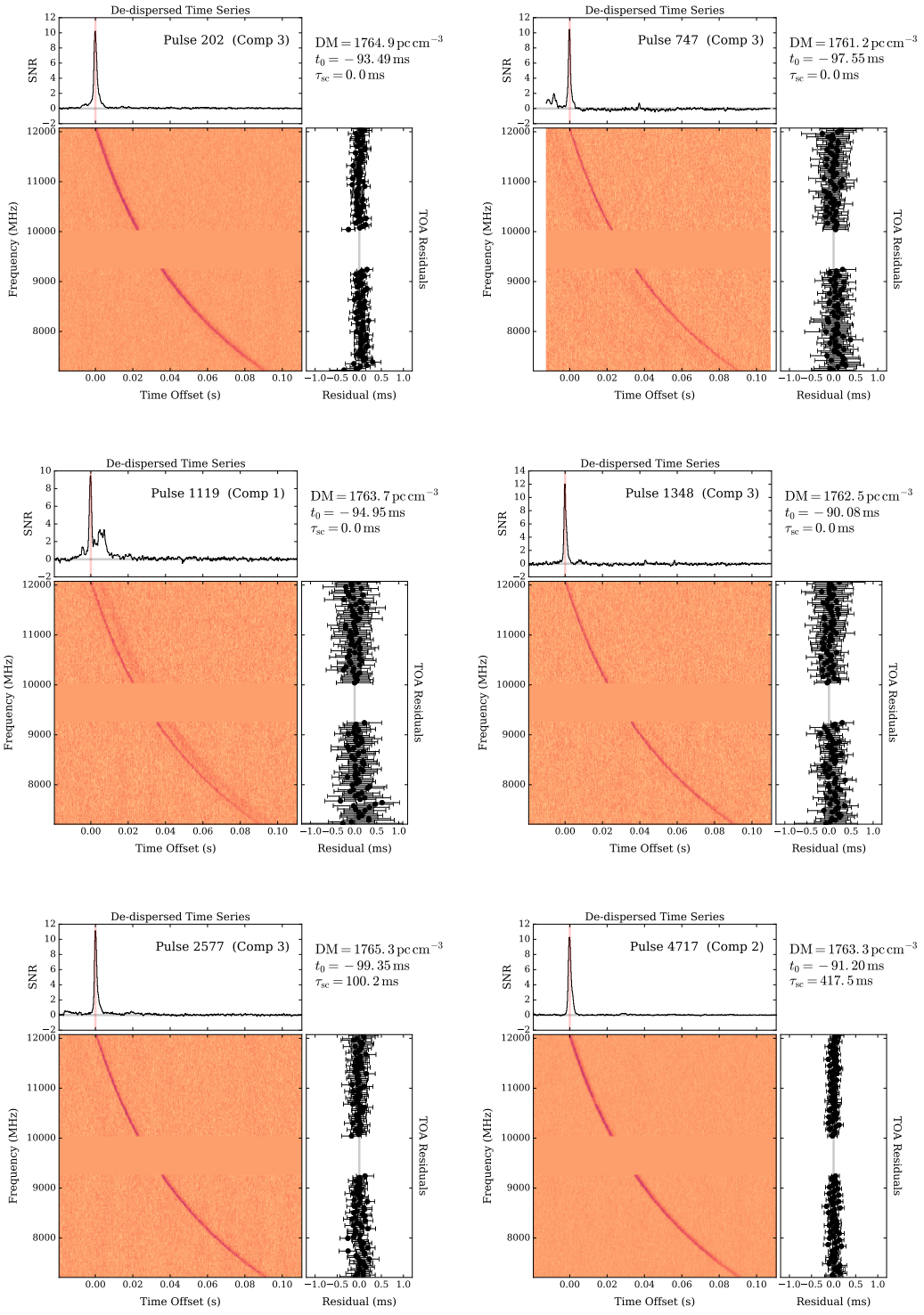

Figure 4.8: **Six bright pulses from MJD 56915 used for dispersion and scattering parameter estimation**. Each panel shows the dynamic spectrum (middle), the de-dispersed time series (top), and residual TOAs after subtracting the best-fit timing model (right).

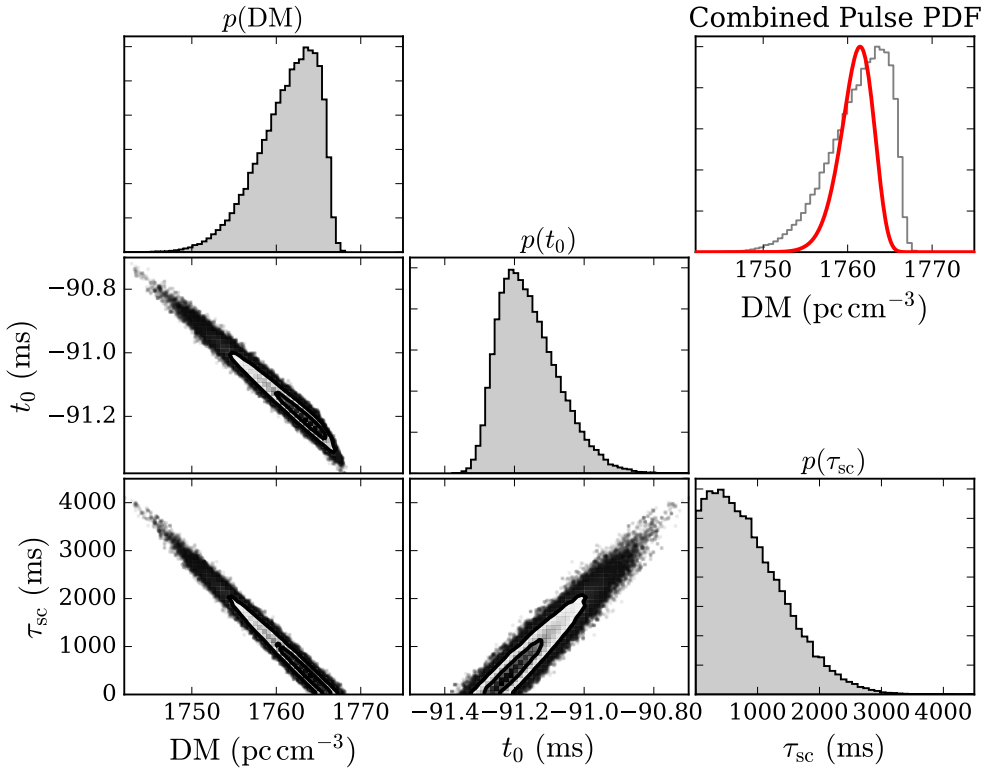

Figure 4.9: **Marginalized posterior distributions for three-parameter model fits for Pulse 4717**. The plots along the diagonal are the fully marginalized posterior distributions for each parameter. The two dimensional distributions in the lower left give the posterior distribution marginalized over the third parameter. The parameter estimates for the dispersion measure (DM) and 1 GHz scattering time (τ_{sc}) are very strongly correlated. The upper right plot gives the distribution of the average DM (red) calculated from the marginalized PDFs of the DM posteriors from each of the six bright pulses in Figure 4.8.

GBT in two observing bands to cover 1.4–2.4 GHz and used a wide-band model to simultaneously fit the scattering and dispersion parameters. Over ~ 30 days of observing, they measured values that were roughly consistent with Eatough et al. (2013) and Spitler et al. (2014a), but with an apparent variability in both time and frequency.

Our single pulse estimates for the dispersion measure of J1745−2900 (DM = $1761.5^{+1.8}_{-2.1}$ pc cm^{-3}) are consistently lower than the values reported by Eatough

et al. (2013) and Pennucci et al. (2015). Our measurements of the scattering time are consistent with the values of Spitler et al. (2014a). It may be the case that the dispersion measure changed in the ~ 400 days between our observations and the original measurements. Alternatively, it may just be that the much larger scattering times and wider average pulse widths in the previous observations have biased the DM measurements upward. A consistent long-term observing campaign to measure the DM would be needed to better address this issue. On time scales of ~ 6 hours, however, we see no change in the dispersion measure of the single pulses (Figure 4.10).

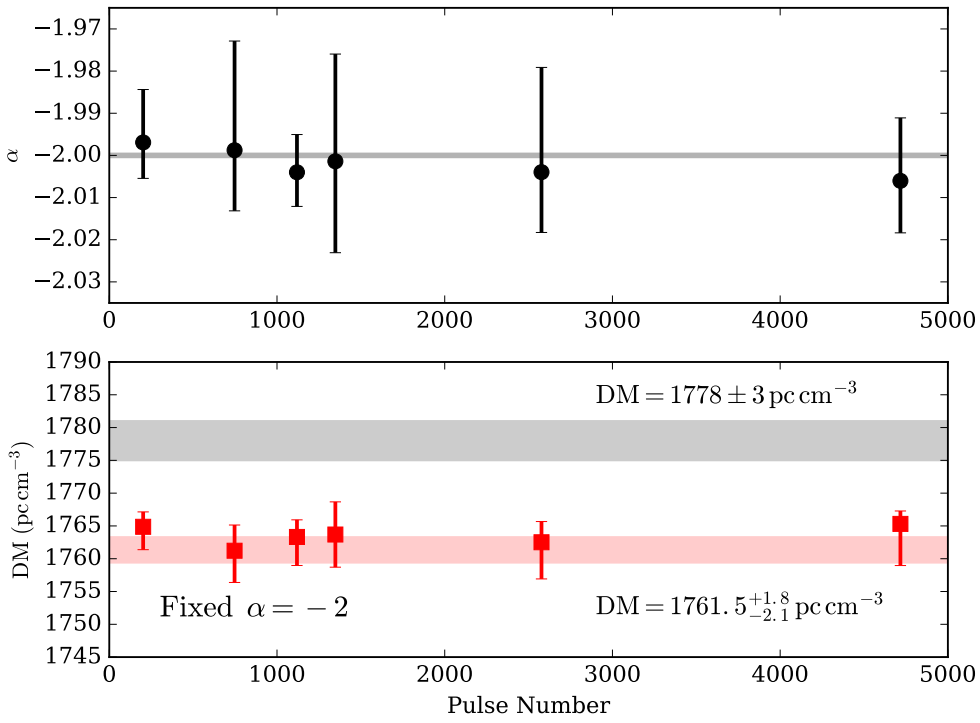

Figure 4.10: **Parameter fits for each pulse**. The top plot shows the fits of the dispersion index (α) in the α-free model. The bottom plot shows the DM values (red squares) for each pulse in the model with the dispersion index fixed at $\alpha = -2$. The red band shows the average DM value of DM $= 1761.5^{+1.8}_{-2.1}$ pc cm^{-3}. The grey band shows the DM $= 1778 \pm 3$ pc cm^{-3} value reported by Eatough et al. (2013).

4.6 Conclusions

We have conducted a detailed study of pulses from the radio-emitting magnetar J1745−2900 using the VLA in its phased-array pulsar mode at 8–12 GHz. Using two 6.5 hour observations on consecutive days, we found that the average pulse profile was fairly stable on ∼day timescales. However, comparison with additional phased VLA observations at 8.5 GHz from July 2013 to February 2015, shows that the average pulse profile of J1745−2900 changes on timescales of $\lesssim$100 days, which is consistent with the results of Lynch et al. (2015). Using the full 4 GHz of simultaneous bandwidth, the frequency evolution of the average pulse profile is shown to be relatively small. This is consistent with previous studies that used nearly contemporaneous obserservations at multiple frequencies (Spitler et al. 2014a; Torne et al. 2015).

Using a matched-filter technique, the individual sub-pulses in each component are characterized for every available rotation of J1745−2900. The variance in the TOAs of these pulses is found to be dominated by pulse jitter. Comparing the occurrence, amplitude, and TOA of pulses in each profile component, we find no correlation in the amplitude or phase of pulses occurring in different profile components. However, we do find a statistically significant over-abundance of pulses occuring during the same rotation in both components C1 and C2, possibly suggesting a common or related origin for pulses in these two profile components.

Finally, we measured the dispersion and scattering parameters of J1745−2900 using a collection of bright and narrow single pulses. Our observations are particularly well suited for measuring the DM because the observed frequency range (7.5–12 GHz) covers a large bandwidth at frequencies where the scattering is relatively small ($\tau_{\rm sc} \sim 0.1$ ms at 10 GHz). Using single pulses also avoids any uncertainty

in constructing a complex pulse profile template. We find that the index of the dispersion law is consistent with the $\alpha = -2$ expected from a cold electron plasma. We also find that the dispersion measure is DM $= 1761.5^{+1.8}_{-2.1}$ pc cm^{-3}, which is lower than the DM $= 1778 \pm 3$ pc cm^{-3} measured by Eatough et al. (2013) shortly after the discovery of J1745−2900. The discrepancy could be the result of a bias introduced by the much larger scattering in the earlier measurements conducted at lower frequencies or could indicate an actual change in the dispersion measure of J1745−2900. A long-term monitoring program would be necessary to confirm this possibility.

CHAPTER 5

A PHASED VLA SEARCH FOR PULSARS WITHIN 0.15 PC OF SGR A*[1]

5.1 Introduction

The discovery of a radio pulsar orbiting the black hole Sgr A* would provide an excellent probe of the Galactic center environment. Timing even a single canonical pulsar ($P_{\rm spin} \sim 1$ s, $B_{\rm p} \sim 10^{12}$ G) in a $P_{\rm orb} \sim 10 - 100$ year orbit around Sgr A* would be sufficient to measure the mass, spin, and quadrupole moment of the black hole to exquisite precision (Liu et al. 2012). Measuring these parameters would allow tests of the fundamental properties of black holes including their simplicity (No Hair Theorem) and the existence of an event horizon (Cosmic Censorship Conjecture). However, despite considerable effort, no such pulsar has yet been discovered. The radio-emitting magnetar J1745−2900 is not suitable becuase of extremely high timing noise (Lynch et al. 2015).

The Galactic center is a very challenging region for conducting pulsar searches because it is very distant ($d_{\rm gc} = 8.3$ kpc) and contains a large number of radio sources that produce a significant background sky temperature. For a single dish telescope, this means that a high gain (i.e., large collecting area) and long observing spans are needed. However, the relatively large beam widths of single dishes ($\theta_{\rm FWHM} \gtrsim 1'$) mean that a lot of background flux is included, which significantly raises the system temperature for high-gain telescopes. Since the target is extremely localized on Sgr A*, the ideal instrument would have the highest gain combined with a very small beam size. These specifications are exactly what are

[1] R.S. Wharton

delivered by the Karl G. Jansky Very Large Array (VLA) in phased-array mode.

The VLA is an appropriate instrument for conducting Galactic center pulsar searches. The large collecting area and receiver bandwidths give it the sensitivity to detect very distant pulsars and the narrow synthesized beam reduces the effect of background sources on the system temperature. Until recently, the phased-array bandwidths were limited to 256 MHz and could not yet take advantage of the $\sim$ GHz bandwidths available in the expanded VLA. We have developed a new phased-array pulsar mode capable of processing the wide available bandwidths and used it to conduct an 8–12 GHz search for pulsars within $\Delta\theta = 3\farcs5$ (0.15 pc at 8.3 kpc) of Sgr A*.

In this paper, we detail the phased-array VLA pulsar mode in Section 5.2. In Section 5.3, we describe the observations conducted as part of the search and in Section 5.4 we present the Galactic center search. The results of the search are given in Section 5.5 and discussed in Section 5.6. Finally, in Section 5.7 we present our conclusions and discuss future work.

5.2 VLA Pulsar Processing

The VLA has long been able to operate in a phased-array mode, which has historically been used for Very Long Baseline Interferometry (VLBI) observations (e.g., Wrobel 1983). In these observations, the signals from each antenna are coherently combined in the VLA correlator and written to disk for correlation with other VLBI stations. Since the data need to be recorded at the Nyquist rate, the bandwidth is ultimately limited by the recorder. The current Mark5C recorder can handle data rates of up to 2 Gbps, which sets a bandwidth limit of 256 MHz

for two polarizations with 2-bit sampling. In order to access the 1–6 GHz bandwidths available with the expanded VLA, a real-time pulsar processing system called YUPPI (Y-Ultimate Pulsar Processing Instrument) has been developed.

Before discussing YUPPI in detail, we first briefly describe the VLA correlator. The WIDAR correlator takes as input the down-converted and sampled data from each of the array antennas and calculates the correlations for all baselines. The signal from each antenna is divided into subbands with bandwidths up to 128 MHz. The correlations between all antennas are then calculated for each subband on Baseline Boards (BlBs). In addition to calculating the correlations for a given subband, the BlB also produces coherently summed phased-array data. The BlBs output the correlation data as time-tagged packets and send them to the Correlator Back-End (CBE) computing cluster to be averaged and combined to produce a visibility data set. The phased-array data is output as VDIF (VLBI Data Exchange Format) packets that are typically either sent to a VLBI recorder or discarded. The purpose of YUPPI is to collect these VDIF packets and convert them to pulsar data in real-time.

YUPPI is an automated processing system that produces pulsar data products from the phased-array data output by the VLA correlator. It is based on the GUPPI system developed for the GBT and uses much of the same code. The YUPPI system has four main components: the `yuppi_controller` to parse metadata and initiate processing, the `yuppi_daq_server` to extract data from VDIF packets, the DSPSR processing tools to produce pulsar data, and the `yuppi_gluer` to collect and combine subband data into one data set for archiving. Since the phased-array data are produced separately for each subband, the data aquisition and pulsar processing also operate on the subbands separately. One subband is

processed by one node in the CBE cluster. Only at the `yuppi_gluer` stage are all the data collected into one place.

A schematic of the YUPPI processing of a single subband on one CBE node is shown in Figure 5.1. The `yuppi_controller` is always running in the background on the CBE computing cluster. At the start of each observation, it parses the observation metadata to determine if it is a phased-array pulsar observation. If it is, then the metadata is read into a shared memory buffer and the `yuppi_daq_server` is activated. The `yuppi_daq_server` listens for and collects data from the phased-array VDIF packet stream. Data is passed to a shared memory buffer where DSPSR is used to either produce folded profiles (using `dspsr`) or filterbanked to produce channelized time series (using `digifil`). At the end of the pulsar observation, the `yuppi_controller` initiates the `yuppi_gluer` to collect all the subband data and combine them into one full-band data set in PSRFITS format.

Finally, the phased-array processing occurs concurrently with the correlations that produce standard interferometric visibilities. This means that every phased-array pulsar observation also produces an imaging data set as well.

5.3 Observations

We used the VLA in phased-array pulsar mode to conduct two 6.5 hour observations of Sgr A* on consecutive days (2014 Sep 15−16, MJD 56915−6) during an array transition from D→DnC configuration. Each observation consisted of alternating scans of Sgr A* for 600 seconds and the calibrator J1744−3116 for 100 seconds. We recorded 4 GHz of bandwidth in two 2 GHz windows centered on 8.2 GHz and 11.1 GHz. This was done to avoid very strong source of radio

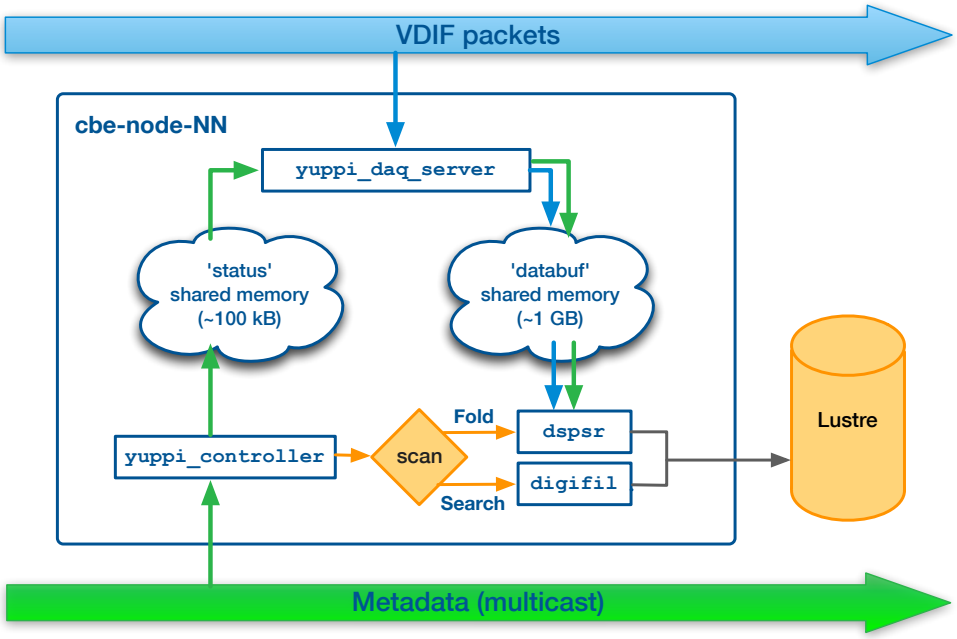

Figure 5.1: **Schematic of the automated pulsar data acquisition software**. This runs independently on each node of the CBE computing cluster. The `yuppi_controller` checks the observation metadata for an upcoming pulsar scan. If one is detected, `yuppi_controller` instructs `yuppi_daq_server` to begin reading in the VDIF packets to be processed with standard pulsar processing software (`digifil`, `dspsr`). At the end of the scan, `yuppi_controller` sends out a signal that stops data acquisition and instructs `yuppi_gluer` to collect, combine, and archive the data products from each of the 32 CBE nodes.

frequency interference (RFI) at around 9.6 GHz. The synthesized beam at 10 GHz in D-configuration is $\approx 7''$, which corresponds to a projected distance of 0.3 pc at 8.3 kpc. The time and frequency resolution of the output pulsar search data were set to be $\delta t = 0.2$ ms and $\Delta\nu = 4$ MHz, which are sufficient to detect pulsars with spin periods greater than a few milliseconds.

5.4 Search for Pulsars Around Sgr A*

Both of the observations produce channelized time series intensity data in the pulsar standard PSRFITS data format, which can be used to search for pulsars and radio transients. We make use of the PRESTO[2] pulsar processing software package to conduct a periodicity and single pulse search (Ransom 2001). The sky coverage of this search is set by the half-power width of the synthesized beam at 10 GHz in D-configuration, which is $\approx 7''$ (0.3 pc at 8.3 kpc).

5.4.1 Preliminary Flagging

Before searching the data, some preliminary processing is needed to improve the quality of the data. This includes the correction of a few data artifacts and the flagging of radio frequency interference. Because these observations were conducted as part of the commissioning of the VLA phased-array pulsar mode, there were a few minor issues with the data. The main one involved amplitude offsets in a few of the subbands. Complex gain calibrations are performed during the calibration scans and the phase and aplitudes are locked in for the on-source scans. In some of the scans, these amplitudes can have significant offsets between subbands. To correct this, we subtract a 10 second rolling average of the intensities for all of the channels. The data also contain some radio frequency interference (RFI). We used the PRESTO task `rfifind` to create an RFI mask to remove contaminated data intervals and channels.

[2]http://www.cv.nrao.edu/~sransom/presto/

5.4.2 De-dispersion

For each observation, we de-disperse the data using 250 trial values of DM from 0 to 5000 pc cm^{-3} in steps of ΔDM = 20 pc cm^{-3} using the PRESTO task `prepsubband`. The limits of the trial DM values safely include the expected DM $\approx$ 2000 pc cm^{-3} near Sgr A*. The DM step size is chosen so as not to introduce a significant amount of pulse smearing across the band due to an incorrect DM. For this DM step size, the greatest error in DM is δDM = 10 pc cm^{-3}, which produces a dispersive delay of

$$\tau_{\delta\mathrm{DM}} = 0.4 \text{ ms } \left(\frac{\delta\mathrm{DM}}{10 \text{ pc cm}^{-3}} \right). \tag{5.1}$$

This is roughly consistent with the expected amount of pulse broadening caused by multipath scattering along the line of sight to Sgr A*. The Spitler et al. (2014a) scattering law of $\tau_{\mathrm{sc}} = 1.5 \text{ s } \nu_{\mathrm{GHz}}^{-3.8}$ predicts pulse broadening times between 0.1 and 0.9 ms over the band from 12.1 to 7.1 GHz.

5.4.3 Periodicity Search

We perform a Fourier search for pulsars in the data sets from both days. The Fourier transform is calculated for the de-dispersed time series for each trial DM. Since narrow pulse profiles can produce many harmonics, we search the power spectra using optimal harmonic summing to maximize the signal to noise ratio of any candidate. We also run an acceleration search using the PRESTO `accelsearch` task. The acceleration search is a simple search technique to find binary pulsars by approximating the orbit with a single parameter (the acceleration). This is a much easier task than searching over all the orbital parameters, but is only applicable for systems with orbital periods much longer than the observing time ($P_{\mathrm{orb}} \gtrsim 20\, T_{\mathrm{obs}}$).

Once periodicity candidates are identified, diagnostic plots showing the folded profile and dynamic spectrum are made and examined by eye.

5.4.4 Single Pulse Search

We also conduct a single pulse search to find pulsars and other radio transients. The single pulse search is particularly important for the Galactic center where otherwise detectable pulsars could be obscured by rapid orbital motion or precession effects that make the beam only intermittently cross the line of sight. We use the PRESTO single pulse search, which is a simplified implementation of the matched-filter search technique described by Cordes & McLaughlin (2003). A series of boxcar templates with widths up to 100 ms are cross-correlated with the data to identify candidates in each of the 250 de-dispersed time series. All candidates are collected and plotted in a time-DM plot to identify real astrophysical sources.

5.5 Results

In both the periodicity and single pulse searches, we clearly detect the radio-emitting magnetar J1745−2900 but do not detect any new pulsars or transients. The observations conducted on MJD 56916 suffered from a significant amount of RFI, so we will mainly focus on the results from MJD 56915.

5.5.1 Periodicity Search

The acceleration search of the MJD 56915 data set produced 680 periodicity candidates about a detection threshold of $(S/N)_{det} = 3$. The magnetar J1745−2900 is clearly detected and is strong enough to produce additional candidates and many different DMs and at harmonics of the spin frequency. Figure 5.2 shows a portion of the power spectrum of the magnetar at DM = 1760 pc cm^{-3}. After filtering out duplicates and harmonically related candidates, we are left with 155 top candidates. Diagnostic plots are made for each of these candidates and examined by eye. All of these appear to be either harmonics of the magnetar or RFI.

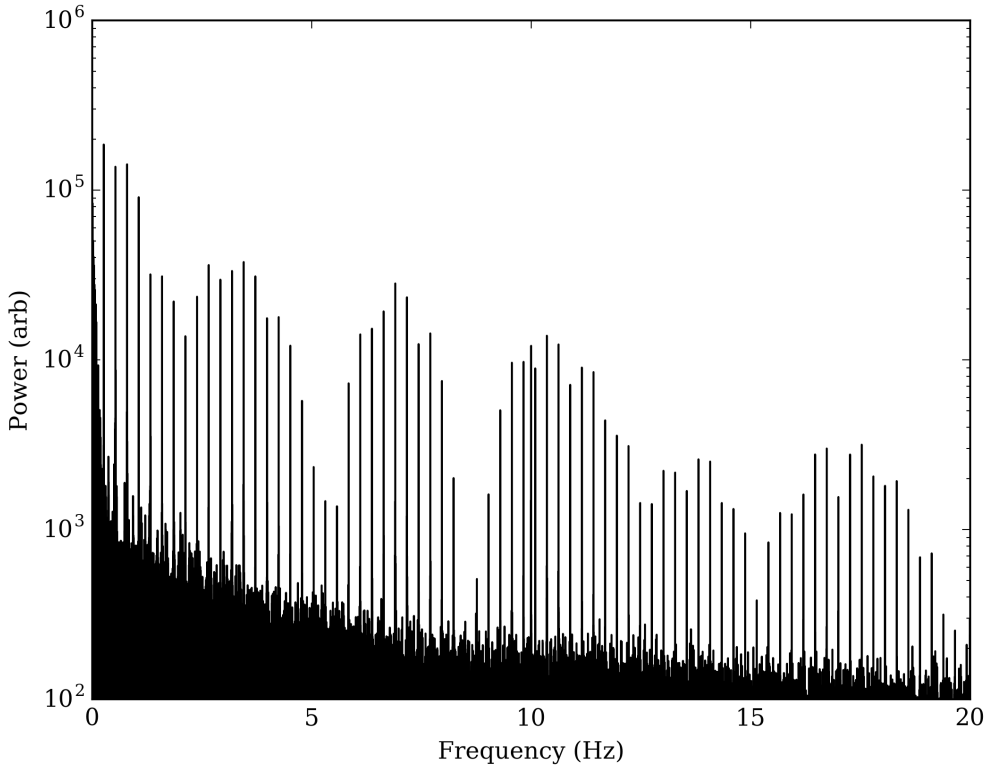

Figure 5.2: **Power spectrum of J1745–2900 detection**. This power spectrum is generated from time series data that was de-dispersed at DM = 1760 pc cm^{-3}. The magnetar is clearly detected in almost 100 harmonics. Only a portion of the full power spectrum is shown here to show the magnetar harmonics. An RFI signal at 10 Hz is also visible.

5.5.2 Single Pulse Search

The single pulse search produces a total of 22 million candidates from all of the 250 de-dispersed time series for $(S/N)_{det} = 5$. We need to reduce this candidate list to a reasonable number of candidates that can be plotted and examined. The first filtering step is to remove candidates that are effectively duplicates of other candidates detected at slightly different times or dispersion measures. All candidates are binned and the highest S/N candidate is taken from each time bin. In the next step, we need to remove the pulses from the magnetar J1745−2900. To do this, we remove all candidates that occur during the times when J1745−2900 is know to emit pulses. In the last filtering step, we remove narrow-band RFI signals using the spectral modulation index technique described in Spitler et al. (2012). Diagnostic plots for the remaining candidates are made and examined by eye.

5.6 Discussion

No new pulsars or transients were discovered in our searches of the 10 GHz phased-array data. From these non-detections, we can set uppper limits on the population of pulsars and other radio transients in the immmediate vicinity of Sgr A*. Since these searches are only sensitive to certain types of systems, the limits will also apply only to a subset of the total population. This is important because a reanalysis of this data set using more sophisticated search techniques could still potentially produce a pulsare discovery.

5.6.1 Population Limits

Based on the sensitivity limits of our periodicity search and the absence of any new discoveries, we can set population limits on the number of pulsars around Sgr A*. The acceleration search technique used in this paper is only sensitive to pulsars that are either isolated or in very wide binaries ($P_{\rm orb} \gtrsim 20\ T_{\rm obs}$), so it is only these systems for which we can set limits. The population of pulsars in orbits shorter than $P_{\rm orb} \approx 5$ days is essentially unconstrained in this search.

The 10σ sensitivity limits of this search are shown in Figure 5.3 along with the population of known pulsars. The sensitivity curve accounts for pulse broadening from scattering and the optimal summing of harmonics. It depends slightly on the pulsar spin period, but for $P_{\rm spin} \gtrsim 100$ ms, the 10σ detection limit is $S_{\rm det} = 4\ \mu$Jy at 10 GHz. This is one of the deepest searches to date around Sgr A* and would have detected about 70% of all currently known pulsars with distance measurements (30% with $P_{\rm spin} < 30$ ms) if they were placed at the Galactic center. While the known pulsar population is a useful benchmark for understanding our search, it is a sample that is biased towards the brightest pulsars. To set a limit on the pulsar population, we would like to use the underlying pulsar luminosity distribution.

By comparing a simulated population with the known Galactic sample, Faucher-Giguère & Kaspi (2006) found that the underlying distribution of pulsar pseudoluminosities ($L = Sd^2$) is well described by a lognormal distribution. They found a best-fit mean and standard deviation for the logarithm of the 1.4 GHz pseudoluminosity (with pseudoluminosity L in units of mJy kpc^2) of $\mu_{\log L} = -2.5$ and $\sigma_{\log L} = 2.1$, respectively. Adopting this as the pseudoluminosity distribution of pulsars in the Galactic center, we can calculate the detection probability of our

survey as the complement of the cumulative distribution function

$$F(S_{\rm det,1.4}) = \frac{1}{2}\left[1 - {\rm erf}\left(\frac{\log(S_{\rm det,1.4}d^2) - \mu_{\log L}}{\sqrt{2}\sigma_{\log L}}\right)\right], \tag{5.2}$$

where $S_{\rm det,1.4}$ is the minimum detectable flux density at 1.4 GHz and $d = 8.3$ kpc is the distance to the Galactic center. Scaling our 10 GHz flux density limit of $S_{\rm det,10} = 4$ μJy to 1.4 GHz using a spectral index $\alpha = -1.6$ ($S_\nu = S_0\nu^\alpha$), we find that $S_{\rm det,1.4} = 0.09$ mJy. From Equation 6.16, this gives a detection probability of $p(S_{\rm det,1.4}) = 0.017$.

Assuming that the detection of a pulsar is a Bernoulli process, we can set a limit on the total number of pulsars that is consistent with zero new detections. If the probability of detection is given by $p_{\rm det} = F(S_{\rm det,1.4})$, the probability of N pulsars given zero detections ($n = 0$) is given by

$$p(N \mid n = 0, p_{\rm det}) = p_{\rm det}\left(1 - p_{\rm det}\right)^N. \tag{5.3}$$

From this distribution, we calculate the 68% (99.7%) upper limit to be $N = 65$ (338) pulsars with $P \gtrsim 100$ ms and $P_{\rm orb} \gtrsim 5$ days within $\Delta\theta = 3\farcs5$ of Sgr A*.

5.6.2 Single Pulse Limits

One of the main benefits of a sinlge pulse search is that it is completely unaffected by the orbital smearing effects that can dramatically reduce the sensitivity of a periodicity search. This is particularly useful in the Galactic center where pulsars orbiting the black hole may be affected by both the typical orbital Doppler shifting and general relativistic effects like orbital precession. These effects would make even a very bright pulsar undetectable by conventional periodicity searches. However, if the pulses are bright enough, they could be detected in a sinlge pulse search.

The sensitivity of a single pulse search is given by

$$S_{\rm sp,det} = \frac{({\rm S/N})_{\rm min} T_{\rm sys}}{G\sqrt{N_{\rm pol}\Delta\nu W}} \tag{5.4}$$

where $({\rm S/N})_{\rm det} = 5$ is the detection S/N, $T_{\rm sys} \approx 35$ K is the system temperature, $G = 2.4$ K Jy^{-1} is the effective gain of the array (with 25 antennas), $N_{\rm pol} = 2$ is the number of summed polarizations, $\Delta\nu = 4$ GHz is the bandwidth, and W is the width of the pulse. For a pulse with $W = 0.3$ ms (typical scattering time at 10 GHz), the minimum detectable pulse flux density is

$$S_{\rm sp,det} = 47 \text{ mJy } \left(\frac{\rm S/N}{5}\right)\left(\frac{W}{0.5 \text{ ms}}\right)^{-1/2}. \tag{5.5}$$

It is instructive to see if this sensitivity is sufficient to detect giant pulses from the Crab pulsar if it were placed in the Galactic center. Cordes et al. (2004) conducted multi-frequency observations of Crab giant pulses using Arecibo. At 8.7 GHz, the brightest giant pulse detected in an hour long observation had a peak flux density of $S_{\rm a} \approx 880$ Jy and a width of $W_{\rm a} \approx 16$ μs. If this same pulse were emitted from the Galactic center the peak flux density would be reduced by a factor of $(2 \text{ kpc}/8.3 \text{ kpc})^{-2} \approx 17$ due to the distance. It would also be reduced by a factor of $(300 \text{ } \mu\text{s}/16 \text{ } \mu\text{s}) \approx 19$ as a result of pulse broadening from scattering. The observed peak flux density of such a pulse emitted from the Galactic center would be $S_{\rm gc} \approx 2.7$ Jy, which would almost certainly be detected in our search.

5.7 Conclusions

Using the VLA in a phased-array pulsar observing mode, we conducted a search for pulsars within $\Delta 3\farcs5$ of Sgr A*. Though we clearly detect the radio-emitting magnetar J1745−2900 in both a periodicity and single pulse search, we do not

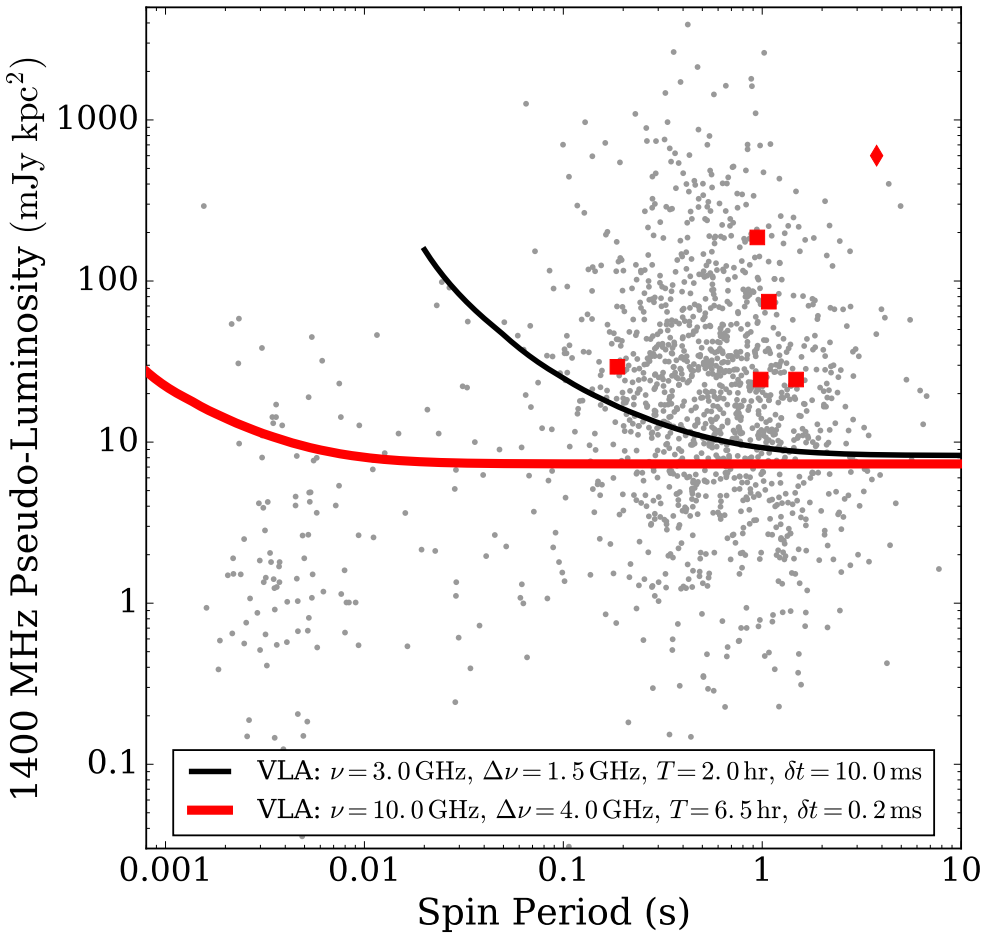

Figure 5.3: **Sensitivity of VLA searches**. Sensitivity curve for this survey (red) and a beam-forming search at 2 GHz (black) that covers the same region around Sgr A*. The curves represent the 10σ detection limit for pulsars of a given 1400 MHz pseudoluminosity placed in the Galactic center. The pulsars are all assumed to be at a distance of 8.3 kpc and have a spectral index of $\alpha = -1.6$ ($S_\nu \propto \nu^\alpha$). We have assumed that the scattering is the $\tau_{\rm sc} = 1.3$ s $\nu_{\rm GHz}^{-4}$ seen toward J1745−2900. The grey dots are pulsars from the ATNF database with known 1400 MHz pseudoluminosities. The red squares are the five pulsars within $10-15'$ from Sgr A* and the red diamond is J1745−2900.

detect any new pulsars or radio transients. From the periodicity search, we can set an upper limit of $N = 65$ (338) pulsars with $P \gtrsim 100$ ms and $P_{\rm orb} \gtrsim 5$ days within $\Delta\theta = 3\farcs5$ of Sgr A*. Given the limitations of the acceleration search technique and the excellent quality of this data set, we plan on conducting more

sophisticated pulsar search techniques to find binary systems including sideband searches (Ransom et al. 2003) and orbital template fitting (Knispel 2011).

CHAPTER 6

FAST VISIBILITY SEARCH FOR PULSARS IN THE GALACTIC CENTER[1]

6.1 Introduction

Many deep searches for radio pulsars have been conducted in the Galactic center (e.g., Johnston et al. 2006; Deneva et al. 2009; Macquart et al. 2010). While several of these surveys have covered a fairly wide region, the ultimate goal is to find a pulsar in orbit around the 4×10^6 $M_\odot$ black hole Sgr A*. Careful timing of the pulses from such a pulsar would allow for precise measurements of the black hole parameters (mass, spin, and quadrupole moment) and tests of general relativity (Liu et al. 2012). However, despite many searches of the Galactic center, only six radio pulsars have been found within $30'$ (72 pc at 8.3 kpc) of Sgr A*. Of the six, five are are at angular separations of $10 - 15'$ ($25 - 35$ pc) (Johnston et al. 2006; Deneva et al. 2009). The only pulsar discovered within $10'$ is the radio-emitting magnetar J1745−2900 located $2''.4$ ($\approx$0.1 pc) from Sgr A* (Eatough et al. 2013).

The discovery of the radio-emitting magnetar J1745−2900 so close to Sgr A* presents an interesting puzzle for models of the Galactic center pulsar population. Previously, the dearth of observed pulsars within $10'$ of Sgr A* was explained by a region of hyper-strong scattering that produced a frequency-dependent pulse broadening time of $\tau_{\rm sc} \sim 1000$ s $\nu_{\rm GHz}^{-4}$, which would have rendered most pulsars undetectable at frequencies below about 10 GHz (Lazio & Cordes 1998a). However, the pulse broadening time of J1745−2900 was measured to be $\tau_{\rm sc} = 1.3$ s $\nu_{\rm GHz}^{-4}$, three orders of magnitude less than the hyper-strong scattering model (Spitler et al.

[1]R.S. Wharton

2014a). Furthermore, radio-emitting magnetars are incredibly rare, comprising only four out of the ≈2600 known pulsars in the Galaxy. Discovering such a rare object so close to Sgr A* would seem to suggest that it is part of a large pulsar population ($N \sim 650$). Given the much lower observed scattering time, why have none of these other pulsars been discovered?

The absence of any other pulsar detections besides J1745−2900 has led Dexter & O'Leary (2013) to claim that there is a missing pulsar problem in the inner parsec ($\theta = 25''$). They suggest that the observed absence of pulsars is real and propose that magnetars are preferentially formed in the Galactic center. However, it remains possible that the lack other detections is simply an observational shortcoming. One example would be if the Galactic center were seen through a heterogeneous scattering region comprised of regions of moderate and hyper-strong scattering. Another possibility is that we do not yet have the sensitivity to strongly constrain the pulsar population. In a re-analysis of previous Galactic center searches, Chennamangalam & Lorimer (2013) find that current observational constraints allow for as many as ∼100 canonical pulsars to exist in the inner parsec. In order to solve the missing pulsar problem, we need to either discover new pulsars in the Galactic center to measure the scattering along new lines of sight or conduct a survey sensitive enough to set meaningful constraints on the pulsar population in the inner parsec.

We have used the Karl G. Jansky Very Large Array (VLA) to conduct the most sensitive search of the Galactic center (to date) for canonical pulsars with $P_{\rm spin} \sim 1$ s. Operating in the fast-visibility mode at 2–4 GHz, we recorded interferometric visibilities every 10 ms. By recording visibilities, we are able to form beams and extract pulsar search data from any sky location in the field of view. Though

constraints set by the VLA correlator restrict it to a fairly coarse time resolution, the beam-forming search provides a advantages for a Galactic center search like reduced background noise and excellent localization for any detections.

In this paper, we describe the methodology and preliminary search of the inner parsec around Sgr A*. In Section 6.2, we outline the basic principles of beamforming. In Section 6.3 we describe the observations. The preliminary processing steps are detailed in Section 6.4. Section 6.5 we present a test of the beamforming on known pulsars in the region. In Section 6.6 we describe the survey of the inner parsec and in Section 6.7 we provide the results. In Section 6.8 we discuss the implications of our search on the pulsar population in the Galactic center and in Section 6.9 we summarize our results and conclusions.

6.2 Beam Forming

Usually, the goal of radio interferometry is to reconstruct a map of the time-averaged brightness of some region of the sky using measurements from two or more telescopes. The time resolution for such observations is set by calibration requirements and is typically several seconds. By decreasing the sampling time down to milliseconds, it becomes possible to use radio interferometric observations to conduct pulsar searches. Here, we briefly review interferometric observations and describe how they can be used for pulsar searches.

6.2.1 Visibilities

Unlike single dish radio telescopes that measure the electric field at one point in the sky, radio interferometric arrays measure the spatial coherence function of the electric field. The spatial coherence function (typically called the visibility function) is defined as the time-averaged correlation between the electric field measured at two points in the observing plane,

$$V_\nu(\mathbf{r}_1, \mathbf{r}_2) = \langle \mathbf{E}_\nu(\mathbf{r}_1)\mathbf{E}^*_\nu(\mathbf{r}_2)\rangle. \tag{6.1}$$

The visibility function can (under a set of reasonable assumptions) be expressed as the Fourier transform of the sky brightness, so

$$V_\nu(u, v) = \iint I_\nu(\ell, m)e^{-2\pi i(u\ell+vm)}d\ell dm, \tag{6.2}$$

where $I_\nu(\ell, m)$ is the sky brightness as a function of the directional cosines (ℓ, m) and the visibility function is expressed in terms of positional coordinates (u, v) in units of wavelength. By inverting Equation 6.2, one can determine the the sky brightness. Thus, the visibility data contain information over a region of the sky instead of just one point as in single dish observations.

In synthesis imaging, all the visibility data are combined and a time-averaged map of they sky brightness is made by inverting Equation 6.2. However, we can also extract time-frequency data from narrow beams within the field of view in a process called beam-forming. It is the beam-forming technique that allows us to conduct a pulsar search within the field of view.

6.2.2 Extracting Pulsar Search Data

The process of extracting pulsar search data by beam-forming mostly follows the same steps as synthesis imaging. First, we invert Equation 6.2

$$I(\ell, m) = \int_{-\infty}^{\infty} \int_{-\infty}^{\infty} V(u, v) e^{2\pi i(u\ell + vm)} du\, dv \tag{6.3}$$

to get the sky brightness, $I(\ell, m)$, in terms of the visibility function $V(u, v)$. Since we are only sampling the visibility function, we actually get the brightness of the "dirty map"

$$I^D(\ell, m) = \int_{-\infty}^{\infty} \int_{-\infty}^{\infty} S(u, v)\, V(u, v) e^{2\pi i(u\ell + vm)} du\, dv \tag{6.4}$$

where the sampling function

$$S(u, v) = \sum_{k=1}^{M} \delta(u - u_k, v - v_k) \tag{6.5}$$

is needed because we are only making visibility measurements at the (u_k, v_k) of the M baselines. The dirty map is the brightness map convolved with the point spread function produced by the Fourier transform of the sampling function.

In synthesis imaging, we calculate the Fourier transform in Equation 6.4 to get a map of $I^D(\ell, m)$ for all (ℓ, m) at the same time. In beam-forming, we instead directly evaluate Equation 6.4 as

$$I^D(\ell, m) = \sum_{k=1}^{M} V(u_k, v_k) e^{2\pi i(u\ell + vm)}, \tag{6.6}$$

which gives the brightness at along each direction (ℓ, m). Since visibilities are recorded per frequency channel and time sample, we can re-write Equation 6.6 to make these dependencies explicit

$$I^D_{\nu t}(\ell, m) = \sum_{k=1}^{M} V(u_{\nu t,k}, v_{\nu t,k}) e^{2\pi i(u_{\nu t}\ell + v_{\nu t} m)}, \tag{6.7}$$

which is exactly the time-frequency data needed to search for pulsars. In order to extract time-frequency data from a beam along the direction to (ℓ, m), we just need to apply the delays to phase up our visibilities along that direction (the exponential term in Equation 6.7), then average the re-phased visibilities.

6.2.3 Benefits

There are a number of benefits to conducting a beam-forming search instead of a single dish or single beam phased-array search. For one, the beam-forming search combines the observational survey speed of a large single dish with the localization of a single-beam phased array search. In the beam-forming search, data are collected over the full field of view accessible to the VLA. At 3 GHz, the FWHM of the VLA primary beam is $\theta_{\mathrm{VLA},3} = 15'$, which gives a sky coverage that is six times larger than the GBT at 2 GHz ($\theta_{\mathrm{GBT},2} = 6'$). The full field of view can be tiled in beams and pulsar data extracted. Any detection will therefore localize a pulsar to a single beam, with a FWHM of arseconds. A single fast-sample interferometric observation for a beam-forming search is essentially equivalent to tens of thousands of single beam phased-array observations. Since the beam-forming data extraction takes place after the observation, it effectively trades observing time for computating time.

The beam-forming search is also much more robust against radio frequency interference (RFI) than other types of searches. Since the time-frequency data in each beam is the combination of correlations between many pairs of telescopes, the effect of RFI in a single telescope is significantly reduced. Furthermore, only astrophysical signals will be localized on the sky, so spurious RFI candidates can be identified and removed if they show up in many non-neighboring beams. A

search that is robust against RFI is particularly important for Galactic center searches because allows for a lower signal-to-noise (S/N) threshold to search for faint pulsars.

The beam-forming search is also much less affected by the high background temperatures in the Galactic center than large sigle dish observations. The single-harmonic detection threshold for a single-dish pulsar search is

$$S_{\rm min,SD} = \beta\,(\mathrm{SEFD} + S_{\rm gc}) \tag{6.8}$$

where $S_{\rm gc}$ is the background flux density and

$$\beta = \frac{(\mathrm{S/N})_{\rm min}}{\sqrt{n_{\rm pol}\Delta\nu T_{\rm obs}}}. \tag{6.9}$$

Large single-dish instruments have low SEFDs ($S_{\rm gc} \gg$ SEFD), so the detection threshold $S_{\rm min,SD} \approx \beta\, S_{\rm gc}$ is completely dominated by the background and increasing the size of the telescope (which lowers the SEFD) would have little effect on the sensitivity. For the beam-forming search, the detection threshold is

$$S_{\rm min,vis} = \beta\,(\mathrm{SEFD} + S_{\rm gc})\, N_{\rm bl}^{-\frac{1}{2}}, \tag{6.10}$$

where SEFD $\approx$ 300 Jy for a single VLA antenna at 3 GHz and $N_{\rm bl} = 351$ is the number of baselines. A conservative estimate of the flux in a VLA primary beam at the GC is $S_{\rm gc} \sim 700$ Jy, which makes SEFD + $S_{\rm gc} \approx 4S_{\rm Sgr}$, giving a sensitivity of $S_{\rm min,vis} = 4\beta S_{\rm Sgr}/\sqrt{N_{\rm bl}}$. All else being equal, a visibility search is $\sqrt{N_{\rm bl}}/4 \approx 4.7$ times more sensitive than single-dish searches. The beam-forming search is thus particularly well-suited for finding pulsars in the Galactic center.

6.3 Observations

We observed the Galactic center on three consecutive days in May 2016 (May 11–13, MJD 57519–21) for a total of 7 hours. All three observations were conducted at 2–4 GHz, recording data in two polarizations (RR, LL) with 512×4 MHz frequency channels and a time resolution of 10 ms. The array was in the CnB configuration, which gives a naturally weighted beam with a major axis size of $\theta_{\rm maj} \approx 7''$ at 3 GHz. Each 140 minute observation consisted of a short scan on the flux density calibrator 3C286 followed by a series of alternating 16 minute scans of Sgr A* with 2 minute scans of the phase-calibrator J1751−2524.

In order to record full interferometric visibilities on millisecond time scales, we used the new fast-sample visibility observing mode available with the VLA. The frequency and time resolutions available in this mode are ultimately limited by the 285 MB s^{-1} ($\approx$1 TB hr^{-1}) throughput limit of the VLA correlator (Law et al. 2012). For two polarizations (RR, LL) and the largest available channel size (2 MHz) available for the 2–4 GHz receiver, time samples can be no smaller than 20 ms to meet the correlator throughput limit. We were able to double the size of the channels to 4 MHz by averaging the data before sending it through the correlator, which allowed for the time resolution to be halved down to 10 ms. Since the dispersive smearing of a pulse across a 4 MHz channel at 2 GHz and a nominal Galactic center dispersion measure of DM = 2000 pc cm^{-3} is

$$\tau_{\rm DM,ch} = 8.3 \text{ ms } \left(\frac{\Delta\nu}{4 \text{ MHz}}\right) \left(\frac{\nu}{2 \text{ GHz}}\right)^{-3} \left(\frac{\rm DM}{2000 \text{ pc cm}^{-3}}\right), \tag{6.11}$$

any additional expansion of the frequency channel width to reduce the time resolution would be counter-productive.

6.4 Processing

Each observation produces a very large data set that needs to be calibrated, flagged, and model-subtracted. After these preliminary steps, pulsar search data can be extracted from a tiling of beams covering the desired search area. Each of these processing steps are done using existing tools from the Common Astronomy Software Applications (CASA; McMullin et al. 2007b) package and custom python code.

6.4.1 Calibration, Imaging, and Model Subraction

The result of each observation is a 2.5 TB visibility data set in CASA Measurement Set (MS) format. Before anything else can be done, we first need to determine the complex gain (phase and amplitude) calibrations for the visibility data. Phase and amplitude corrections are relatively slow varying, so we first time-average the data from 10 ms to 3 s sample times. This coarse time resolution data set is 300 time smaller than the original full resolution data set, which makes calibration and imaging much easier. After time-averaging the data set, we use CASA task `gencal` on the coarse time resolution data set to produce a set of calibration tables. The calibration tables can be applied to both the coarse and full resolution data sets using the CASA task `applycal`.

Next, we can make a map of the sky brightness using the calibrated coarse time resolution data set. We use the CASA task `clean` to bin and Fourier transform the visibilities and to deconvolve the resulting image using the CLEAN algorithm. The result of the imaging process is shown in Figure 6.1.

By using the CLEAN algorithm to deconvolve our image, we also produce a noise-less model of the sky brightness. Calculating the inverse Fourier transform of this model gives the model visibilities. By subtracting the model visibilities from our data visibilities, we can subtract out a lot of the structures that would produce artifacts in the pulsar search data as sidelobes sweep in and out of different beams. We use the CASA task `ft` to calculate the model visibilities from the coarse time resolution sky model and subtract these visibilities from the full resolution visibilities using the task `uvsub`. We now have a calibrated and model-subtracted full time resolution data set and are ready to extract pulsar search data.

6.4.2 Extract Pulsar Search Data

The next step is to extract time-frequency pulsar search data from the calibrated and model-subtractted full resolution visibility data. In order to extract time-frequency data at a point along direction (ℓ, m), we need to calculate

$$I^D_{\nu t}(\ell, m) = \sum_{k=1}^{M} V(u_{\nu t,k}, v_{\nu t,k}) e^{i\phi}, \tag{6.12}$$

where $V(u_{\nu t,k}, v_{\nu t,k})$ is the measured visibility at time t, frequency channel ν, and baseline k, and

$$\phi = 2\pi \left(u_{\nu t}\ell + v_{\nu t}m\right), \tag{6.13}$$

is the phase delay at (ℓ, m) relative to the phase center.

We have created custom python software to perform the pulsar data extraction. We use the `pwkit` package (Williams et al. 2017) to run CASA routines inside python. The CASA routines are used to read the visibility data from the Measurement Set data files. Phase corrections are applied and the data are summed. The output intensity data are written to file in PSRFITS format. At the end of the

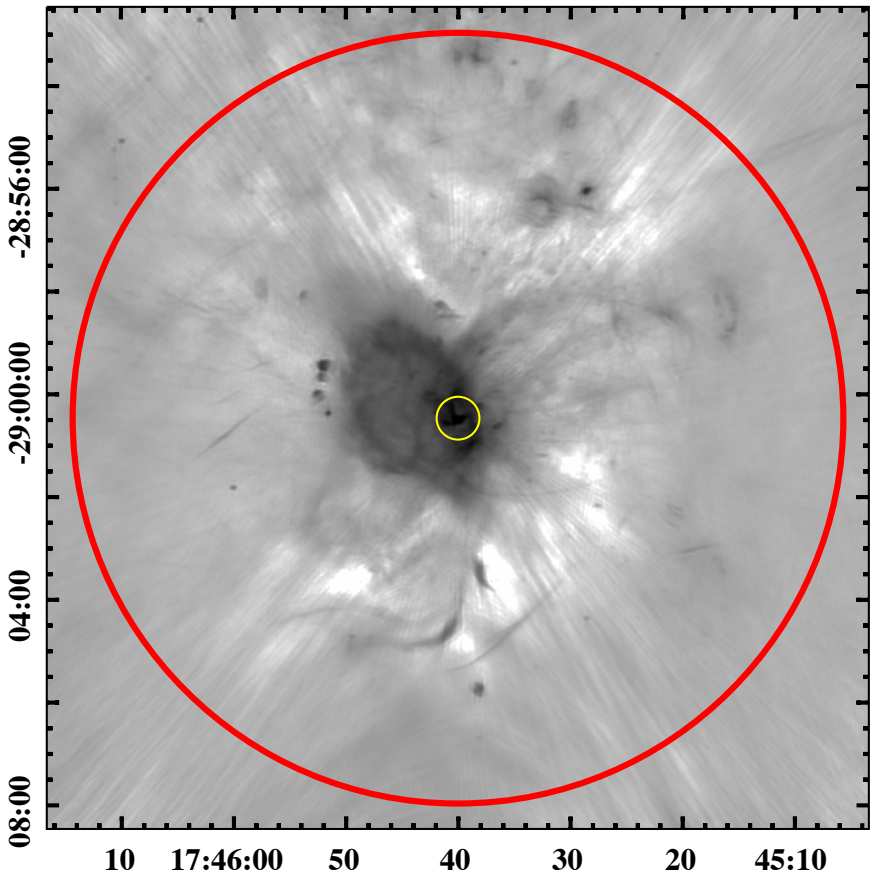

Figure 6.1: **Image of the Galactic center from data collected during the first observation**. The red circle has a diameter of $\theta = 15'$ and represents the FWHM sensitivity of the VLA antennas at 3 GHz. The yellow circle has a diameter of $\theta = 50''$ and represents the survey region searched in this paper. The colorbar has a logarithmic spacing. Many of the familiar structures of the GC are clearly visible, including Sgr A West, Sgr A East, and a number of supernova remnants and nonthermal radio filaments.

processing stage, we have produced PSRFITS files containing pulsar search data for each beam in the survey.

6.5 Known Pulsars within 15′ of Sgr A*

As a test of our processing pipeline, we conducted a targeted search to see if we could detect the six previously discovered pulsars within 15′ of Sgr A*. With the exception of the magnetar J1745−2900, all the other pulsars are separated from Sgr A* by $10 - 15'$ (Figure 6.2. Since the FWHM sensitivity of the VLA primary beam extends only 7′.5 from Sgr A*, the sensitivity to these pulsars is significantly diminished. Using a model of the VLA primary beam at 3 GHz (Perley, EVLA Memo 195), we calculate the beam attenuation for each of these pulsars.

Figure 6.3 shows a sensitivity curve for the beam-forming search of the Galactic center. Each of the six pulsars within 15′ of Sgr A* is shown. The magnetar J1745−2900 is very near to the pointing center, so will not show any attenuation. However, for the other five pulsars include both the reported flux density and the apparent flux density accounting for beam attenuation. Of the six pulsars, we would expect only to be able to detect J1745−2900, J1745−2856, and J1746−2850.

We clearly detect J1745−2900 (S/N $\approx$ 850) with the most significant detection occurring in the beam containing the known position of the magnetar. Figure 6.4 shows a collection of 100 beams with color indicating the significance of the detection in each beam. There are spokes of higher detection significance emanating from the known position. These spokes trace out the sidelobes in the PSF of the array. Figure 6.5 shows the detection significance in each beam as a function of distance from the known pulsar position. Even though the magnetar can be localized to one beam (max significance), it also will show up in many neighboring beams because it is strong enough to be detected in sidelobes.

We marginally detect J1745−2856 (S/N $\approx$ 4), but the detection improves if we

only consider the lowest 200 MHz of the band (S/N $\approx$ 16). The spectral index of J1745−2856 is fairly steep ($\alpha = -2.8$), but this is not enough to account for the dramatic drop-off with frequency (Schnitzeler et al. 2016). Instead, it is likely due to the fact that the pulsar is at the very edge of the primary beam. The size of the beam scales as $\theta \propto \nu^{-1}$, so only the lowest frequencies are included.

Besides J1745−2900 and J1745−2856, we do not detect any other of the known pulsars in the Galactic center. Of the remaining four, only J1746−2850 was expected to be detected from our survey. However, the non-detection of J1746−2850 is not too surprising because it is known to have intermittent emission, dimming by a factor of at least 10 for ∼years (Dexter et al. 2017).

6.6 Search for Pulsars within 1 pc of Sgr A*

Using the first of three 140 minute observations of the Galactic center at 2–4 GHz, we conducted a beamforming search for radio pulsars within 25″ (1 pc at 8.3 kpc) of Sgr A*. We extract time-frequency data from all beams and search each for both periodic signals and single pulses. Candidates from all beams are then compared to remove spurious signals and a final candidate list is produced. The details of each of these searches are provided here.

6.6.1 Beam Tiling

In order to search the inner parsec for radio pulsars, we need to extract time-frequency search data from beams tiling the region of interest. The choice of beam tiling will depend on the size of synthesized beam and the maximum sensitivity

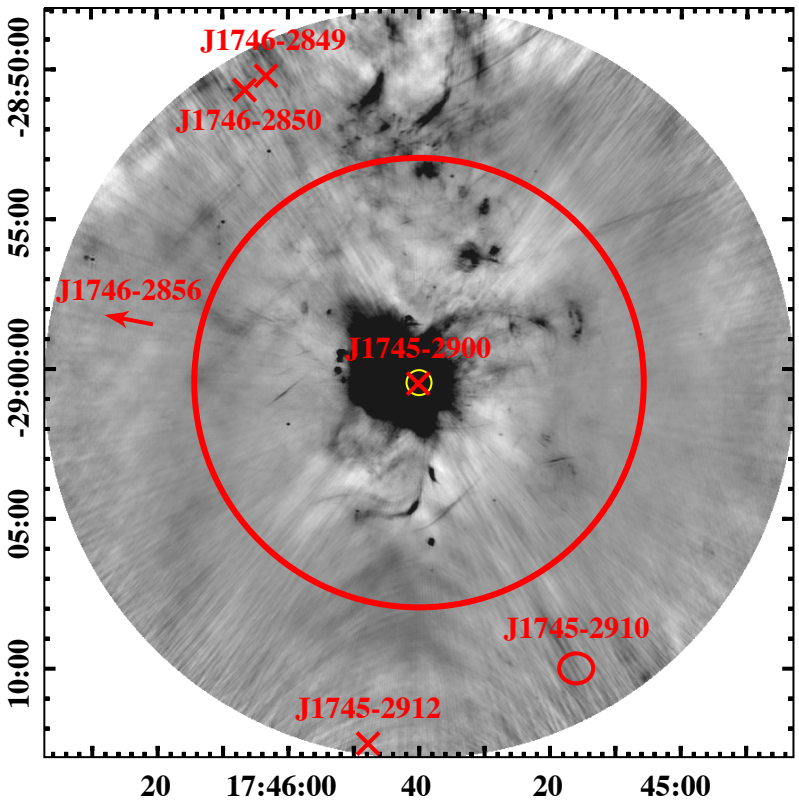

Figure 6.2: **Image of the Galactic center showing extendend structure**. A linear color stretch from -10 mJy to +10 mJy is used to show the extended structures. Note that the base of the Arched Filaments HII region is shown at the top of the field. Also included are the positions of the known radio pulsars (J1756−2856 falls just out of view). The red and yellow circles are the same as in Figure 6.1 and have diameters of $\theta = 15'$ and $\theta = 50''$, respectively.

loss that is acceptable in the survey. The synthesized beam is essentially the point spread function of the array. The naturally weighted synthesized beam for our observation has a half-power ellipse with shape $\theta_{\rm synth} \approx 7'' \times 5''$.

We tile the region as a close packing of circles with diameters of $\theta_{\rm b} = 3''$. The furthest point from the center of any beam is then $\Delta\theta = \theta_{\rm b}/(2\sqrt{3})$. Approximating the synthesized beam sensitivity pattern as an elliptical gaussian with minor axis

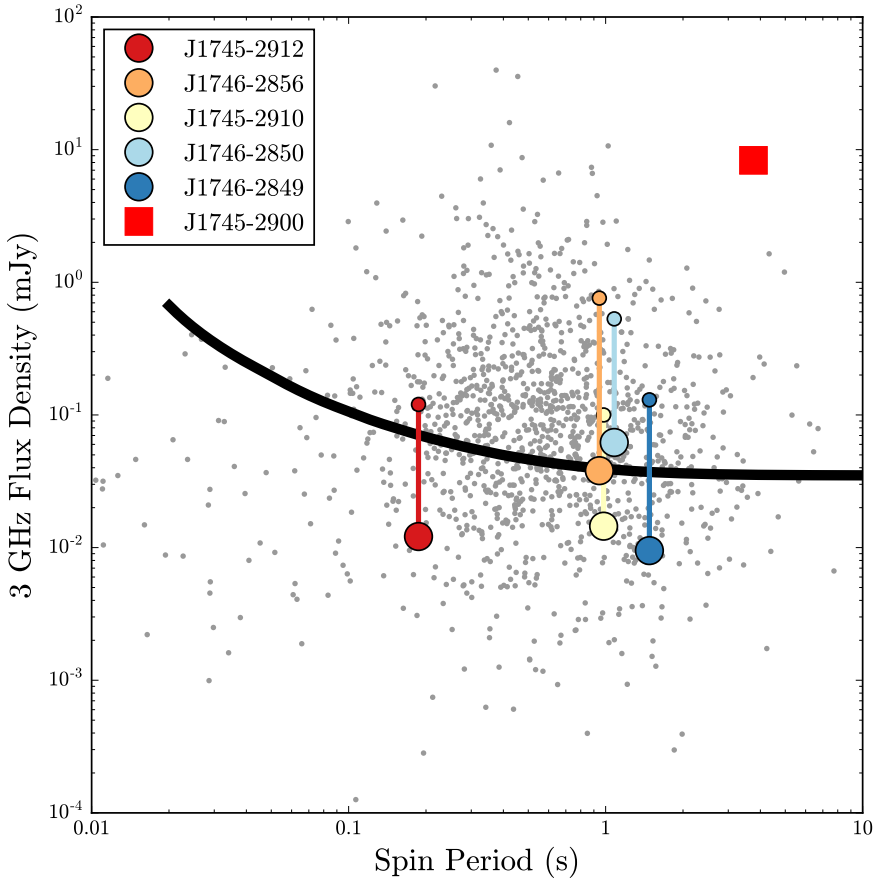

Figure 6.3: **Predicted 10σ sensitivity curve for our 2-4 GHz beam-forming search with the VLA**. This curve (black line) assumes a scattering time of $\tau_{\rm sc} = 1300$ ms $\nu_{\rm GHz}^{-4}$. The grey dots give the period and (approximate) 3 GHz flux density of known Galactic pulsars if they were placed at the Galactic center. The 3 GHz flux density is calculated for pulsars in the ATNF catalog with reported 1.4 GHz pseudo-luminosities using a distance of 8.5 kpc ($S = L/D^2$) and a spectral index ($S \propto \nu^{\alpha}$) of $\alpha = -1.6$. The flux densities of the known pulsars within $15'$ of Sgr A* are also shown as two connected markers. The smaller marker gives the known flux density of the pulsar and the larger marker gives the apparent flux density of the pulsar after accounting for beam attenuation. The red square gives the apparent flux density of the magnetar J1745−2900.

of $5''$, this means that the worst attenuation caused by an offset from a beam center reduces the apparent flux by a factor of ≈ 0.72. The 300 beam tiling of the inner parsec is shown in Figure 6.6.

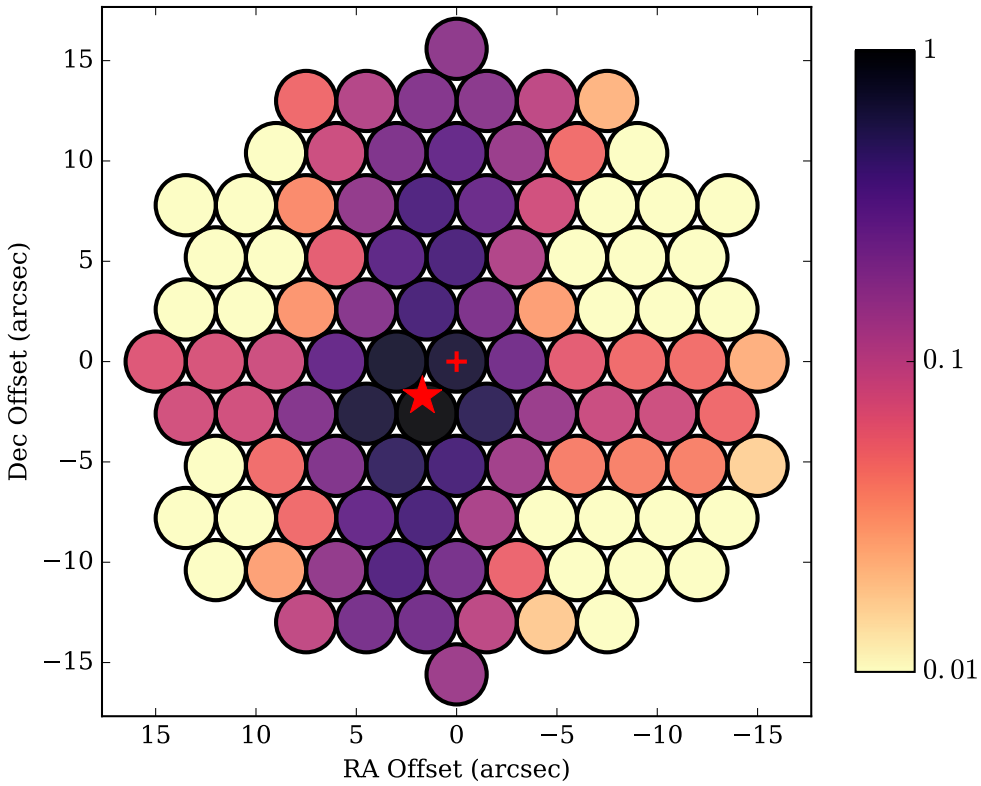

Figure 6.4: **S/N of magnetar in each beam**. Scaled S/N of the profile formed by folding the data from each beam with the magnetar period and DM. The position of the magnetar is indicated by a red star and Sgr A* by a red cross. The max SNR profile comes from the beam closest to the known position of the magnetar. The regions of high SNR trace out the PSF.

6.6.2 Beam-forming and Flagging

Using custom software, we extract pulsar search data from the calibrated and model-subtracted visibilities with the procedure described in Section 6.4. The channelized time series intensity data extracted from each beam is then written to file in the standard PSRFITS data format. With the data in PSRFITS format, we can use the PRESTO[2] pulsar processing package for RFI flagging and de-dispersion (Ransom 2001).

[2]http://www.cv.nrao.edu/~sransom/presto/

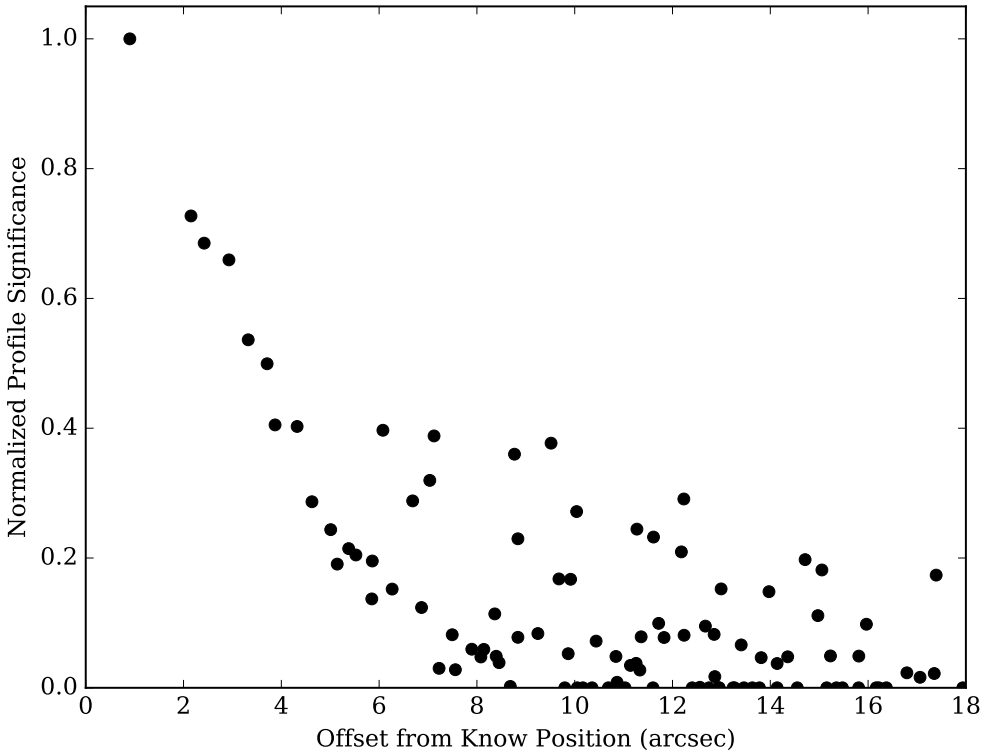

Figure 6.5: **S/N of magnetar as a function of phased beam location**. As in Figure 6.4, we calculate the normalized SNR of the profile formed by folding the data from each beam with the magnetar period and DM. This is then plotted against the distance of the center of each beam from the known position of the magnetar.

Because it was produced from interferometric visibilities, the pulsar search data produced for each beam are much less affected by RFI than typical single dish data. However, we still need to do some flagging to remove sections of data that were corrupted by RFI. We use the PRESTO routine `rfifind`, which analyzes the data in small time-frequency chunks to identify statistical outliers and produces a mask to exclude this data in subsequent steps. We run `rfifind` on the data sets extracted from each of the 300 beams in the survey.

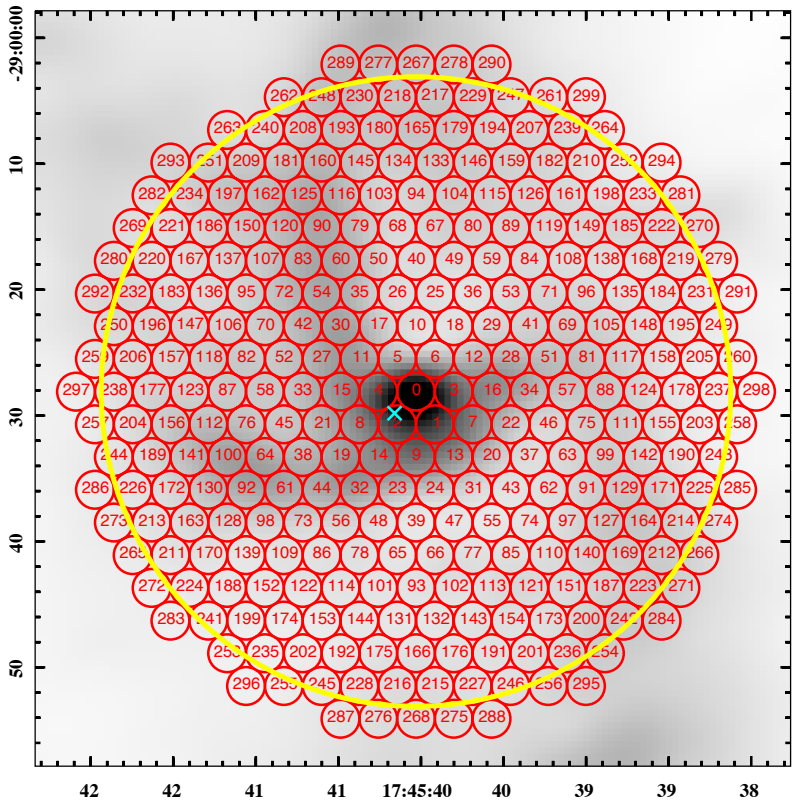

Figure 6.6: **Tiling for beam-forming search**. Galactic center search tiling of 300 beams with diameters of $\theta_b = 3''$ (naturally weighted PSF has a full-width half-power ellipse of $\theta \approx 5'' \times 7''$). The location of the magnetar is marked with a cyan "x". The yellow circle has a radius of $25''$, which corresponds roughly to 1 parsec at 8.3 kpc.

6.6.3 De-dispersion

De-dispersion is the process of removing the frequency-dependent delays caused by the propagation of a radio signal through the cold electron plasma in the interstellar medium. The delay relative to some reference frequency ν_0 is given by

$$\tau_{\rm DM} = 4.15 \text{ ms } \left(\nu_{\rm GHz}^{-2} - \nu_{0,\rm GHz}^{-2}\right) \left(\frac{\rm DM}{1 \text{ pc cm}^{-3}}\right) \tag{6.14}$$

and can be calculated exactly for known DM. Since we do not know the DM of an undiscovered pulsar, we need to search over a number of trial DM values.

We de-disperse the data at 250 trial DM values from DM $= 0 - 5000$ pc cm^{-3} in steps of ΔDM $= 20$ pc cm^{-3} using the PRESTO routine `prepsubband`. This range comfortably includes the expected DM $= 2000$ pc cm^{-3} at the Galactic center. The step size was chosen so that the maximum DM error (δDM $= 10$ pc cm^{-3}) will only produce a small smearing time of

$$\tau_{\delta\mathrm{DM}} = 7.8 \text{ ms } \left(\frac{\delta\mathrm{DM}}{10 \text{ pc cm}^{-3}} \right), \tag{6.15}$$

which is less than the 10 ms sampling time. The de-dispersion step produces 250 de-dispersed time series for each beam that can be searched for periodic signals and single pulses.

6.6.4 Periodicity Search

We perform a Fourier domain search for periodic signals in each of the 300 beams. For each beam, the Fourier transform of each de-dispersed time series is calculated. Pulsar pulses can be very narrow (which produces many harmonics in the spectrum), so harmonics are optimally summed before evaluating candidates.

We also perform an acceleration search using the PRESTO routine `accelsearch`. The acceleration search is a simple method for searching for pulsars in relatively long period orbits. It approximates the orbit with one parameter (the acceleration) that produces a constant shift in the observed spin frequency over the course of the observation. The acceleration search technique is sensitive to systems with orbital periods much longer than the observing time ($P_{\mathrm{orb}} \gtrsim 20\ T_{\mathrm{obs}}$).

Candidates from each of these searches are collected from each of the 300 beams in the search. Since astrophysical sources should only show up in (at most) a few contiguous beams, we determine duplicate candidates and flag those that show up in too many beams. This greatly reduces the number of candidates that then need to be folded and examined by eye.

6.6.5 Single Pulse Search

In addition to a search for periodic signals, we also conduct a search for single pulses. This is particularly important for the Galactic center because even fairly bright pulsars can be missed in acceleration searches if they are in tight binaries with other stars or even with the black hole. We use the PRESTO single pulse search code, which is a simple implementation of the (Cordes & McLaughlin 2003) matched-filter technique. Simple box-car templates of various widths are cross-correlated with the data to detect candidates.

We run the single pulse search separately on each of the 300 beams and then remove duplicates that show up in many disparate beams. The magnetar J1745−2900 is very bright and many of its pulses are detected in almost every beam. To filter these out, we identify all the pulses in the beam containing the magnetar (Beam 0002), and then exclude a small window around those times in all other beams. This reduces the total number of candidates to a number that can easily be examined by eye.

6.7 Results

We clearly detect the magnetar J1745−2900 in both a periodicity and single pulse search, but do not detect any other pulsars.

6.7.1 Periodicity Search

Over all 300 beams, we find a total of 7844 candidates above a detection threshold of $(S/N)_{det} = 3$. After removing duplicates and harmonics, we are left with 149 unique candidates. Diagnostic plots are made showing the folded profile and dynamic spectrum for each of these candidates. The diagnostic plots are examined by eye to determine which if any of the candidates are real. The magnetar J1745−2900 is clearly detected in this blind search out to about 30 harmonics (Figure 6.7), but no other convincing candidates are found. There are ≈ 10 marginal candidates that are promising, but are too weak to be classified as detections. Processing the data from the next two days will be important for following up on these candidates.

6.7.2 Single Pulse Search

In the single pulse search, candidates are found for each of the 250 de-dispersed time series in each of the 300 beams. For a detection threshold of $(S/N)_{det} = 5$, this gives over 25 million pulse candidates. Obviously, we need to do a fair amount of filtering to get down to a reasonable number of candidates that we can plot and examine by eye.

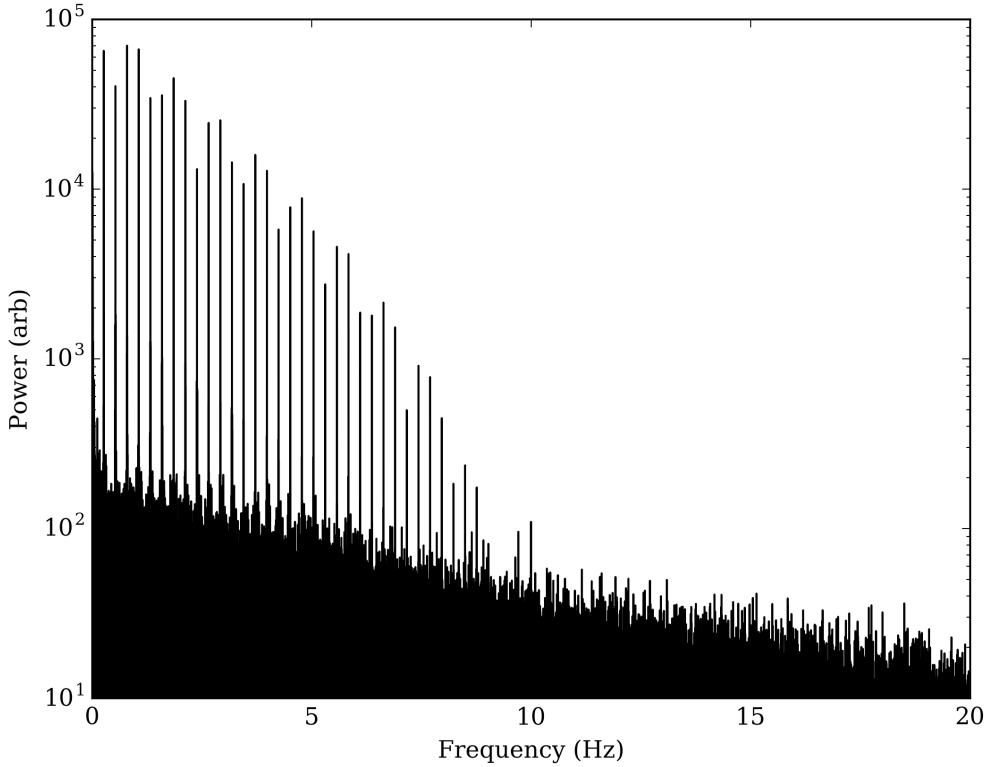

Figure 6.7: **Power spectrum for J1745–2900 detection in Beam0002**. This power spectrum was generated from time series data de-dispersed at DM = 1760 pc cm^{-3}. The magnetar is clearly detected out to about 30 harmonics. An RFI signal is present at 10 Hz.

The first stage of the filtering is to identify all of the pulses from the magnetar J1745−2900. We identify all of the pulses at the known dispersion measure (DM = 1780 pc cm^{-3}) and location (Beam0002) of the magnetar. We remove all candidates that occur within a 1 second window (roughly the disperive lag time across the band) around any of the detected magnetar pulses. After filtering out the candidates within windows around each J1745−2900 pulse, there are 2.2×10^5 remaining candidates.

The next stage of filtering seeks to remove duplicate pulses that show up in multiple beams or multiple trial DMs. Taking all of the 2.2×10^5 remaining candidates, we identify the highest S/N candidate in each 1 second of the observation.

This will remove the duplicate candidates that show up from RFI in many beams and will also return the maximum S/N pulse from a real astrophysical source that may be strong enough to be detected in multiple trial DMs. This reduces the total number of candidates down to 2.8×10^4.

The final filtering stage removes candidates arising from narrow-band RFI signals. Following Spitler et al. (2012), we calculate the spectral modulation index of each pulse candidate and remove from consideration pulses that are narrow-band. This process reduces the total number of candidates down to about 2000. Diagnostic plots are made for all 2000 of these pulses showing they dynamic spectrum of the pulse as well as the de-dedispersed pulse profile. To avoid contamination by any pulse from J1745−2900, we also plot the de-dispersed time series of the magnetar beam (Beam0002) at the same time.

6.8 Discussion

The non-detections in both the periodicity and single pulse searches allow us to set limits on the number of certain types of pulsars in the inner parsec (projected) around Sgr A*. It is important to note that we were only sensitive to certain types of systems. The periodicity search was sensitive to relatively long period pulsars $P \sim 1$ s that were either isolated or in wide binaries ($P_{\rm orb} \gtrsim 50$ hr). Pulsars that have millisecond spin periods or orbital periods less than a day would be missed by this type of search. In principle, these pulsars could be detected in the single pulse search if they emit giant pulses. We calculate the limits set by these non-detections and discuss the implications on the missing pulsar problem.

6.8.1 Population Limits

Since no pulsars were detected in the periodicity searches of the inner parsec, we can set an upper limit to the number of pulsars that could exist in this region. For pulsars with spin periods $P_{\rm spin} \gtrsim 1$ s, the 10σ detection limit of our survey was $S_{\rm det} = 40$ μJy at 3 GHz. As shown in Figure 6.3, this sensitivity is sufficient to find nearly half of all currently detected Galactic pulsars if they were placed in the Galactic center. However, currently known pulsars are a biased sample (brighter pulsars are easier to find), so instead we want to use the intrinsic (instead of observed) luminosity distribution.

Faucher-Giguère & Kaspi (2006) compared a simulated pulsar population to known observations and found that the underlying pseudoluminosities ($L = Sd^2$) were best described by a lognormal distribution. The best fit mean and standard deviation for the logarithm of the 1.4 GHz pseudoluminosity were found to be $\mu_{\log L} = -2.5$ and $\sigma_{\log L} = 2.1$ (with pseudoluminosity L in units of mJy kpc^2). Using this distribution, we can calculate the detection probability from the complement of the cumulative distribution function as

$$F(S_{\rm det,1.4}) = \frac{1}{2}\left[1 - {\rm erf}\left(\frac{\log(S_{\rm det,1.4}d^2) - \mu_{\log L}}{\sqrt{2}\sigma_{\log L}}\right)\right], \tag{6.16}$$

where $S_{\rm det,1.4}$ is the minimum detectable flux density at 1.4 GHz and $d = 8.3$ kpc is the distance to the Galactic center. We can scale our 3 GHz flux density limit to 1.4 GHz by using a typical pulsar spectral index $\alpha = -1.6$ ($S_\nu = S_0\nu^\alpha$), so $S_{\rm det,1.4} = 0.135$ mJy. From Equation 6.16, this gives a detection probability of $p(S_{\rm det,1.4}) = 0.01$.

Given the probability of detecting a pulsar, we can set a limit on the total population that would be consistent with zero detections. The detection of a

pulsar can be represented as a Bernoulli process with probability of success give by $p_{\rm det} = F(S_{\rm det,1.4})$. The probability distribution of the total number of pulsars (N) given zero detections $n = 0$ and detection probability $p_{\rm det}$ is

$$p(N \mid n = 0, p_{\rm det}) = p_{\rm det} \left(1 - p_{\rm det}\right)^N . \tag{6.17}$$

From this distribution, we calculate the 68% (99.7%) upper limit to be $N =$ 112 (557) pulsars with $P \sim 1$ s and $P_{\rm orb} \gtrsim 50$ hr in the inner parsec around Sgr A*.

6.8.2 Single Pulse Limits

Our periodicity search is insensitive to fast-spinning pulsars and systems with short orbital periods, but the single pulse search is completely unaffected by these effects. The single pulse search thus offers an opportunity to discover a potentially exotic pulsar system in the Galactic center. However, the great distance to the Galactic center means that pulses will have to be bright to be detected.

The sensitivity of a single pulse search is given by

$$S_{\rm sp,det} = \frac{({\rm S/N})_{\rm min} T_{\rm sys}}{G\sqrt{N_{\rm pol} \Delta\nu W}} \tag{6.18}$$

where $({\rm S/N})_{\rm det} = 5$ is the detection S/N, $T_{\rm sys} \approx 100$ K is the system temperature (both antenna and sky contributions), $G = 2.7$ K Jy^{-1} is the effective gain of the array (with 25 antennas), $N_{\rm pol} = 2$ is the number of summed polarizations, $\Delta\nu = 2$ GHz is the bandwidth, and W is the width of the pulse. For a pulse with $W = 20$ ms (consistent with scattering at 3 GHz), the minimum detectable pulse flux density is

$$S_{\rm sp,det} = 20 \text{ mJy } \left(\frac{\rm S/N}{5}\right) \left(\frac{W}{20 \text{ ms}}\right)^{-1/2} . \tag{6.19}$$

An obvious test of this search would be to see if it could detect giant pulses from the Crab pulsar if placed at the Galactic center. Cordes et al. (2004) conducted a multi-frequency study of giant pulses from the Crab pulsar using Arecibo. One of the frequencies they observed at was 2.8 GHz, which should be comparable to our observations. In about 1 hour of observing, the brightest pulse seen by Cordes et al. (2004) had a peak flux density of about $S_{\rm a,pk} \approx 74$ Jy and a width of $W_{\rm a} \approx 0.1$ ms. If such a pulse were emitted at the Galactic center, the flux would be reduced by a factor of $(8.3 \text{ kpc}/2 \text{ kpc})^{-2}$ because of the increased distance. The pulse would also be smeared out to a width of about $W \approx 20$ ms due to scattering, which would reduce the peak flux density by a factor of $(W/W_{\rm a})$. After accounting for these two effects, an equivalent pulse emitted by a Crab-like pulsar in the Galactic center would have a peak flux density of

$$S_{\rm gc,pk} \approx 20 \text{ mJy } \left(\frac{\rm W}{20 \text{ ms}}\right)^{-1/2}. \tag{6.20}$$

The brightest giant pulse seen in a 1 hour observation of the Crab pulsar would just barely be detectable by this survey. Since the flux distribution of Crab giant pulses is a long-tailed power law, brighter pulses will be seen in longer observations.

6.8.3 Implications for the Missing Pulsar Problem

One of the primary goals of conducting this search was to determine whether there is a missing pulsar problem in the Galactic center. While the characterization of the pulsar population in the inner $10'$ or so will need to wait for future processing of these observations, we can start to put meaningful constraints on the population in the inner parsec. The beamforming search presented here is the most sensitive search ever conducted for $P \sim 1$ s radio pulsars in the inner parsec of the Galactic

center. The absence of any new detections allows us to set upper limits on the number of these types of pulsars at $N = 112$ (557) at the 68% (99.7%) confidence level. The single pulse search puts a modest constraint on the existence of Crab-like pulsars in the Galaictic center since it would have been able to detect only the very brightest giant pulses.

Chennamangalam & Lorimer (2013) have argued that the detection of only a single radio-emitting magnetar and no other pulsars is not necessarily inconsistent with the demographics of the Galactic pulsar population. Using the Faucher-Giguère & Kaspi (2006) log-normal pseudoluminosity distribution instead of the observed pseudoluminosity distribution, they find that the non-detections of previous surveys are consistent with a population of hundreds of pulsars in the inner parsec. The limits produced by our survey are largely consistent with these results, however they are constraining enough to introduce some tension with a model assuming the Galactic center population is demographically similar to that of the Galactic plane. Of the $\approx$ 2600 currently discovered pulsars in the Galaxy, only four are radio-emitting magnetars. Assuming a similar population in the Galactic center, this would suggest at least 650 pulsars in a population associated with J1745−2900.

There are a number of ways to remove the tension between the number of expected pulsars and our limits. For one, it could be that magnetars are preferentially produced in the Galactic center (Dexter & O'Leary 2013). Of course, this does not necessarily mean that magnetars are exclusively produced, just that there is some preferential formation channel compared to the Galactic plane. Another possibility is that pulsars in the Galactic center are more likely to be in tight binaries than pulsars in the Galactic plane. This could naturally arise from a higher probability

interactions in the high stellar density environment of the inner parsec. If these pulsars are in orbits shorter than about 50 hours, our one-parameter acceleration search would be insufficient to find them. Finally, the possibility remains that the scattering screen along the line of sight to the Galactic center is heterogeneous and pulsars are being hid behind regions of greatly increased scattering.

Though there are still several viable explanations for the possible tension between the number of observed and predicted pulsars in the inner parsec, future work with the data set described in this paper could help differentiate between them. Two particularly promising approaches would be higher dimensional orbital searching and more sophisticated single pulse searches. Employing searches over more than one orbital parameter would allow us to search for pulsars in tighter orbits. Since the data from each beam is relatively small given the coarse time resolution, this could allow for computationally intensive searches that might be impractical with typical high resolution pulsar data. More sophisticated single pulse searches also present an excellent opportunity to find Crab-like pulsars in the Galactic center. Since we are just at the threshold of detecting Crab-like giant pulses, it is very important that we maximize our sensitivity to these types of pulses. The discovery of a Crab-like pulsar in the Galactic center would provide another line of sight to probe the scattering and would greatly constrain pulsar formation mechanisms around Sgr A*.

6.9 Conclusions

Using the VLA in its fast-sample visibility mode, we have conducted the deepest search for $P \sim 1$ s pulsars in the inner parsec around Sgr A*. We clearly

detect the radio-emitting magnetar J1745−2900 in both a periodicity search and in single pulses, but we do not detect any new pulsars or transients. We set an upper limit on the total number of pulsars ($P \sim 1$ s, $P_{\rm orb} \gtrsim 50$ hr) of $N = 112$ (557) at the 68% (99.7%) confidence level. We set a single pulse limit of $S_{\rm max} = 20$ mJy (W/20 ms)$^{-1/2}$, which is roughly comparable with the brightest Crab giant pulses at these frequencies. These limits are in tension with the population inferred from the existence of the rare radio-emitting magnetar J1745−2900. Future work with this data set include searching for pulsars in the inner $10'$ of the Galactic center and to conducting more sophisticated searches of the inner parsec.

CHAPTER 7

DIRECT LOCALIZATION OF A FAST RADIO BURST AND ITS ENIGMATIC COUNTERPART[1]

7.1 Introduction

Fast radio bursts (Lorimer et al. 2007; Thornton et al. 2013) (FRBs) are astronomical radio flashes of unknown physical nature with durations of milliseconds. Their dispersive arrival times suggest an extragalactic origin and imply radio luminosities orders of magnitude larger than any other kind of known short-duration radio transient (Cordes & Wasserman 2016). Thus far, all FRBs have been detected with large single-dish telescopes with arcminute localizations, and attempts at counterpart identification have relied on contemporaneous variability of field sources (Keane et al. 2016) or the presence of peculiar field stars (Loeb et al. 2014) or galaxies (Keane et al. 2016). These have not resulted in an unambiguous association (Williams & Berger 2016; Vedantham et al. 2016) with a host or multi-wavelength counterpart. Here we report the sub-arcsecond localization of FRB 121102, the only known repeating burst source (Spitler et al. 2014b, 2016; Scholz et al. 2016; Petroff et al. 2015), using high-time-resolution radio interferometric observations that directly image the bursts themselves. Our precise localization reveals that FRB 121102 lies within 100 milliarcseconds of a $\sim$180 μJy persistent radio source having a continuum spectrum consistent with non-thermal emission, and a faint ($r_{\rm AB} = 25.1 \pm 0.1$ mag) optical counterpart. The persistent radio source flux density varies by tens of percent on day timescales, and very long baseline radio interferometry yields an angular size less than 1.7 milliarcseconds. Our observations are

[1]Previously Published: Chatterjee, S., Law, C. J., Wharton, R. S., et al. 2017, *Nature*, 541, 58

inconsistent with a Galactic origin or a prominent star-forming galaxy. Instead, the source appears to be co-located with a low-luminosity active galactic nucleus or a previously unknown type of extragalactic source. Localization and identification of a host or counterpart has been essential to understanding the origins and the physics of any kind of transient event, including gamma-ray bursts (Metzger et al. 1997; Bloom et al. 2002) and tidal disruption events (Gezari et al. 2006). However, the faintness of the radio and optical counterparts to FRB 121102 imply that, to the extent that it is representative, direct sub-arcsecond localizations of FRBs may be the only way to provide reliable associations.

7.2 Burst Detection

The repetition of bursts from FRB 121102 (Spitler et al. 2016; Scholz et al. 2016) enabled a targeted interferometric localization campaign with the Karl G. Jansky Very Large Array (VLA) in concert with single-dish observations using the 305-m William E. Gordon Telescope at the Arecibo Observatory. We searched for bursts in VLA data with 5-ms sampling using both beam-forming and imaging techniques (Law et al. 2015). In over 83 hr of VLA observations distributed over six months, we detected nine bursts from FRB 121102 in the 2.5–3.5 GHz band with signal-to-noise ratios ranging from 10 to 150, all at a consistent sky position. These bursts were initially detected with real-time de-dispersed imaging and confirmed by a beam-formed search (Figure 7.1). From these detections, the average J2000 position of the burst source is right ascension $\alpha = 05^{\rm h}31^{\rm m}58.70^{\rm s}$, declination $\delta = +33°08'52.5''$, with an uncertainty of $\sim 0.1''$, consistent with the Arecibo localization (Spitler et al. 2016) but with three orders of magnitude better precision. The dispersion measure (DM) for each burst is consistent with the previously

reported value (Spitler et al. 2016) of 558.1±3.3 pc cm^{-3}, with comparable DM uncertainties. Three bursts detected at the VLA (2.5–3.5 GHz) had simultaneous coverage at Arecibo (1.1–1.7 GHz). After accounting for dispersion delay and light travel time, one burst is detected at both telescopes (Table 7.1), but the other two show no emission in the Arecibo band, implying frequency structure at ∼1 GHz scales. This provides new constraints on the broadband burst spectra, which previously have shown highly variable structure across the Arecibo band (Spitler et al. 2014b, 2016; Scholz et al. 2016).

7.3 Radio Continuum Source

Radio images at 3 GHz produced by integrating the VLA fast-sampled data reveal a continuum source within 0.1″ of the burst position, which we refer to hereafter as the persistent source. A cumulative 3 GHz image (RMS ∼2 μJy; Figure 7.2) shows 68 other sources within a 5′ radius, with a median flux density of 26 μJy. Given the match between burst positions and the continuum counterpart, we estimate a probability $< 10^{-5}$ of chance coincidence. The persistent source is detected in follow-up VLA observations over the entire frequency range from 1 to 26 GHz. The radio spectrum is broadly consistent with non-thermal emission, though with significant deviation from a single power-law spectrum. Imaging at 3 GHz over the campaign shows that the persistent source exhibits $\sim 10\%$ variability on day timescales (Figure 7.2). Variability in faint radio sources is common (Williams & Berger 2016; Vedantham et al. 2016); of the 69 sources within a 5′ radius, nine (including the persistent counterpart) were significantly variable (see Methods). There is no apparent correlation between VLA detections of bursts from FRB 121102 and the flux density of the counterpart at that epoch (Figure 7.2, and

Methods).

Observations with the European VLBI Network and the Very Long Baseline Array detect the persistent source and limit its size to < 1.7 milliarcseconds (see Methods). The lower limit on the brightness temperature is $T_b > 8 \times 10^6$ K. The source has an integrated flux density consistent with that inferred at lower resolution in contemporaneous VLA imaging, indicating the absence of any significant flux on scales larger than a few milliarcseconds.

7.4 Multiwavelength Counterparts

We have searched for counterparts at submillimeter, infrared, optical, and X-ray wavelengths using archival data and a series of new observations. A coincident unresolved optical source is detected in archival 2014 Keck data ($R_{\rm AB} = 24.9 \pm 0.1$ mag) and recently obtained Gemini data ($r_{\rm AB} = 25.1 \pm 0.1$; Figure 7.2), with a chance coincidence probability $< 3.5 \times 10^{-4}$ (see Methods). The source is undetected in archival infrared observations, in ALMA 230 GHz observations, and in *XMM-Newton* and *Chandra* X-ray imaging (see Methods). The spectral energy distribution of the persistent source is compared in Figure 7.3 to some example spectra for known source types, none of which matches our observations well.

7.5 Discussion

The observations reported here corroborate the strong arguments (Scholz et al. 2016) against a Galactic location for the source. While stellar radio flares can exhibit swept-frequency radio bursts on sub-second timescales (Maoz et al. 2015),

they do not strictly adhere to the ν^{-2} dispersion law seen for FRB 121102 (Spitler et al. 2016; Scholz et al. 2016), nor are they expected to show constant apparent DM. The sizable DM excess, 3× the Galactic maximum predicted by the NE2001 electron-density model (Cordes & Lazio 2002), is not revealed as a HII region, a supernova remnant, or a pulsar-wind nebula in our Galaxy that would appear extended at radio, infrared, or Hα (Scholz et al. 2016) wavelengths. Spitzer mid-infrared limits constrain sub-stellar objects with temperatures > 900 K to be at distances of 70 pc or greater, and the Gemini detection sets a minimum distance of $\sim$1 kpc and 100 kpc for stars with effective temperatures greater than 3000 K and 5000 K, respectively, ruling out Galactic stars that could plausibly account for the DM and produce the radio continuum counterpart. We conclude that FRB 121102 and its persistent counterpart do not correspond to any known class of Galactic source.

The simplest interpretation is that the burst source resides in a host galaxy which also contains the persistent radio counterpart. If so, the DM of the burst source has contributions from the electron density in the Milky Way disk and halo (Cordes & Lazio 2002), the intergalactic medium (IGM, Inoue 2004), and the host galaxy. We estimate $\mathrm{DM_{IGM}} = \mathrm{DM} - \mathrm{DM_{NE2001}} - \mathrm{DM_{halo}} - \mathrm{DM_{host}} \approx 340$ pc cm^{-3} $-\mathrm{DM_{host}}$ with $\mathrm{DM_{NE2001}} = 188$ pc cm^{-3} and $\mathrm{DM_{halo}} \approx 30$ pc cm^{-3}. The maximum redshift, for $\mathrm{DM_{host}} = 0$, is $z_{\mathrm{FRB}} \lesssim 0.32$, corresponding to a maximum luminosity distance of 1.7 Gpc. Variance in the mapping of DM to redshift ($\sigma_z = \sigma_{\mathrm{DM}}(dz/d\mathrm{DM}) \approx 0.1$, McQuinn 2014) increases the upper bound to $z \sim 0.42$. Alternatively, a sizable host galaxy contribution could imply a low redshift and a negligible contribution from the IGM, although no such galaxy is apparent. Hereafter we adopt $z_{\mathrm{FRB}} \lesssim 0.32$.

The faint optical detection and the non-detection at 230 GHz with ALMA imply a low star formation rate from any host galaxy. For our ALMA 3σ upper limit of 51 μJy and a sub-mm spectral index of 4, we estimate the star formation rate (Carilli & Yun 1999) to be less than 0.06 to 19 $M_\odot$ yr^{-1} for redshifts z ranging from 0.01 to 0.32 (luminosity distances of 43 Mpc to 1.7 Gpc), respectively. The implied absolute magnitude ~ -16 at $z = 0.32$ is similar to that of the Small Magellanic Cloud, whose mass $\sim 10^9$ $M_\odot$would comprise an upper limit on the host galaxy mass.

The compactness of the persistent radio source ($\lesssim$8 pc for $z \lesssim 0.32$) implies that it does not correspond to emission from an extended galaxy or a star forming region (Condon 1992), although our brightness temperature limits do not require the emission to be coherent. Its size and spectrum appear consistent with a low-luminosity active galactic nucleus (AGN) but X-ray limits do not support this interpretation. Young extragalactic supernova remnants (Lonsdale et al. 2006) can have brightness temperatures in excess of 10^7 K but they typically have simple power-law spectra and exhibit stronger variability.

The burst source and persistent source have a projected separation $\lesssim$500 pc if $z \lesssim 0.32$. There are three broad interpretations of their relationship. First, they may be unrelated objects harboured in a host galaxy, such as a neutron star (or other compact object) and an AGN. Alternatively, the two objects may interact, e.g., producing repeated bursts from a neutron star very close to an AGN (Pen & Connor 2015; Cordes & Wasserman 2016; Lyubarsky 2014). A third possibility is that they are a single source. This could involve unprecedented bursts from an AGN (Romero et al. 2016) along with persistent synchrotron radiation; or persistent emission might comprise high-rate bursts too weak to detect individually,

with bright detectable bursts forming a long tail of the amplitude distribution. In this interpretation the difficulty in establishing any periodicity in the observed bursts (Spitler et al. 2016; Scholz et al. 2016) may result from irregular beaming from a rotating compact object or extreme spin or orbital dynamics. The Crab pulsar and some millisecond pulsars display bimodality (Lundgren et al. 1995; Kinkhabwala & Thorsett 2000) in giant and regular pulses. However, they show well-defined periodicities and have steep spectra inconsistent with the spectrum of the persistent source that extends to at least 25 GHz. Magnetars show broad spectra that extend beyond 100 GHz in a few cases but differ from the roll-off of the persistent source spectrum.

All things considered, we cannot favor any one of these interpretations. Future comparison of spectra from the persistent source and from individual bursts could rule out the 'single source' interpretation. The proximity of the two sources and their physical relationship can be probed by detecting a burst in VLBI observations or by using interstellar scintillations, which can resolve separations less than 1 milliarcsecond.

If other FRBs are similar to FRB 121102, our discovery implies that direct subarcsecond localizations of bursts are so far the only secure way to find associations. The unremarkable nature of the counterparts to FRB 121102 suggests that efforts to identify other FRB counterparts in large error boxes will be difficult, and given the lack of correlation between the variability of the persistent source and the bursts, rapid post-FRB follow-up imaging in general may not be fruitful.

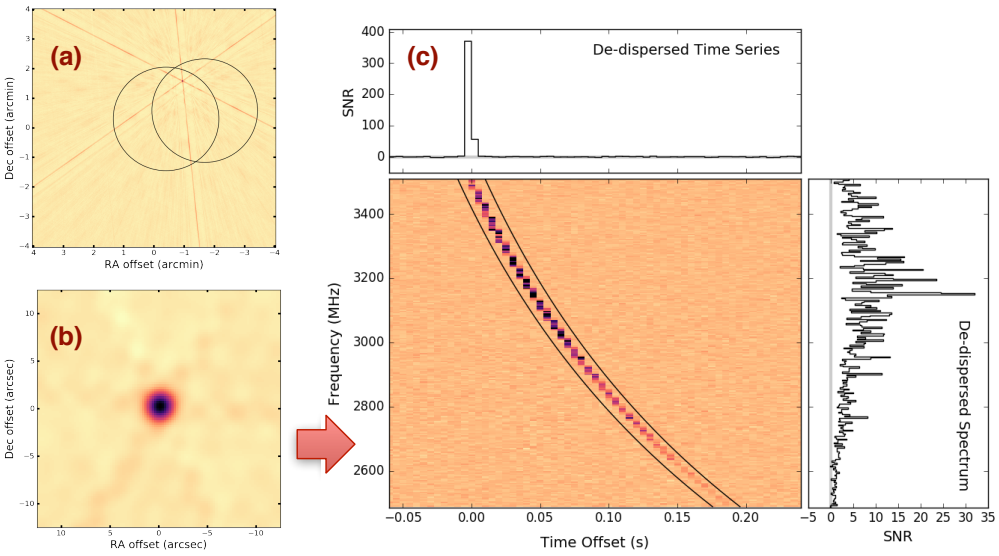

Figure 7.1: **VLA detection of FRB 121102**. (a) A 5-ms dispersion-corrected dirty image shows a burst from FRB 121102 at MJD 57633.67986367 (2016 Sep 02). The approximate localization uncertainty (3′ beam FWHM) from previous Arecibo detections (Spitler et al. 2016) is shown with overlapping circles. (b) A zoomed in portion of the above image, de-convolved and re-centered on the detection, showing the ∼0.1″ localization of the burst. (c) Time-frequency data extracted from phased VLA visibilities at the burst location shows the ν^{-2} dispersive sweep of the burst. The solid black lines illustrate the expected sweep for DM= 558 pc cm^{-3}. The de-dispersed lightcurve and spectra are projected to the upper and right panels, respectively.

7.6 Methods

7.6.1 Observation strategy

Detection and precise localization of an FRB requires ∼arcsecond angular resolution, ∼millisecond time resolution, and ∼MHz frequency resolution. In November 2015, we conducted 10 hours of fast dump (5 ms) observations of the FRB 121102 field with the VLA (Scholz et al. 2016) at 1.6 GHz, with no burst detections. In April–May 2016, we observed for 40 hours at 3 GHz, and again detected no bursts

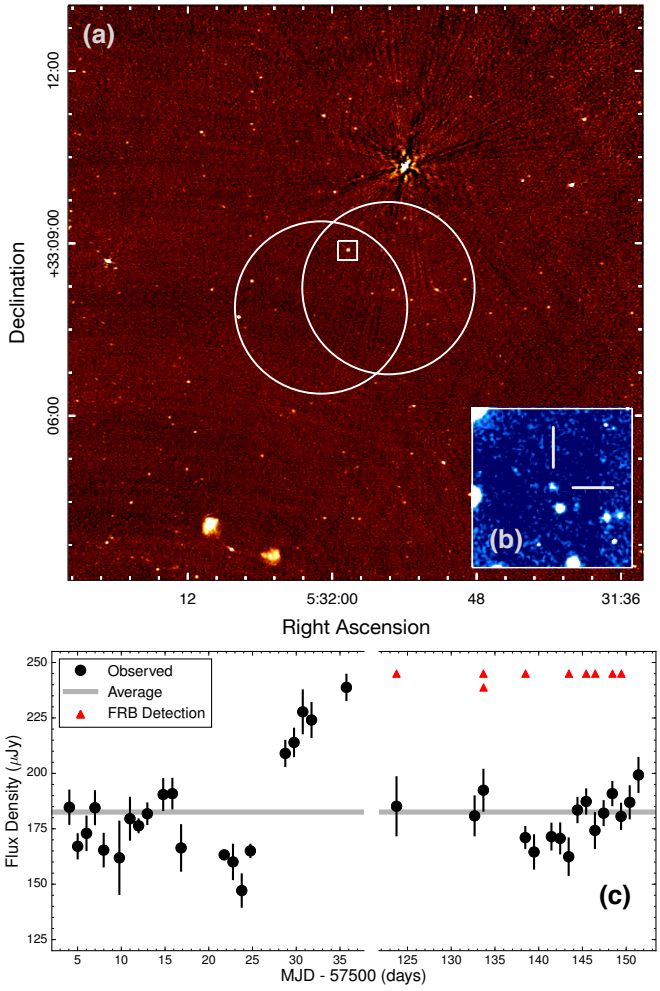

Figure 7.2: **Radio and optical images of the FRB 121102 field**. (a) VLA image at 3 GHz with a combination of array configurations. The image resolution is $2''$ and the RMS is $\sigma = 2$ μJy beam^{-1}. The Arecibo detection (Spitler et al. 2016) uncertainty regions ($3'$ beam FWHM) are indicated with overlapping white circles. The radio counterpart of the bursts detected at the VLA is highlighted with a $20''$ white square within the overlap region. (b) Gemini r-band image of the $20''$ square shows an optical counterpart ($r_{\rm AB} = 25.1 \pm 0.1$ mag), as identified by the $5''$ bars. (c) The lightcurve of the persistent radio source coincident with FRB 121102 over the course of the VLA campaign, indicating variability on timescales shorter than 1 day. Error bars are 1σ. The average source flux density of $\sim$180 μJy is marked, and the epochs at which bursts were detected at the VLA are indicated (red triangles). The variability of the persistent radio counterpart is uncorrelated with the detection of bursts (see Methods).

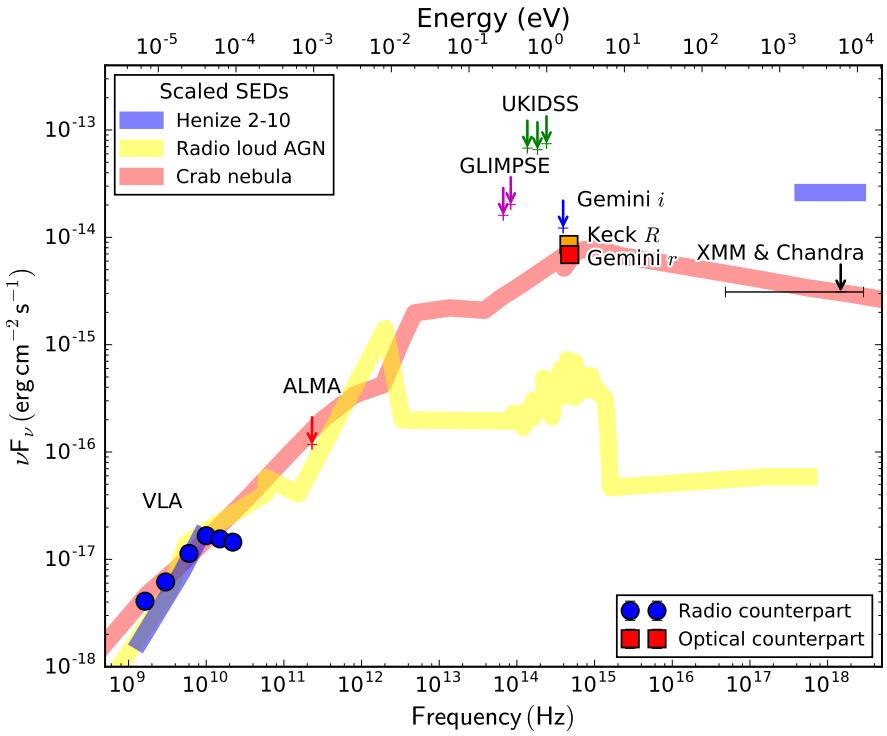

Figure 7.3: **Broadband spectral energy distribution (SED) of the counterpart**. Detections of the persistent radio source (blue circles), the optical counterpart (squares) and 5σ upper limits at various frequency bands (inverted arrows) are shown; see Methods for details. SEDs of other radio point sources are scaled to match the radio flux density at 10 GHz and overlaid for comparison: (Blue) Low luminosity AGN in Henize 2-10, a star-forming dwarf Galaxy (Reines & Deller 2012) placed at 25 Mpc; (Yellow) radio loud AGN QSO 2128−123 (Elvis et al. 1994) scaled by $10^{-4.3}$ to simulate a lower luminosity AGN and placed at 3 Gpc, and (Red) the Crab nebula (Bühler & Blandford 2014) at 4 Mpc.

with either our fast imaging or beam-forming pipeline (described below). Detections of FRB 121102 with the 305-m Arecibo telescope (Spitler et al. 2016; Scholz et al. 2016) suggested that VLA detections might be sensitivity limited, leading us to conduct a simultaneous observing campaign where Arecibo would identify a burst in the time domain and contemporaneous VLA observations would precisely localize it. In practice, this proved to be unnecessary for VLA detection, but it

provided a wider frequency band to characterize the burst spectra.

7.6.2 Arecibo observations

Arecibo observations used the L-wide receiver, which provides a frequency range of $1.15 - 1.73$ GHz. The PUPPI pulsar backend recorded full Stokes polarization information, with time and frequency resolutions of 10.24 μs and 1.5625 MHz, respectively. Each frequency channel was coherently dedispersed to 557 pc cm^{-3}, thereby eliminating intra-channel dispersion smearing.

7.6.3 VLA fast-dump observations.

The VLA fast-sampled interferometric data were recorded with 5 ms integration time, 256 channels, and bandwidth 1024 MHz centred at 3 GHz. We first detected FRB 121102 on 2016 August 23 with a signal-to-noise ratio S/N$\sim$35. Through 2016 September, we continued coordinated Arecibo and VLA observations, detecting another 8 bursts at the same location and DM. In total, we acquired $\sim$83 hrs of fast-dump interferometric observations in three sessions: 2015 November (Scholz et al. 2016) at 1.6 GHz, 2016 April-May at 3 GHz, and 2016 August-September at 3 GHz with some observing at 6 GHz.

7.6.4 Millisecond imaging with fast-dump visibility data

During the coordinated campaign, all bursts were detected with real-time analysis within hours of the data being recorded by the *realfast* (Law et al. 2015) system at

the VLA. The real-time processing system de-dispersed visibilities to a small range of values centred on DM = 557.0 pc cm^{-3}. For each integration and DM value, the pipeline formed a Stokes I image on time scales from 5 to 80 ms and saved images with peak S/N greater than 7.4, a threshold based on the known false positive rate due to thermal noise.

All candidates were re-analyzed offline with improved calibration, data cleaning, and refined localization using both custom, Python-based software and CASA. We calibrated and imaged de-dispersed visibilities with a typical sensitivity (1σ) of 5 mJy in 5 ms. Table 7.1 lists burst properties, and the brightest detection is shown in Figure 7.1. By fitting a model of the synthesized beam to an image of the burst, we measure burst locations with statistical errors better than $0.3''$. However, the locations are affected by systematic errors at the level of about 1% of the synthesized beam sizes, a modest effect that is evident when comparing the localizations of the first four VLA burst detections (beam sizes $\sim 2.5'' \times\ 2''$) with the last five (beam sizes $\sim 1.3'' \times\ 0.8''$). Using just the last five burst centroids (with lower residual systematics due to the narrower beam), we find that the burst locations are consistent with the persistent radio continuum conterpart centroid (Table 7.3 and Figure 7.4). The radio continuum counterpart location is measured from the error-weighted mean of the location measured in deep imaging from 1 to 26 GHz (see below). The error in the offset is calculated from the quadrature sum of errors in each burst and the counterpart.

7.6.5 Beam-forming analysis with fast-dump visibility data

Beam-forming is complementary to millisecond imaging: instead of de-dispersing interferometric visibilities and searching for bursts in the image domain, the vis-

ibilities are summed with appropriate phasing to produce time-frequency data that can be searched for dispersed bursts. For the VLA observations, the calibration tables generated from time-averaged data (see below) were applied to the fast-dump visibility data, and custom Python software and existing CASA tools were used to extract time-frequency data per beam from a tiling of synthesized beams covering the search region. The time-frequency data from each beam were then written to PSRFITS format and run through a single pulse search pipeline that used PRESTO pulsar processing tools. Single pulse candidates from all the synthesized beams were jointly filtered to remove candidates that occurred simultaneously in many beams, as well as candidates that were narrow-band, as these were likely caused by radio frequency interference. Diagnostic plots for the remaining candidates were examined by eye for bursts. The beam-forming pipeline was used to independently verify the times and positions of each of the VLA detected bursts. For the example shown in Figure 7.1, the instrumental time resolution for the observations (5 ms) is much larger than both the intrinsic pulse width and the intra-channel DM smearing, leading to a pixelated appearance.

7.6.6 VLA imaging observations of the persistent counterpart

The 3 GHz VLA fast-dump observations were also averaged down to lower time resolution, calibrated using the standard VLA pipeline procedures with CASA (McMullin et al. 2007a), and imaged at each epoch. Once the persistent counterpart to FRB 121102 had been identified, we used these per-epoch images to construct the light curve of the source, as well as a deep average image of the sky (Figure 7.2 and Table 7.2). The variability of the persistent radio counterpart is

uncorrelated with the detection of bursts; the point biserial correlation coefficient between the detection (or not) of a burst and the flux density of the counterpart is $r = -0.054$, which would be exceeded by chance $\sim$75% of the time. Of the 69 sources detected within a $5'$ radius, nine (including the persistent counterpart) showed significant variability, as measured by $\chi^2_r = 1/(N-1)\ \Sigma_t (S_t - \bar{S})^2/\sigma_t^2 > 5.0$, where S_t is the source flux density and σ_t the image RMS at epoch t, and $\bar{S}$ is the epoch-averaged flux density.

We also acquired VLA imaging data covering a contiguous frequency range from 1 to 26 GHz. These observations utilized six separate receivers on the VLA: L- (1-2 GHz); S- (2-4 GHz); C- (4-8 GHz); X- (8-12 GHz); Ku- (12-18 GHz); and K-band (18-26 GHz). Observations were carried out on 2016 September 6 and 9, when the VLA was in the B-configuration, with maximum spacing between antennas of roughly 11 km (on September 9, a few antennas had been moved to their A-configuration locations). A third epoch was observed on September 28, only at C-band, with the VLA in the most extended A-configuration. Visibilities were dumped every 2 seconds, with channels of width either 1 or 2 MHz (depending on band). Calibration of the flux density scale was done using an observation of 3C 48 at all bands (Perley & Butler 2013), and the secondary calibrator J0555+3948 was used to monitor complex gain (amplitude and phase) fluctuations as a function of time throughout each of the observations. Standard calibration was done with the VLA calibration pipeline, and subsequent imaging done in both CASA and AIPS. Final flux densities were estimated by a number of techniques to provide a cross-check, including *imfit* in CASA, JMFIT in AIPS, summing up CLEAN component flux density, and summing up flux density in the image pixels. Positions were measured using JMFIT. The two epochs (three for C-band) were imaged separately, and results between the two (three) were found to agree to within the

uncertainties (Figure 7.5), so visibility data from the two epochs (three for C-band) were combined together to make final images. Results are reported in Table 7.3 and the measurements are plotted as part of the broad-band SED (Figure 7.3).

7.6.7 Very Long Baseline Interferometry with the European VLBI Network.

The European VLBI Network (EVN) observed at 1.65 GHz in five epochs (2016 February 2, 10–11, 11–12 and 2016 May 24, May 25) for about two hours per session. The array included the 100 m Effelsberg, the 76 m Jodrell Bank, the 32 m Medicina, the 25 m Onsala, the 32 m Torun, the 25 m Westerbork (single dish), and the 305 m Arecibo telescopes. The data were streamed to the EVN Software Correlator (SFXC) at the Joint Institute for VLBI ERIC (JIVE) in Dwingeloo, at a data rate of 1024 Mbit/s (512 Mbit/s for Arecibo) in real-time. The individual station voltages were recorded simultaneously as well. During the first epoch, the ICRF source J0518+3306 was used as a phase-reference calibrator (separation from the field $\sim$2.9°) and observations were alternated between the field (8 minutes) and the calibrator (2 minutes). For subsequent epochs we used J0529+3209 as phase-reference calibrator (separation $\sim$1.1°) since it was proven to be sufficiently bright ($\sim$60 mJy) and compact for the EVN from the first epoch observations.

Following the VLA localization of FRB 121102, we re-correlated all our observations with the phase center at the FRB 121102 position. The data were analyzed with AIPS following standard procedures, and the images were made with the Caltech Difmap package. We did not detect the persistent counterpart during the first epoch due to a combination of technical failures and the distant phase

calibrator. In the subsequent epochs we detected the persistent counterpart as a slightly resolved source with typical peak brightness of about 100 μJy beam^{-1} and integrated flux density of about 200 μJy, and deconvolved source size of about 5 $\times$ 3 milliarcseconds at a position angle of 140°. The naturally-weighted beam size was about 18×2.2 milliarcseconds in all cases, with a major axis position angle of −54°; the noise was 7μJy beam^{-1}. Brightness temperature lower limits from the four successful epochs are 7×10^6 K. (See Figure 7.5 and Table 7.3.)

7.6.8 Very Long Baseline Interferometry with the Very Long Baseline Array

The NRAO Very Long Baseline Array (VLBA) observed on 2016 Sep 09, 16 with 8 hour tracks per epoch. First epoch observations were at $1.392 - 1.680$ GHz, with a synthesized beam size of 11.3 $\times$ 5.0 milliarcseconds at a position angle = 163.7°. Second epoch observations were at $4.852 - 5.076$ GHz (beam size 2.74 $\times$ 1.43 milliarcseconds at a position angle = 174.8°). A total recording bandwidth of 2 Gbps with dual circular polarizations was obtained for each observation. As in the EVN observations, the compact calibrator J0529+3209 was used to provide phase referencing solutions for FRB 121102. Standard interferometric calibrations were applied using AIPS. Images of the field achieved 17 and 12 μJy beam^{-1} RMS at 1.5 and 5.0 GHz, respectively. The persistent counterpart to FRB 121102 was clearly detected in both observations with partially resolved compact structure. At 1.5 GHz, two-dimensional Gaussian deconvolution yields a size of 4.6×3.3 milliarcseconds, while the 5.0 GHz upper limit on the deconvolved size is <1.73 milliarcseconds. Brightness temperature lower limits from the two epochs are 8×10^6 and 3×10^6 K, respectively. (See Figure 7.5 and Table 7.3.)

7.6.9 Atacama Large Millimeter Array observations

The Atacama Large Millimeter and Submillimeter Array (ALMA) observed on 2016 Sep 15, using Band 6 and covering 8 GHz of bandwidth in the range $220-240$ GHz (with 2-MHz channels). We used 38 antennas in the C40-6 configuration, yielding a resolution of $0.32'' \times 0.13''$. Calibration and imaging was provided by the ALMA observatory, and done using CASA via the ALMA pipeline. The image RMS noise level was 17 μJy beam^{-1} and did not reveal any significant sources.

7.6.10 Optical and infrared imaging

We used the following optical imaging data: 630-s Keck R-band image from 2014 November 19, 120-s Gemini i-band image (2016 March 17), and 1250-s Gemini r-band image (2016 October 24 and 25). The data were reduced with a combination of `IRAF`, `IDL` and Python tools. We used the URAT1 catalog (Zacharias et al. 2015) as an astrometric reference frame. The astrometric errors were $< 80-90$ mas (RMS) in all frames. We used the IPHAS photometry (Drew et al. 2005) to measure the zero-point correction for the coadded images. A counterpart to FRB 121102 is detected in archival Keck image at $R_{\rm AB} = 24.9 \pm 0.1$ mag and in Gemini GMOS r-band image at $r_{\rm AB} = 25.1 \pm 0.1$ mag, consistent with being point-like in $0.7''$ seeing. A non-detection in the i-band image yields an upper limit of $i > 24$. The r-band centroid position was measured to be $\alpha = 05^{\rm h}31^{\rm m}58.69^{\rm s}$, $\delta = +33^\circ08'52.51''$ (J2000) with an astrometric error of ≈ 100 mas, consistent with the R-band position. We measure a stellar density of 1.12×10^{-2} arcsec^{-2} for $r_{\rm AB} < 25.1$. Thus, the chance coincidence probability of finding the optical counterpart within a 100 mas radius of the radio position is $< 3.5 \times 10^{-4}$. In regions around the FRB 121102, we derive

an upper limit of $r < 26.2$ AB mag arcsec^{-2} (5 σ) for any diffuse emission from an extended galaxy, ruling out most of the massive ultra-low surface brightness galaxies (van Dokkum et al. 2015). These galaxies are as large as the Milky Way and would have been more than 5″ in diameter if placed at a $z_{DM} = 0.3$. Smoothing the image with a 5″ FWHM Gaussian kernel reveals no significant emission on those scales.

The counterpart is not detected in near and mid-infrared observations from the UKIDSS (Lawrence et al. 2007) and Deep GLIMPSE (Benjamin et al. 2003b; Churchwell et al. 2009b) surveys with upper limits of $J = 19.8$, $H = 19.0$ and $K = 18.0$ for UKIDSS and 17.8 and 17.3 for the GLIMPSE 3.6 and 4.5 μm bands. At the location of FRB 121102, the total V-band absorption, as determined from the COBE/DIRBE dust maps (Schlegel et al. 1998), is 2.42 mag. We use published extinction coefficients (Schlafly & Finkbeiner 2011) to correct for absorption in the other bands. Published zeropoints and effective wavelengths (Bessell et al. 1998; Fukugita et al. 1996; Hewett et al. 2006) and the IRAC Instrument Handbook v2.1.2 were used to obtain the flux density measurements and limits shown in the broadband spectrum of the persistent counterpart (Figure 7.3).

7.6.11 X-ray Imaging with *XMM-Newton* and *Chandra* X-ray Observatory

X-ray observations were done with *XMM-Newton* (IDs 0790180201, 0790180501, 0792382801, and 0792382901) and the *Chandra* X-ray Observatory (ID 18717). The cameras aboard *XMM-Newton* consist of one EPIC-pn (Strüder et al. 2001) and two EPIC-MOS (Turner et al. 2001) CCD arrays. The *Chandra* observation used

the ACIS-S3 detector in TE mode. Two *XMM-Newton* observations occurred in 2016 February–March, before we achieved our precise localization, with pn in Large Window mode and the MOS cameras in Full Frame mode. Two more observations were performed in 2016 September with the pn camera in Small Window mode and the MOS cameras in Timing mode. A 40 ks *Chandra* observation was performed in 2015 November. In the first two *XMM-Newton* observations, the pn data were not usable for imaging FRB 121102 as it was positioned at the edge of a CCD chip. The MOS Timing mode observations are also not usable for imaging purposes. We therefore used 41 ks of pn data from 2016 September and 60 ks of MOS data from 2016 February–March for X-ray imaging.

We used standard tools from the XMM Science Analysis System (SAS) version 14.0, HEASoft version 6.19 and CAIO version 4.7 to reduce the data. The *XMM-Newton* images were mosaicked together using `emosaic` using exposure maps from `eexpmap`. The number of counts in a 18″ and 1″ radius circular region, for *XMM-Newton* and *Chandra*, respectively, centered at the position of FRB 121102 were compared to several randomly selected background regions. No significant deviation from the background was found; the 5σ count rate limits are $< 3 \times 10^{-4}$ counts s^{-1} and $< 2 \times 10^{-4}$ counts s^{-1}. To place a flux limit we assume a photoelectrically absorbed power-law spectrum with a spectral index of $\Gamma = 2$ and $N_{\rm H} = 1.7 \times 10^{22}\,{\rm cm}^{-2}$ (the hydrogen column density implied by the DM–$N_{\rm H}$ relation (He et al. 2013)). Taking into account the telescopes' energy-dependent effective area and Poisson statistics, we place a 5σ limit of $5 \times 10^{-15}\,{\rm erg\,s^{-1}\,cm^{-2}}$ at 0.5–10 keV on an X-ray point source at the location of FRB 121102 using the mosaicked *XMM-Newton* image. Using the same procedure on the *Chandra* image also results in a limit of $5 \times 10^{-15}\,{\rm erg\,s^{-1}\,cm^{-2}}$ at 0.5–10 keV.

7.6.12 Observational constraints on FRB 121102 and its persistent counterpart

Our observations support the conclusion that no Galactic source can explain the observed DM excess. If the compact counterpart contributes the excess DM over the maximum predicted by NE2001 along this line of sight, the requirement that it be optically thin (Scholz et al. 2016) at 1.4 GHz implies a lower limit on its size (L $>$ 0.03 pc), and hence the source distance. The VLBA and EVN compactness limits ($<$ 1.7 mas in any case, ignoring scattering contributions to angular extent) imply a minimum distance $>$ 3.6 Mpc, far beyond our Galaxy. The absence of an X-ray detection constrains an AGN counterpart. The fundamental plane relation (Körding et al. 2006) between radio and X-ray luminosities and the black hole mass predicts that X-ray emission should be detected for black hole systems with $z < 0.32$ and $M_{BH} < 10^9\,M_\odot$. However, not all AGN follow this relationship, including radio-loud AGN and systems with jet-ISM interactions. Radio-loud AGN are likely excluded based on the low radio luminosity $L_R \approx 3 \times 10^{41}$ erg s^{-1} at $z = 0.32$. A $10^6\,M_\odot$ black hole, which is plausible given the $\sim 10^9 M_\odot$ stellar mass upper limit, would have to accrete at $< 10^{-2}$ below the Eddington rate to match the X-ray upper limit. Our observations are also inconsistent with a young radio supernova remnant, which is typically variable on a time scale of months and associated with star formation (Lonsdale et al. 2006).

For a nominal Gpc distance D corresponding to redshifts $z \lesssim 0.3$, the received fluence A_ν from each burst implies a burst energy

$$E_{\rm burst} = 4\pi D^2 (\delta\Omega/4\pi) A_\nu \Delta\nu \approx 10^{38}\,{\rm erg}\,(\delta\Omega/4\pi) D^2_{\rm Gpc} (A_\nu/0.1\ {\rm Jy\ ms}) \Delta\nu_{\rm GHz}.$$

The unknown emission solid angle $\delta\Omega$ could be very small due to relativistic beam-

ing, and together with a distance possibly much smaller than 1 Gpc, could reduce the energy requirement significantly. However, the *total* energy emitted could be larger depending on the duration of the emission in the source frame and other model-dependent details. Either way, the burst energies from FRB 121102 are not inconsistent with those that might be expected from the magnetosphere of a compact object (Cordes & Wasserman 2016).

Date	ΔMJD from 57620.0	ΔRA (s)	RA error (″)	ΔDec (″)	Dec error (″)	Beam size (″, ″)	S/N ratio	VLA flux density (mJy)	AO flux density (mJy)
23 Aug	3.74402686	0.68	0.05	0.65	0.07	2.8 × 2.3	27†	120	–
02 Sep	13.67986367	0.70	0.01	0.48	0.01	2.5 × 2.3	149	670	–
02 Sep	13.69515938	0.70	0.3	0.3	0.3	2.6 × 2.3	7†	25	–
07 Sep	18.49937435	0.71	0.07	0.50	0.07	1.9 × 1.7	13	63	–
12 Sep	23.45730263	0.70	0.01	0.55	0.03	1.9 × 0.9	66	326	–
14 Sep	25.42958602	0.69	0.07	0.54	0.12	1.3 × 0.7	10	39	$\lesssim 10$
15 Sep	26.46600650	0.70	0.05	0.56	0.05	1.2 × 0.7	10†	50	–
17 Sep	28.43691490	0.70	0.03	0.57	0.03	1.3 × 0.8	18	86	$\sim$50
18 Sep	29.45175697	0.70	0.02	0.49	0.02	1.3 × 0.8	34	159	$\lesssim 10$

Table 7.1: **VLA 3 GHz detections of bursts from FRB 121102 and Arecibo constraints**. Dates are all in the year 2016. Position offsets ΔRA and ΔDec are measured from RA = $05^{\rm h}31^{\rm m}58^{\rm s}$, Dec = $+33°08'52''$(J2000). Topocentric burst MJDs are reported as offsets from MJD 57620 and are dedispersed to the top of the VLA band at 3.5 GHz. The flux densities and signal-to-noise ratios are estimated from a 5 ms visibility integration, leading to an underestimate since the burst durations are typically shorter in Arecibo detections. Instantaneous beam sizes are listed. Bursts with simultaneous coverage at Arecibo at 1.4 GHz are indicated with estimated detection peak flux density or 5σ upper limits for non-detections.

† The real-time analysis of events on 23 August, 02 September, and 15 September resulted in detections with S/N ratio of 35, 16, and 16, respectively. These differences are due to different calibration and flagging approaches between the real-time and offline analyses. The real-time analysis does not include flux density scale calibration, so the offline analysis gives the best estimate of their flux density.

Date (in 2016)	MJD	Beam size ($''$, $''$)	Flux density (μJy)	Bursts detected
26 Apr	57504.0565	6.25 × 2.42	184.72 ± 7.97	0
27 Apr	57505.0100	6.33 × 1.98	167.08 ± 5.91	0
28 Apr	57506.0181	6.44 × 1.96	172.93 ± 8.01	0
28 Apr	57506.9871	6.14 × 1.98	184.49 ± 7.90	0
29 Apr	57507.9843	6.12 × 1.98	165.37 ± 7.81	0
01 May	57509.7766	8.21 × 1.89	161.90 ± 16.79	0
02 May	57510.9890	6.44 × 2.02	179.54 ± 9.91	0
03 May	57511.9746	6.29 × 2.02	176.34 ± 3.36	0
04 May	57512.9725	6.29 × 1.95	181.78 ± 5.10	0
06 May	57514.7883	7.12 × 1.96	190.43 ± 7.43	0
07 May	57515.8362	6.23 × 2.00	190.86 ± 7.13	0
08 May	57516.8335	6.19 × 2.03	166.36 ± 10.72	0
13 May	57521.7640	6.83 × 1.95	163.23 ± 2.23	0
14 May	57522.7649	6.78 × 1.95	160.06 ± 8.22	0
15 May	57523.7658	6.61 × 1.95	147.13 ± 7.77	0
16 May	57524.7550	8.31 × 1.94	165.03 ± 3.23	0
20 May	57528.7452	1.79 × 1.58	209.01 ± 6.14	0
21 May	57529.7440	1.80 × 1.60	213.95 ± 6.65	0
22 May	57530.7439	1.76 × 1.60	227.76 ± 10.13	0
23 May	57531.7441	1.78 × 1.60	224.08 ± 8.14	0
27 May	57535.7339	1.77 × 1.60	238.78 ± 6.18	0
23 Aug	57623.7454	2.12 × 1.68	185.15 ± 13.56	1
01 Sep	57632.6730	2.22 × 1.71	180.82 ± 9.24	0
02 Sep	57633.6800	1.83 × 1.66	192.39 ± 9.69	2
07 Sep	57638.4685	1.90 × 0.61	171.03 ± 5.21	1
08 Sep	57639.4684	2.02 × 0.60	164.53 ± 7.96	0
10 Sep	57641.4579	1.52 × 0.59	171.46 ± 6.28	0
11 Sep	57642.4581	1.55 × 0.59	170.65 ± 7.21	0
12 Sep	57643.4272	1.56 × 0.58	162.40 ± 8.72	1
13 Sep	57644.4332	1.04 × 0.54	183.47 ± 5.96	0
14 Sep	57645.4307	1.01 × 0.49	187.32 ± 5.92	1
15 Sep	57646.4280	0.99 × 0.49	174.24 ± 8.38	1
16 Sep	57647.4245	1.01 × 0.48	182.05 ± 5.87	0
17 Sep	57648.4161	1.03 × 0.49	190.88 ± 5.69	1
18 Sep	57649.4162	1.02 × 0.49	180.58 ± 6.16	1
19 Sep	57650.4058	1.07 × 0.51	186.93 ± 7.69	0
20 Sep	57651.4058	1.02 × 0.49	199.29 ± 8.12	0

Table 7.2: **VLA 3 GHz observations of the persistent counterpart to FRB 121102 over time**. Most observations were acquired during array reconfigurations (C→CnB; CnB→B; B→A). Horizontal lines denote changes in array configuration, as indicated by the changes in the synthesized beam size.

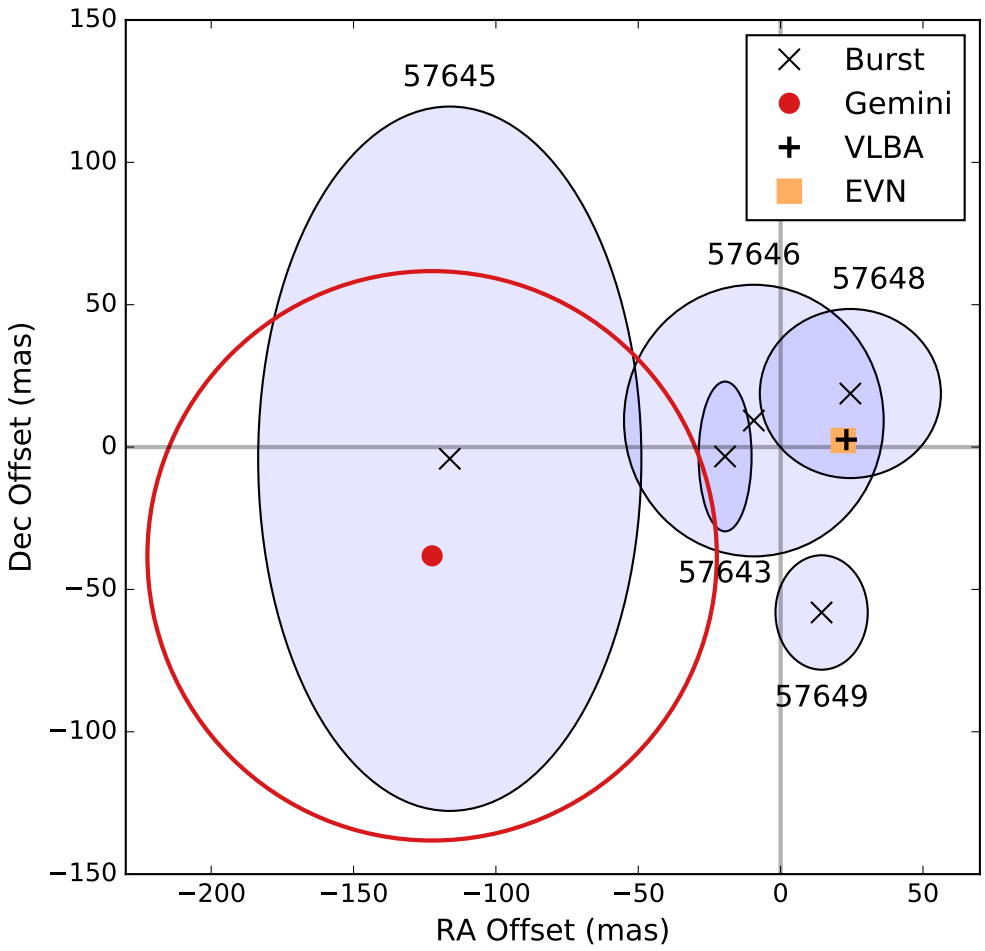

Figure 7.4: **The offset of FRB 121102 from the PRS**. Five bursts detected at the VLA with the highest resolution (A-array, 3 GHz) are plotted, with epoch indicated by MJD values. The (RA, Dec) coordinate difference (burst relative to counterpart) is shown with an ellipse indicating the 1σ error calculated as the quadrature sum of errors in the two sources. VLBA and EVN positions are indicated, with 1σ errors smaller than the symbols. The centroid of the Gemini optical counterpart is shown (red dot) with an estimated 1σ error circle of 100 mas (red) from fitting and radio-optical frame tie uncertainties.

Telescope	Frequency (GHz)	Flux density (μJy)	ΔRA (s)	ΔDec ($''$)
VLA	1.63	250 $\pm$ 39	0.694 $\pm$ 0.018	0.43 $\pm$ 0.26
	3.0	206 $\pm$ 17	0.705 $\pm$ 0.005	0.43 $\pm$ 0.07
	6.0	203 $\pm$ 7	0.701 $\pm$ 0.005	0.54 $\pm$ 0.01
	10.0	166 $\pm$ 9	0.701 $\pm$ 0.001	0.54 $\pm$ 0.02
	15.0	103 $\pm$ 7	0.691 $\pm$ 0.002	0.65 $\pm$ 0.02
	22.0	66 $\pm$ 7	0.699 $\pm$ 0.001	0.56 $\pm$ 0.01
VLA Weighted Average			0.6998 $\pm$ 0.0004	0.548 $\pm$ 0.006
EVN	1.67	200 $\pm$ 20	0.70150 $\pm$ 0.00003	0.5505 $\pm$ 0.0003
VLBA	1.55	218 $\pm$ 38	0.70159 $\pm$ 0.00002	0.5508 $\pm$ 0.0006
	4.98	151 $\pm$ 19	0.701530 $\pm$ 0.000003	0.54952 $\pm$ 0.00009
Gemini			0.69 $\pm$ 0.01	0.51 $\pm$ 0.10

Table 7.3: **Flux density and position measurements of the persistent counterpart to FRB 121102**. Position offsets ΔRA and ΔDec are measured from a nominal RA = $05^{\rm h}31^{\rm m}58^{\rm s}$, Dec = $+33^\circ08'52''$ (J2000). The Gemini r-band detection position is also included. 1-σ errors are quoted in all cases.

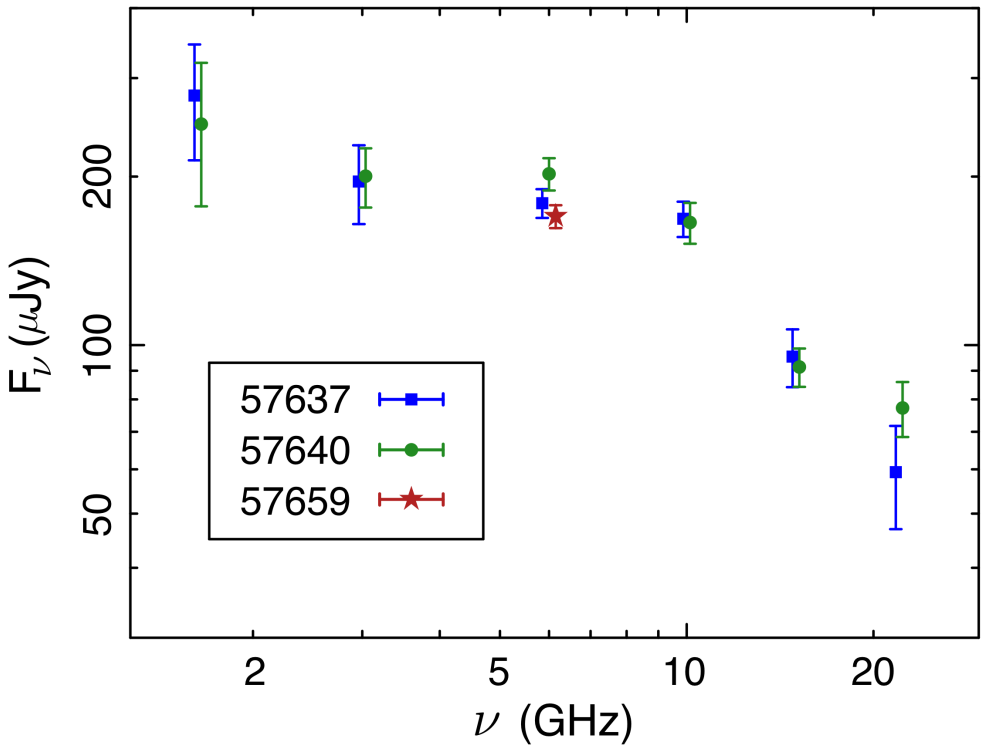

Figure 7.5: **VLA spectrum of the persistent counterpart to FRB 121102**. The integrated flux density is plotted for each epoch of observation (listed by MJD) over a frequency range ν from 1 to 25 GHz. The spectrum is non-thermal and inconsistent with a single power law.

CHAPTER 8

CONCLUSIONS AND FUTURE WORK

At the beginning of the research for this dissertation, we set out to answer two main questions:

1. Why had no pulsars been detected (at the time) within 1 pc from Sgr A*?
2. Can we discover these pulsars with current telescopes?

Each of the chapters presented in this dissertation is motivated by one of these two questions or (in the case of the FRB localization) is made possible by work to this aim. Before presenting our best answers for these questions, let us first summarize the results from each chapter.

In Chapter 2, we set out to determine what limits current observations set on the pulsar population in the Galactic center. Using observations over a wide range of wavelengths from radio to gamma-ray, we found that there could be as many as $\sim$100 canonical and $\sim$1000 millisecond pulsars that are beamed toward Earth residing within a parsec of Sgr A*. One major assumption made in these estimates is that the pulsar population in the Galactic center is similar to that of the Galactic plane. For now it is probably a good assumption, but it may need to be revisited in the future.

In Chapter 3, we explored the distribution of free electrons along the line of sight to the Galactic center. The distribution of free electrons sets the amount of dispersion and scattering in a pulsar signal along that line of sight. Mapping out this distribution allows for future surveys to maximize sensitivity by observing at an optimal observing frequency. In our study, we considered three basic electron

density models. The first was a single scattering of infinite transverse extent located between the observer and the Galactic center. The second model supplemented the single screen of Model 1 with a Galactic component and a uniform Galactic center component. The third model had a highly inhomogenous Galactic center component. Comparing these models with observational data, we found that none satisfies all observational constraints. However, Models 2 and 3 satisfy most, which suggests that the true distribution probably resembles a combination of the two.

In Chapter 4, we conducted a single pulse study of the Galactic center magnetar, J1745–2900. This radio-emitting magnetar was discovered in 2013 (after the results of Chapter 2 were published) and had a pulse broadening time that was three orders of magnitude less than what had previously been expected. In our study, we confirmed the dispersion measure and the scattering time and found them to be consistent with previous results. Additionally, we analyzed the relationship between single pulses emitted from each of the magnetar's evolving profile components.

In Chapter 5, we present the results of a search for pulsars around Sgr A* using the VLA in phased-array mode at 8–12 GHz. The large simultaneous bandwidth and large collecting area of the VLA make this one of the most sensitive searches for pulsars around Sgr A*. We very clearly detect the radio-emitting magnetar J1745–2900 (in fact, we find a pulse at almost every rotation of the neutron star). An acceleration search produces no significant candidates beyond the magnetar.

In Chapter 6, we present the preliminary results of a novel beamforming search for pulsars in the Galactic center at 2–4 GHz with the VLA. We record full interferometric data at 10 ms time samples and use custom software to extract pulsar search data from a tiling of synthesized beams over the survey region. The

beamforming process is computationally intensive, but allows us to produce pulsar search data at any point in the primary beam. As a test case, we presented a search of 300 beams covering the inner parsec. We clearly detect the magnetar, but have yet to find any other significant detections.

Finally, in Chapter 7, we use the fast-sample visibility mode of the VLA to achieve the first sub-arcsecond localization of a Fast Radio Burst. This observing mode and the methods developed in our Galactic center search provide an excellent tool for localizing more FRBs and understanding the nature of this mysterious phenomenon.

At the begining of this work, our best guesses to the initial two questions posed above were that pulsars in the Galactic center were obscured by a hyperstrong scattering screen and detections could be made if observations were conducted with sensitive telescopes at high frequencies (> 10 GHz). Where do we stand now? We know that up to 100 canonical pulsars and up to 1000 millisecond pulsars could potentially reside in the inner parsec. The existence of a rare radio-emitting magnetar near Sgr A* is consistent with a population of several hundred pulsars (assuming Galactic demographics). However, the much smaller pulse broadening time of J1745–2900 means that (at least along some lines of sight) a hyperstrong scattering screen cannot be the only reason other pulsars have not yet been discovered. There are plenty of other ways to hide pulsars, though. The high stellar density of the Galactic center over-produce binary pulsars in orbits shorter than a day. Even bright pulsars could be missed this way in acceleration searches of several hour observations. Of course, it is always possible that the pulsars in the Galactic center (however many there are) are just too faint.

Putting this all together gives us a partial answer to the first question. The lack

of pulsar discoveries in the inner parsec can be attributed to a lack of sensitivity, orbital modulation, or complex heterogeneous scattering along different lines of sight. The answer to the second question will of course depend on the answers to the first. If we are sensitivity limited, then there is little hope of detecting any new pulsars in the inner parsec with existing telescopes. If the issue is just that the pulsars are in short-period binaries, then we could detect them with current telescopes (current data, even!) if we utilize orbital search techniques that are more sophisticated than the one parameter acceleration search. If the issue is instead that pulsars are hidden behind a complex scattering screen with a hyperstrong component, then a multi-frequency approach is needed.

While we have only partially answered the questions we started with, the gaps in our current knowledge clearly indicate the necessary future work. To discover pulsars in tight orbits, we need to search the available data as deeply as possible using more computationally intensive search techniques like sideband searches and circular orbit fitting. To better understand the scattering environment, we need to discover more pulsars in the inner 15 arcminutes around Sgr A*. These pulsars will provide new lines of sight that will constrain the distribution of free electrons. Processing and searching the tens of thousands of beams in the fast-visibility VLA data presents an excellent opportunity to discover new pulsars in this region. Additionally, we can conduct another survey of OH/IR stars. The OH maser emission from these stars (which populate the inner half degree or so) provides a radio point source that can be used to measure angular scatter broadening. Finally, we can conduct high frequency observations using telescopes like ALMA and completely ignore all scattering effects. Each of these projects will further elucidate the nature of the Galactic center and will aid in the detection of a pulsar orbiting around the supermassive black hole Sgr A*.

BIBLIOGRAPHY

Abazajian, K. N. 2011, Journal of Cosmology and Astroparticle Physics, 3, 10

Abdo, A. A., Ackermann, M., Ajello, M., et al. 2009a, Science, 325, 848

—. 2009b, Astrophys. J., Suppl. Ser., 183, 46

—. 2010a, Astrophys. J., Suppl. Ser., 187, 460

—. 2010b, Astron. Astrophys., 524, A75

Alpar, M. A., Cheng, A. F., Ruderman, M. A., & Shaham, J. 1982, Nature, 300, 728

An, T., Goss, W. M., Zhao, J.-H., et al. 2005, Astrophys. J., Lett., 634, L49

Anantharamaiah, K. R., & Bhattacharya, D. 1986, Journal of Astrophysics and Astronomy, 7, 141

Anderson, L. D., Bania, T. M., Balser, D. S., et al. 2011, Astrophys. J., Suppl. Ser., 194, 32

—. 2013, ArXiv e-prints, arXiv:1312.6202

Bartko, H., Martins, F., Trippe, S., et al. 2010, Astrophys. J., 708, 834

Bates, S. D., Johnston, S., Lorimer, D. R., Kramer, M., et al. 2011, Mon. Not. R. Astron. Soc., 411, 1575

Benjamin, R. A., Churchwell, E., Babler, B. L., et al. 2003a, Publ.. Astron. Soc. Pac., 115, 953

—. 2003b, Publ.. Astron. Soc. Pac., 115, 953

Bessell, M. S., Castelli, F., & Plez, B. 1998, Astron. Astrophys., 333, 231

Bhat, N. D. R., Cordes, J. M., Camilo, F., Nice, D. J., & Lorimer, D. R. 2004, Astrophys. J., 605, 759

Bhattacharya, D., & van den Heuvel, E. P. J. 1991, Phys. Rep., 203, 1

Bloom, J. S., Kulkarni, S. R., & Djorgovski, S. G. 2002, Astron. J., 123, 1111

Blum, R. D., Ramírez, S. V., Sellgren, K., & Olsen, K. 2003, Astrophys. J., 597, 323

Bower, G. C., Deller, A., Demorest, P., Brunthaler, A., et al. 2014, Astrophys. J., Lett., 780, L2

Bower, G. C., Deller, A., Demorest, P., et al. 2015, Astrophys. J., 798, 120

Bower, G. C., Falcke, H., Herrnstein, R. M., et al. 2004, Science, 304, 704

Bower, G. C., Goss, W. M., Falcke, H., Backer, D. C., & Lithwick, Y. 2006, Astrophys. J., Lett., 648, L127

Boyarsky, A., Malyshev, D., & Ruchayskiy, O. 2011, Physics Letters B, 705, 165

Bridle, A. H. 1989, in Astronomical Society of the Pacific Conference Series, Vol. 6, Synthesis Imaging in Radio Astronomy, ed. R. A. Perley, F. R. Schwab, & A. H. Bridle, 443–+

Bühler, R., & Blandford, R. 2014, Reports on Progress in Physics, 77, 066901

Burke-Spolaor, S., Johnston, S., Bailes, M., et al. 2012, Mon. Not. R. Astron. Soc., 423, 1351

Camilo, F., Ransom, S. M., Gaensler, B. M., & Lorimer, D. R. 2009, Astrophys. J., Lett., 700, L34

Camilo, F., Ransom, S. M., Halpern, J. P., & Reynolds, J. 2007, Astrophys. J., Lett., 666, L93

Camilo, F., Ransom, S. M., Halpern, J. P., Reynolds, J., et al. 2006, Nature, 442, 892

Carey, S. J., Noriega-Crespo, A., Mizuno, D. R., et al. 2009, Publ.. Astron. Soc. Pac., 121, 76

Carilli, C. L., & Yun, M. S. 1999, Astrophys. J., Lett., 513, L13

Cheng, K. S., Taam, R. E., & Wang, W. 2006, Astrophys. J., 641, 427

Chennamangalam, J., & Lorimer, D. R. 2013, ArXiv e-prints, arXiv:1311.4846

Churchwell, E., Babler, B. L., Meade, M. R., et al. 2009a, Publ.. Astron. Soc. Pac., 121, 213

—. 2009b, Publ.. Astron. Soc. Pac., 121, 213

Clark, G. W. 1975, Astrophys. J., Lett., 199, L143

Condon, J. J. 1992, Ann. Rev. Astron. Astrophys., 30, 575

Cordes, J. M., Bhat, N. D. R., Hankins, T. H., et al. 2004, Astrophys. J., 612, 375

Cordes, J. M., & Lazio, T. J. W. 1997, Astrophys. J., 475, 557

—. 2001, Astrophys. J., 549, 997

—. 2002, ArXiv Astrophysics e-prints, arXiv:astro-ph/0207156

Cordes, J. M., & McLaughlin, M. A. 2003, Astrophys. J., 596, 1142

Cordes, J. M., & Rickett, B. J. 1998, Astrophys. J., 507, 846

Cordes, J. M., & Wasserman, I. 2016, Mon. Not. R. Astron. Soc., 457, 232

Crocker, R. M., Jones, D. I., Aharonian, F., et al. 2011, Mon. Not. R. Astron. Soc., 413, 763

Davies, R. D., Walsh, D., & Booth, R. S. 1976, Mon. Not. R. Astron. Soc., 177, 319

Deneva, I. S. 2010, PhD thesis, Cornell University

Deneva, J. S., Cordes, J. M., & Lazio, T. J. W. 2009, Astrophys. J., Lett., 702, L177

Dexter, J., Degenaar, N., Kerr, M., et al. 2017, Mon. Not. R. Astron. Soc., 468, 1486

Dexter, J., & O'Leary, R. M. 2013, ArXiv e-prints, arXiv:1310.7022

Diehl, R., Halloin, H., Kretschmer, K., et al. 2006, Nature, 439, 45

Drew, J. E., Greimel, R., Irwin, M. J., et al. 2005, Mon. Not. R. Astron. Soc., 362, 753

Eatough, R. P., Falcke, H., Karuppusamy, R., et al. 2013, Nature, 501, 391

Elvis, M., Wilkes, B. J., McDowell, J. C., et al. 1994, Astrophys. J., Suppl. Ser., 95, 1

Emmering, R. T., & Chevalier, R. A. 1989, Astrophys. J., 345, 931

Falcke, H., Goss, W. M., Matsuo, H., et al. 1998, Astrophys. J., 499, 731

Faucher-Giguère, C.-A., & Kaspi, V. M. 2006, Astrophys. J., 643, 332

Faucher-Giguère, C.-A., & Loeb, A. 2011, Mon. Not. R. Astron. Soc., 415, 3951

Figer, D. F. 2008, in IAU Symposium, Vol. 250, IAU Symposium, ed. F. Bresolin, P. A. Crowther, & J. Puls, 247–256

Foreman-Mackey, D., Hogg, D. W., Lang, D., & Goodman, J. 2013, Publ.. Astron. Soc. Pac., 125, 306

Frail, D. A., Diamond, P. J., Cordes, J. M., & van Langevelde, H. J. 1994, Astrophys. J., Lett., 427, L43

Fruchter, A. S., & Goss, W. M. 1990, Astrophys. J., Lett., 365, L63

Fukugita, M., Ichikawa, T., Gunn, J. E., et al. 1996, Astron. J., 111, 1748

Gaensler, B. M., & Slane, P. O. 2006, Ann. Rev. Astron. Astrophys., 44, 17

Gaustad, J. E., McCullough, P. R., Rosing, W., & Van Buren, D. 2001, Publ.. Astron. Soc. Pac., 113, 1326

Genzel, R., Eisenhauer, F., & Gillessen, S. 2010, Rev. Mod. Phys., 82, 3121

Genzel, R., Thatte, N., Krabbe, A., Kroker, H., & Tacconi-Garman, L. E. 1996, Astrophys. J., 472, 153

Gezari, S., Martin, D. C., Milliard, B., et al. 2006, Astrophys. J., Lett., 653, L25

Ghez, A. M., Duchêne, G., Matthews, K., et al. 2003, Astrophys. J., Lett., 586, L127

Ghez, A. M., Salim, S., Weinberg, N. N., & et al. 2008, Astrophys. J., 689, 1044

Gillessen, S., Eisenhauer, F., Trippe, S., et al. 2009, Astrophys. J., 692, 1075

Gillessen, S., Plewa, P. M., Eisenhauer, F., et al. 2017, Astrophys. J., 837, 30

Goodman, J., & Weare, J. 2010, Comm. App. Math. Comp. Sci., 5, 65

Haffner, L. M., Reynolds, R. J., & Tufte, S. L. 1998, Astrophys. J., Lett., 501, L83

Handa, T., Sofue, Y., Nakai, N., et al. 1987, Publ. Aston. Soc. Jpn., 39, 709

He, C., Ng, C.-Y., & Kaspi, V. M. 2013, 768, 64

Heger, A., Fryer, C. L., Woosley, S. E., Langer, N., & Hartmann, D. H. 2003, Astrophys. J., 591, 288

Helfand, D. J., Manchester, R. N., & Taylor, J. H. 1975, Astrophys. J., 198, 661

Hewett, P. C., Warren, S. J., Leggett, S. K., & Hodgkin, S. T. 2006, Mon. Not. R. Astron. Soc., 367, 454

Hooper, D., & Goodenough, L. 2011, Physics Letters B, 697, 412

Inoue, S. 2004, Mon. Not. R. Astron. Soc., 348, 999

Johnston, S., Kramer, M., Lorimer, D. R., et al. 2006, Mon. Not. R. Astron. Soc., 373, L6

Kaspi, V. M., Archibald, R. F., Bhalerao, V., et al. 2014, Astrophys. J., 786, 84

Katz, J. I. 1975, Nature, 253, 698

Keane, E. F., Johnston, S., Bhandari, S., et al. 2016, Nature, 530, 453

Kennea, J. A., Burrows, D. N., Kouveliotou, C., et al. 2013, Astrophys. J., Lett., 770, L24

Kinkhabwala, A., & Thorsett, S. E. 2000, Astrophys. J., 535, 365

Knispel, B. 2011, PhD thesis, Albert-Einstein-Institut

Körding, E., Falcke, H., & Corbel, S. 2006, Astron. Astrophys., 456, 439

Kramer, M. 1998, Astrophys. J., 509, 856

Kramer, M., Xilouris, K. M., Lorimer, D. R., et al. 1998, Astrophys. J., 501, 270

Laguna, P., & Wolszczan, A. 1997, Astrophys. J., Lett., 486, L27+

Lambert, H. C., & Rickett, B. J. 1999, Astrophys. J., 517, 299

Lang, C. C., Goss, W. M., Cyganowski, C., & Clubb, K. I. 2010, Astrophys. J., Suppl. Ser., 191, 275

Lang, C. C., Goss, W. M., & Morris, M. 2001, Astron. J., 121, 2681

Lang, C. C., Johnson, K. E., Goss, W. M., & Rodríguez, L. F. 2005, Astron. J., 130, 2185

LaRosa, T. N., Kassim, N. E., Lazio, T. J. W., & Hyman, S. D. 2000, Astron. J., 119

Law, C. J., Bower, G. C., Pokorny, M., et al. 2012, Astrophys. J., 760, 124

Law, C. J., Yusef-Zadeh, F., Cotton, W. D., et al. 2008, Astrophys. J., Suppl. Ser., 177, 255

Law, C. J., Bower, G. C., Burke-Spolaor, S., et al. 2015, Astrophys. J., 807, 16

Lawrence, A., Warren, S. J., Almaini, O., et al. 2007, Mon. Not. R. Astron. Soc., 379, 1599

Lazio, T. J. W. 2004, Astrophys. J., 613, 1023

Lazio, T. J. W., Anantharamaiah, K. R., Goss, W. M., et al. 1999, Astrophys. J., 515, 196

Lazio, T. J. W., & Cordes, J. M. 1998a, Astrophys. J., 505, 715

—. 1998b, Astrophys. J., Suppl. Ser., 118, 201

—. 2008, Astrophys. J., Suppl. Ser., 174, 481

Levin, L., Bailes, M., Bates, S., Bhat, N. D. R., et al. 2010, Astrophys. J., Lett., 721, L33

Levin, L., Bailes, M., Bates, S. D., Bhat, N. D. R., et al. 2012, Mon. Not. R. Astron. Soc., 422, 2489

Lindqvist, M., Habing, H. J., & Winnberg, A. 1992, Astron. Astrophys., 259, 118

Liu, K., Wex, N., Kramer, M., Cordes, J. M., & Lazio, T. J. W. 2011, ArXiv e-prints, arXiv:1112.2151

—. 2012, Astrophys. J., 747, 1

Lo, K. Y., Backer, D. C., Ekers, R. D., et al. 1985, Nature, 315, 124

Lo, K. Y., Backer, D. C., Kellermann, K. I., et al. 1993, Nature, 362, 38

Loeb, A., Shvartzvald, Y., & Maoz, D. 2014, Mon. Not. R. Astron. Soc., 439, L46

Löhmer, O., Kramer, M., Mitra, D., Lorimer, D. R., & Lyne, A. G. 2001, Astrophys. J., Lett., 562, L157

Lonsdale, C. J., Diamond, P. J., Thrall, H., Smith, H. E., & Lonsdale, C. J. 2006, Astrophys. J., 647, 185

Lorimer, D. R., Bailes, M., McLaughlin, M. A., Narkevic, D. J., & Crawford, F. 2007, Science, 318, 777

Lorimer, D. R., Faulkner, A. J., Lyne, A. G., et al. 2006, Mon. Not. R. Astron. Soc., 372, 777

Lorimer, D. R., & Kramer, M. 2004, Handbook of Pulsar Astronomy

Lorimer, D. R., Yates, J. A., Lyne, A. G., & Gould, D. M. 1995, Mon. Not. R. Astron. Soc., 273, 411

Lundgren, S. C., Cordes, J. M., Ulmer, M., Matz, S. M., et al. 1995, Astrophys. J., 453, 433

Lynch, R. S., Archibald, R. F., Kaspi, V. M., et al. 2015, Astrophys. J., 806, 266

Lyne, A., Graham-Smith, F., Weltevrede, P., et al. 2013, Science, 342, 598

Lyne, A. G., Manchester, R. N., Lorimer, D. R., et al. 1998, Mon. Not. R. Astron. Soc., 295, 743

Lyubarsky, Y. 2014, Mon. Not. R. Astron. Soc., 442, L9

Macquart, J.-P., Kanekar, N., Frail, D. A., & Ransom, S. M. 2010, Astrophys. J., 715, 939

Manchester, R. N., Hobbs, G. B., Teoh, A., & Hobbs, M. 2005, Astron. J., 129, 1993

Maoz, D., Loeb, A., Shvartzvald, Y., et al. 2015, Mon. Not. R. Astron. Soc., 454, 2183

Maron, O., Kijak, J., Kramer, M., & Wielebinski, R. 2000, Astron. Astrophys. Suppl. Ser., 147, 195

Marshall, D. J., Robin, A. C., Reylé, C., et al. 2006, Astron. Astrophys., 453, 635

Mathis, J. S. 1990, Ann. Rev. Astron. Astrophys., 28, 37

McMullin, J. P., Waters, B., Schiebel, D., Young, W., & Golap, K. 2007a, in Astronomical Society of the Pacific Conference Series, Vol. 376, Astronomical Data Analysis Software and Systems XVI, ed. R. A. Shaw, F. Hill, & D. J. Bell, 127

McMullin, J. P., Waters, B., Schiebel, D., et al. 2007b, in Astronomical Society of the Pacific Conference Series, Vol. 376, Astronomical Data Analysis Software and Systems XVI, ed. R. A. Shaw, F. Hill, & D. J. Bell, 127

McQuinn, M. 2014, Astrophys. J., Lett., 780, L33

Metzger, M. R., Djorgovski, S. G., Kulkarni, S. R., et al. 1997, Nature, 387, 878

Miralda-Escudé, J., & Gould, A. 2000, Astrophys. J., 545, 847

Molnar, L. A., Mutel, R. L., Reid, M. J., & Johnston, K. J. 1995, Astrophys. J., 438, 708

Moran, J. M., Rodriguez, L. F., Greene, B., & Backer, D. C. 1990, Astrophys. J., 348, 147

Mori, K., Gotthelf, E. V., Zhang, S., An, H., et al. 2013, Astrophys. J., Lett., 770, L23

Morris, M. 1993, Astrophys. J., 408, 496

Muno, M. P., Baganoff, F. K., Bautz, M. W., et al. 2004, Astrophys. J., 613, 326

Muno, M. P., Baganoff, F. K., Brandt, W. N., Morris, M. R., & Starck, J.-L. 2008, Astrophys. J., 673, 251

Muno, M. P., Clark, J. S., Crowther, P. A., et al. 2006, Astrophys. J., Lett., 636, L41

Paumard, T., Genzel, R., Martins, F., et al. 2006, Astrophys. J., 643, 1011

Pedlar, A., Anantharamaiah, K. R., Ekers, R. D., et al. 1989, Astrophys. J., 342, 769

Pen, U.-L., & Connor, L. 2015, Astrophys. J., 807, 179

Pennucci, T. T., Possenti, A., Esposito, P., et al. 2015, Astrophys. J., 808, 81

Perley, R. A., & Butler, B. J. 2013, Astrophys. J., Suppl. Ser., 204, 19

Petroff, E., Johnston, S., Keane, E. F., et al. 2015, Mon. Not. R. Astron. Soc., 454, 457

Pfahl, E., & Loeb, A. 2004, Astrophys. J., 615, 253

Pfahl, E., Rappaport, S., & Podsiadlowski, P. 2002, Astrophys. J., 573, 283

Pfuhl, O., Fritz, T. K., Zilka, M., et al. 2011, Astrophys. J., 741, 108

Ransom, S. M. 2001, PhD thesis, Harvard University

Ransom, S. M., Cordes, J. M., & Eikenberry, S. S. 2003, Astrophys. J., 589, 911

Rea, N., Esposito, P., Pons, J. A., Turolla, R., et al. 2013, Astrophys. J., Lett., 775, L34

Reid, M. J., & Brunthaler, A. 2004, Astrophys. J., 616, 872

Reines, A. E., & Deller, A. T. 2012, Astrophys. J., Lett., 750, L24

Roberts, M. 2004, The Pulsar Wind Nebula Catalog (March 2005 version), http://www.physics.mcgill.ca/~pulsar/pwncat.html, ,

Rodríguez-Fernández, N. J., Martín-Pintado, J., & de Vicente, P. 2001, Astron. Astrophys., 377, 631

Romero, G. E., del Valle, M. V., & Vieyro, F. L. 2016, Phys. Rev. D, 93, 023001

Roshi, D. A., & Anantharamaiah, K. R. 2001, Astrophys. J., 557, 226

Roy, S. 2013, Astrophys. J., 773, 67

Roy, S., & Rao, A. P. 2004, Mon. Not. R. Astron. Soc., 349, L25

Roy, S., & Rao, A. P. 2009, in Astronomical Society of the Pacific Conference Series, Vol. 407, The Low-Frequency Radio Universe, ed. D. J. Saikia, D. A. Green, Y. Gupta, & T. Venturi, 267

Schlafly, E. F., & Finkbeiner, D. P. 2011, Astrophys. J., 737, 103

Schlegel, D. J., Finkbeiner, D. P., & Davis, M. 1998, Astrophys. J., 500, 525

Schnitzeler, D. H. F. M., Eatough, R. P., Ferrière, K., et al. 2016, Mon. Not. R. Astron. Soc., 459, 3005

Schödel, R., Merritt, D., & Eckart, A. 2009, Astron. Astrophys., 502, 91

Schödel, R., Ott, T., Genzel, R., et al. 2002, Nature, 419, 694

Scholz, P., Spitler, L. G., Hessels, J. W. T., et al. 2016, ArXiv e-prints, arXiv:1603.08880

Schraml, J., & Mezger, P. G. 1969, Astrophys. J., 156, 269

Schultheis, M., Chen, B. Q., Jiang, B. W., Gonzalez, O. A., et al. 2014, Astron. Astrophys., 566, A120

Serylak, M., Stappers, B. W., Weltevrede, P., et al. 2009, Mon. Not. R. Astron. Soc., 394, 295

Shannon, R. M., & Johnston, S. 2013, Mon. Not. R. Astron. Soc., 435, L29

Shannon, R. M., Osłowski, S., Dai, S., et al. 2014, Mon. Not. R. Astron. Soc., 443, 1463

Sharpless, S. 1959, Astrophys. J., Suppl. Ser., 4, 257

Simpson, J. P., Colgan, S. W. J., Cotera, A. S., et al. 2007, Astrophys. J., 670, 1115

Sjouwerman, L. O., van Langevelde, H. J., Winnberg, A., & Habing, H. J. 1998, Astron. Astrophys. Suppl. Ser., 128, 35

Skrutskie, M. F., Cutri, R. M., Stiening, R., et al. 2006, Astron. J., 131, 1163

Spitler, L. G., Cordes, J. M., Chatterjee, S., & Stone, J. 2012, Astrophys. J., 748, 73

Spitler, L. G., Lee, K. J., Eatough, R. P., et al. 2014a, Astrophys. J., Lett., 780, L3

Spitler, L. G., Cordes, J. M., Hessels, J. W. T., et al. 2014b, Astrophys. J., 790, 101

Spitler, L. G., Scholz, P., Hessels, J. W. T., et al. 2016, Nature, 531, 202

Staelin, D. H. 1969, IEEE Proceedings, 57, 724

Strüder, L., Briel, U., Dennerl, K., et al. 2001, 365, L18

Tauris, T. M., & Manchester, R. N. 1998, Mon. Not. R. Astron. Soc., 298, 625

Taylor, J. H. 1992, Royal Society of London Philosophical Transactions Series A, 341, 117

Taylor, J. H., & Cordes, J. M. 1993, Astrophys. J., 411, 674

Thornton, D., Stappers, B., Bailes, M., et al. 2013, Science, 341, 53

Torne, P., Desvignes, G., Eatough, R. P., Karuppusamy, R., et al. 2017, Mon. Not. R. Astron. Soc., 465, 242

Torne, P., Eatough, R. P., Karuppusamy, R., Kramer, M., et al. 2015, Mon. Not. R. Astron. Soc., 451, L50

Trotter, A. S., Moran, J. M., & Rodriguez, L. F. 1998, Astrophys. J., 493, 666

Turner, M. J. L., Abbey, A., Arnaud, M., et al. 2001, 365, L27

van Dokkum, P. G., Abraham, R., Merritt, A., et al. 2015, Astrophys. J., Lett., 798, L45

van Langevelde, H. J., & Diamond, P. J. 1991, Mon. Not. R. Astron. Soc., 249, 7P

van Langevelde, H. J., Frail, D. A., Cordes, J. M., & Diamond, P. J. 1992, Astrophys. J., 396, 686

van Langevelde, H. J., Janssens, A. M., Goss, W. M., et al. 1993, Astron. Astrophys. Suppl. Ser., 101, 109

Vedantham, H. K., Ravi, V., Mooley, K., et al. 2016, Astrophys. J., Lett., 824, L9

Wang, Q. D., Dong, H., Cotera, A., Stolovy, S., et al. 2010, Mon. Not. R. Astron. Soc., 402, 895

Wang, W., Jiang, Z. J., & Cheng, K. S. 2005, Mon. Not. R. Astron. Soc., 358, 263

Watters, K. P., Romani, R. W., Weltevrede, P., & Johnston, S. 2009, Astrophys. J., 695, 1289

Wex, N., & Kopeikin, S. M. 1999, Astrophys. J., 514, 388

Wilkinson, P. N., Narayan, R., & Spencer, R. E. 1994, Mon. Not. R. Astron. Soc., 269, 67

Williams, P. K. G., & Berger, E. 2016, Astrophys. J., Lett., 821, L22

Williams, P. K. G., Clavel, M., Newton, E., & Ryzhkov, D. 2017, pwkit: Astronomical utilities in Python, Astrophysics Source Code Library, , , ascl:1704.001

Wrobel, J. M. 1983, Astron. J., 88, 1757

Yusef-Zadeh, F., Roberts, D. A., Goss, W. M., et al. 1999, Astrophys. J., 512, 230

Zacharias, N., Finch, C. T., Subasavage, J. P., et al. 2015, in American Astronomical Society Meeting Abstracts, Vol. 225, American Astronomical Society Meeting Abstracts, 433.01

Zhang, L., & Cheng, K. S. 1997, The Astrophysical Journal, 487, 370. http://stacks.iop.org/0004-637X/487/i=1/a=370